Dynamic Earth Energy Storage: Terawatt-year, Grid-scale Energy Storage Using Planet Earth as a Thermal Battery (GeoTES): Phase I Project Final Report

Travis L. McLing, Wencheng Jin, Ghanashyam Neupane, and Trevor Atkinson
Idaho National Laboratory

Patrick Dobson, Christine Doughty, and Nic Spycher
Lawrence Berkeley National Laboratory

Robert W. Smith
University of Idaho

iNL Idaho National Laboratory

Dynamic Earth Energy Storage: Terawatt-year, Grid-scale Energy Storage using Planet Earth as a Thermal Battery (GeoTES): Phase I Project Final Report

Travis L. McLing, Wencheng Jin, Ghanashyam Neupane, and Trevor Atkinson
Idaho National Laboratory

Patrick Dobson, Christine Doughty, and Nic Spycher
Lawrence Berkeley National Laboratory

Robert W. Smith
University of Idaho

April 2022

Idaho National Laboratory
Idaho Falls, Idaho 83415

http://www.inl.gov

Page intentionally left blank

EXECUTIVE SUMMARY

Grid-scale energy storage has been identified by the U.S. Department of Energy's (DOE) Energy Storage Grand Challenge as a necessary technology to support the continued build-out of intermittent renewable energy resources required to attain a carbon-free energy future. To meet this goal, the 2018 Department of Energy Research and Innovation Act mandated the creation of a comprehensive program to accelerate the development and commercialization of next-generation energy storage technologies. One of numerous energy storage technology options is the storage of excess energy as heated geothermal brine in suitable geologic formations. This concept, known as reservoir thermal energy storage (RTES), geologic thermal energy storage (GeoTES), aquifer thermal energy storage (ATES), etc., relies on the storage of thermal energy in geologic formations for recovery and use in large-scale direct use geothermal (e.g., district heating, industrial processes, etc.) and electrical power generation applications. This thermal energy is derived from excess or waste heat from any high-temperature heat source, such as concentrated solar or from conventional thermal/nuclear generation. As such, RTES can potentially play a significant role in meeting the energy storage shortfall in the coming decades. RTES can provide energy arbitrage through both the storage and production of thermal energy stored in geologic formations for direct use applications and can serve as a source of hot fluids that can be used to generate electricity to support peak demand ramping, thus easing stress on transmission and distribution. This energy storage option has geographic benefits in that energy can be stored locally or regionally depending on the various needs/loads. RTES can also be located across an enormous geographic area, without the need for a traditional hydrothermal resource but where thermal gradients and hydrogeology allow economic exploitation of subsurface heat. The work conducted for this project includes (1) a review of lessons learned from past high-temperature RTES international projects; (2) geochemical experimental investigation and numerical simulations of potential domestic sedimentary reservoirs and (3) development of a thermo-hydrological-mechanical (THM) numerical simulation tool for optimizing formation properties and design parameters to maximize thermal energy storage performance.

A review of international RTES projects has shown, similarly to many subsurface projects, that a variety of factors are responsible for the success/failure of an RTES system. These range from insufficient site characterization, scaling and corrosion issues, availability of and market constraints on heat to charge the system, and inappropriate water treatment systems, among other factors. Further modeling, drilling, sampling, and analysis prior to system initiation, as well as close monitoring and mitigation techniques during operations are essential to the success of a project. Geochemical modeling and subsequent experimentation under reservoir conditions (T=140-250°C and P=1-50 bars PCO_2) indicate that depending on the formation and brine compositions, scaling and corrosion factors may be anticipated and planned for to mitigate future operational problems. In addition to this, CO_2-charged brines originally thought to help with scaling problems have proven to be complicated in that under certain conditions, they may induce dissolution in the reservoir and cause further complications in top side equipment or mechanical stability of the subsurface formation. Thermal-hydrological and chemical modeling with TOUGH was evaluated for two formations (Weber and Tuscaloosa sandstones) under varying operational scenarios identifying potential issues with scale minerals and subsurface hydrogeological changes induced by injection and extraction of heated fluids over a 10-year period. Generally, energy recovery factors increase over the life of an RTES system due to increased ability to extract previously injected heat. Sensitivity analyses were also conducted to evaluate flow rates, porosity and permeability heterogeneity, and buoyancy effects. Geochemical modeling indicates various levels of dissolution and precipitation of quartz, calcite, and anhydrite occurring within these formations downhole in the immediate areas surrounding injection/extraction wells depending on the operational scenario. It was also learned that the total dissolved solids (TDS) concentration of the brine does not necessarily correlate with amounts of mineral precipitation within a system. Finally, a comparison of the TOUGH work with modeling utilizing INL's Multiphysics Object-Oriented Simulation Environment shows good agreement between the two modeling platforms. Thermal-hydro-mechanical (THM) modeling was conducted and

found that hydrogeological changes are often caused by changing geomechanical conditions in the reservoir. Further stochastic simulation-enabled machine learning was conducted to develop a site feasibility workflow assessment for an RTES system utilizing reservoir size, thickness, permeability, porosity, and thermal conductivity data as well as operational conditions such as well separation, injection temperature, and flow rates. System optimization is largely dependent on operational parameters that can vary by location and performance.

The results described in this report shed light on various aspects of RTES including project siting, operational performance, mitigation of both subsurface and surface infrastructure issues, and system longevity. Additionally, the reviews of international projects provide valuable lessons associated with exploration, initiation, operation, and sustainable maintenance of RTES. Overall site characterization, THM modeling, risk evaluation, and flexible operations are key aspects to a suitable RTES project. Geochemical modeling supported by laboratory experiments show that understanding the intricacies in brine chemistry and fluid evolution within changing thermal and pressure environments is important because resultant diagenetic reactions and subsequent scaling exist even in unexpected scenarios. Thermo-hydro-chemical (THC) and THM modeling with MOOSE and TOUGH also inform the potential for hydrogeological and geochemical changes within the reservoir and best operational parameters over the life of an RTES system. The results of this study help define future RTES research projects that will facilitate successful future deployment of such systems and make RTES a more viable option for energy storage in the U.S.

Page intentionally left blank

CONTENTS

FIGURES

TABLES

ACRONYMS

ANN	artificial neural network
ARMA	American Rock Mechanics Association
ATES	aquifer thermal energy storage
BGS	below ground surface
BMSL	below mean sea level
BRGM	French Geological Survey
CCUS	carbon capture, utilization, and storage
CF	clay-sized fraction
CHP	combined heat and power
DIC	dissolved inorganic carbon
DOE	Department of Energy
DTS	distributed temperature sensing
EDS	energy dispersive X-ray spectroscopy
EOS	equation of state
FEM	finite element method
FY	fiscal year
GCB	Gulf Coast Basin
GeoTES	geologic thermal energy storage
GTO	Geothermal Technologies Office
GWB	The Geochemist's Workbench®
HT-RTES	High Temperature Reservoir Thermal Energy Storage
HT	high temperature
HTX	heat exchanger
IC	ion chromatography
ICP-MS	inductively coupled-plasma – mass spectroscopy
ICP-OES	inductively coupled-plasma – optical emission spectroscopy
INL	Idaho National Laboratory
LBNL	Lawrence Berkeley National Laboratory
LLNL	Lawrence Livermore National Laboratory

LT	low temperature
ML	machine learning
MOOSE	Multiphysics Objective Oriented Simulations Environment
RTES	Reservoir Thermal Energy Storage
SECARB	Southeast Regional Carbon Sequestration Partnership
SEM	scanning electron microscopy
SI	saturation indices
TDS	total dissolved solids
TES	thermal energy storage
TH	thermal-hydrologic
THC	thermal-hydrological-chemical
THM	thermal-hydrological-mechanical
TOC	total organic carbon
WR	whole rock
WY-CUSP	Wyoming Carbon Underground Storage Project
XRD	X-ray diffraction

Dynamic Earth Energy Storage: Terawatt-year, Grid-scale Energy Storage using Planet Earth as a Thermal Battery (GeoTES): Phase I Project Final Report

1.   INTRODUCTION

1.1   Project Objectives

We propose an advancement on the concept of energy storage that involves converting excess electrical energy to heat and storing it geologically in deep saline aquifers. Additionally, available/excess thermal energy (from thermal generation sources) can be directly stored geologically with minimal processing. Stored heat can then be withdrawn at a later time to be used directly (as process heat for industrial applications) or indirectly (electrical generation). Given the size, extent, and distribution of deep saline aquifers, the amount of energy that can be stored is enormous.

This study identifies methodologies that can be used to develop and manage the storage of heat by injecting and recovering hot brines in suitable geologic formations. The stored heat can be recovered when needed to produce dispatchable electrical power, or for large-scale direct use applications. The Geologic Thermal Energy Storage (RTES) system (heat input, storage, heat recovery, and heat to electric conversion), also known as Reservoir Thermal Energy Storage (RTES), has the potential to provide a unique pathway for using the suite of renewable energy sources, including geothermal energy, to decarbonize the US grid. Further, the RTES system can be used both to meet the nation's flexible energy needs while also improving grid stability and reliability through firming intermittent renewable energy sources. An additional benefit of the RTES concept is that it would help the U.S. Department of Energy's (DOE) Geothermal Technologies Office (GTO) increase the national footprint of geothermal energy into areas formerly thought to be unsuitable.

The operation of a RTES system encompasses three basic steps: (1) convert excess electricity to heat (or unwanted excess hot water) and store in a suitable geologic reservoir when economically feasible (e.g.), excess electricity produced by intermittent sources; (2) heat the subsurface over a long period of time (which could be combined with desalination and/or pressure management of large-scale carbon capture, utilization, and storage (CCUS) projects); and (3) produce the heat thereafter when needed for direct use or the generation of electricity using geothermal technology. The proposed solution is simple, efficient, and relies very little on external, unmanageable factors.

The goal for Phase I of the project is to bring the RTES analysis to a point where the science, engineering, and methods are mature enough to attract an industry partner for a field pilot demonstration. The focus of Phase I is centered around two primary tasks: 1) Reservoir characterization and suitability, and 2) Thermal storage modeling and scenario testing. The first task will review key lessons learned from past high-temperature reservoir thermal energy storage projects, identify appropriate geologic formations as possible candidate locations, conduct laboratory experiments using representative rock types at RTES temperatures, pressures, and fluid chemistries, and conduct geochemical modeling to validate the RTES concept. The second task involves defining thermal base cases, selecting appropriate reservoir criteria based on the first task, conducting THC and THM modeling, and refining both the injection and recovery well strategies and rock and fluid types to create a final focused case model. Key features that will be evaluated include:

1. **Determination of RTES battery charge and operation time** (i.e., how long does a reservoir need to be heated in order to recover beneficial heat): The charge time is a function of the amount of heat injected (rate and temperature), the size of the reservoir, and the amount of energy to be recovered (the desired ΔT or change in temperature). The RTES Team will consider a variety of operational parameters to bound the effective charge time.

2. **Round trip thermal efficiency of stored energy**: This requires a detailed understanding and high-resolution model of reservoir properties, such that we can determine the efficiency of thermal storage and recovery and estimate how much heat/fluid is lost to the surrounding environment.

3. **System sustainability**: The ability to store large quantities of recoverable thermal energy in geologic reservoirs will depend on a) the amount of heat that can be stored and recovered; b) how long can these systems operate under economically viable conditions (need to specify minimum thermal storage and flow reservoir requirements).

4. **Mitigation strategies**: Changing the thermal state of an equilibrated geologic reservoir will result in water-rock interaction, and most certainly will cause some issues with wellbore and reservoir scaling and/or corrosion, thus impacting resulting fluid flow from the system. Our THC-THM models will identify such effects and will evaluate potential mitigation strategies to increase long-term operation of the thermal battery.

The results of these evaluations will provide GTO with a range of thermal charge times for reservoirs of different sizes, well configurations, and injection/extraction parameters, and allow for RTES to be evaluated using a consistent set of thermal energy storage metrics (e.g., Ginosar and Wendt, 2021).

1.2   Phase I Tasks

Phase I of the project consists of the following tasks: Task 1 – Reservoir characterization and suitability, and Task 2 – Thermal storage modeling and scenario testing. Task 1 had two distinct activities: a review of lessons learned from past high-temperature underground thermal energy storage projects, and a series of laboratory experiments and corresponding coupled process modeling simulations using mineral and brine samples from selected potential reservoir thermal energy storage (RTES) sites to evaluate the potential for scaling and their potential for thermal energy storage. Our team conducted an extensive literature review of a suite of high-temperature reservoir thermal energy storage (HT-RTES) projects in Germany and the Netherlands to identify how site selection and characterization, project design and development, and systems operations impacted the success and/or failure of these projects. For the second component, we did coupled process modeling evaluations of potential sedimentary reservoirs in Wyoming, Illinois, and Mississippi, and conducted experimental studies on core and brine samples from the Weber Sandstone from the Rock Springs Uplift in Wyoming and from the Lower Tuscaloosa Formation from the Gulf Coast Basin in Mississippi. Modeling work using the Geochemist's Workbench ® (GWB) was conducted to compare experimental results with geochemical modeling results.

Task 2 consists of developing a modeling optimization framework to identify how different reservoir (formation thickness, depth, porosity, permeability, and thermal conductivity) and design and operational (well distance, injection temperature, flow rate) parameters impact the different performance metrics of a generic HT-RTES. A series of Monte Carlo stochastic models were run to determine how these parameters affect the charging time, functioning time, recovery rate, and storage capacity of the system. Machine learning models were trained based on the numerical data and used to formulate the multi-objective optimization framework in conjunction with a genetic algorithm.

2. RESULTS

2.1 Task 1 Results

2.1.1 Task 1.1 Lessons Learned from Past High-temperature Aquifer Thermal Energy Storage Projects

Europe is leading the world in designing and deploying aquifer thermal energy storage (ATES) projects, with over 2,500 systems currently in operation (Fleuchaus et al., 2018). However, almost all of these systems are operated at temperatures < 25°C, and only a handful of projects have been developed that store thermal waters at temperatures > 50°C. At first glance, this is a bit surprising, given that thermal energy storage at higher temperatures would yield more useful heat, and should provide more efficient thermal energy storage. However, regulatory, and operational issues have complicated the development of such systems.

Our team has conducted a case study review of selected projects in Germany and the Netherlands to evaluate how these projects were conceived, developed, and operated, with the objective of identifying lessons learned that could be applied to new projects. Here, we present an abbreviated summary of this review: a much more detailed review has been developed as a manuscript. The case study review consists of four high-temperature (>50°C) ATES projects in Germany and four high-temperature and two moderate temperature (25-50°C) ATES projects in the Netherlands (Table 1 and Figure 1). Some of these projects were conceived but not developed, others developed and later suspended or terminated, a few are operating, and one is currently in development. Each of the case studies examined are briefly described below, and key lessons learned are summarized.

Table 1. Key attributes of reviewed moderate (MT) and high-temperature (HT) ATES projects.

Site	Storage T (°C)	Fluid TDS (ppm)	Depth (m)	Lithology	Annual storage capacity (GWh$_{th}$)	# wells	Heat source	Years of operation
Developing projects								
TU Delft (N)	70	4700	560-580	Sandstone	TBD	1	Deep geot.	NA
Operational projects								
Rostock-Brinkmanshohe (G)	50		13-27	Sand	0.295	2	Solar	2000 – present
Monster (Koppert-Cress) (N)	40	9000 – 11000	160	Sand	6.1 – 7.8	8	Solar, CHP	2015 – present
Wageninen (N)	45		225-295	Fine sand	1.283	2	Solar	2012 – present
Middenmeer (N)	92	16000	360-383	Fine sand		2	Deep geot.	2021 – present

Site	Storage T (℃)	Fluid TDS (ppm)	Depth (m)	Lithology	Annual storage capacity (GWh$_{th}$)	# wells	Heat source	Years of operation
Suspended/Abandoned projects								
Berlin (G)	70	29000	320	Sandstone	2.65	2	Cogen.	1999-2018
Neubrandenburg (G)	87	130000	1250	Sandstone	15	2	Cogen.	2005-2019
BMW (G)	130	880	500	Limestone	NA	1	Cogen.	NA
Utrecht (N)	90		220-260	Med/fine sand	6	2	Cogen.	1991 – 1999
Hooge Burch Zwammerdam (N)	90		130-150	Med/fine sand	2.25	2	Cogen.	1998 – 2009

N – Netherlands; G – Germany; Deep geot. – Deep geothermal; Cogen. – cogeneration; CHP – combined heat and power system (uses natural gas); TBD – to be determined; NA – not applicable. Storage capacity values reflect design values. Data obtained from Kabus and Seibt, 2000; Kabus et al., 2000; Sanner et al., 2005; Böttcher, 2012; Wolfgram et al., 2011; Fleuchaus et al., 2020; Kabus et al., 2005; Seibt and Wolfgramm, 2008; Kabus et al., 2009; Seibt and Kabus, 2006; Wolfgramm and Seibt, 2006; Vetter et al., 2012; Schmidt and Müller-Steinhagen, 2004; 2005; Nußbicker-Lux et al., 2009; Bauer et al., 2010; Pavlov and Olesen, 2012; Schmidt et al., 2000; Bartels et al., 2003; Agster et al., 2004; Ueckert et al., 2016; 2020; Ueckert and Baumann, 2019; Hopman, 2015; Oerlemans, 2018; Bloemendal et al., 2019; 2020; 2021; Vardon et al., 2021; Bakema and Drijver, 2019; Bakema et al., 2019; Kallesøe and Vangkilde-Pedersen, 2019; van Loon and van der Heide, 1992; Drijver, 2012; Godschalk 2020; Dijkstra et al., 2020; AgriHolland, 2014; van Velden, 2019; Drijver et al., 2019.
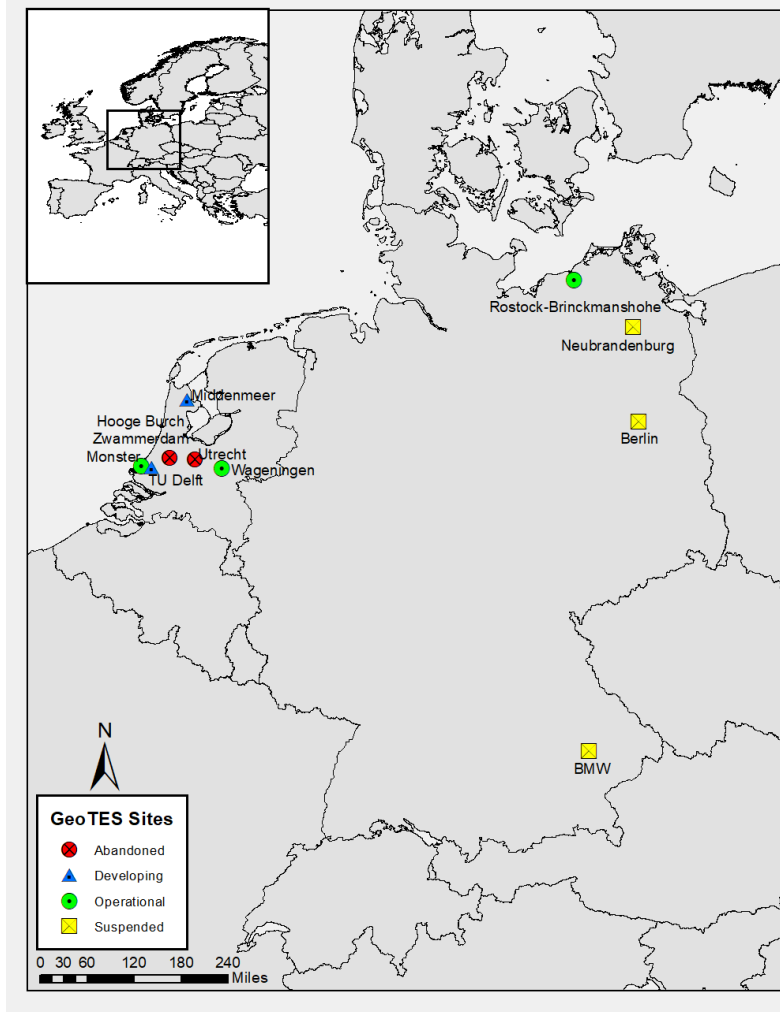
Figure 1. Map depicting locations of MT-ATES and HT-ATES sites described in this review.

2.1.2 Developing Projects

2.1.2.1 *TU Delft*

Delft University of Technology (TU Delft) has been designing an integrated system for decarbonizing their campus energy system (Figure 2). The current plans call for two different geothermal systems. Two deep (~2 km) wells would provide a source of hot water throughout the year, and a shallow HT-ATES reservoir would be used to store unneeded hot water produced during the summer months, thus augmenting the potential supply of hot water needed for heating during the wintertime. Site characterization and detailed numerical simulations and technoeconomic modeling studies have been conducted to evaluate the viability of this system (Vardon et al., 2021; Bloemendal et al., 2021). Two potential sandstone intervals are being considered to host the ATES reservoir.
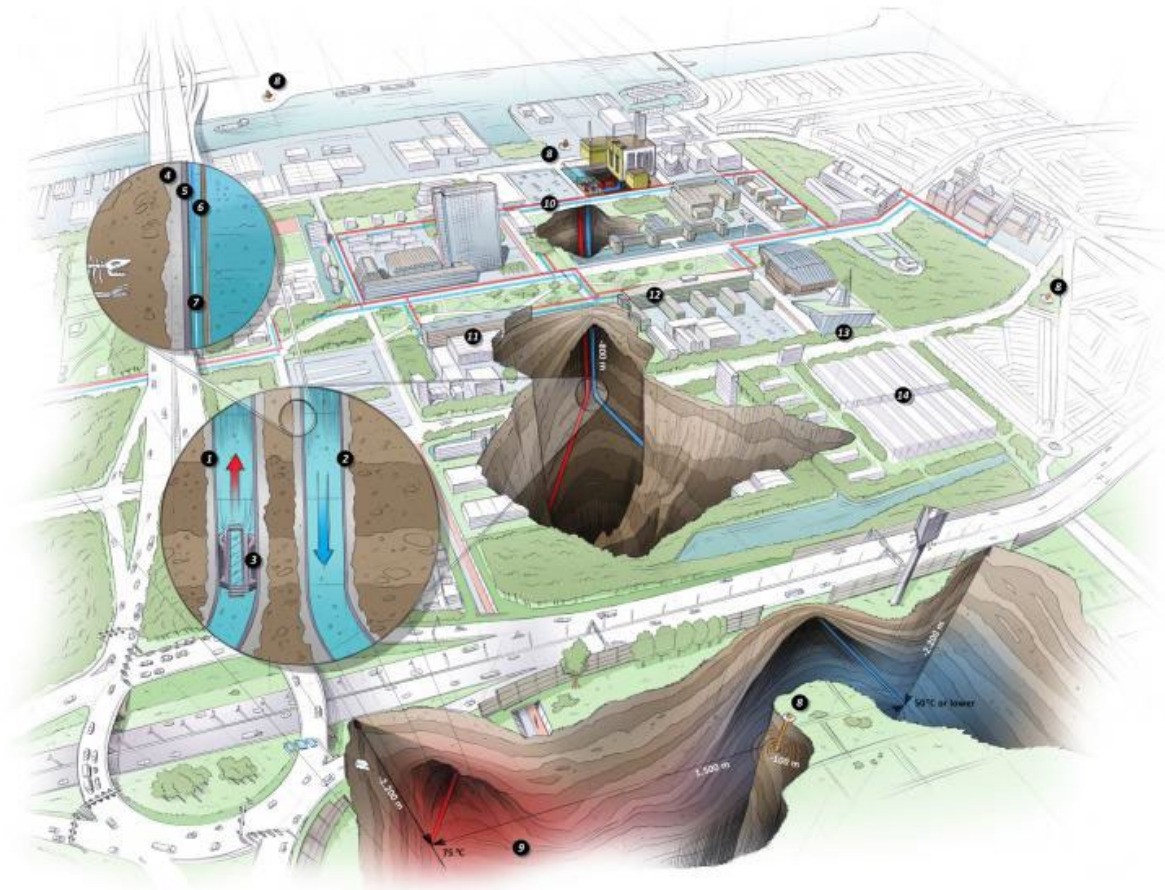
Figure 2. Conceptual illustration of the planned deep doublet well system for the TU Delft campus. The production well (shown in red) would produce 75°C water using a submersible pump to withdraw water at a rate of ~320 m^3/h (Vardon et al., 2021). The hot water would be used for heating the campus (utilizing the existing district heating system), and water not needed for heating during the summer months would be stored in a HT-ATES system at an intermediate depth. Source: https://www.delta.tudelft.nl/article/how-tu-delft-campus-will-switch-geothermal-heat.

Lessons Learned

- Combination of deep geothermal with HT-ATES, with expanded use of thermal water by the surrounding community, provides better project economics
- Potential interference with existing ATES systems in the Maassluis Formation
- Possible geochemical issues with the deeper Ommelanden Formation
- Density effects on the thermal plume have been identified as potentially impacting the system performance based on modeling results.

2.1.3 Operating Projects

2.1.3.1 Rostock-Brinkmanshohe

A HT-ATES system coupled with a central solar heating system began operation in Rostock-Brinckmanshöhe in 2000 (Figure 3). It was one of a number of hybrid solar assisted heating-seasonal thermal energy storage projects developed as part of the German research program "Solarthermie-2000" (Nußbicker-Lux et al., 2009). The HT-ATES system, integrated with a heat pump, is used for space and hot water heating for an apartment complex of 108 units. The system consists of a well doublet spaced 55 m apart and about 30 m deep, with the ATES reservoir located in Quaternary sediments. The system is charged between March and October using the solar collector system, and the stored water is used to power the district heating system during the winter months.
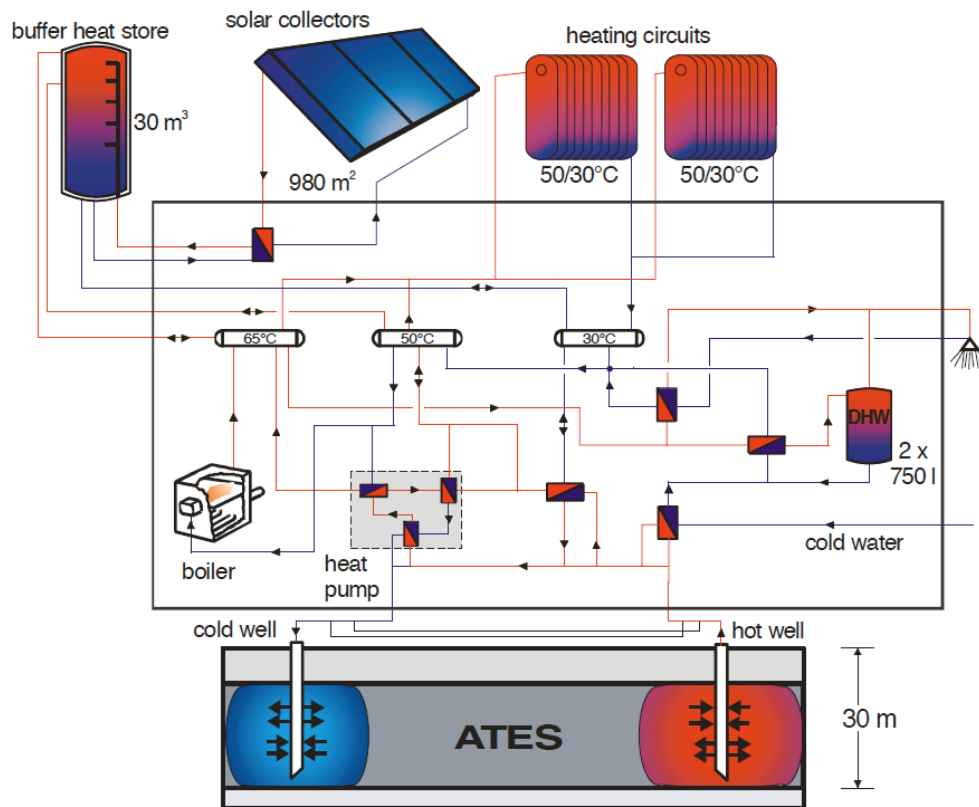
Figure 3. Schematic of Rostock Brinckmanshöhe ATES system (Schmidt and Müller-Steinhagen, 2004).

Lessons Learned

- Initial numerical modeling was conducted to help determine the proper spacing between the hot and cold wells

- Heating of the HT-ATES was limited to 50°C to avoid changes in groundwater chemistry that might cause scaling

- Breakthrough of groundwater to the surface at the cold well during a period of high flow attributed to the well screen being blocked – this was subsequently repaired

- Use of nitrogen appears to have prevented influx of oxygen into the reduced reservoir

- Failure of a downhole pump led to major downtime of the system during one winter cycle

- Annual variations in system performance results from differences in energy supply and demand, along with operational issues (pumps, leaking pipes)

- The site is actively monitored (7 monitoring wells with over 50 temperature sensors), and temperature profiles indicate some vertical heterogeneity in the permeability of the aquifer

- Relatively high estimated cost of levelized heat for this project (264 euros/MWh$_{th}$) partially attributed to the high cost of the solar collectors (Yang et al., 2021).

2.1.3.2 Monster (Koppert-Cress)

An ATES system has been operating since 2012 at the Koppert-Cress horticulture plant in Monster, the Netherlands, with the purpose of heating greenhouses (Bloemendal et al., 2019; 2020). The original system was designed to store water heated to 25°C, but the system was upgraded in 2015 to allow injection of fluids up to 45°C. The system consists of four warm wells and four cold wells, and utilizes two different sandstone aquifers, one at a depth of 55-75 m, and the other at a depth of 135-160 m. The water is heated using solar collectors and a combined heat and power (CHP) system from a neighboring greenhouse facility. Unlike many of the other ATES projects, this system often operates on a daily cycle, with heat being stored during the day, and then being used at night to maintain greenhouse temperatures. The system has been evolving over time, with additional greenhouses requiring more heat supplied by the ATES. A comprehensive monitoring system has been installed, involving monitoring wells and distributed temperature sensing (DTS) array deployed in the subsurface to evaluate the thermal conditions of the subsurface aquifers (Figure 4).
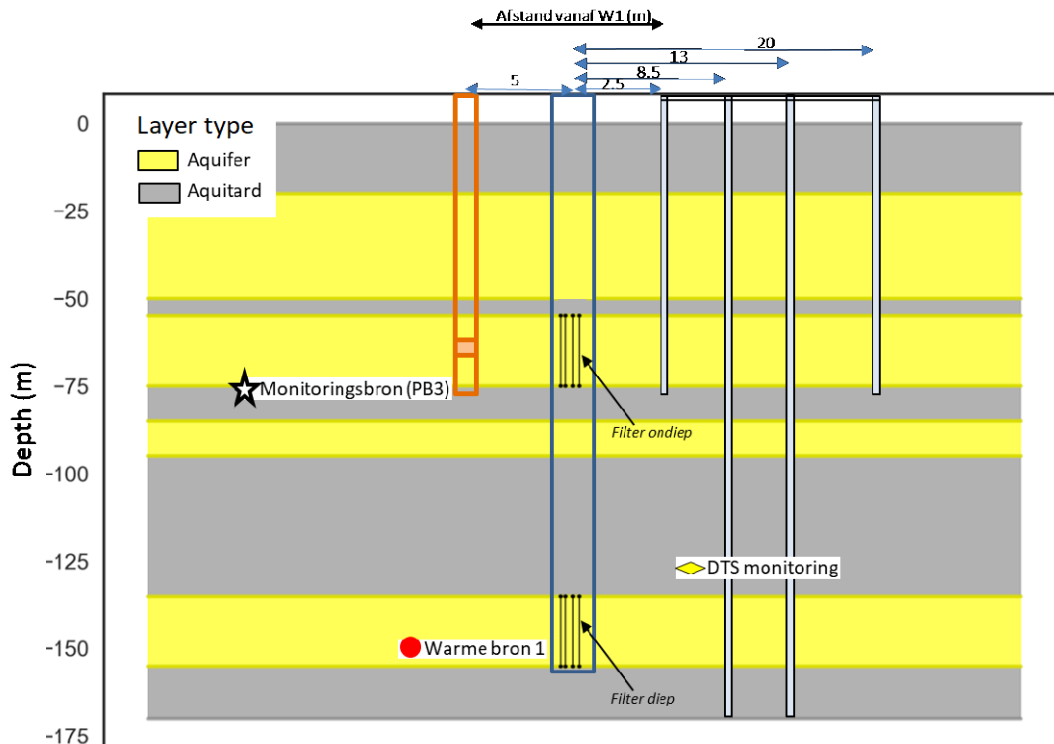
Figure 4. Cross section depicting the location of one warm well (W1), one monitoring well (PB3), and the DTS monitoring system in a series of boreholes located 2.5, 8.5, 13, and 20 m from the warm well (Bloemendal et al., 2020). The screened intervals in the warm well denote the two reservoir horizons used for thermal energy storage.

Lessons Learned

- Changing the storage warm water injection temperature from 25°C to 45°C was successful, and injecting even hotter water into the system is under consideration

- No significant issues with scaling have been reported to date

- Diurnal heating cycles has led to high utilization of the warm wells, and to an imbalance between the cold and warm portions of the subsurface aquifers (impacted area around cold wells is much larger than around warm wells)

- The monitoring system provides critical information relating to system performance and allows for modeling to evaluate different future operational scenarios.

2.1.3.3   *Wageningen*

A low-temperature (LT) ATES and a MT-ATES system (Figure 5) have been operating at the Netherlands Institute of Ecology of the Royal Netherlands Academy of Sciences (NIOO-KNAW) in Wageningen since 2012 (Bakema and Drijver, 2019; Bakema et al., 2019; Kallesøe and Vangkilde-Pedersen, 2019). The MT-ATES system, storing heat provided by solar collectors, is hosted by the Oosterhout Formation at a depth of 220-290 m; the LT-ATES system is located in a shallower reservoir horizon (Bakema et al., 2019; Kallesøe and Vangkilde-Pedersen, 2019). The MT-ATES consists of a well doublet spaced ~60 m apart. The amounts of stored and recovered heat from this system are much lower than the original design parameters; this poor performance is in part due to lower-than-expected flow in the aquifer[9], a reduced number of solar collectors to heat the water, and high building cut-off temperature, which allowed for minimal use of the stored heat. Subsurface temperatures are monitored in the warm and cold wells, along with the monitoring well; however, the monitoring well is too far away from the MT-ATES system to detect any thermal changes for the deeper MT-ATES reservoir horizon.

Figure 5. Locations of LT and MT-ATES (heat store) wells at NIOO-KNAW, Wageningen (Bakema and Drijver, 2019; Kallesøe and Vangkilde-Pedersen, 2019).

Lessons Learned

- The initial site characterization did not identify the large vertical variations in reservoir permeability, which has led to suboptimal performance (reduced well flow rates and reservoir storage capacity)

- A sufficient source of heating for the system (proper number of solar collectors) is needed to charge the system as designed

- Lowering the cut-off temperature required for the building heating system in 2016 has led to improved thermal recovery for the MT-ATES

- Improper drilling fluids may have led to clay swelling and resulting formation damage, also decreasing system performance

- No decrease in well capacity has been observed, suggesting that scaling is not an issue.

2.1.3.4 *Middenmeer*

This new HT-ATES demonstration site near Middenmeer is located at one of the largest greenhouse complexes in the Netherlands (Godschalk, 2020; Dijkstra et al., 2020; AgriHolland, 2014; van Velden, 2019). It is utilizing geothermal fluids from three deep (~2.5 km) sets of doublet wells producing hot water (~85°C) from the Permian Rotliegend Sandstone to heat greenhouses at the Agriport complex. The objective of the HT-ATES system is to store the produced geothermal hot water during the summer months, when it is not needed for heating greenhouses, and thus augment the amount of hot water available to heat the greenhouses during the winter months. Test well drilling conducted in 2019 evaluated the suitability of two candidate reservoirs: an aquifer in the Maassluis Formation, and a deeper aquifer in the Oosterhout Formation. Higher flow rates found in the upper reservoir, combined with significant levels of methane detected in the lower reservoir, led to the selection of the Maassluis Formation aquifer for the HT-ATES system. Drilling of the hot and cold wells to a depth of 380 m was initiated in June of 2020, and the charging of the hot well was begun in the summer of 2021 (Dinkelman, pers. comm.). The wells have installed fiber optic cables to allow for continuous monitoring of temperature. A comprehensive risk assessment of the project was conducted to evaluate potential issues and identify mitigation strategies; the highest risk factor was the accuracy of the demand and price forecast for the project. Geochemical modeling studies were conducted to evaluate the potential for carbonate scaling around the hot well, and to assess the potential effectiveness of co-injection of CO_2 to mitigate this risk.

Lessons Learned

- The test well helped characterize key hydrologic properties of the two candidate aquifer systems, and identified a major safety issue (presence of methane) that led to not selecting the deeper aquifer as a storage location

- Geochemical modeling identified the potential for carbonate scaling, thus helping to develop potential mitigation strategies prior to operation of the system

- A business case model (Dinkelman, 2019) and risk assessment (van Unen et al., 2020) were conducted to optimize system design and operations, and to identify early on potential high-risk issues

- Due to the early stages of this project, there are few results that can be evaluated to determine the initial success of this project; future project updates could provide this feedback.

2.1.4   Suspended/Abandoned Projects

2.1.4.1   Berlin

Both HT and LT-ATES systems were installed at the Reichstag complex in Berlin to assist with meeting its heating and cooling demands (Kabus et al., 2000; Kabus and Seibt, 2000; Sanner et al., 2005; Wolfgram et al., 2011; Böttcher, 2012) (Figure 6). The HT-ATES is hosted in Jurassic sandstones at a depth of ~300 m and is served by two wells that are about 300 m apart. The wells were designed so that they can serve as both injection and production wells, with the flow direction reversed depending on the season. The heat source for hot fluids injected in the HT-ATES during the summer months is a biofuel-powered cogeneration plant. Stepwise operation of the system began in 1999, with full operation commencing in 2003. The system was initially designed so that it could meet 90% of the annual heat demand. However, due to the higher demand for cooling in the summer months, excess heat from the cogeneration plant that would normally be used to charge the HT-ATES was redirected to operate the absorption cooling system, which led to reduced operational efficiency of the HT-ATES, and the eventual suspension of the HT-ATES system in 2018 (Fleuchaus et al., 2020).
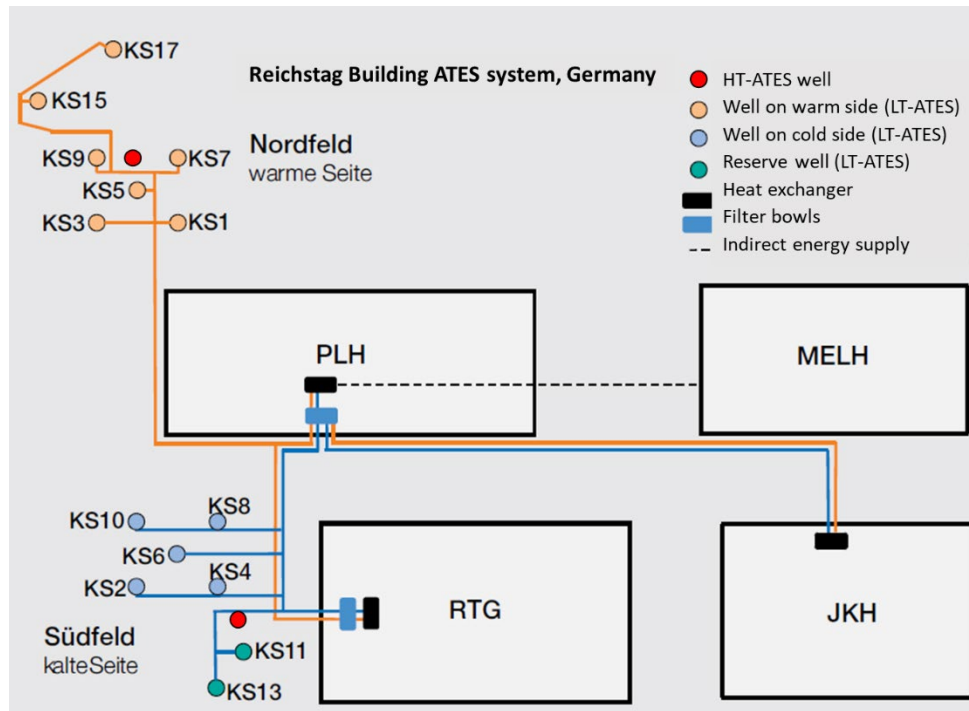
Figure 6. Schematic map showing the location of the HT-ATES and LT-ATES wells at the Reichstag building, Berlin. PLH – Paul Lobe Löbe House, RTG = Reichstag Building, JKH= Jakob Kaiser House, MELH= Marie Elisabeth Lüders House (modified from Wolfgramm et al., 2011).

Lessons learned:

- Changes in the availability of excess heat to charge the system can lead to reduced system performance, such as occurred when increased summertime cooling needs led to redirecting hot water produced by the cogen plant to power the absorption chiller units instead of recharging the HT-ATES.

- Reliance on a doublet well system for the HT-ATES system led to system shutdown during the winter of 2006-2007 when a submersible pump broke down. Including system redundancy or having a more rapid way to conduct repairs could lead to having a more resilient system.

- Careful design and completion of the wells, along with the use of nitrogen as headspace gas, appears to have been successful in mitigating potential geochemical issues in the wells.

2.1.4.2   Neubrandenburg

The HT-ATES system that was initiated at Neubrandenburg in 2005 was able to make use of two of the deep wells that were formerly part of a geothermal heating system that was commissioned in 1989 and later abandoned in 1998. The reconditioned wells, with depths between 1250 and 1300 m, are located ~1300 m apart, and were completed in the Lower Postera sandstone (Zenke et al., 2000; Seibt and Kellner, 2003; Kabus, 2003; Kabus et al., 2005; Seibt and Kabus, 2006; Seibt and Wolfgramm, 2008; Seibt et al., 2010). The wells reverse roles on a seasonal basis, one serving as an injector while the other one is a producer (Figure 7). Surplus heat from a gas and steam turbine cogeneration plant is used to supply the heat to charge the system in the summer months. The HT-ATES provided heat to the Rostocker Strasse district heating system, greatly reducing reliance to a peaking boiler system that had been used to provide extra heat to the district heating system during the wintertime. A bypass system was installed to facilitate monitoring of fluid chemistry, corrosion potential, and microbial activity. Corrosion-related problems associated with microbial activity led to breakdown of the submersible pumps, which led to system outages in 2006, 2008, 2009, and 2011 (Kabus et al., 2009; Lerm et al., 2013; Westphal et al., 2016). The HT-ATES system was operated until 2019, when the public utility system opted to use a surface storage tank to balance short-term differences in supply and demand (Fleuchaus et al., 2020).
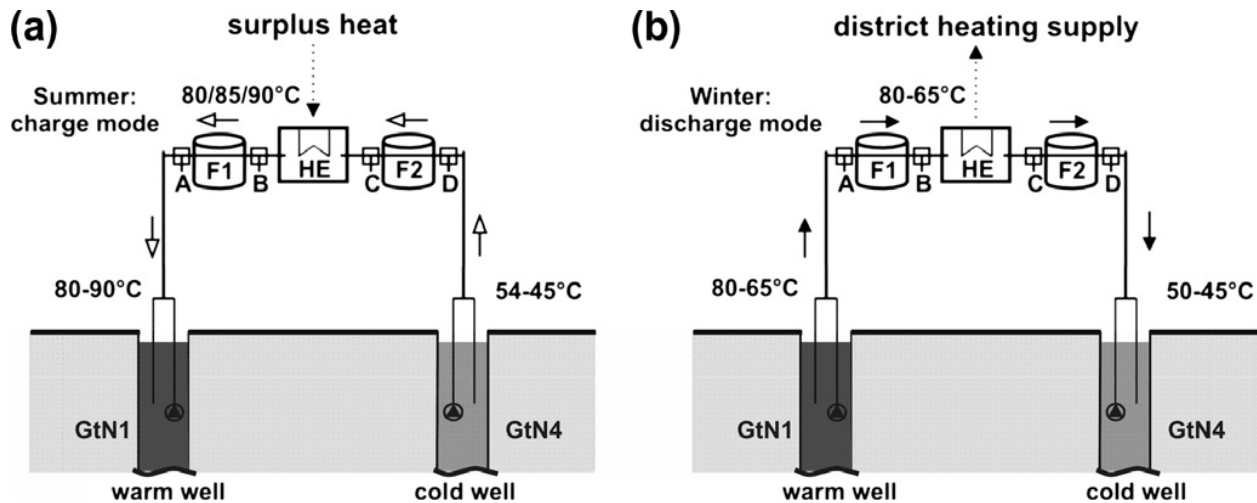
Figure 7. Schematic model of the Neubrandenburg HT-ATES system, depicting seasonal charging and discharging modes (Vetter et al., 2017).

Lessons learned:

- Reductions in heating demand due to energy conservation improvements and the addition of a sewage gas-powered cogen plant lowered the need for geothermal water for heating

- Repeated breakdown of the submersible pumps due to corrosion issues made this system unreliable for heating

- The use of nitrogen as a headspace gas reduced oxygenation of the HT-ATES aquifer, leading to fewer geochemical operational issues

- Acid treatments of the wells appear to have enhanced well injectivity, perhaps dissolving any scale forming in the wellbore and filters.

2.1.4.3 BMW

A design concept was developed by the BMW group to evaluate the viability of a proposed HT-ATES system in Dingolfing, near Munich, Germany. The original conceptual design consisted of a well doublet, consisting of a hot well and a cold well that would be completed in the Malm carbonate aquifer. The concept involved storing excess heat available from a combined heat and power plant during the summer months and retrieving the hot water for heating purposes during the winter. A 472 m deep test well was drilled and used to conduct push-pull well tests, where progressively hotter water was injected into the formation, followed by flow-back of the well. The injected water was amended with CO_2 to suppress the precipitation of carbonate minerals. Detailed thermal and geochemical modeling studies were conducted to assess how the Malm reservoir would perform as an HT-ATES (Ueckert and Baumann, 2019; Ueckert et al., 2020). Analysis of the push-pull tests indicated a lower-than-expected thermal recovery from the system. In addition, modeling studies conducted to evaluate the use of CO_2 to mitigate the precipitation of carbonate suggested that increasing amounts of CO_2 would be needed over time and would also lead to degradation of the HT-ATES performance. An alternative design involving a third warm well (Ueckert and Baumann, 2019) was developed to address this issue (Figure 8), but this added to the project cost, and a decision was made to suspend the project.
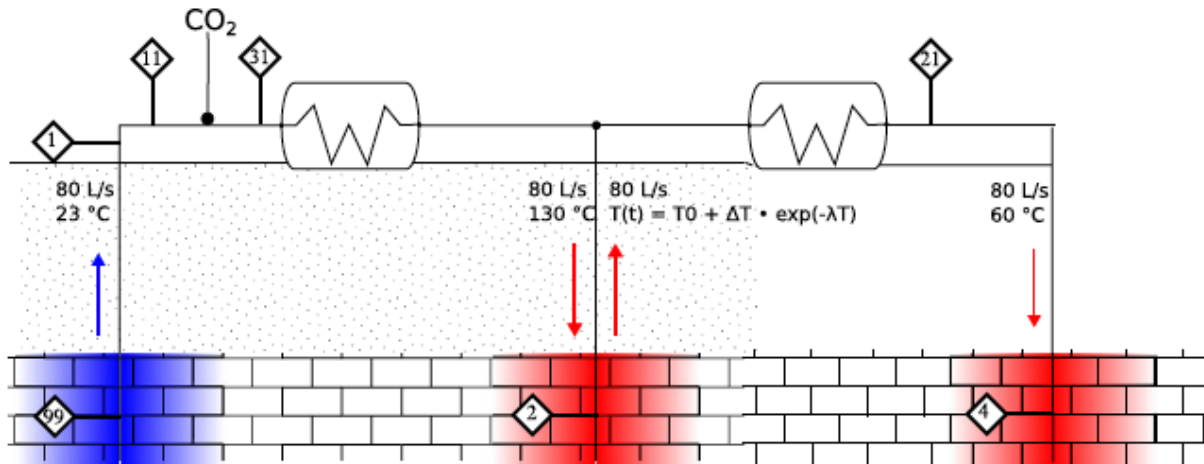
Figure 8. Conceptual model of triplet well system for BMW HT-ATES project (Ueckert and Baumann, 2019).

Lessons learned:

- Developing a HT-ATES within a carbonate reservoir requires special mitigation measures to inhibit the precipitation of retrograde carbonate minerals in the hot well

- A triplet well system developed to reduce scaling issues led to higher estimated project costs, and also would not satisfy the thermal energy quality requirements of the off taker

- Drilling a test well provided the opportunity to characterize the reservoir and evaluate system performance; these field tests were critical in determining the viability of such a system, leading to project suspension prior to construction

- Thermal and geochemical modeling, constrained by the field tests, were used to predict system performance.

2.1.4.4   Utrecht

The first HT-ATES system in Europe was put into operation at Utrecht University in 1991 (van Loon and van der Heide, 1992; Bakema and Drijver, 2019; Bakema et al., 2019; Kallesøe and Vangkilde-Pedersen, 2019). Excess heat supplied by a combined heat and power (CHP) plant during the summer was stored in a HT-ATES sandstone reservoir, located at a depth of 220-260 m in the Oosterhout Formation. The HT-ATES system had a cold well and hot well doublet, spaced about 60 m apart (Figure 9). A number of monitoring wells were also drilled to monitor changes in temperature. The initial injection temperature into the hot well was 65°C and was increased to 90°C after several months. The system never achieved the design operational efficiency, due in part to an undersupply of hot water provided by the CHP plant and high return temperature cut-off for the buildings being heated. The hot well also experienced significant clogging (either from clay swelling or calcite precipitation), and it ultimately cracked and failed, leading to abandonment of the system in 1999 (Bakema et al., 2019).
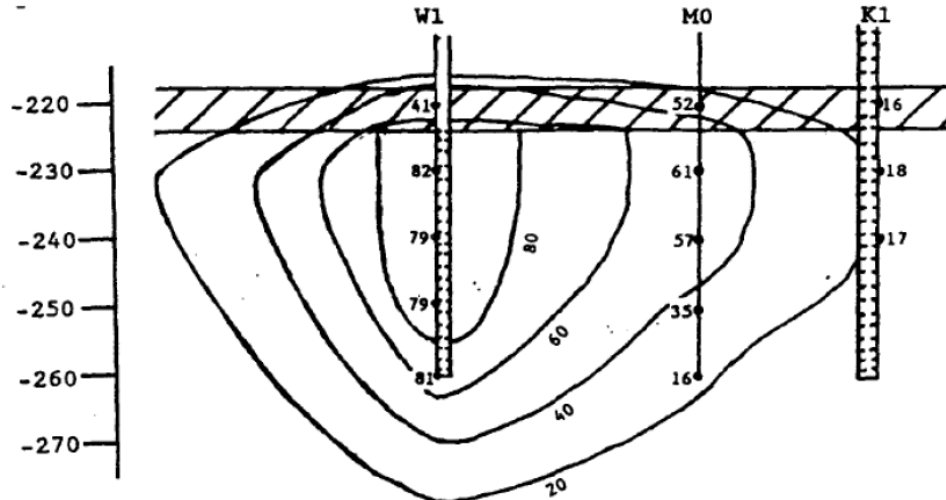
Figure 9. Cross section depicting hot (W1), cold (K1), and monitoring (M1) wells for the Utrecht HT-ATES system. The well depths are indicated on the y-axis; note that the upper portion of the wells (above the confining layer) are not depicted. The points depict measured temperatures and the contours represent isotherms of simulated temperatures after the first storage cycle (Bakema and Drijver, 2019).

Lessons learned:

- A Ca-Na ion exchange system was installed to treat the injected water, as lower Ca concentrations would reduce the tendency for carbonate precipitation (Drijver, 2011). However, the increased Na concentrations in the injected water may have resulted in clay swelling in the aquifer, and reduced injectivity into the formation. Geochemical modeling performed after this system was installed suggested that only a portion of the injected water should be treated to avoid this issue (Willemsen et al., 1992).

- The high return cut-off temperature for the building heating systems resulted in low thermal recovery efficiencies. Improved design of the district heating system would have resulted in much better performance.

- Clogging of the hot well ultimately led to well failure and resulted in the system being shut down. Improved design and operation of the system may have avoided this problem.

2.1.4.5   Hooge Burch Zwammerdam

A HT-ATES system was designed and installed at the Hooge Burch health care facility in Zwammerdam to store excess heat generated by a combined heat and power plant during the summer months and produce this hot water for heating of the facility during the winter (Bakema and Drijver, 2019; Bakema et al., 2019; Kallesøe and Vangkilde-Pedersen, 2019). A pair of hot and cold wells were drilled to a depth of around 150 m and completed in a sandstone reservoir (Figure 10). The system also had three boreholes to monitor changes in temperature, water chemistry, hydraulic head, and microbiologic communities (Bakema and Drijver, 2019). The heated water was treated with HCl to mitigate carbonate scale formation (Drijver, 2011). The performance of the system did not meet design expectations, as the thermal recovery efficiency values ranged from 3-11%. The poor system performance may have been due in part to lower amounts of stored hot water, a corresponding decrease in extraction temperature over time, and incomplete utilization of the thermal energy of the produced fluids (return temperatures were higher than the design parameter). The use of the cogen plant was reduced due to a change in the electricity feed-in fee, and as a result, heat storage of the system was no longer deemed profitable, resulting in the system being taken out of operation in 2003.
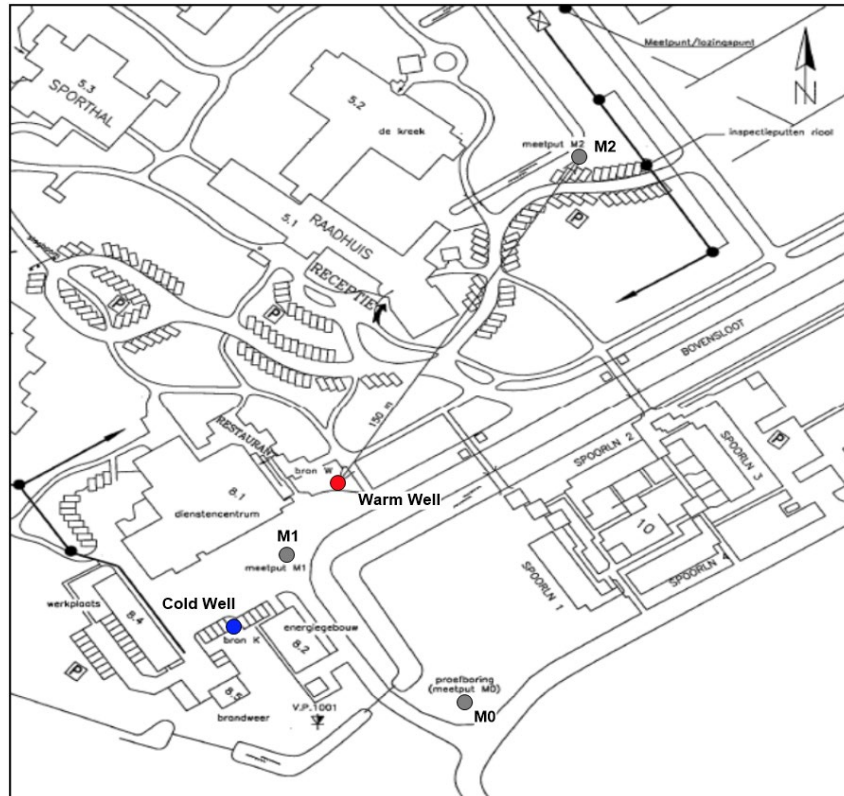
Figure 10. Location of the warm, cold, and monitoring (M) wells at the Hooge Burch Zwammerdam HT-ATES system (Bakema and Drijver, 2019).

Lessons learned:

- Operational parameters may change for a variety of reasons, leading to poor system performance. Changes in the economics of the cogen plant resulted in less thermal heat available for storage, leading to inadequate charging of the system.

- The use of HCl was successful in mitigating the precipitation of carbonate scale.

- Thermal breakthrough between the hot and cold wells would have been reduced if the spacing between the two wells had been greater.

- More effective use of the produced heat (by having a lower temperature cut-off for returned fluids) would result in better system performance.

2.1.5   General Observations

Most of the HT-ATES systems reviewed in this study are no longer operational due to a variety of factors. Many of the HT-ATES systems experienced a number of issues that led to poorer system performance than expected. These issues can be summarized as follows:

- **Insufficient site characterization**. Reservoir heterogeneity often resulted in lower injection/production rates than expected.

- **Thermal breakthrough** between hot and cold wells. This occurred in several sites, and was due to insufficient separation of the wells, or an imbalance in the hot and cold portions of the aquifer.

- **Scaling**. This was more prevalent in HT-ATES aquifers that had elevated TDS, and in particular, in formations with abundant carbonate minerals. Because of the retrograde solubility of carbonate minerals, heating formation waters saturated in carbonate often leads to precipitation of carbonate scale.

- **Corrosion**. Most of the aquifers are reducing environments, and if oxygenated water is introduced, it can stimulate microbiological activity that leads to the formation of corrosive fluids. A number of the HT-ATES systems had corrosion problems with the submersible pumps that resulted in significant downtime.

- **Availability of excess heat for system charging**. Due to a variety of factors (competing demands, reduction in production, poor economics, etc.), a number of the HT-ATES systems were not able to obtain the amount of excess heat in the summer months needed to fully charge the thermal reservoir.

- **High return cut-off temperatures**. Many of the systems had poor thermal recovery performance because only a fraction of the thermal heat that was produced from the HT-ATES was actually being utilized by the district heating system.

- **Inappropriate water treatment systems**. One of the systems installed a cation exchange system to mitigate carbonate scaling, but the replacement of Ca with Na may have caused clay swelling in the reservoir, leading to poor injectivity in the reservoir.

- **System reliability**. Most of the systems utilize a well doublet system, so there is no backup available if one well goes down for whatever reason (such as filter clogging, pump failure, etc.). When these failures occurred, the entire HT-ATES system was forced to go offline for months before repairs could be completed.

There were a variety of factors that improved the overall design and performance of the HT-ATES systems. These include:

- The use of numerical models to predict fluid and heat flow, and geochemical reactions that may impact system performance.

- Drilling of test wells and conducting field tests to verify actual reservoir conditions prior to finalizing system design and initiating construction.

- Conducting risk assessment of the project components to identify high risk factors for the project.

- Installing and operating monitoring systems to evaluate system performance and identify issues before they seriously impact operations.

- Instigating good operational practices, such as good well completion design and using nitrogen as a headspace gas, to avoid introducing oxygen into the reducing aquifers.

- Having flexibility in system operations to accommodate changes in thermal energy supply and demand that will occur with time.

2.1.6 Task 1.2 Experimental Assessment of Scaling Potential and Efficacy of Geochemical Models

2.1.6.1 Objectives

The transfer and interaction of high enthalpy fluid with surface and subsurface infrastructure is conducive to creating potentially adverse geochemical consequences, such as mineral scaling. The introduction of brine at elevated temperatures (relative to the reservoir) enhances the water-rock reactions that can potentially alter the porosity and permeability of the reservoir. Our early RTES assessment efforts (McLing et al., 2019; Wendt et al., 2019) using geochemical reactions models indicated that the introduction of thermal energy into a sedimentary reservoir alters the steady-state/equilibrium geochemical conditions and results in the precipitation of pore-filling minerals and/or the dissolution of reservoir cements that may degrade the performance of both the surface (e.g., heat exchangers) and subsurface (e.g., wells) engineered systems and the underground reservoir.

Numerical simulations described in 2.1.7 of the potential for the precipitation of retrograde-solubility scale minerals (chiefly anhydrite and carbonates) associated with hypothetical RTES operations in four well-characterized reservoirs located in the Green River Basin (Weber Sandstone), the Illinois Basin (St. Peter and Mt. Simon Sandstones), and the Gulf Coast Basin (Lower Tuscaloosa Sandstone) show that the scaling potential is primarily a function of the brine composition, in particular alkalinity and sulfate concentration, rather than total dissolved solids (TDS) content of the brine (Figure 46; Spycher et al. 2021a). Materials (reservoir sediments and post-heat exchanger synthetic brines) from two of the above reservoirs, one with high scaling potential (i.e., high sulfate and alkalinity) but lower TDS (Weber Sandstone) and the other with lower scaling potential (low sulfate and alkalinity) but higher TDS (Lower Tuscaloosa Sandstone) were selected for experimental investigation. These experiments were designed to mimic reservoir brines heated at the surface to temperatures of 140°C to 250°C, treated with CO_2 to inhibit scale formation, and reinjected into the reservoir for time scales of two to three months. The temperatures, treatments, and time scales are all relevant to a seasonal charging cycle of a potential RTES reservoir. The objectives of these experiments were to:

- Collect laboratory-based time-series brine and post-experiment mineralogical characterization data to assess the efficacy and limitations of the geochemical activity models used in this study to evaluate scaling and other brine-rock reactions in RTES systems

- Evaluate the use of CO_2 as an anti-scaling strategy to prevent the precipitation of carbonate minerals; (nominally P_{CO2} of 5, 16, or 50 bars)

- Serendipitously assess the corrosion potential of possible RTES infrastructure and well materials (i.e., 316 SS).

Rational for selected reservoirs: The mineralogies for the two experimental reservoirs are similar in that they are both dominated by quartz sand but differ significantly in term of other constituents. The Weber is comprised of a quartz sand with calcite, dolomite, and anhydrite cements whereas the Lower Tuscaloosa is comprised of quartz sand with abundant chlorite and other clays with minor amounts of carbonates and no anhydrite. The presence or absence of anhydrite likely accounts for differing sulfate concentrations and scaling potentials of the two associated brines. In addition to sulfate, the two brines differ in their chloride concentrations with high-sulfate, high-alkalinity (~6,000 and ~2,000 mg/L, respectively) Weber brine having a lower chloride concentration (~57,000 mg/L) compared to the low-sulfate, low-alkalinity (~240 and ~25 mg/L, respectively) Tuscaloosa brine with a higher chloride concentration (~97,000 mg/L). These differing chloride concentrations resulted in an unanticipated significant difference in their corrosiveness to stainless steel reaction cells as will be described later.

2.1.6.2   Test Site Descriptions

Geologic Setting for RTES

One of the main goals of this study is to geologically store excess thermal energy. To efficiently accomplish this, suitable geologic formations must be identified and analyzed. Many characteristics determine a formation's suitability including, but not limited to, formation size, extent, depth, porosity, permeability, sediment maturity, structural favorability, native fluid geochemical compatibility, storage capacity, thermal regime, etc. For this assessment, we have focused on sandstone formations that have been extensively characterized by previous efforts related to CCUS projects. These formations tend to have eolian and fluvio-deltaic origins which have led to favorable geohydrological characteristics as well as storage capacities and also have a reservoir seal. These types of formations also often contain deep saline fluids that are compatible with storage and retrieval operations associated with RTES. For this study, we focus on the Weber Sandstone and the lower Tuscaloosa Sandstone formations of Wyoming and Mississippi, respectively.

Weber Sandstone Formation

The Weber Sandstone Formation, located in the Green River Basin, Wyoming, is used as a representative sedimentary formation for the evaluation of RTES. The formation was extensively described, and data was used in early modeling for this project (McLing et al., 2019) to which we refer the reader for more details. We present here a summary of the formation. Geologically, the Green River Basin consists of a thick succession of Cambrian to Tertiary sedimentary rocks deposited over the Precambrian basement. Near the proximal center of the basin, a regional N-S extending anticline structure defines the Rock Springs Uplift. The RSU #1 well, a deep 3,905 m well drilled for the Wyoming Carbon Underground Storage Project (WY-CUSP, see below; McLaughlin et al., 2013) on the northeastern flank of the Rock Springs Uplift constrains the subsurface lithology for the area. The CCUS work evaluated both the Weber Sandstone and the Madison Limestone as target reservoirs for CO_2 storage. In this study, we only evaluate the Weber Sandstone for RTES through a series of water-rock interaction experiments.

The Weber sandstone is approximately 657 ft (~200 m) thick and occurs between 11,150 ft and 11,807 ft (~3,400-3,600 m) below ground surface (bgs) at the RSU#1 well site. The lower section of the Weber Sandstone consists of alternating sequences of marine carbonates and sandstones, which are tight and unsuitable for fluid injection. However, the upper ~110 m of Weber Sandstone is a quartz arenite with better reservoir qualities (i.e., porosity and permeability) for fluid injection (Shafer, 2013; McLaughlin and Garcia-Gonzalez, 2013), and potentially for RTES.

WY-CUSP: Funded by the U.S. DOE and the State of Wyoming, the Wyoming Carbon Underground Storage Project[1] was a three-year effort aimed at identifying, characterizing, and analyzing potential carbon storage reservoirs in southwest Wyoming. Focus was given to the Weber Sandstone and Madison Limestone of the Rock Springs Uplift where the project estimates a collective potential storage capacity of 13 billion tons of CO_2. Field and lab studies, together with modeling and analysis, have produced a wealth of data that help characterize the deep saline aquifers for pilot and commercial-scale CO_2 storage potential (Surdam et al., 2009; Surdam, 2013; Shafer, 2013; McLaughlin and Garcia-Gonzalez, 2013). Other partners include Los Alamos National Laboratory, Baker Hughes Inc., ExxonMobil, Geokinetics, EMTEK, New England Research, Core Laboratories, and PetroArc International.

---

[1]   https://www.uwyo.edu/cegr/research-projects/publications/wycusp.html.

Tuscaloosa Sandstone Formation

The Cranfield field is part of the Mississippi Interior Salt Basin within the larger Gulf Coast Basin (GCB) that stretches across multiple southern states. The Cranfield site is in SW Mississippi (Figure 11) and was the focus of a large CCUS pilot project with the Southeast Regional Carbon Sequestration Partnership (SECARB, see below; Lu et al., 2012; Hovorka et al., 2013; Doughty and Freifeld, 2013; Kim and Hosseini, 2013; Rhinehart et al., 2016, Jung and Espinoza, 2017). The GCB is characterized by many deep-seated salt domes that have been extensively explored by oil and gas companies. One of these salt domes is credited for the dome-like structure that creates a regional structural trap at the Cranfield site (Mississippi Oil and Gas Board, 1966; Lu et al., 2013).

The Upper Cretaceous Lower Tuscaloosa Formation was the main reservoir target for SECARB based on its favorable reservoir qualities. The reservoir injection zone, or "D-E" sands unit (Figure 12), consists of a package of cross-bedded conglomerates, fine-grained litharenites, and muddy sandstone deposited in a fluvial-deltaic system interpreted by multiple incision/deposition episodes. These are located at 10,420 ft (3167 m) below mean sea level (bmsl) with a thickness ranging between 50-82 ft (15-25 m) (Kim and Hosseini, 2013).

The reservoir is overlain by a siltstone and very fine-grained sandstone (A, B and C sands) that act as a local seal to the reservoir. Regionally, however, the marine packages of the Middle Tuscaloosa Formation provide a more laterally extensive cap. These along with the salt dome influenced structure make up the regional seal to the overall system. The reservoir system is underlain by low permeability sandstones and mudstones of the Washita-Fredericksburg Group (Lu et al., 2013). The extensive characterization, injection tests, and modeling performed at this site by the SECARB team has proven this formation to be a great candidate for the investigation of RTES.
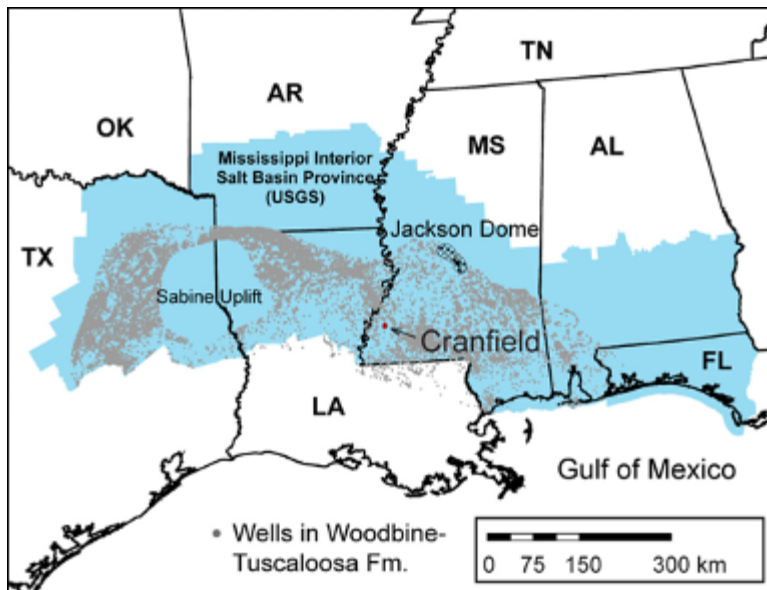
Figure 11. Map of the southern United States showing the Mississippi Interior Salt Basin Province in blue and many oil and gas exploration and production wells in gray. The Cranfield field site is in the SW corner of Mississippi indicated in red. (modified from Lu et al., 2013).
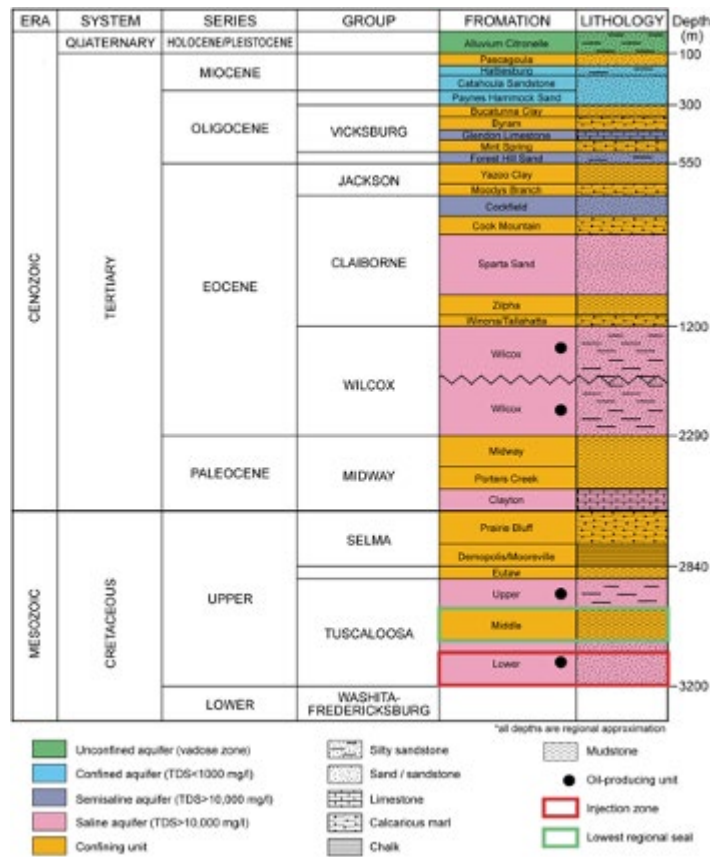
Figure 12. Stratigraphic column for the Cranfield field, Mississippi. The Lower Tuscaloosa D-E Sands are outlined in the red box (modified from Lu et al., 2013).

21

SECARB: In 2008, as part of the Southeast Regional Carbon Sequestration Partnership, the Gulf Coast Carbon Center[2] began studies on what later became the first large-scale CO_2 injection in Denbury Resources Cranfield field in SW Mississippi. The project was funded by the U.S. DOE through the National Energy Technology Laboratory and managed by the Southern States Energy Board. Researchers and scientists from 25 institutions utilized existing oil and gas wells to conduct studies on the injection, movement, monitoring, and storage of CO_2 at depths greater than 10,000 ft bgs. In addition to modeling, analysis, laboratory and field studies, core samples were taken from the Lower Tuscaloosa Formation to better understand the physical-chemical reactions that would occur upon injection of CO_2 into the reservoir. During the five-year project, over five million metric tons of CO_2 were successfully injected into the subsurface.

Rock Sample Descriptions

In this study, core samples of upper Weber Sandstone from Well RSU#1 (Figure 13A) and Lower Tuscaloosa Formation from Well CFU-31-F2 (Figure 14A) were used for laboratory experiments. For the water-rock interaction experiments, intact core sections were obtained from Carbon Management Institute, University of Wyoming (Weber Sandstone cores) and Bureau of Economic Geology, University of Texas (Lower Tuscaloosa Formation). Core samples were crushed using a sledgehammer and a BICO Chipmunk rock crusher/pulverizer. The crushing of Weber Sandstone resulted in well-graded grains (Figure 13B), whereas crushing of Lower Tuscaloosa Formation sandstone resulted in poorly-graded grains (Figure 14B). For the experiments, sieved grain size fractions of 150 μm to 850 μm (Weber Sandstone) and 125 μm to 300 μm (Lower Tuscaloosa Formation) were used. The crushed rock samples were rinsed with nano-pure (>18.2 MΩ·cm) water and air dried at room temperature (Figure 13C and Figure 14C). After the rinsing, the crushed Weber Sandstone was mostly devoid of finer fraction (Figure 13D), however, the rinsing did not completely remove the clay-coating on grains of crushed Lower Tuscaloosa Formation (Figure 14D).

---

2   https://www.beg.utexas.edu/gccc/secarb-cranfield.
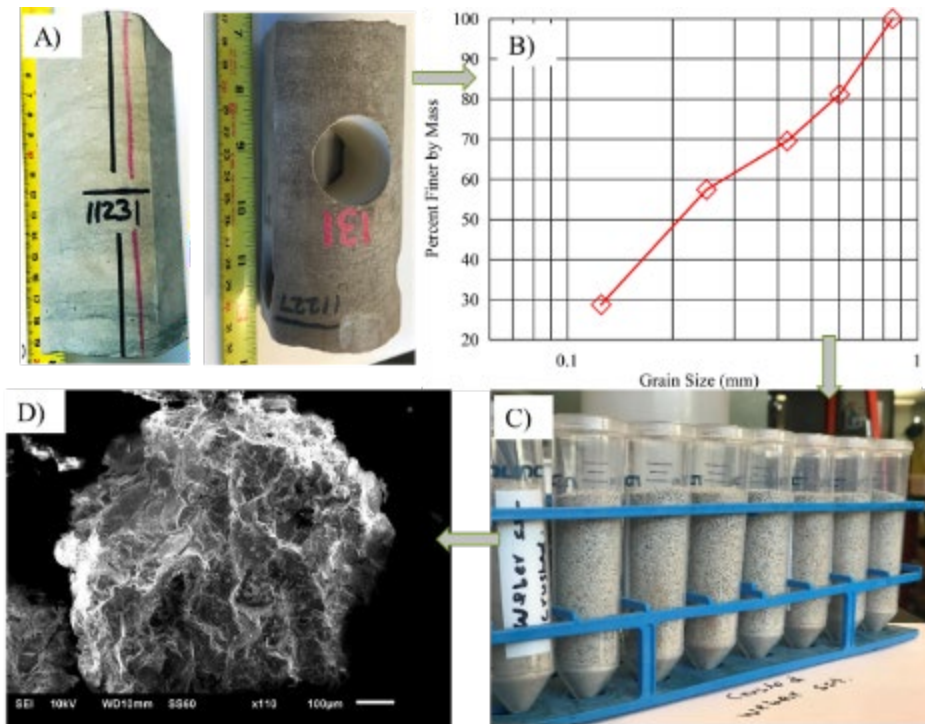
Figure 13. (A) Photograph of core-segments of the upper Weber Sandstone retrieved from RSU#1. (B) Grain-size distribution plot for crushed and sieved Weber Sandstone core. (C) Crushed, sieved, and washed sandstone with grain-size from 0.15 mm to 0.85 mm. (D) Scanning electron microscope (SEM) image of a typical quartz grain in the crushed rock.
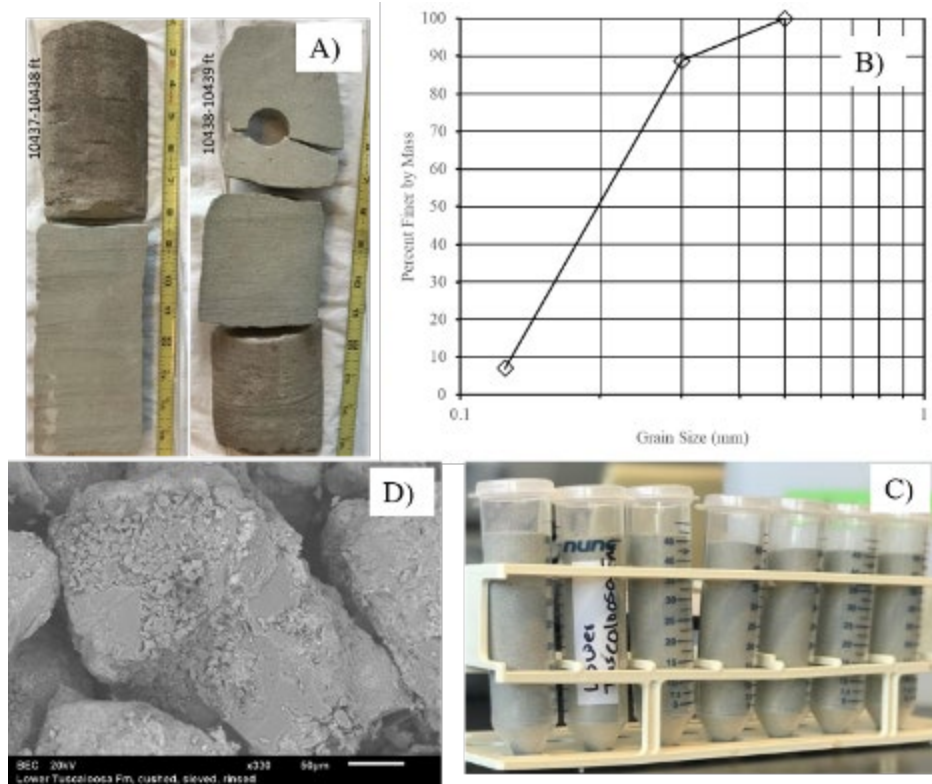
Figure 14. (A) Photograph of core-segments of the Lower Tuscaloosa Formation retrieved from Well CFU-31-F2. (B) Grain-size distribution plot for crushed and sieved Lower Tuscaloosa Formation sandstone core. (C) Crushed, sieved, and washed sandstone with grain-size from 0.125 mm to 0.300 mm. (D) Scanning electron microscope (SEM) image of a typical clay-coated quartz grain in the crushed rock.

X-ray diffraction of the pre-experimental (crushed, sieved, and rinsed) Weber Sandstone (Figure 15A and B) shows the preponderance of quartz with small amounts of K-feldspar, biotite, muscovite, chlorite, and anhydrite. Also, the SEM image of a typical crushed grain of this experimental rock shows a clean quartz grain with conchoidal fractures (Figure 13D). X-ray diffraction of the pre-experimental (crushed, sieved, and rinsed) Lower Tuscaloosa Formation (Figure 14C and D) also reveals quartz as the dominant mineral with small amounts of chlorite and kaolinite. However, unlike the grains of the Weber sandstone, the crushed grains of the Lower Tuscaloosa Formation are coated with clay minerals (e.g., kaolinite and chlorite) (Figure 16A and B).
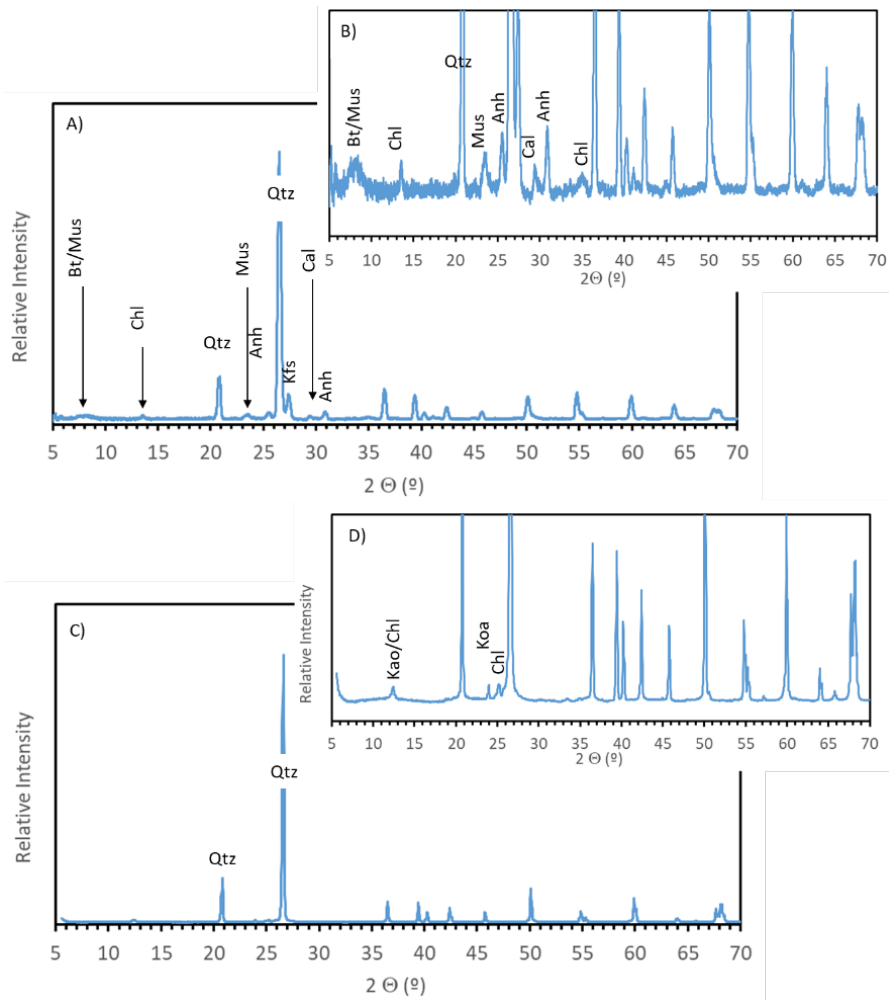
Figure 15. (A) X-ray diffraction patterns for the pre-experimental Weber Sandstone. (C) Lower Tuscaloosa Formation rocks. The XRD spectra in B and D are enlarged portions of A and B, respectively, that reveal the diffraction peaks of small amounts of non-quartz minerals. Minerals are: Qtz = quartz, Kao = kaolinite, Chl = chlorite, Anh = anhydrite, Bt = biotite, Mus = muscovite, Kfs = K-feldspar, and Cal = calcite.
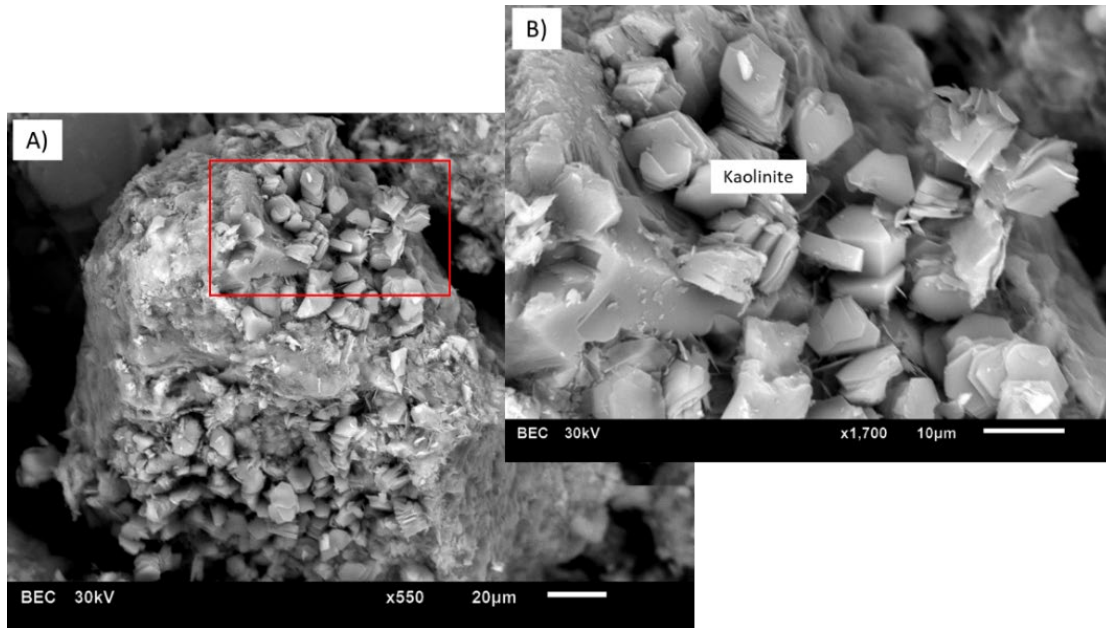
Figure 16. Scanning electron microscopy images of the pre-experimental Lower Tuscaloosa Formation (crushed) rock. (A) A rock grain (quartz) coated with clays. (B) An enlarged part of a grain (red box in A) showing clay minerals. Based on the results of XRD (Figure 15C and D) and energy dispersive X-ray spectroscopy (EDS), the platy minerals are identified as kaolinite.

Brine Chemistry

The concentrations of selected analytes for the formation brines associated the Weber sandstone (Quillinan and McLaughlin 2013; McLing et al., 2019;) and Lower Tuscaloosa sandstone (Soong et al., 2016) are given in Table 2. Both are sodium chloride brines but differ in that the lower TDS Weber brine has much higher SO_4^{2-} and alkalinity (and corresponding lower Ca^{2+}, Mg^{2+}, and Sr^{2+}) concentrations than does the higher TDS Tuscaloosa brine. This provides Weber brine with a higher potential for the formation of carbonates and sulfate scale minerals when compared to the Tuscaloosa Brine (Section 2.1.7, Spycher et al., 2021a). However, the much higher Cl^- concentration of the Tuscaloosa brine increases the likelihood of increased corrosion of ferrous metal RTES infrastructure (pumps, piping, etc.) as will be discussed later.

Table 2. Concentrations of select analytes for brines associated with the Weber and Tuscaloosa formations.

	Weber[1]	Tuscaloosa[1]
Ca^{2+}	539	12,400
Fe^{2+}	44	130
Mg^{2+}	45	1,090
Sr^{2+}	14	730
K^+	1,910	433
Na^+	36,500	46,000
Cl^-	57,400	96,900
HCO3$^-$	4,000	315
Alkalinity[2]	2,100	25

	Weber[1]	Tuscaloosa[1]
SO_4^{2-}	6,030	250
TDS[3]	107,000	150,000
pH	6.46	5.46

[1]mg/L
[2]as $CaCO_3$
[3]total dissolved solids

2.1.6.3   Methods

Experimental Methods

The laboratory experiments simulating the RTES reservoirs in Weber Sandstone and Lower Tuscaloosa Formation at different temperatures were conducted in 1.0 L stainless steel (Type 316) reaction vessels (Model 4523 Parr® Instrument) equipped with independent stirring, temperature, pressure control, and sampling accessories (Figure 17). A computer-controlled heating jacket coupled with a temperature probe was used to maintain a set temperature for each reaction vessel. A sampling vessel (Model 4351-I-D-V-C Parr® Instrument) was used to obtain time-series fluid samples from an ongoing reaction vessel without interrupting the experimental conditions.

Figure 17. A) Parr® reactor system showing reaction vessel, cooling coil, pressure gauge, and thermistor. B) Parr® system with attached sampling vessel during actual testing condition.

Laboratory experiments were conducted at temperatures of 140, 160, 200, and 250°C and brine saturation pressures augmented with different partial pressures of CO_2. All experiments had an initial near-constant water-rock ratio of 10:1 (600 g of brine and 60 g of rock) and were conducted for two to three months with the collection of brine samples at times of 1, 2, 4, 8, 16, 32, and 64, 73 or 80 days (the water-rock ratio decreased slightly over time as collected fluid samples were withdrawn from the system). Atmospheric oxygen in the headspace of the reactor was purged by CO_2 prior to bringing the experiments to temperature. The length of these experiments was designed to represent a relevant timeframe of a charging phase of seasonal/cyclical heat storage and extraction scenarios with injection of heated water during summer months followed by extraction of hot water from the reservoir in the winter with or without an intermediate static storage phase in between. At each sampling event, a small amount of fluid was transferred to a sealed sampling vessel without interrupting the main reaction vessel, cooled to room

temperature, pH measured, filtered through a 0.45 μm filter, and separate aliquots for analyses of anions and cations were collected in separate nanopure water- or acid-washed bottles. A separate vial was used to collect a head-space free sample for analysis of dissolved inorganic carbon. An aliquot for cations was acidified to pH<2 with Optima nitric acid. All fluid samples were stored at 4°C until analyses by aqueous analytical equipment [ion chromatography (IC), inductively coupled-plasma – optical emission spectroscopy (ICP-OES), inductively coupled-plasma – mass spectroscopy (ICP-MS), total organic carbon (TOC) analyzer] at Energy Laboratories Inc. in Billings, Montana. At the end of experiments, the reaction cells were rapidly (10-15 minutes) quenched from experimental temperature to room temperature (~21ºC) by circulating cold water through the cooling coil. The residual pressure (mostly from CO_2) was released by venting the reaction cells to atmospheric pressure, and the cells were disassembled (Figure 18).

Table 3. Recipes for shelf-stable synthetic brines.

Salt	Weber[1]	Tuscaloosa[1]
KCl	3.8	0.6
NaCl	82.0	113.1
$CaCl_2$	0.2	36.0
$MgCl_2$		4.6
$NaHCO_3$	0.9	0.3
Na_2SO_4	16.7	0.1
H_2O	1,000.0	1,000.0

[1]g/L
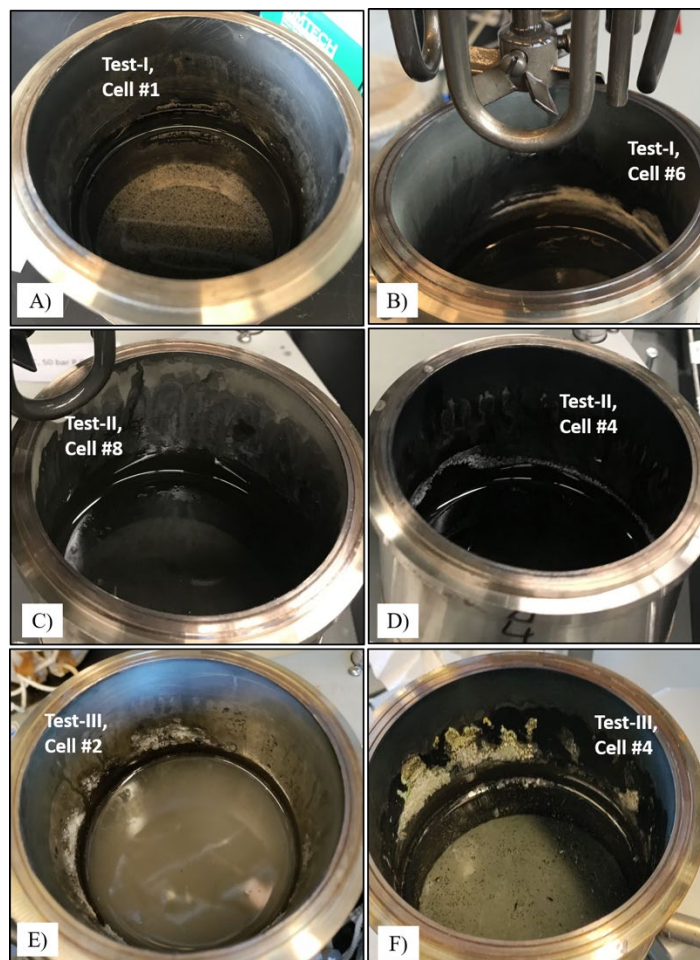
Figure 18. Photographs of post-experimental reaction cells. The inside diameter of the reaction cell is 10 cm. A) T = 160ºC, P_{CO2} = 1.7 bars, B) T = 200ºC, P_{CO2} = 3.4 bars, C) T = 250ºC, P_{CO2} = 15.9 bars, D) T = 250ºC, P_{CO2} = 17.4 bars, no rock, E) T = 140ºC, P_{CO2} = 15.3 bars, and F) T = 250ºC, P_{CO2} = 42.6 bars. Test-I and Test-II runs were conducted with Weber Sandstone and its corresponding synthetic brine and Test-III runs were conducted with Lower Tuscaloosa Formation and its corresponding synthetic brine (Table 3).

Residual brine in the reaction cells was collected, filtered, and stored at 4ºC for later analysis. The solid materials from each reaction cell were split into two portions – one portion was rinsed several times with nano-pure water to remove the residual brine from the reacted rock. Both rinsed and unrinsed post-experimental rock samples were air dried, stored at room temperature, and used for characterization by X-ray diffraction (XRD), scanning electron microscopy (SEM), and energy dispersive X-ray spectroscopy (EDS). Rigaku SmartLab was used for XRD of whole rock as well as clay fraction within a range of 2Θ from 5º to 70º. Air-dried bulk samples were powdered either by using a pair of ceramic mortar and pestle or a ball mill (with ceramic balls and container). Air-dried samples were gold-coated prior to collection of SEM images and EDS spectra using a JEOL JSM-6610LV.

Experimental Synthetic Brine

The experimental program was focused on understanding the impact of the re-injection of brine that has been heated at the surface (via a heat exchanger) and treated with CO_2 as a scale inhibitor back into the respective formation as part of the operation of a RTES system. Because carbonate and sulfate scale minerals exhibit retrograde solubility–decreasing solubility with increasing temperature–it is likely that scale precipitation or brine treatment would be implemented at the surface, altering the composition of the re-injected brine. To account for these changes, two synthetic brines mimicking the Weber and Tuscaloosa brines were developed for use in the brine-rock experiments. The synthetic brines were formulated using The Geochemist's Workbench (GWB, 2021) software package to simulate the equilibrium (with respect to carbonate and sulfate minerals) heating of the native brines to 200°C (Weber) or 250°C (Tuscaloosa). The resulting brine composition was reduced and renormalized to a recipe of inorganic salts that when mixed with deionized water yielded shelf-stable synthetic brines characteristic of their respective formations. The recipes for the two brines are given in Table 3. A detailed discussion of the approach used to develop the synthetic brines is given by Neupane et al. (2020). In formulating the two synthetic brines, SiO_{2aq}, Sr^{2+}, and Fe^{2+} were not included as the appearance of these constituents in sampled experimental brines served as indicators of silicate and carbonate/sulfate dissolution as well as potential corrosion of 316 stainless steel reaction cells (in the case of Fe). In addition, Mg^{2+} was not included in the Weber brine nor SO_4^{2-} in the Tuscaloosa brine as both had extremely low calculated concentrations.

Geochemical Models

Numerical simulation to design the experimental synthetic brine as well as to aid interpretation of experimental results were conducted using the commercially available Professional version of The Geochemist's Workbench® Release 15 (GWB, 2021) software package. The GWB software package consists of several individual modules for managing compositional data for waters and brines, balancing chemical reactions, producing activity-activity diagrams, conducting aqueous speciation and mass transfer calculations, and simulating 1- and 2-dimensonal reactive transport. In addition, the package includes interactive graphing capability facilitating the production of standard and customized plots of results. The calculations are supported by numerous included thermodynamic data bases[3] of which the default *thermo30* (based on the Lawrence Livermore National Laboratory (LLNL) dataset, EQ3/6 data file *data0.3245r46*) and *thermo_ymp.R2* (based on the Yucca Mountain Project dataset, EQ3/6 data file *data0.ypf.R2*) were used here.

The saturation state of the experimental brines with respect to various scale minerals were calculated as Saturation Indices (SI)

$$SI = \log\frac{Q_{i,T}}{K_{i,T}} \tag{1}$$

where $Q_{i,T}$ and $K_{i,T}$ are the ion activity product (or quotient) and the equilibrium constant for *ith* mineral dissolution reaction at temperature T, respectively. $Q_{i,T}$ is the numerical product of activities of the individual species appearing in the *ith* reaction raised to the power (positive for product and negative for reactants) of the stochiometric coefficient of that species in the reaction. The GWB speciation calculations result in activities of individual species, which are given as the product of the concentration and the activity coefficient of the species. The sign of *SI* indicates the saturation state of the brine with respect to the mineral; supersaturated (positive), equilibrium (zero), or undersaturated (negative).

---

[3] The Geochemist's Workbench® Thermodynamic Datasets (gwb.com).

2.1.6.4 Results and Discussion

Evaluation of Thermodynamic Data

Ion Activity Models
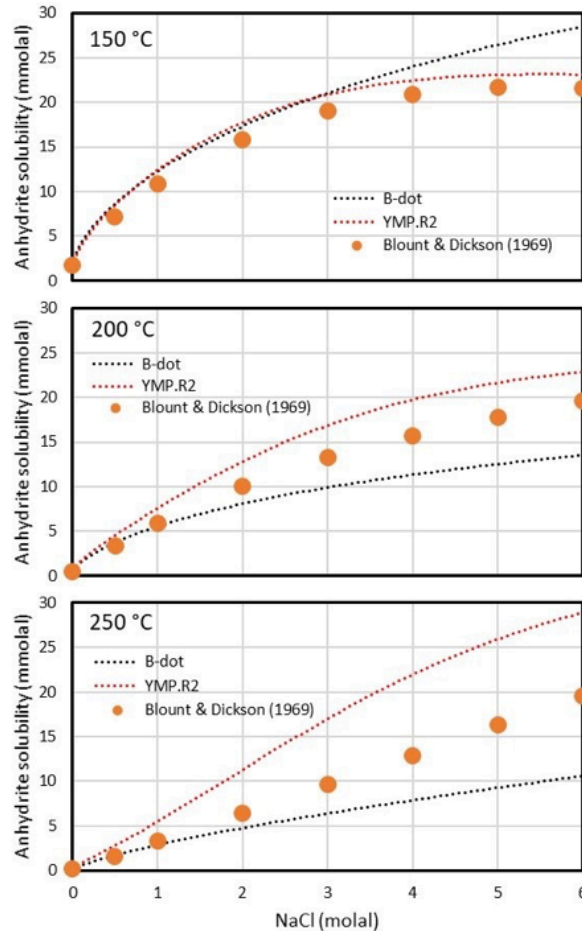
Figure 19. Measured solubility of anhydrite as a function of NaCl concentration compared to predicted solubilities.

The calculation of mineral-brine equilibrium at elevated temperatures requires approaches to account for the non-ideal behavior of electrolyte solutions. There are two widely used strategies (with variations) to account for this non ideality. The first is the B-dot method (Helgeson, 1969) which uses an extension of the Debye-Hückle equation to calculate individual ion activity coefficients and explicitly account for the equilibrium formation of ion pairs in solution. Helgeson (1969) parameterized this method for NaCl-dominated brines of up to 3 molal and temperatures up to 300°C. This approach accurately predicts the activity coefficients of Na^+ and Cl^- up to concentrations of 3 molal and other species to ionic strengths of 0.3 to 1.0 molal (Bethke, 2007). The advantage of the B-dot approach is that it is readily expandable to include new aqueous species and components. The second approach is referred to as the Pitzer formalism or equations. This approach uses virial equations to accurately calculate ion activity coefficients to very high salinities. Harvie et al. (1984) represents an early adoption of this approach for modeling geochemical systems. The Pitzer equations do not explicitly account for the formation of ion pairs rather they use empirically determined two- and three-way ion interactions parameters determined from mixed salt experiments to calculate activities. The limitation of this approach is that it is not easily expandable

31

either in terms of adding new components or calculations at different temperatures as any expansion requires the experimental determination of new interaction parameters and/or their extrapolation to higher temperatures. Both approaches are implemented in GWB and discussed in detail by Bethke (2007). Here we evaluated the two approaches for predicting the measured solubilities of two common scale minerals (anhydrite and calcite) using GWB and its associated provided default B-dot *thermo32* and the Pitzer formalism *thermo_ymp.R2* thermodynamic databases.

Figure 19 presents the GWB-calculated solubility of anhydrite at 150, 200, and 250°C as a function of NaCl concentration using both the B-dot method and the Pitzer formalism compared to the experimental solubility measurements of Blounot and Dickson (1969). There is good agreement between both methods and experimental measurements at low temperatures and low (1 to 3 molal) NaCl concentrations. At higher temperatures, the two models deviate from the experimental solubilities with the B-dot method underpredicting anhydrite solubility by a factor of 1.5 and the Pitzer formalism overpredicting anhydrite solubility by a factor of 1.8 at 250°C and 3 molal NaCl.

Figure 20 presents the GWB-calculated solubility of calcite at NaCl concentrations of 0.1, 0.2, 0.5, 1.0, and 4.0 molal as functions of temperature using both the B-dot method and the Pitzer formalism compared to the experimental solubility measurements of Ellis (1963) and Shi et al. (2013). There is good agreement between both methods and experimental measurements at low NaCl concentrations (1.0 molal and less) and to temperatures of up to 275°C. However, at higher NaCl concentrations (4.0 NaCl) and temperatures above 100°C the two methods increasingly deviate from measured experimental solubilities as well as from each other with the B-dot method underpredicting calcite solubility by a factor of 2.7 and the Pitzer formalism overpredicting calcite solubility by a factor of 6.1 at 250°C. The large discrepancy of the Pitzer formalism in predicting calcite solubility is likely due at least in part to uncertainty in the calculated value of the activity coefficient for HCO_3^-. For example, in 3 molal NaCl at 250°C the calculated activity coefficient for HCO_3^- is 0.011, a factor of 12 smaller than the activity coefficient of 0.13 for similarly charged $HsiO_3^-$.
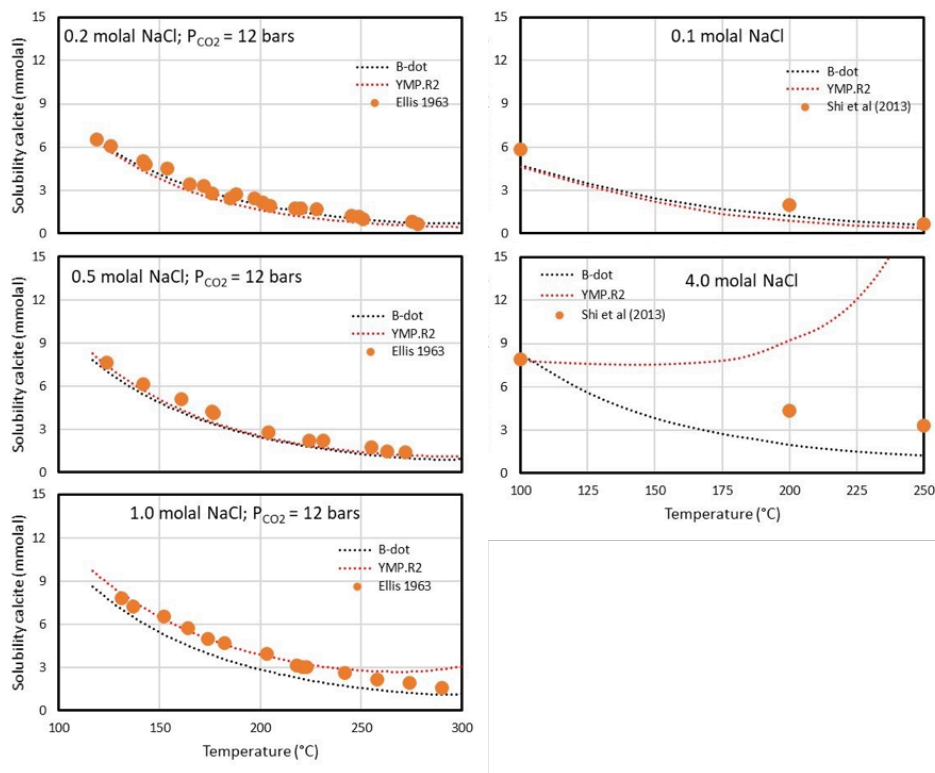
Figure 20. Measured solubility of calcite as a function of temperature compared to predicted solubilities.

It is interesting to note that for both anhydrite and calcite, the B-dot method underpredicts solubility and the Pitzer formalism overpredicts solubility. Given the better agreement between the Pitzer formalism and experimental results across all temperatures of interest and ionic strengths of up to at least one molal, the Pitzer approach was selected for interpretation and modeling of our experimental results as well as our field scale simulations. However, the observations described above suggested that results of geochemical modeling using the currently available parameterization of the Pitzer formalism for experiments or formations involving higher salinity brines (e.g., Tuscaloosa) should be undertaken with caution with the realization that scale mineral solubilities are likely overpredicted; meaning that some systems for which scale mineral formation would not be predicted may in fact be precipitating said minerals.

Table 4. Experimental Conditions. Listed P_{CO_2} represent average values over the duration of the experiment and was calculated from the total pressure as described in the text. W–Weber, T–Tuscaloosa, N–No rock.

Test	Cell	T (°C)	P_{CO_2} (bar)	Brine	Rock
I	1	200	9.5	W	W
I	2	200	1.5	W	W
I	3	160	1.3	W	W
I	4	160	3.8	W	W
I	5	160	3.7	W	W
I	6	200	3.0	W	W
I	7	200	10.9	W	W
I	8	160	11.6	W	W
II	2	250	14.7	W	W
II	4	250	14.5	W	N
II	6	250	4.2	W	W
II	7	250	6.0	W	W
II	8	250	11.6	W	W
III	1	200	44.6	T	N
III	2	140	15.3	T	T
III	3	200	3.5	T	T
III	4	250	42.6	T	T
III	5	250	2.7	T	T
III	6	250	13.1	T	T
III	7	200	49.8	T	T
III	8	200	13.3	T	T

2.1.6.5 *Thermodynamic Databases*

To evaluate the model sensitivity to thermodynamic datasets and ion activity models, the evolution of pH and saturation indices of calcite and anhydrite were evaluated as a function of temperature for the Weber Formation brine, using four sources of thermodynamic data and associated ion activity models (Figure 21): (1) the database *data0.ypf.R2* used for other simulations presented in this paper (Jove-Colon et al., 2007) with implementation of the Pitzer ion activity model, specifically tailored for high salinity brines (curves labeled _eq36_ptz on Figure 21); (2) database *data0.ymp.R5* from the same group (Wolery and Jarek, 2003) but with the implementation of the Debye-Hückel ion activity model limited to lower salinity waters (curves labeled _eq36); (3) the French Geological Survey (BRGM) thermoddem database (Blanc et al., 2012) and (4) the *soltherm.h06* database (Reed and Palandri, 2006), both also developed for use with the Debye-Hückel model (curves labeled _tddem and _solth, respectively). Figure 21 shows that below about 200°C, extending the Debye-Hückel model to high salinity brines is likely to underpredict the amount of precipitated calcite and anhydrite because this model underestimates the "salting out" of these minerals (i.e., their decreased solubility with increasing brine salinity). Additional investigations were performed to compare model results with laboratory experiments, as described in the next Sections (also see Neupane et al., 2021).
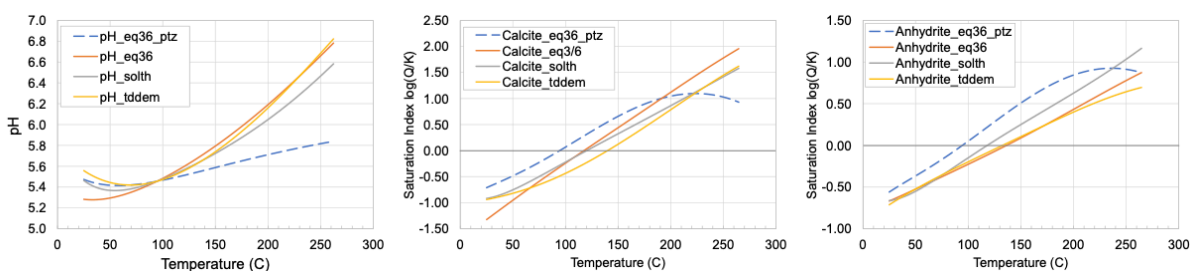
Figure 21. Evolution of pH (left), saturation indices of calcite (center) and anhydrite (right) computed as a function of temperature for the Weber Formation brine, using different sources of thermodynamic data and integrated ion activity models (see text). In the present case, minerals are not allowed to form, and all simulations start at the same formation temperature (94°C) and pH.

2.1.6.6 *Experimental Brines*

Table 4 summarizes the conditions for the 21 individual brine-rock experiments (including 3 replicates and 2 brine-only blanks) that were conducted for periods of up to 84 days and over a temperature and P_{CO2} range of 140°C to 250°C and 1 to 50 bars (P_{total} of 7 to 89 bars), respectively. Seven brine samples were collected over the course of the experiments, with the compositions given in Appendix A. At each sampling event, about 15 mL of fluid was withdrawn for pH measurement and aqueous chemical analyses. Each fluid sampling resulted in loss of small mass of brine and dissolved CO_2 from the reaction cell. Subsequent to each sampling, the loss of dissolved CO_2 caused a decrease in total system pressure (i.e., brine saturation pressure plus partial pressure of CO_2) in the reaction cell as a result of the re-equilibration of H_2O and CO_2 between the brine and the now larger reaction cell headspace. The loss of brine due to sampling also altered the relative volumes of brine and available headspace resulting in small amount of H_2O liquid in the brine partitioning into the headspace as H_2O vapors resulting in a net increase in concentration of non-volatile constituents in the remaining brine. Figure 22 shows the increasing trends of normalized Cl (i.e., concentration of Cl at each sampling time divided by the initial concentration of Cl) in the brine over time because of this partitioning of water into the newly available headspace after each sampling event.
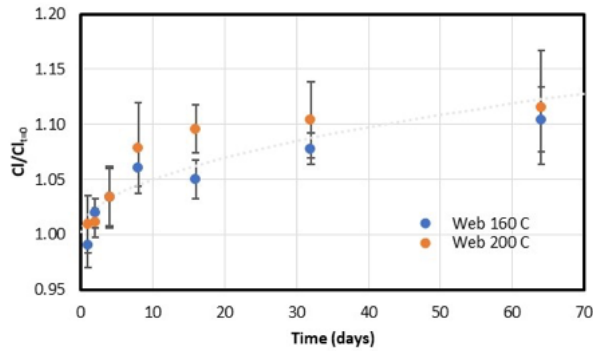
Figure 22. Average trends of normalized concentrations of Cl (by its initial concentration) for Weber experiments conducted at 160 and 200°C (Test I, Table 4).
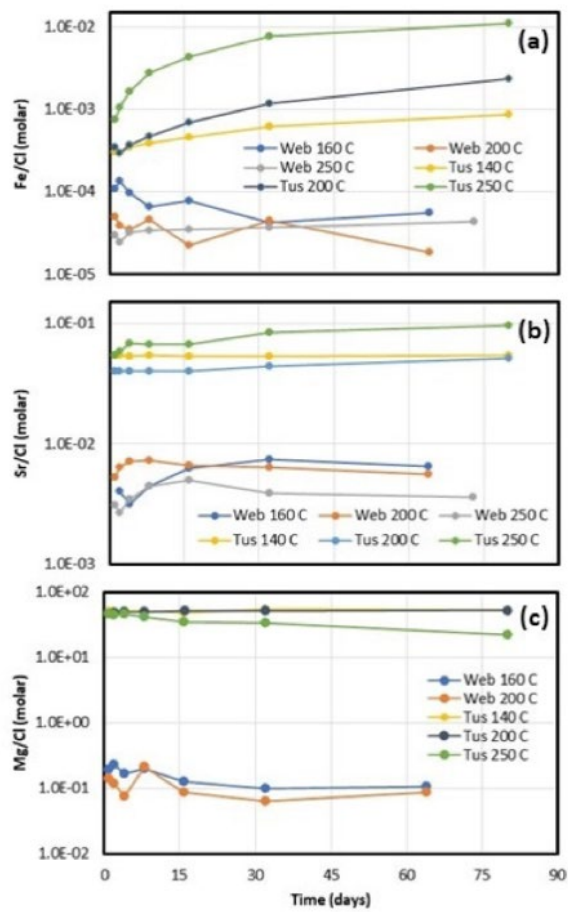
Figure 23. Chloride-normalized reacted brine concentrations of Fe (a), Sr (b), and Mg (c). Concentrations are averages across all P_{CO2} levels at indicated temperature.

To remove the concentrating effects associated with sampling of the brine, concentrations of selected constituents were normalized to the measured Cl concentration of the same brine sample. Figure 23 shows the evolution of Cl-normalized concentrations (averaged for each temperature and brine-rock type) of Fe^{2+} (a), Sr^{2+} (b), and Mg^{2+} (c). It is worthwhile to note that both Fe^{2+} and Sr^{2+} were not present in any of the initial brines, and Mg^{2+} was not present in the Weber initial brine, and these constituents entered the brine from the rock as a result of dissolution and/or leaching. Although plotted on the same figure, absolute values of ratios are not directly comparable between Weber and Tuscaloosa results as the nominal Cl concentrations of the two brines differ by a factor of 2. The normalized Fe^{2+} concentration (Figure 23a) show an early increase followed by a decrease (Weber) or a continuing increase (Tuscaloosa). The results suggest rapid dissolution of an iron-bearing phase (perhaps an artifact of reaction cell/sediment preparation). At later times the normalized concentration for Weber brine samples decreases reflecting loss of iron through the possible formation of Fe-bearing clays or carbonates. The Tuscaloosa brine samples show continuing increases in the normalized Fe^{2+} concentration (with greater increases at higher temperatures) resulting from ongoing corrosion of the stainless-steel cells, dissolution of Fe-chlorite, or both. The trends for the normalized Sr^{2+} concentrations (Figure 23b) are similar to that of iron in that for the Weber experiments, it shows increasing normalized concentration at early time as a result of mineral dissolution reactions followed by decreasing normalized concentration at later times possibly because of Sr^{2+} being sequestered into solid phases, either by precipitation or sorption onto secondary minerals. In the Tuscaloosa experiment the normal Sr^{2+} concentration increases throughout the experiment reflecting silicate and/or carbonate dissolution. Also, because Sr^{2+} is not a constituent of stainless steel its behavior is the result solely of brine-rock interactions. The normalized Mg^{2+} concentration (Figure 23c) for the 160°C and 200°C Weber brines (Mg^{2+} concentration was below detection in the 250°C brines) again showed initially an increasing normalized concentration (rock dissolution) followed by decreasing normalized concentrations (precipitation of Mg-clays?) at later times. Although the Tuscaloosa brine initially contained Mg^{2+}, its normalized concentration also decreases with increasing time reflecting the precipitation of Mg-clays and/or Mg-bearing carbonates.

pH and DIC: Because it was not possible to measure the in situ experimental pH and dissolved inorganic carbon (DIC) these values were calculated at experimental conditions from the measured room temperature pH, DIC, and measured ion concentrations for collected degassed brine samples using GWB by matching the predicted to observed total pressures in the reaction cells prior to sampling. This approach assumes that the brine is in equilibrium with the reaction cells headspace consisting solely of water vapor and CO_2. The calculations were conducted by speciating each sample at room temperature and then simulating the heating of the fluid to the experimental temperature and increasing the partial pressure of CO_2 until the sum of the calculated partial pressures of water vapor and CO_2 matched the observed total pressure. Because the calculated partial pressures of the two gases depend on the overall composition of the system, the calculations were conducted recursively until the agreement between the calculated and measured pressure was less than 0.01 bar. In matching the total pressures, GWB calculates the equilibrium pH and DIC concentrations.

At Temperature pH: Because calculated pH is strongly dependent on carbonate speciation in the system, the pH is sensitive to uncertainties in the activity of HCO_3^- (as shown below), which in turn is sensitive to uncertainties in the activity coefficient, which as described previously may be quite large at high temperatures and high salinities.

$$CO_2 + H_2O \leftrightarrow H^+ + HCO_3^- \tag{2}$$
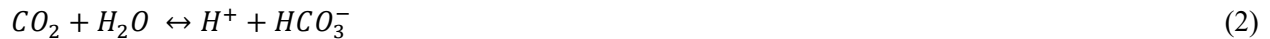
$$pH = -\log\frac{K_1 f_{CO2} a_{H2O}}{a_{HCO3-}} \tag{3}$$
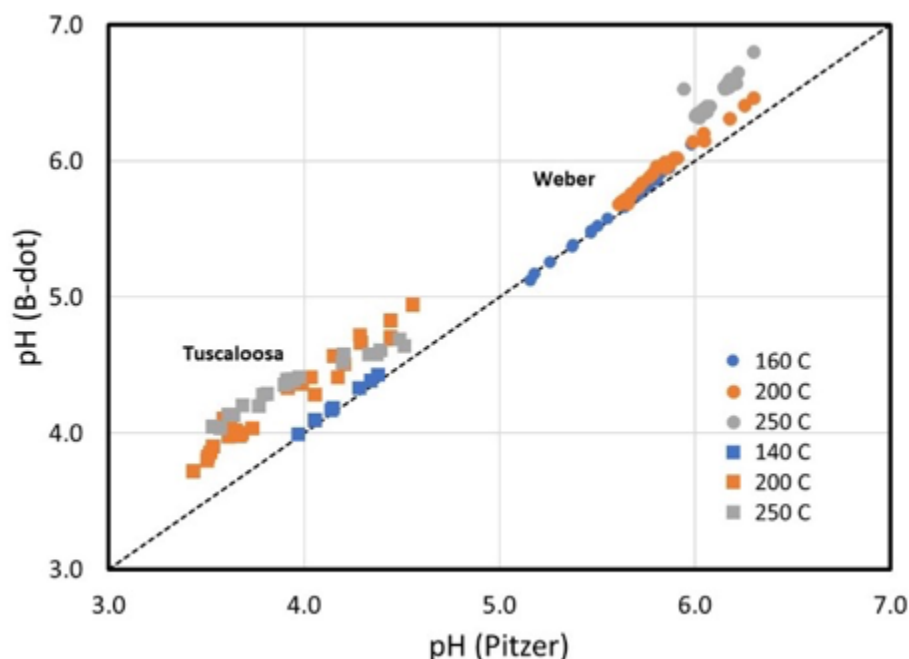
Figure 24. Comparison of pH values calculated using the Pitzer formalism and the B-dot method.

To test the impact of differing activity models on the calculated pH, both the B-dot and Pitzer formalism were used. The results of these calculations are presented in Figure 24. As may be seen in Figure 24, there is good agreement between the two approaches up to temperatures of at least 160°C and salinities observed for both the Weber and Tuscaloosa brines. At temperatures of 200°C and above, there is increasing deviation between the two approaches with both increasing temperature and increasing salinities. Using the Pitzer formalism the calculated pH is systematically lower than similar calculations using the B-dot method with average deviations of -0.03, -0.11, and -0.36 at 160, 200, and 250°C, respectively for the Weber brine and -0.05, -0.36, and -0.40 at 160, 200, and 250°C, respectively for the Tuscaloosa brine. The reasons for the increasing divergence at higher temperature and salinities may be the result of a failure of the B-dot method, the lack of high-temperature parametrization of the Pitzer formalism, or combinations of both.

2.1.6.7   Experimental Solids

Table 5 summarizes the results (Appendix B) of pre- and post-experimental mineralogical characteristics of Weber and Tuscaloosa sediments. The characterization results included XRD studies of the whole rock and of clay size fraction separates as well as SEM and EDS examinations.

Table 5. Mineralogical characterization of pre- and post-experiment sediments.

Test	Cell	Rock	Temp (°C)	PCO$_2$ (bar)	Minerals and methods
Pre-Exper.		W			WR XRD: quartz, K-feldspar, anhydrite, calcite, biotite/muscovite
I	1	W	200	9.5	WR XRD: quartz, K-feldspar, anhydrite, biotite/muscovite CF XRD: illite, vermiculite (?), quartz, gypsum/anhydrite, K-feldspar SEM: anhydrite, Mg-Fe clay (vermiculite/illite) SEM

Test	Cell	Rock	Temp (°C)	PCO$_2$ (bar)	Minerals and methods
I	2	W	200	1.5	WR XRD: quartz, K-feldspar, anhydrite, calcite, biotite/muscovite CF XRD: illite, vermiculite (?), quartz, K-feldspar
I	3	W	160	1.3	WR XRD: quartz, K-feldspar, anhydrite, biotite/muscovite CF XRD: illite, vermiculite(?), anhydrite, K-feldspar, quartz
I	4	W	160	3.8	WR XRD: quartz, K-feldspar, anhydrite, biotite/muscovite CF XRD: illite
I	6	W	200	3.0	WR XRD: quartz, K-feldspar, anhydrite, biotite/muscovite CF XRD: illite
I	7	W	200	10.9	WR XRD: quartz, K-feldspar, anhydrite, biotite/muscovite CF XRD: illite, vermiculite (?), K-feldspar, quartz SEM: Fe-Ca carbonate (ankerite), Fe-Mg clay (illite [glauconite?])
I	8	W	160	11.8	WR XRD: quartz, K-feldspar, anhydrite, biotite/muscovite CF XRD: illite, quartz
II	2	W	250	14.7	CF XRD: illite, chlorite, quartz SEM: Fe-Mg-Ca clays (illite/glauconite/chlorite)
II	6	W	250	4.2	CF XRD: illite, Na-Beidellite SEM: Na-Ca clays (Beidellite), Fe-Mg-Ca clays (illite/glauconite/chlorite)
II	7	W	250	6.0	CF XRD: illite SEM: Fe-Mg-Ca clays, K-Na-Ca clays (Beidellite), Calcite
II	8	W	250	11.6	CF: Illite, chlorite, quartz
Pre-Exper.		T			WR XRF: quartz, kaolinite, chlorite
III	1	T, B	200	44.6	WR XRD: ankerite
III	2	T	140	15.3	WR XRD: quartz, kaolinite, chlorite, ankerite SEM: Kaolinite, chlorite
III	3	T	200	3.5	WR XRD: quartz, kaolinite, chlorite, ankerite SEM: kaolinite
III	5	T	250	2.7	SEM: secondary nickel bearing chlorite
III	6	T	250	13.1	SEM: ankerite
III	7	T	200	49.8	SEM: kaolinite, Fe-Mg clays, secondary calcite

W – Weber rock/brine. T – Tuscaloosa rock/brine. WR XDR – whole rock x-ray diffraction. B – brine only blank. CF XDR – clay-sized fraction x-ray diffraction. SEM scanning electron microscopy.

2.1.6.8   Scaling and Corrosion

Table 6 lists the SI values (log Q/K) for anhydrite (ANH), calcite (CAL), dolomite (DOL), quartz (QTZ), strontianite (STR), siderite (SID), and ankerite (ANK) using the measured brine concentrations given in Appendix A. Because many of the brine samples had non-detectable levels of magnesium and/or sulfate, SI values for anhydrite and dolomite could not be calculated for these samples. In addition, most brine samples had non-detectable levels of aluminum precluding the calculation of SI values for aluminosilicate minerals.

Table 6. Calculated P_{CO2} and Saturation Indexes (log Q/K) calculated for selected scale mineral. Anhydrite (ANH), calcite (CAL), dolomite (DOL), quartz (QTZ), strontianite (STR), siderite (SID), and ankerite (ANK).

Sample ID	Time day	Temp C	P$_{CO2}$ bars	ANH	CAL	DOL	QTZ	STR	SID	ANK
Test I Cell 1 Out 1	1	200	10.74	-0.16	-0.19	-0.48	-0.17	-2.75	**0.32**	**0.61**
Test I Cell 1 Out 2	2	200	10.25	-0.31	-0.35	-0.78	-0.19	-2.32	**0.22**	**0.34**
Test I Cell 1 Out 3	4	200	10.22	-0.08	-0.27	-1.35	-0.14	-2.41	**0.02**	**0.23**
Test I Cell 1 Out 4	8	200	10.07	-0.01	**0.09**		-0.13	-2.09	**0.24**	**0.80**
Test I Cell 1 Out 5	16	200	9.59	**0.05**	**0.26**		-0.13	-1.96	**0.18**	**0.90**
Test I Cell 1 Out 6	32	200	7.81	-0.14	-0.13		-0.18	-2.27	-0.17	**0.16**
Test I Cell 1 Out 7	64	200	7.71	-0.14	-0.29		-0.17	-2.49	-0.33	-0.15
Test I Cell 2 Out 1	1	200	0.76				-0.23	-2.29	**0.10**	
Test I Cell 2 Out 2	2	200	0.81	**0.05**	**0.09**	-0.32	-0.18	-2.16	**0.14**	**0.70**
Test I Cell 2 Out 3	4	200	0.96	-0.12	-0.23	-0.77	-0.14	-2.40	-0.21	**0.03**
Test I Cell 2 Out 4	8	200	1.34	-0.19	-0.40	-1.00	-0.11	-2.53	**0.05**	**0.13**
Test I Cell 2 Out 5	16	200	1.79	-0.13	-0.52	-1.42	-0.02	-2.98	-0.54	-0.59
Test I Cell 2 Out 6	32	200	2.10	-0.22	-0.60	-1.83	0.00	-2.89	**0.13**	0.00
Test I Cell 2 Out 7	64	200	2.39	-0.40	-0.82	-1.79	-0.02	-2.88	-0.67	-1.02
Test I Cell 3 Out 1	1	160	1.55	-0.07	-0.88	-2.11	-0.46		-0.53	-0.58
Test I Cell 3 Out 2	2	160	1.40	**0.12**	-0.44	-1.22	-0.26	-3.35	-0.29	**0.09**
Test I Cell 3 Out 3	4	160	1.34	-0.08	-0.54	-1.23	-0.13	-2.75	-0.07	**0.22**
Test I Cell 3 Out 4	8	160	1.24	-0.11	-0.72		-0.10	-2.67	-0.50	-0.40
Test I Cell 3 Out 5	16	160	1.17	-0.05	-0.89		-0.08	-2.79	-0.65	-0.71
Test I Cell 3 Out 6	32	160	1.20	-0.15	-0.91		-0.07	-2.73	-0.91	-1.00
Test I Cell 3 Out 7	64	160	1.26	-0.18	-0.47		-0.09	-2.32	-0.06	**0.29**
Test I Cell 4 Out 1	1	160	4.29	**0.13**	-0.22	-0.74	-0.47		**0.22**	**0.82**
Test I Cell 4 Out 2	2	160	4.19	**1.24**	**0.78**	**1.22**	-0.18	-2.58	**0.20**	**1.81**
Test I Cell 4 Out 3	4	160	3.87	**0.05**	-0.07	-0.62	-0.11	-2.72	**0.38**	**1.13**
Test I Cell 4 Out 4	8	160	3.71	**0.04**	-0.18	-0.84	-0.07	-2.71	**0.04**	**0.68**
Test I Cell 4 Out 5	16	160	3.60	-0.02	-0.17	-1.11	-0.04	-2.39	**0.32**	**0.97**
Test I Cell 4 Out 6	32	160	3.51	-0.09	-0.22	-1.17	-0.03	-2.23	-0.04	**0.56**
Test I Cell 4 Out 7	64	160	3.45	-0.14	-0.30		-0.09	-2.37	-0.08	**0.45**
Test I Cell 5 Out 1	1	160	4.32	**0.09**	-0.51	-1.25	-0.45		-0.08	0.23
Test I Cell 5 Out 2	2	160	4.06	**0.06**	-0.71	-1.70	-0.34	-3.61	-0.26	-0.14
Test I Cell 5 Out 3	4	160	3.84	-0.01	-0.33	-0.93	-0.14	-3.17	**0.01**	**0.51**
Test I Cell 5 Out 4	8	160	3.61	**0.03**	-0.22	-0.87	-0.08	-2.64	**0.07**	**0.67**
Test I Cell 5 Out 5	16	160	3.42	-0.02	-0.41	-1.19	-0.07	-2.53	**0.07**	**0.49**
Test I Cell 5 Out 6	32	160	3.30	-0.12	-0.65	-1.95	-0.05	-2.63	-0.43	-0.25
Test I Cell 5 Out 7	64	160	3.13	-0.12	-0.65	-1.95	-0.06	-2.79	-0.21	-0.03
Test I Cell 6 Out 1	1	200	2.78	-0.07	**0.02**		-0.09	-2.06	-0.10	**0.39**
Test I Cell 6 Out 2	2	200	2.75	**0.04**	-0.01	-0.40	-0.13	-2.13	-0.28	**0.17**
Test I Cell 6 Out 3	4	200	2.89	**0.03**	-0.29	-1.14	-0.10	-2.42	-0.47	-0.29
Test I Cell 6 Out 4	8	200	3.02	**0.11**	-0.13	-0.08	-0.15	-2.27	-0.11	**0.24**
Test I Cell 6 Out 5	16	200	3.04	**0.01**	-0.22	-0.93	-0.14	-2.37	-0.59	-0.34
Test I Cell 6 Out 6	32	200	3.36	-0.08	-0.40	-1.31	-0.11	-2.78	-0.50	-0.43
Test I Cell 6 Out 7	64	200	3.31	-0.12	-0.39	-1.24	-0.16	-3.02	-0.78	-0.70
Test I Cell 7 Out 1	1	200	12.14	**0.02**	-0.04	-0.46	-0.20		**0.28**	**0.72**
Test I Cell 7 Out 2	2	200	11.60	-0.13	-0.17	-0.53	-0.19	-2.42	**0.19**	**0.49**
Test I Cell 7 Out 3	4	200	11.45	-0.04	-0.11	-0.70	-0.15	-2.30	**0.10**	**0.46**
Test I Cell 7 Out 4	8	200	10.95	**0.06**	-0.09	-0.76	-0.17	-2.35	**0.11**	**0.49**
Test I Cell 7 Out 5	16	200	10.59	-0.08	-0.27		-0.15	-2.44	-0.24	-0.05
Test I Cell 7 Out 6	32	200	10.10	-0.10	-0.22		-0.13	-2.39	-0.12	0.12
Test I Cell 7 Out 7	64	200	9.56	-0.11	-0.07		-0.13	-2.19	-0.13	0.27
Test I Cell 8 Out 1	1	160	13.16	**0.06**	-0.78	-1.41	-0.52		-0.21	-0.17
Test I Cell 8 Out 2	2	160	12.55	-0.01	-0.69	-1.14	-0.39	-3.49	-0.06	**0.07**
Test I Cell 8 Out 3	4	160	12.01	-0.03	-0.53	-0.91	-0.28	-3.42	**0.12**	**0.42**
Test I Cell 8 Out 4	8	160	11.53	0.05	-0.42	-0.63	-0.22	-2.95	**0.05**	**0.45**
Test I Cell 8 Out 5	16	160	11.10	-0.06	-0.32	-0.57	-0.12	-2.91	**0.09**	**0.59**

Sample ID	Time day	Temp C	P$_{CO2}$ bars	ANH	CAL	DOL	QTZ	STR	SID	ANK
Test I Cell 8 Out 6	32	160	10.73	-0.07	-0.44	-0.92	-0.07	-3.00	-0.17	**0.22**
Test I Cell 8 Out 7	64	160	10.30	-0.12	-1.14	-2.34	-0.07	-3.69	-0.86	-1.17
Test II Cell 2 Out 1	1	250	15.02	-0.15	**0.45**		-0.20	-2.50	**0.52**	**1.02**
Test II Cell 2 Out 2	2	250	15.12	-0.06	**0.59**		-0.16	-2.50	**0.45**	**1.09**
Test II Cell 2 Out 3	4	250	14.98	-0.16	**0.45**		-0.12	-2.46	**0.52**	**1.02**
Test II Cell 2 Out 4	8	250	14.67	-0.15	**0.42**		-0.15	-2.59	**0.30**	**0.77**
Test II Cell 2 Out 5	16	250	14.61	-0.15	**0.49**		-0.13	-2.39	**0.55**	**1.08**
Test II Cell 2 Out 6	32	250	14.72	-0.16	**0.43**		-0.10	-2.45	**0.41**	**0.88**
Test II Cell 2 Out 7	73	250	14.05	-0.05	**0.47**		-0.07	-2.38	**0.54**	**1.06**
Test II Cell 4 Out 1	1	250	15.12	-0.15	**0.37**		-1.48		**0.63**	**1.05**
Test II Cell 4 Out 2	2	250	14.67	-0.10	**0.44**		-1.42		**0.61**	**1.10**
Test II Cell 4 Out 3	4	250	14.59	-0.12	**0.40**		-1.48		**0.59**	**1.04**
Test II Cell 4 Out 4	8	250	14.91	-0.17	**0.37**		-1.56		**0.59**	**1.00**
Test II Cell 4 Out 5	16	250	14.48	-0.19	**0.35**		-1.61		**0.61**	**1.00**
Test II Cell 4 Out 6	32	250	14.13	-0.06	**0.53**		-1.60		**0.62**	**1.20**
Test II Cell 4 Out 7	73	250	13.52	-0.17	**0.40**		-1.59		**0.62**	**1.06**
Test II Cell 6 Out 1	1	250	3.39	-0.04	**0.43**		-0.06	-2.28	**0.19**	**0.66**
Test II Cell 6 Out 2	2	250	3.76	**0.01**	**0.36**		-0.01	-2.52	**0.21**	**0.62**
Test II Cell 6 Out 3	4	250	4.13	-0.11	**0.21**		-0.02	-2.45	**0.03**	**0.29**
Test II Cell 6 Out 4	8	250	4.39	-0.15	-0.04		-0.06	-2.38	**0.15**	**0.16**
Test II Cell 6 Out 5	16	250	4.44	-0.20	**0.12**		-0.09	-2.05	**0.46**	**0.63**
Test II Cell 6 Out 6	32	250	4.64	-0.16	**0.19**		-0.06	-2.22	**0.56**	**0.80**
Test II Cell 6 Out 7	73	250	4.72	-0.41	-0.02		-0.08	-2.39	**0.61**	**0.64**
Test II Cell 7 Out 1	1	250	5.41	-0.02	**0.50**		-0.17	-2.37	**0.44**	**0.98**
Test II Cell 7 Out 2	2	250	5.88	**0.06**	**0.55**		-0.13	-2.44	**0.15**	**0.75**
Test II Cell 7 Out 3	4	250	5.87	-0.07	**0.34**		-0.10	-2.51	**0.14**	**0.53**
Test II Cell 7 Out 4	8	250	5.96	-0.08	-0.06		-0.11	-2.94	-0.18	-0.19
Test II Cell 7 Out 5	16	250	5.99	-0.09	**0.37**		-0.09	-2.59	**0.30**	**0.72**
Test II Cell 7 Out 6	32	250	6.35	-0.03	**0.45**		-0.08	-2.52	**0.29**	**0.78**
Test II Cell 7 Out 7	73	250	6.52	**0.04**	**0.53**		-0.08	-2.56	**0.23**	**0.81**
Test II Cell 8 Out 1	1	250	13.96	-0.08	**0.56**		-0.13	-2.40	**0.57**	**1.17**
Test II Cell 8 Out 2	2	250	13.50	-0.08	**0.59**		-0.14	-2.50	**0.53**	**1.16**
Test II Cell 8 Out 3	4	250	13.87	-0.06	**0.55**		-0.13	-2.42	**0.70**	**1.30**
Test II Cell 8 Out 4	8	250	13.59	-0.16	**0.40**		-0.13	-2.48	**0.61**	**1.06**
Test II Cell 8 Out 5	16	250	13.40	-0.10	**0.54**		-0.12	-2.47	**0.47**	**1.06**
Test II Cell 8 Out 6	32	250	13.53	-0.10	**0.54**		-0.09	-2.44	**0.57**	**1.16**
Test II Cell 8 Out 7	73	250	13.01	-0.05	**0.54**		-0.09	-2.43	**0.56**	**1.15**
Test III Cell 1 Out 1	1	200	48.04		-2.04	-4.19		-6.03	-3.65	-5.24
Test III Cell 1 Out 2	2	200	47.46		-0.98	-2.02	-1.61	-5.04	-2.54	-3.05
Test III Cell 1 Out 3	4	200	45.78		-1.44	-2.93		-5.37	-2.72	-3.69
Test III Cell 1 Out 4	8	200	44.69		-1.22	-2.50		-5.17	-2.28	-3.03
Test III Cell 1 Out 5	16	200	43.72		-1.22	-2.50		-5.18	-2.07	-2.82
Test III Cell 1 Out 6	32	200	42.09		-1.33	-2.69	-1.45	-5.30	-1.87	-2.73
Test III Cell 1 Out 7	80	200	40.42		-0.68	-1.39	-1.21	-4.64	-0.93	-1.14
Test III Cell 2 Out 1	1	140	16.71		-0.73	-1.13	-0.33	-3.87	-1.86	-1.58
Test III Cell 2 Out 2	2	140	16.11		-0.48	-0.64	-0.24	-3.61	-1.62	-1.09
Test III Cell 2 Out 3	4	140	15.63		-0.38	-0.43	-0.13	-3.51	-1.44	-0.81
Test III Cell 2 Out 4	8	140	15.12		-0.32	-0.31	-0.02	-3.45	-1.34	-0.65
Test III Cell 2 Out 5	16	140	14.70		-0.85	-1.38	-0.01	-3.95	-1.75	-1.59
Test III Cell 2 Out 6	32	140	14.34		-1.01	-1.65	0.05	-4.12	-1.79	-1.80
Test III Cell 2 Out 7	80	140	14.14		-1.02	-1.73	0.17	-4.20	-1.78	-1.79
Test III Cell 3 Out 1	1	200	3.65		-0.69	-1.46	-0.11	-4.48	-2.53	-2.75
Test III Cell 3 Out 2	2	200	3.56		-1.25	-2.59	-0.08	-4.99	-3.09	-3.86
Test III Cell 3 Out 3	4	200	3.72		-0.73	-1.56	-0.02	-4.53	-2.38	-2.64
Test III Cell 3 Out 4	8	200	3.58		-1.33	-2.76	-0.03	-5.11	-2.79	-3.65
Test III Cell 3 Out 5	16	200	3.54		-0.80	-1.69	-0.04	-4.57	-2.04	-2.37
Test III Cell 3 Out 6	32	200	3.42		-1.56	-3.18	-0.03	-5.35	-2.54	-3.63
Test III Cell 3 Out 7	80	200	3.22		-0.52	-1.19	0.00	-4.28	-1.28	-1.33

Sample ID	Time day	Temp C	P$_{CO2}$ bars	ANH	CAL	DOL	QTZ	STR	SID	ANK
Test III Cell 4 Out 1	1	250	45.41		-0.86	-2.05	-0.11	-5.21	-2.17	-2.98
Test III Cell 4 Out 2	2	250	44.85		-1.47	-3.32	-0.09	-5.75	-2.62	-4.05
Test III Cell 4 Out 3	4	250	42.88		-1.23	-2.87	-0.08	-5.51	-2.19	-3.38
Test III Cell 4 Out 4	8	250	41.94		-1.43	-3.28	-0.08	-5.68	-2.16	-3.54
Test III Cell 4 Out 5	16	250	40.63		-1.48	-3.41	-0.10	-5.70	-2.03	-3.47
Test III Cell 4 Out 6	32	250	41.06		-1.48	-3.49	-0.08	-5.60	-1.66	-3.09
Test III Cell 4 Out 7	80	250	41.64		-0.98	-2.60	-0.04	-5.10	-1.11	-2.04
Test III Cell 5 Out 1	1	250	2.39		-1.19	-2.78	-0.18	-5.50	-2.44	-3.58
Test III Cell 5 Out 2	2	250	1.95		-0.94	-2.29	-0.20	-5.17	-1.96	-2.85
Test III Cell 5 Out 3	4	250	2.70		-0.95	-2.29	-0.19	-5.17	-1.87	-2.77
Test III Cell 5 Out 4	8	250	2.61		-1.54	-3.59	-0.19	-5.70	-2.07	-3.57
Test III Cell 5 Out 5	16	250	2.59		-1.12	-2.78	-0.22	-5.26	-1.50	-2.57
Test III Cell 5 Out 6	32	250	2.89		-0.82	-2.24	-0.19	-4.90	-0.99	-1.76
Test III Cell 5 Out 7	80	250	3.75		-1.25	-3.30	-0.14	-5.31	-1.27	-2.47
Test III Cell 6 Out 1	1	250	13.91		-1.29	-2.98	-0.13	-5.59	-2.48	-3.72
Test III Cell 6 Out 2	2	250	13.19		-1.18	-2.75	-0.12	-5.51	-2.31	-3.45
Test III Cell 6 Out 3	4	250	12.88		-1.36	-3.15	-0.12	-5.58	-2.22	-3.54
Test III Cell 6 Out 4	8	250	13.27		-1.26	-2.93	-0.13	-5.49	-1.98	-3.19
Test III Cell 6 Out 5	16	250	12.89		-1.60	-3.69	-0.13	-5.82	-2.07	-3.62
Test III Cell 6 Out 6	32	250	12.78		-1.25	-3.07	-0.07	-5.37	-1.54	-2.74
Test III Cell 6 Out 7	80	250	12.65		-1.10	-2.91	-0.10	-5.21	-1.24	-2.29
Test III Cell 7 Out 1	1	200	53.02		-1.04	-2.21	-0.12	-4.87	-2.19	-2.76
Test III Cell 7 Out 2	2	200	53.13		-1.10	-2.27	-0.05	-4.94	-2.33	-2.96
Test III Cell 7 Out 3	4	200	50.18		-1.42	-2.91	-0.02	-5.25	-2.54	-3.49
Test III Cell 7 Out 4	8	200	50.66		-1.57	-3.21	0.00	-5.40	-2.62	-3.72
Test III Cell 7 Out 5	16	200	48.89		-1.43	-2.93	0.00	-5.25	-2.35	-3.31
Test III Cell 7 Out 6	32	200	47.13		-1.26	-2.60	0.00	-5.08	-1.99	-2.78
Test III Cell 7 Out 7	80	200	45.25		-1.47	-3.00	**0.02**	-5.22	-1.89	-2.89
Test III Cell 8 Out 1	1	200	14.57		-0.71	-1.50	-0.13	-4.50	-2.08	-2.32
Test III Cell 8 Out 2	2	200	14.35		-1.02	-2.12	-0.06	-4.83	-2.48	-3.03
Test III Cell 8 Out 3	4	200	14.00		-0.45	-0.98	-0.03	-4.26	-1.85	-1.82
Test III Cell 8 Out 4	8	200	13.47		-1.56	-3.19	-0.01	-5.38	-2.83	-3.91
Test III Cell 8 Out 5	16	200	12.99		-1.05	-2.14	**0.02**	-4.90	-2.14	-2.73
Test III Cell 8 Out 6	32	200	12.20		-0.95	-1.99	**0.04**	-4.72	-1.81	-2.28
Test III Cell 8 Out 7	80	200	11.65		-0.41	-0.93	**0.08**	-4.20	-1.02	-0.95
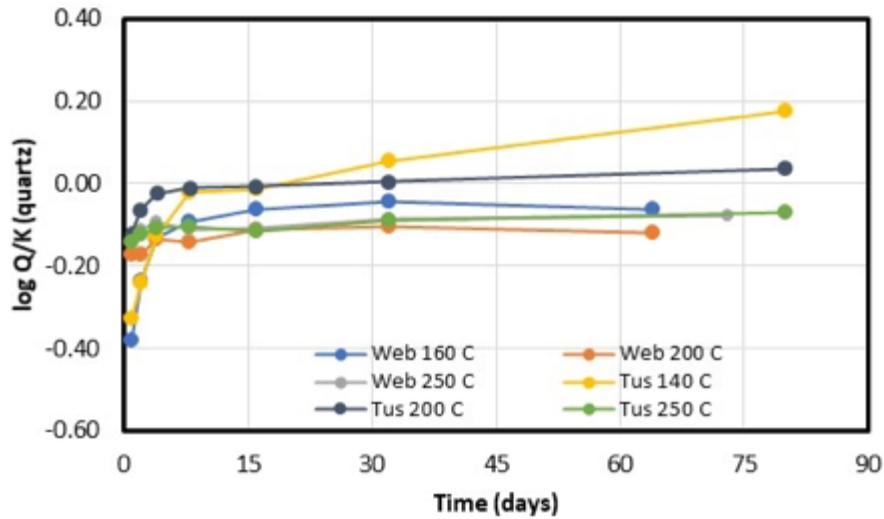
Figure 25. Calculated saturation indices (log Q/K) for quartz.

Silica Scaling: The SI values of quartz as a function of time and averaged across all samples collected from experiments having the same rock, brine, and temperature conditions are shown in Figure 25. As may been seen in the figure, the SI values for all samples approach steady state values that are near (0.12 to 0.17) but different from equilibrium with quartz (SI = 0). As there is no $SiO_{2,aq}$ in the initial synthetic brine, its increasing concentration with time reflects the dissolution of silica and aluminosilicate minerals with more rapid approach to steady state at higher temperatures and slower approach at lower temperatures consistent with mineral dissolution kinetics. Similar SI values for both the Weber and Tuscaloosa experiments suggest that similar reactions control $SiO_{2,aq}$ concentrations. The deviation of the steady state experimental results from quartz equilibrium may indicate that $SiO_{2,aq}$ concentration was not controlled by equilibrium with quartz or had not truly reach steady-state. Alternatively, this may reflect uncertainties in the activity coefficient for $SiO_{2,aq}$ and the parameterization of the Pitzer formalism used to calculate them. Given that solubility of silica decreases with decreasing temperature, these results indicate that silica scale formation in the heat exchanger and other infrastructure will be an operational concern during the energy recovery phase of an RTES system. During the recovery phase, potential silica scaling issues are likely to require additional facilities to handle silica precipitation and/or cyclical maintenance of the heat exchanger system. In addition, during the charging period, the injection of heated, silica-depleted brine is likely to rapidly aquire $SiO_{2,aq}$ concentrations to equilibrium values in the reservoir. Therefore, the silica scaling is likely to be an ongoing concern through the operation phase of a RTES project.
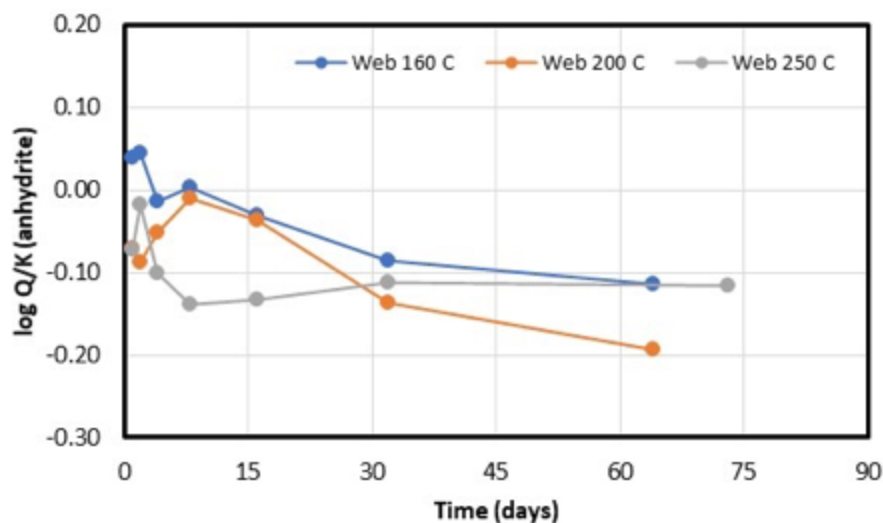
Figure 26. Calculated saturation indices (log Q/K) for anhydrite.

Sulfate Scaling: The SI values of anhydrite as a function of time and averaged across all samples collected from experiments at a given temperature using Weber brines and rock are shown in Figure 26. Experiments conducted using Tuscaloosa brine and rock did not have detectable concentrations of sulfate and anhydrite SI values could not be calculated. As may be seen the SI values for Weber brines at all temperatures are initially near zero but trend to more negative values with increasing time. Because anhydrite is a mineral identified (XRD and SEM) in the pre- and most of the post-experimental Weber sediments (except in a 200°C and low PCO_2 (1.5 bars) experiment; Test I Cell 2 (Figure B-10)), increasing negative SI values with reaction time was unexpected. The modeling of the previously discussed anhydrite solubility experiments of Blount and Dickson (1969) yielded calculated anhydrite SI values of -0.04, -0.10, and -0.25 for 3 m NaCl solution at 150, 200, and 250°C. These results suggest that Weber experimental brines may indeed be equilibrated with anhydrite but the Pitzer formalism overpredicts the solubility of anhydrite to an increasing degree with increasing temperature. If this is the case, precipitation may occur from brines predicted to be undersaturated with anhydrite. The experimental results also indicate that careful consideration of the quality of the parameterization of the Pitzer formalism at higher temperatures and salinities is needed to use this modeling approach in the design of an RTES system. Finally, the contrast between the Weber and Tuscaloosa experiments highlights the importance of site selection (brine composition in particular) for an RTES system; choosing a reservoir with little or no anhydrite (or other sulfate minerals) eliminates concerns for sulfate scaling.

Carbonate Scaling: The SI values of calcite as a function of time, temperature, and P_{CO2} (low, medium, or high) are shown in Figure 27. With the exception of the 250°C Weber experiments, which were saturated or supersaturated with respect to calcite (SI ≥ 0), all other experiments were undersaturated with respect to calcite. Secondary calcite was identified (SEM) in the 250°C Weber experiments (Figure 28), consistent with the calculated supersaturation SI value. However, secondary calcite was also identified (SEM) in the 250°C Tuscaloosa experiments that had SI values indicating the brines were undersaturated with respect to calcite. The precipitation of calcite from brines calculated to be undersaturated with respect to the mineral demonstrate the limitation of the Pitzer formalism as currently parameterized in that it appears to overpredict the solubility of calcite at high temperatures and salinities as shown in Figure 20.

43
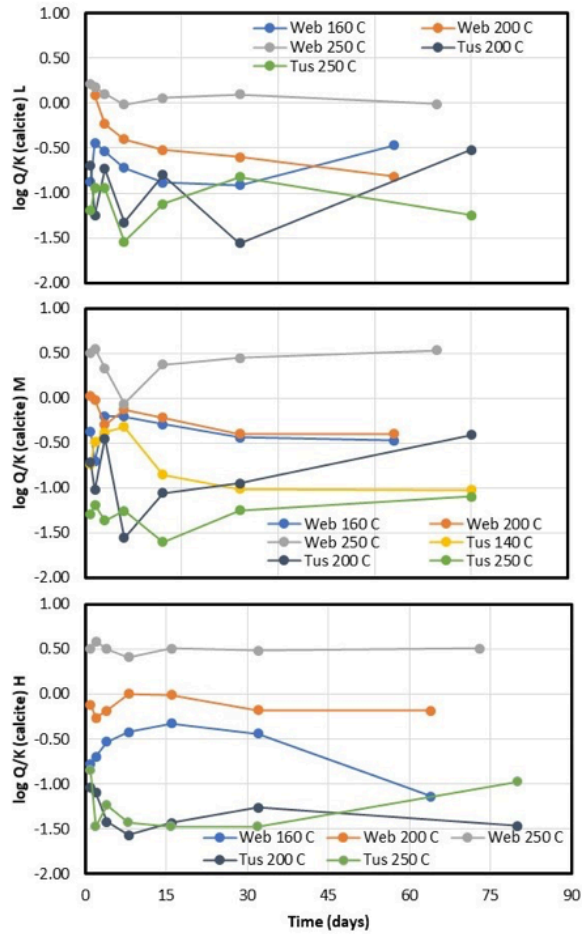
Figure 27. Calculated saturation indices (log Q/K) for calcite at low (L), medium (M), and high (H) P_{CO2}.
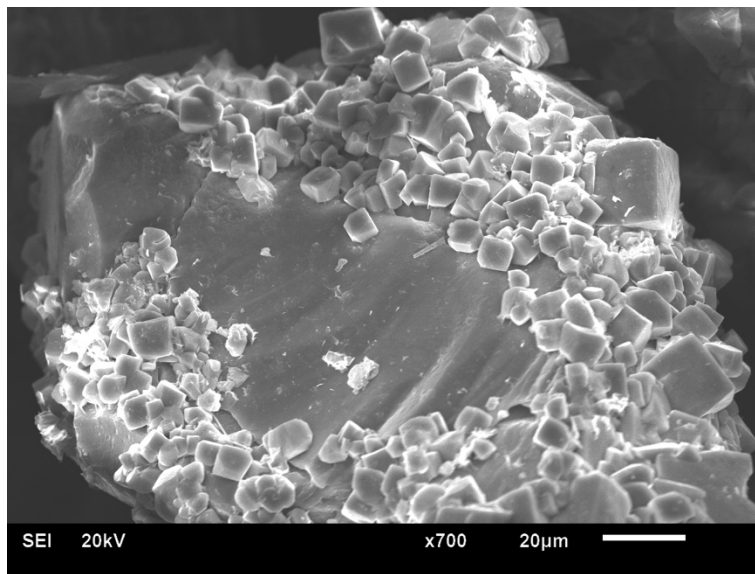
Figure 28. SEM image of post-experimental Test-II Cell 7 (T = 250 ºC, P_{CO2} = 6.0 bars) reacted rock sample showing a quartz grain coated with secondary silica (quartz) and euhedral calcite crystals.

One of the project objectives was to assess the effectiveness of using CO_2 as a carbonate scale inhibitor. However, for the Weber experiments the calcite SI values exhibit no consistent trend with increasing P_{CO2}. A small amount of calcite was identified (XRD) in pre-experimental Weber sediments (Figure 27) but it was only identified in one [200°C and low P_{CO2} (1.5 bar)] of the 200°C post-experimental sediments (Figure 22). As mentioned above, this is the same experiment (Test I Cell 2) where no anhydrite was detected. The lack of calcite in most of the 160 and 200°C post-experimental sediments may be the result of the complete dissolution of pre-existing calcite during the high brine:rock ratio (10:1) experiments at higher level of P_{CO2}. If the addition of CO_2 to prevent carbonate scaling in surface RTES infrastructure does result in the dissolution of carbonates in the reservoir via

$$CaCO_3 + CO_2 + H_2O \rightarrow Ca^{2+} + 2HCO_3^- \tag{4}$$

the long-term impact of this approach for scale inhibition may result in increased rather than decreased potential for carbonate scale formation during future cycling of the brine particularly at lower temperatures.

Although iron was not an initial constituent, it was detected in all sampled brines indicating either dissolution of iron-bearing minerals, corrosion of the pressure cells, or a combination of both. SI values for ankerite as a function of time, temperature, and P_{CO2} (low, medium, or high) are shown in Figure 29. The SI values show both undersaturation and supersaturation of ankerite in the Weber experiments. In the Tuscaloosa experiments SI values indicate undersaturation with respect to ankerite. However, secondary ankerite is observed (XRD and SEM) in all the Tuscaloosa experiments (including the brine-only blank, Figure B-28 and Figure B-29).
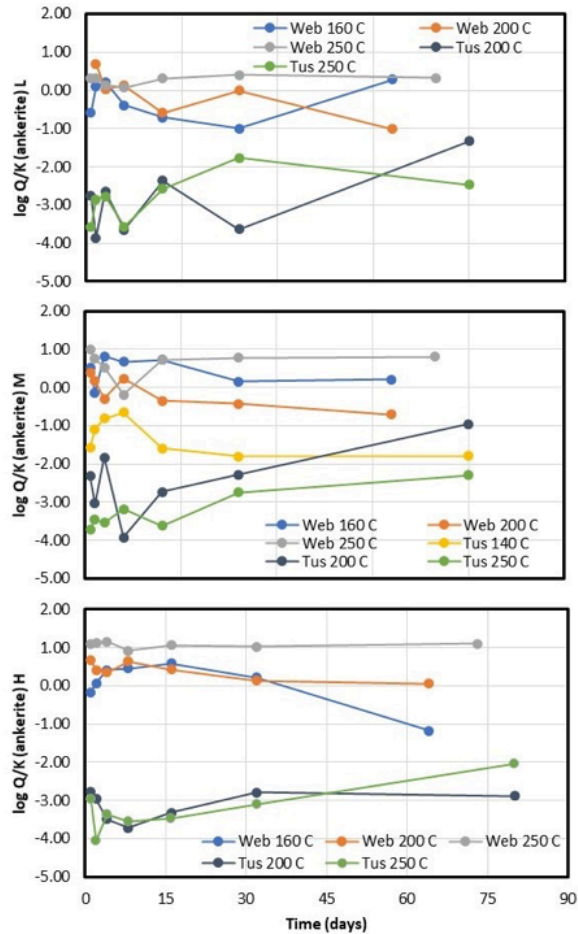
Figure 29. Calculated saturation indices (log Q/K) for ankerite at low (L), medium (M), and high (H) P_{CO2}.

The occurrence of secondary ankerite allows an alternative approach for estimating at temperature pH values. Assuming equilibrium between the Tuscaloosa brines and ankerite results in calculated pH values that are 0.4 to 0.5 units higher than those calculated from the measured total experimental pressures as described previously. However, the pH values calculated from ankerite equilibrium are on average only 0.1 units higher than those independently calculated using the measured total pressures and the B-dot method (Figure 24). Using the ankerite equilibrium-based higher pH values for the Tuscaloosa brines results in more positive, near equilibrium SI values for calcite. However, if challenges associated with estimating pH and the substantial overprediction of calcite solubility are the results of uncertainties in the calculated activity coefficient for HCO_3^-, the pH values calculated from equilibrium with ankerite may also be problematic as these calculations also incorporate the activity coefficient for HCO_3^-. In summary, caution should be taken when using the currently parameterized Pitzer formalism to model high-temperature, high-salinity brines such as those found in the Lower Tuscaloosa Formation.

Corrosion: The brine-rock experiments included two brine-only blanks, one using Weber brine at 250°C and the other using Tuscaloosa brine at 200°C. The normalized Fe^{2+} concentrations as a function of time for these experiments are shown in Figure 30. Because iron was absent from the initial synthetic brine and these experiments did not include rock, the only source of dissolved iron was from reactions between the stainless steel-reaction cells and the brines (i.e., corrosion). The Weber brine shows a low initial normalized concentration that remains nearly constant with time suggesting that little corrosion of the stainless steel occurs at temperature up to 250°C. However, the 200°C Tuscaloosa brine experiments show an increasing normalized concentration ratio with time indicating ongoing corrosion of the stainless steel. In addition, ankerite scales were identified (XRD) in the post-experiment reaction cell (Figure 31). Finally, nickel (a component of stainless steel) bearing chlorite was also identified in the sediments from one of the 250°C brine-rock Tuscaloosa experiments (Figure 32).
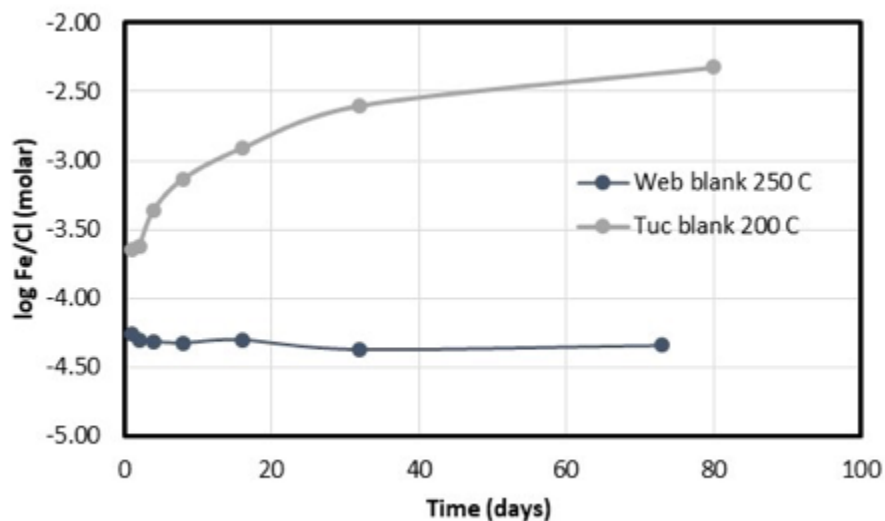
Figure 30. Chloride-normalized Fe concentrations of for brine-only blank experiments.
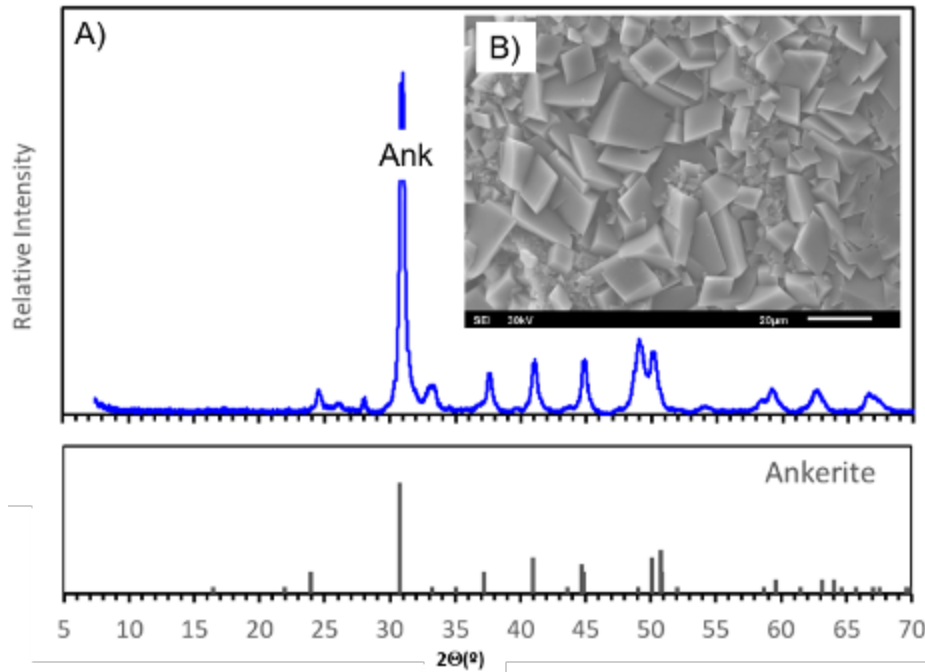
Figure 31. A) XRD spectrum of post-experimental Test-III Cell 1 (T = 250 ºC, P_{CO2} = 44.6 bars) scale deposits retrieved from the reaction cell wall. B) SEM image of reaction-wall scale showing Ni-bearing euhedral ankerite crystals. Test-III Cell 1 was brine-only reaction cell without Lower Tuscaloosa Formation rock.
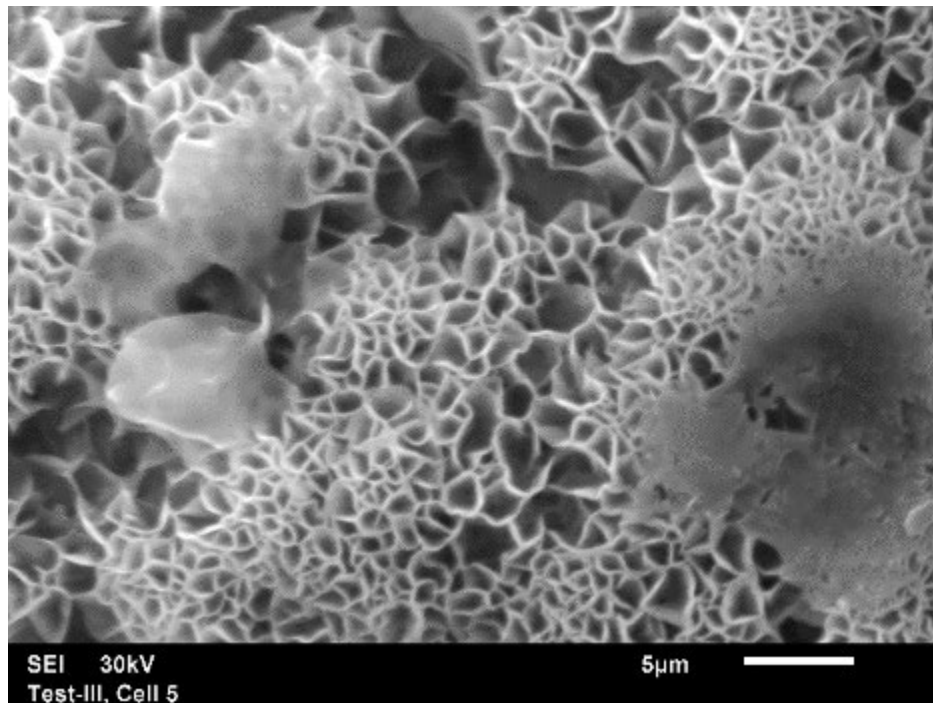
Figure 32. Scanning electron microscopy image of the post-experimental Lower Tuscaloosa Formation from Test-III Cell 5 (T = 250 ºC, P_{CO2} = 2.7 bars). The grain-coating material is Na-Fe-Ca-Mg-Ni clay (chlorite).

However, examination of the reaction cells following the experiment did not reveal any obvious indications of corrosion. The major difference between the Weber and the Tuscaloosa brines were the chloride concentrations at ~1.5 and 3.2 molal, respectively. Results presented here suggest that at chloride concentrations between 1.5 and 3.2 molal corrosion of ferrous metal infrastructure (e.g., stainless steel) may become an issue and that in addition to scaling potential, the potential for corrosion by heated brines should be considered in selecting a reservoir for RTES systems.

2.1.6.9   Mass Transfer Simulations

Mass transfer modeling of the Weber experiments (Test I and Test II) were conducted using TOUGHREACT ECO2N along with the Pitzer *data0.ypf.R2* thermodynamic database (equivalent to GWB database *thermo49.ymp.R2*). This modeling explicitly accounts for CO_2-H_2O partitioning resulting in changes in pressure and headspace volume resulting from the sampling events. The model was constructed as a single grid block, "batch" reactor with "liquid-unsaturated" conditions (i.e., gaseous headspace). The experimental amounts of brine, rock and CO_2 for each model run were used, along with sampling at specified times (20 mL) of the experiments. The predicted pressure evolution was calibrated against measured total pressure data by adjusting initial brine CO_2 content and (if needed) the initial headspace proportion $V_{gas}/(V_{gas+Vliq})$. The Weber sediment grain size (surface area) was adjusted to match the measured trends in $SiO_{2,aq}$ concentrations. Simulations were initiated at elevated temperature and pressure, followed by pressure reduction (at constant temperature) resulting from the removal of fluid samples at prescribed time intervals; heating from ambient to experimental temperature was not modeled.
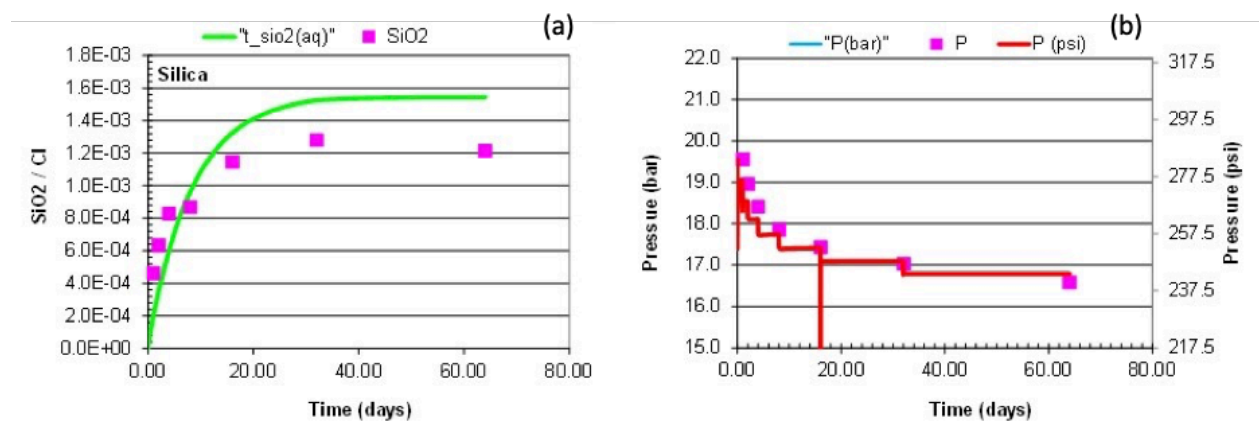
Figure 33. Comparison of measured and model-calibrated normalized $SiO_{2,aq}$ concentration (a) and total pressure for experiment Test I Cell 8.

Examples of calibration results from the 160°C Test I Cell 8 experiment are shown in Figure 33. Normalized calcium and sulfate concentrations, and pH values, for this experiment are shown in Figure 34 and compared to the simulation results. Simulated relative volume changes in minerals are shown in Figure 35. Similar figures for other Test I and Test II experiments are shown in Appendix C. The simulation predicts trends similar to those observed for total pressure, Ca, SO_4, and $SiO_{2,aq}$, although the simulated normalized concentrations of $SiO_{2,aq}$ (Figure 33) and Ca (Figure 34) are higher than observed. These observations for Ca and $SiO_{2,aq}$ are consistent with the results regarding silica and carbonate scaling. The simulations also predict higher pH values than those calculated, as described previously. In addition, in some cases the simulations predict much higher room temperature degassed pH values than those observed (Figure 35). This is possibly the result of known challenges of accurately measuring pH in high TDS brines or incomplete degassing of the collected sample prior to the measurement of pH. The agreement between simulated and measured concentrations of other constituents is highly variable (not shown) and may in part reflect 1) a mismatch in the volume of the brine collected

for each sample (15 compared to 20 mL) affecting pressure and evaporative concentration, 2) the fact that the actual P_{CO2} cannot be measured directly and measured DIC values were impacted by degassing during sampling, and/or 3) the simulations were not conditioned on the observed post-experimental mineralogy.
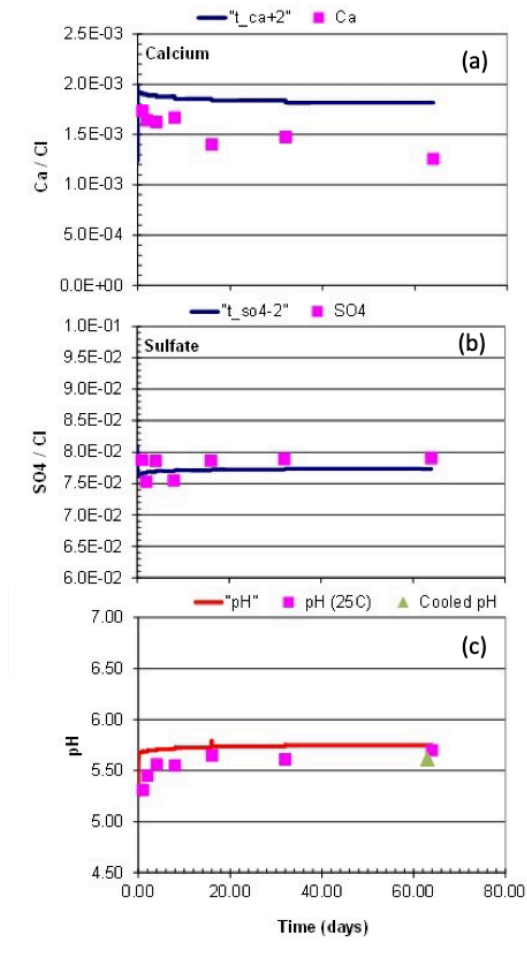
Figure 34. Comparison of measured and simulated normalized Ca (a) and SO_4 (b) and pH for experiment Test I Cell 8 (at 160°C and pressure as shown on Figure 33b).

Example (Test I Cell 8) simulated volumes of minerals dissolved and precipitated are shown in Figure 35 with similar figures for other experiments shown in Appendix C. These simulations suggest that, except at the lowest temperature and lowest P_{CO2} where anhydrite dissolved and calcite precipitated, calcite dissolves and anhydrite along with varying amounts of ankerite were precipitated. The extent of these reactions increased with increased temperature. These results are generally consistent with the post-experimental mineral characterization (Table 5) of the 160 and 200°C experiments that showed loss of calcite and the appearance of ankerite. However, in at least one of the 250°C experiments (Test II Cell 7), calcite precipitation was observed. Because anhydrite was present in the initial sediments, a definitive statement as to the precipitation of additional anhydrite cannot be made although the log Q/K values (Figure 26) suggest that the Weber brines became increasing undersaturated with respect to anhydrite as the experiments proceeded. The simulated volumes of mineral precipitation/dissolution indicate that at 160 and 200°C, the reservoir porosity would decrease and that there would be minimal porosity changes at 250°C.
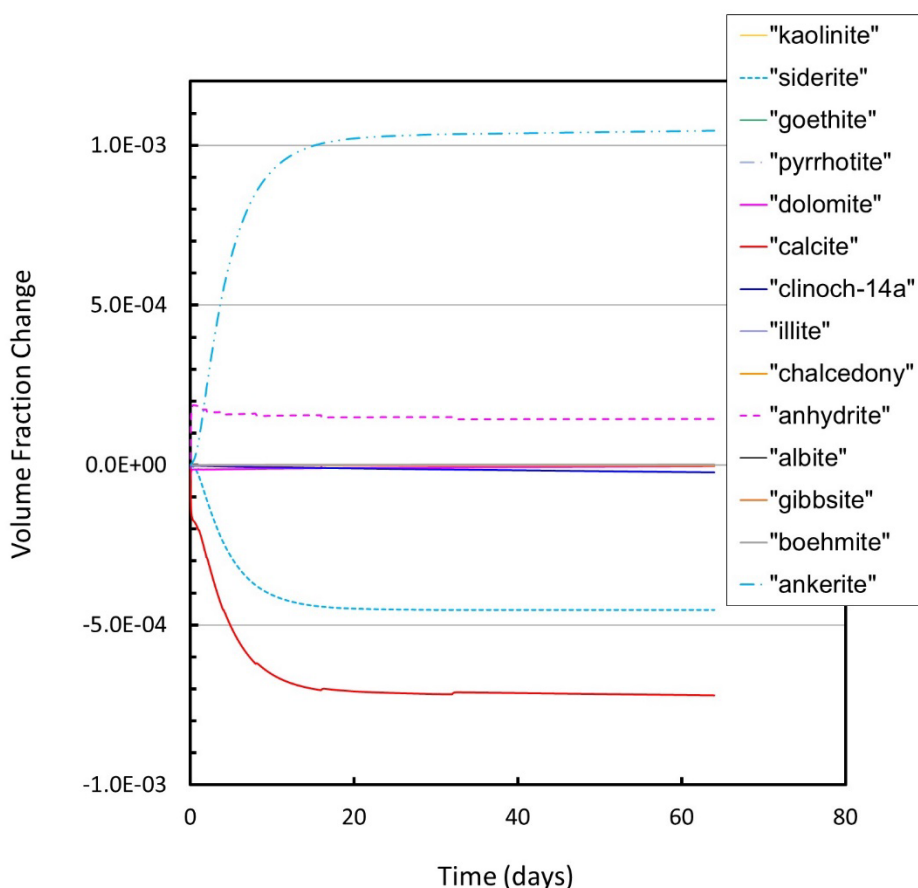
Figure 35. Simulated mineral dissolution and precipitation for experiment Test I Cell 8 (at 160°C and pressure as shown on Figure 33b).

2.1.6.10   Implication for Modeling, Designing, and Operating RTES Systems

One of the goals of the experimental study was to provide measured data against which the efficacy of the existing models can be assessed. In developing an RTES system there will be at least two types of modeling studies that will be conducted. The first will be part of site screening, selection, and characterization. At this stage the goal of modeling will be to assess a potential reservoir for favorable and unfavorable characteristics (e.g., scaling and corrosion potential) often with limited data. In these cases, the parameterized Pitzer formalism used in this study is adequate for modeling with a recognition that the results need to be used with caution at high temperatures and salinities. This adequacy is especially true if the temperatures considered are less than 200°C as is the case for the field-scale examples considered in Section 2.1.7. Although greater accuracy in the geochemical model is desirable, uncertainties in the geochemical model are probably less significant than the uncertainties arising from uncharacterized reservoir physical and chemical heterogeneities (e.g., permeability, porosity, mineralogy, etc.).

The second type of modeling studies support the design and operation of the RTES system. Here the accuracy of geochemical simulations (supported by experimental studies) is critical. For example, an uncertainty in the calculated solubility of calcite of a factor of three too low to a factor of six too high could translate into an uncertainty in the amount of potential scale formation of approximately 2 kg/m^3 of brine. This degree of uncertainty would have significant impact of the design, magnitude, and cost and scope of scale mitigation or brine treatment systems needed for an RTES system. However, this model uncertainty could be addressed in part by updating the parametrization of the Pitzer formalism with results from more recent studies focused on high salinity brines at high temperature and as functions of total pressure (e.g., Dai et al., 2016).

Another goal of the experimental study was to assess the use of CO_2 as a possible carbonate scale inhibitor. We found that although this approach can inhibit scale formation in surface RTES infrastructure during thermal charging, the injected hot CO_2 charged brine will promote dissolution of carbonate mineral in the reservoir, potentially increasing the future scaling potential of the brine if it is recycled. Also shown by the experimental studies was that an understanding of brine chemistry beyond predicting the formation of scaling minerals is important, as the potential for corrosion (impacting the choice of RTES infrastructure materials) exists even for brines with low scale formation potential.

2.1.7   Task 1.3 THC Modeling

2.1.7.1   *Objective and Approach*

The first objective of the THC modeling is to learn about the effect of the hydrogeological setting and operational parameters on RTES performance. The second objective is to examine the possible deleterious effects of geochemical reactions. The modeling approach is to use physics-based models for a variety of case studies to assess system performance and determine whether geochemical issues are likely to be prohibitive for high-temperature RTES. For each case study, the first step is developing a thermal-hydrologic (TH) model of the site, then geochemical reactions (THC) are added. These studies are complemented by stochastic simulations described in Task 2 later in this report, using a wide range of geologic and operational parameters to determine how RTES metrics depend on them.

The basic RTES operation scenarios we consider consist of a pair of wells operating as injection and production wells (flow-through operation) or as an injection/production well and a supply well (push-pull operation). Unless otherwise noted, injection and production rates are of equal magnitude, to minimize pressure changes in the reservoir. We consider annual cycles, with three months of charging during periods of energy excess (summer), three months of thermal energy storage, three months of discharge during periods of energy shortage (winter), and three months of rest. We model multiple years to understand how the RTES system charges up over the first few years to establish a steady heat balance.

The key metrics for physics-based simulations are the energy recovery factor, defined as the annual energy produced divided by the energy injected, and the storage capacity, defined as the total energy stored each year. The stochastic simulations described in Task 2 also quantify the charging time and operating time, defined as the time to fully charge the reservoir for a fixed formation setting and operational conditions and the time to generate electricity, respectively.

The physics-based numerical simulation codes we use are the integral-finite-difference method based TOUGH and TOUGHREACT, and the finite-element-method based MOOSE (i.e., Multiphysics Object-Oriented Simulation Environment) framework. TOUGH3 considers thermal-hydrologic (TH) processes and was used to perform all the TH simulations in Task 1. TOUGHREACT adds reactive geochemistry to TOUGH3 capabilities, resulting in a THC solver. For Task 2, MOOSE was used for the stochastic simulations, and for the mechanical-induced changes in heat transfer, we employed the Tensor Mechanics and Porous Flow modules in MOOSE to solve the THM problem.

2.1.7.2 Physics-Based Thermal-Hydrological (TH) Case Studies

Simulation Tools

TOUGH3-EOS7 (Jung et al., 2018; Pruess, 2004) was used for the TH simulations. TOUGH3 is a general-purpose numerical simulator for fluid flow and heat transport through geological media, based on the integral-finite-difference method. Fluid flow is modeled using Darcy's Law. Different equation of state (EOS) modules are chosen to customize the code for the fluids of interest. EOS7 considers water, brine, air, and heat. Water may be in the liquid or gas phase, but for the present problem we strive to maintain pressure/temperature conditions in the system such that fluid remains liquid. Within the storage reservoir, heat transfer occurs by conduction and convection. Conductive heat loss to the cap and bedrock is modeled with a semi-analytical solution (Vinsome and Westerveld, 1980), so no grid is needed above or below the storage reservoir.

2.1.7.3 Case Study 1: Weber/Tensleep Formation

The Weber/Tensleep Formation in the Rock Springs Uplift in Wyoming is approximately 200 m thick and occurs at depths of 3400−3600 m. For the TH model, layering was simplified from the Rock Springs Uplift well-log interpretations of density porosity, and yields porosities ranging from 0.03 to 0.10 and permeabilities ranging from 1 to 10 mD. Thermal conductivity, 1.3 W/mK, is taken from literature values (Labus and Labus, 2018; Maqsood and Kamran, 2005; Robertson, 1988). Initial conditions are a brine-saturated formation with a salinity of 107,000 ppm, and hydrostatic pressure and geothermal temperature gradients that yield P ~ 3.5 Mpa and T~94°C at formation depth. Subsequent THC simulations use a higher salinity, which is considered more realistic, but the difference should not affect the present results.

The injection/production rate is chosen to be the maximum rate for which pressure remains below the value that can create fractures during injection and above the boiling point during production. The initial injection temperature is specified at ~160°C. The injection enthalpy is held fixed, so as pressure increases during injection, the temperature declines correspondingly.

Three well geometries are considered: (1) a single-well push-pull system, in which the same well is used for injection and production (RZ model); (2) an isolated injection-well/production-well pair (also known as a doublet); and (3) an injection-well/production-well pair within a field of many such pairs in a five-spot pattern. The first two geometries include a laterally extensive model to represent an infinite system, whereas the third geometry has closed (no-flow) lateral boundaries, to represent the symmetry of the five-spot pattern. All three grids have the same vertical discretization and layering.

Full details of the modeling are presented in McLing et al. (2019) and Jin et al. (2020), but the key (TH) result, outlet temperature as a function of time, is shown in Figure 36.
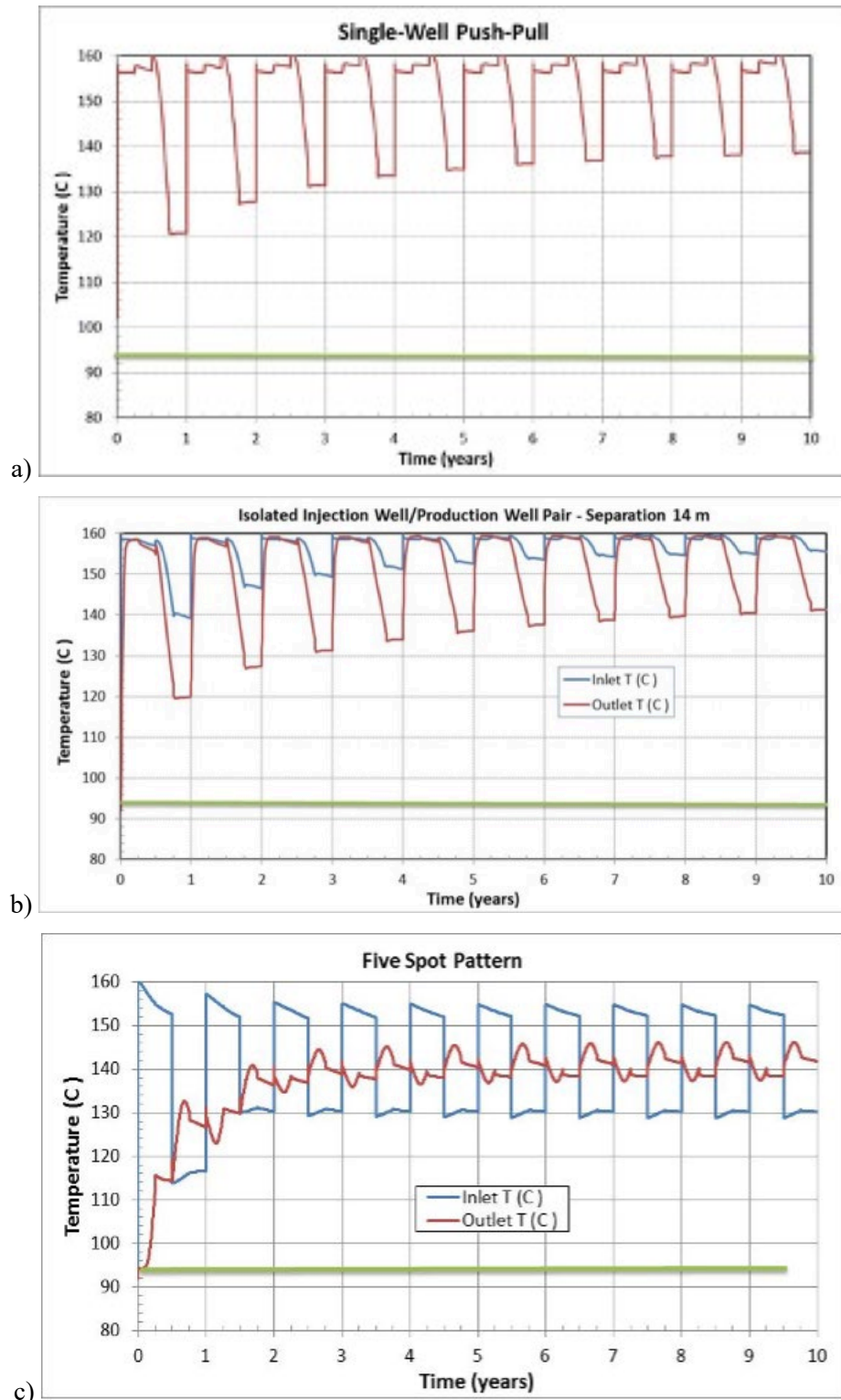
Figure 36. Inlet temperature and outlet temperature for (a) single well push-pull, also described as RZ model, (b) isolated injection-well/production-well pair, (c) five-spot pattern. The green line shows the average initial reservoir temperature.

For the single-well push-pull and the isolated well pair, doublet well configurations, production (outlet) temperature drops from 160°C to 120°C during the first-year production period. There is a gradual improvement for the first five years, then a steady state develops with production temperature dropping from 160°C to 140°C each cycle. This large production temperature range is a problem for incorporating RTES into a thermal power-plant, which requires nearly constant temperature water for best performance.

For the five-spot pattern, after the first three years, production temperature stays in the range of 141°C to 146°C. During each third-quarter production period, the production temperature gradually increases, then declines, with the peak occurring when the thermal front passes the production well. After some trial and error, it was found that making the well separation somewhat bigger than the extent of the thermal plume yields a production temperature with the smallest range of variation, which is important for power-plant operations.

2.1.7.4   Case Study 2: Lower Tuscaloosa Formation

The Lower Tuscaloosa Formation in the Mississippi Gulf Coast has been extensively studied as part of a pilot CO_2 geologic storage project at the Cranfield oil field in Natchez, Mississippi (Lu et al., 2012; Hovorka et al., 2013). The storage reservoir is 24 m thick, and lies at a depth of about 3000 m. The hydrogeologic properties are the same as those presented by Doughty and Freifeld (2013) for simulations of CO_2 injection at the Cranfield site and include vertically heterogenous but horizontally homogenous geologic layers with hydrologic properties taken from well-log data (Figure 37). Porosities range from 0.07 to 0.33 and permeabilities range from 0.03 to 423 mD. Thermal conductivity, 2.5 W/mK, is taken from literature values (Labus and Labus, 2018; Maqsood and Kamran, 2005; Robertson, 1988). Initial conditions are a brine-saturated formation with a salinity of 155,000 ppm, and hydrostatic pressure and geothermal temperature gradients that yield P ~ 3 MPa and T~126°C at formation depth.

The five-spot well configuration was used in this simulation, in which an infinite array of injection well/production well pairs are arranged as shown in Figure 37. Assuming the thermal properties and formation thickness do not vary laterally, then by symmetry, only one-eighth of the region between a single injection well/production well pair needs to be modeled. We initially constructed our model based on the practical formation sizes, denoted as "smaller-scale", where the injection and production wells are separated by 28.3 m, comparable to the actual well spacing used for the Cranfield pilot CO_2 storage project. Flow rate (1.5 kg/s ~ 24 gpm) is typical of CO_2 storage operations. To achieve Terawatt energy storage would require over a thousand of such well pairs, so we created a synthetic "larger-scale" model in which all dimensions are multiplied by a factor of 4, and typical flow rate is about 95 kg/s ~ 1500 gpm, to more accurately represent typical conditions of large scale RTES batteries.
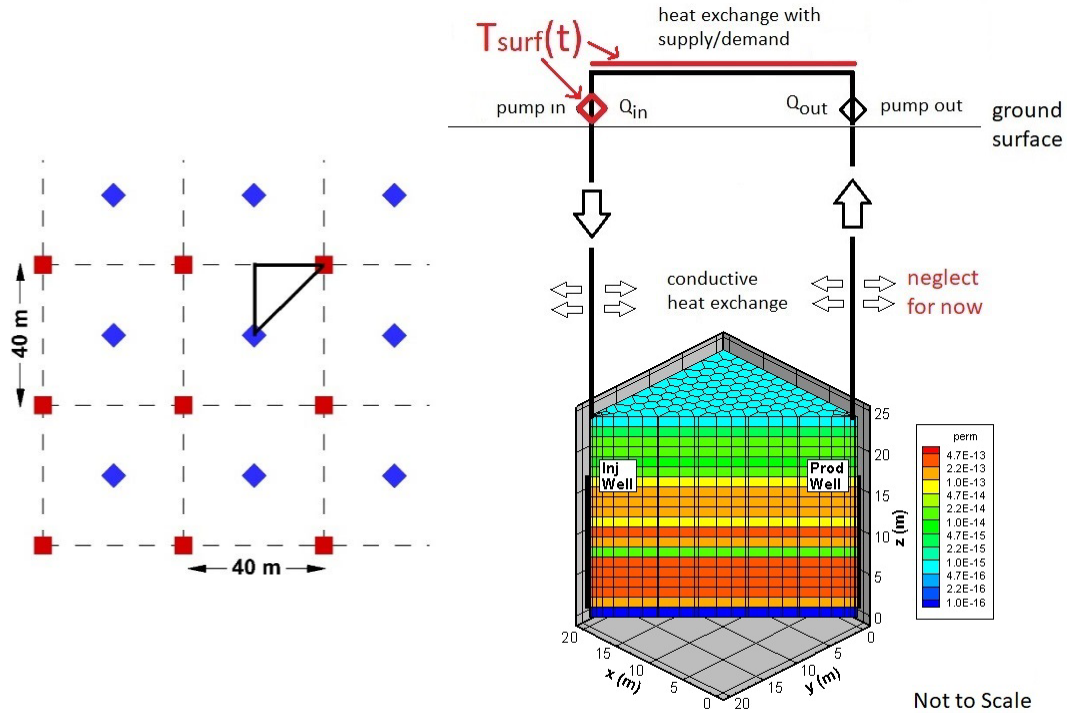
Figure 37. The left-hand plot shows a plan view of the smaller-scale five-spot pattern, with injection wells shown as blue diamonds and production wells shown as red squares. The black triangle shows the 1/8th symmetry element used for the model. The right-hand plot shows a perspective view of the model, with permeability in m². Perforated well intervals are shown as black bars.

Fluid flow into or out of the subsurface is modeled as a mass source or sink at the top of the perforated interval of the injection or production wells, respectively. The well elements have very high vertical permeability to enable flow distribution over the perforated interval. In the smaller-scale model, the perforated interval is the lower portion of the formation and the magnitude of the flow rate is comparable to that used for the Cranfield CO_2 storage project, not necessarily tuned to any actual energy/supply demand scenario. For the larger-scale model, pumping rates are increased to produce comparable fluid residence times for the two models. Fully-penetrating wells are used for the larger-scale model, rather than the partially-penetrating wells shown in Figure 37, but because the permeability in the upper portion of the formation is relatively low, this change will not have a great impact on the model results.

The temperature of the injected fluid $T_{surf}(t)$ varies seasonally with a sinusoidal variation. The maximum of $T_{surf}(t)$ is 180°C, representing output of solar collectors, excess heat from a conventional power plant, or another seasonal energy source; the minimum of $T_{surf}(t)$ is 126°C, the ambient reservoir temperature of the Lower Tuscaloosa Formation at Cranfield (Figure 37).

In addition to simulating thermal and hydrological processes within the Lower Tuscaloosa Formation, a heat exchanger at the surface is modeled in a simplified manner as illustrated schematically in Figure 37. The temperature adjacent to the heat exchanger is prescribed with the same seasonal sinusoidal variation as is used for fluid injection $T_{surf}(t)$. Note that we are neglecting the heat exchange (loss or gain) occurring in the wellbore between the RTES reservoir and the ground surface. In deep systems, there may be considerable heat loss along the wellbore during the early phase of the project. More details on model development are presented in Spycher et al. (2021a).

56

Two modes of operation are considered. In flow-through operation, one well is always the injection well and the other well is always the production well, and fluid always flows through the formation in the same direction from the injection well to the production well. In push-pull operation, one well acts as the injection/production well and the other well acts as the supply well. During summer, hot water is injected, and during winter that water is produced from the same well, thus flow direction in the reservoir and heat exchanger is reversed. The supply well always has the same magnitude flow rate as the injection/production well, to minimize pressure changes in the reservoir.

2.1.7.5 *Smaller-Scale Flow-through TH Model Result*

Ten years of annual cycles were simulated for the smaller-scale model with flow-through operation. Figure 38 shows conditions at the production well over the first three years. Figure 39 shows plan views of the temperature distribution at two levels in the reservoir for various times. Note the overall warming that occurs between one and ten years, due to the improved charging of the thermal "battery" and decreasing conductive heat losses to over- and underlying rock formations. The production temperature variation has a lower amplitude and is delayed compared to the injection temperature, reflecting heat exchange with the formation. The energy recovery factor is shown in Table 7. Produced and injected energy are calculated by integrating over the production-well and injection-well temperature versus time, respectively. The energy recovery factor gradually increases over the first three years, as the system heats up; we expect the system to be stable thereafter.

Brine was co-injected with water to act as a conservative tracer, in order to illustrate the fluid residence time (as shown by the brine mass fraction curve in Figure 38). Fluid residence time in the reservoir is short compared to annual temperature variation: as early as 15 days, the fastest fluid is being injected for its second trip through the formation, and the midpoint of the brine breakthrough curve occurs at 28 days. In one year, fluid makes an average of 6.5 trips through the reservoir. Fluid residence time in the surface pipe (not shown here) is very short, controlled by pipe length, and ranges from 0.2 hours to 2.0 hours.
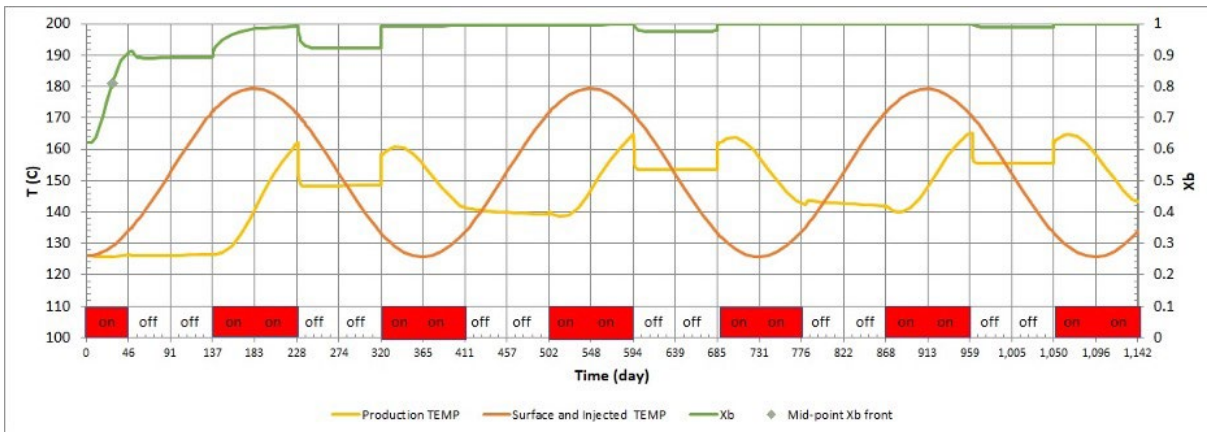
Figure 38. Temperature (T) and brine mass fraction (X_b), at the production well during the first three years simulated with the smaller-scale flow-through TH model. The surface temperature, which equals the injection temperature during summer charging periods, is also shown. The red bars indicate the time periods when fluid flow is on (i.e., when system is charging or discharging). The brine mass fraction acts as a conservative tracer and illustrates the lag in thermal front propagation compared to the tracer front. The green dot shows the midpoint of the brine breakthrough curve at 28 days.
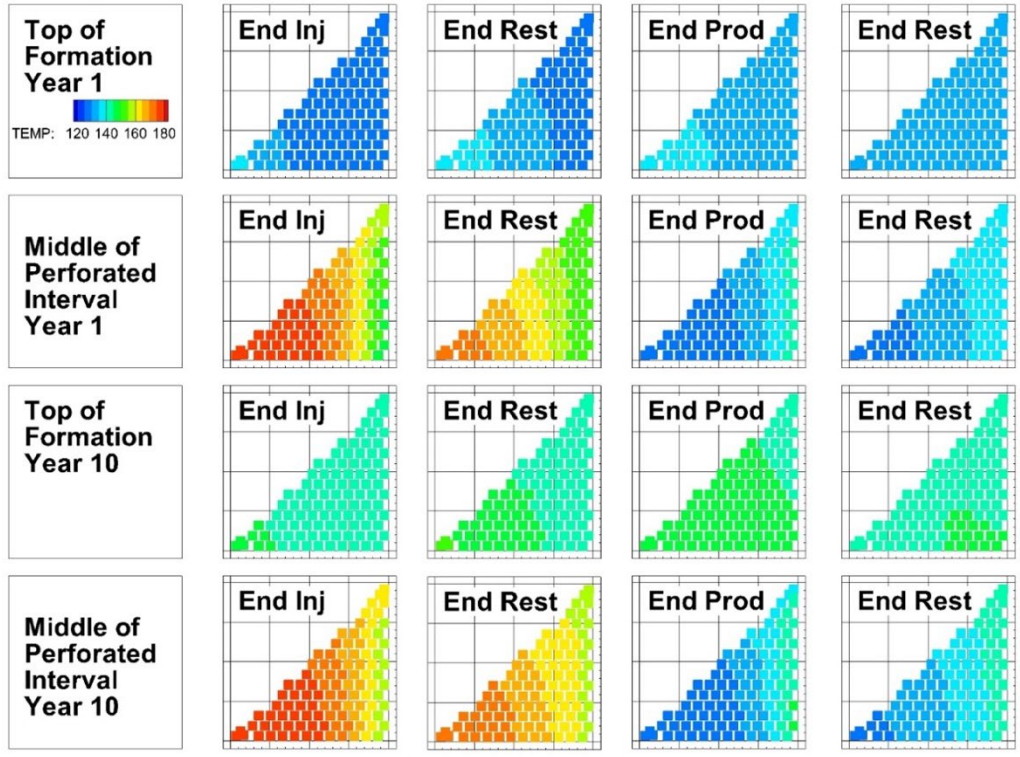
Figure 39. Temperature distributions from the smaller-scale flow-through TH model at various times and depths. Recall the maximum injection temperature is 180°C during the summer injection period and the minimum injection temperature is 126°C during the winter production period. In this plan view, the injection well is in the lower left corner and the production well is in the upper right corner.

2.1.7.6   Smaller-Scale Push-pull TH Model Result

Previously, in the flow-through model, flow is always from the injection well to the production well. Now we consider a push-pull operation in which flow reverses direction between summer and winter. We still have rest periods with no fluid flow in spring and fall, and we still consider a sinusoidal surface temperature with a maximum of 180°C and a minimum of 126°C. During the three months of summer, there is injection of high T (170°C – 180°C) water into the injection/production well (aka the hot well) and production from the supply well (aka the cold well), with flow from the production well to the surface heat exchanger. During the three months of winter, there is injection of low T (126°C – 136°C) water in the supply well and production from the injection/production well, with flow from the injection/production well to the surface heat exchanger. A slightly different computational grid is needed for the two seasons, because different wells are connected to the surface heat exchanger. Thus, we need to restart the numerical simulations twice a year with a modified grid. This is done for a total of three years. One half the pumping rate of the previous flow-through simulations is used, to avoid early thermal breakthrough between wells, as illustrated in Figure 38, where the production temperature begins to increase well before the end of the first summer charging period (137-228 days).

Figure 40 shows the temperatures of the hot well and the cold well, for the three-year simulation period. Heat exchanger (HTX) and surface temperatures are also shown. There is a gradual warming trend over the first three years, which is reflected in the increasing energy recovery factor (Table 7); we expect the system to be relatively stable thereafter. To make a fair comparison of flow-through and push-pull energy recovery factors, another flow-through case was simulated, using one-half the original fluid flow rate, to be consistent with the push-pull case. Table 7 indicates that the energy recovery factor for the flow-through cases shows a higher recovery factor for the higher original fluid flow rate, reflecting a better filling of the reservoir for the original flow rate. But the recovery factors for flow-through cases are both smaller than for the push-pull case.
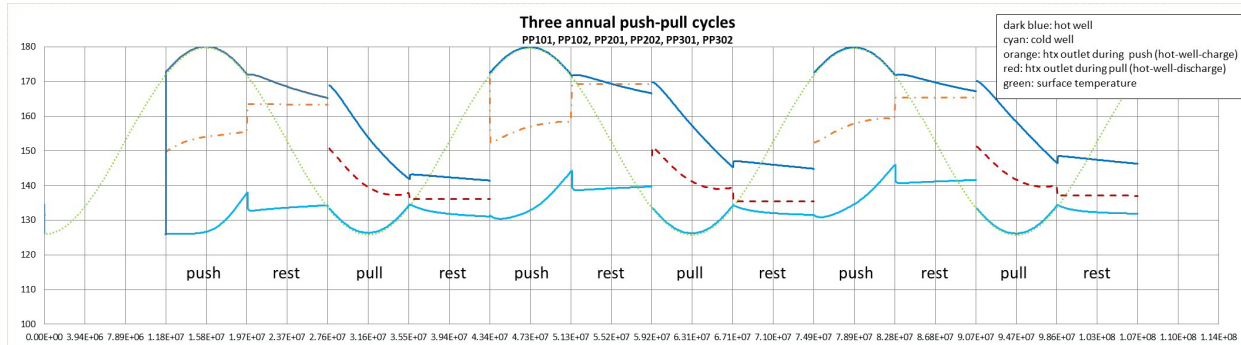
Figure 40. Inlet and outlet temperatures for the smaller-scale push-pull model. The well labeled hot is the injection/production well and the well labeled cold is the supply well.

Table 7. Energy recovery factor for the smaller-scale flow-through and push-pull models.

Year	1	2	3
Flow-through Energy Recovery Factor	0.51	0.55	0.57
Flow-through Energy Recovery Factor (half-flow rate)	0.40	0.49	0.52
Push-pull Energy Recovery Factor (half-flow rate)	0.56	0.63	0.67

2.1.7.7   *Larger-Scale Flow-through TH Model Result*

Figure 41 shows the temperatures of the injection and production wells for the larger-scale flow-through model for a five-year simulation period. Note that during the charging periods (both summer and winter), the injection well temperature is nearly equal to the surface temperature. The useful output of the system is measured by the production-well temperature during the winter. Note that the energy recovery factors for the larger-scale flow-through model (Table 8) are consistently higher than those for the smaller-scale flow-through model (Table 7). This is expected as a larger heated reservoir volume has a smaller surface-to-volume ratio, so it will have less conductive heat loss. Table 8 also shows the range of temperatures obtained during the winter discharge period. If there is a cut-off temperature below which energy is not usable, the integration to obtain the energy recovery factor will end at the cut-off temperature and the recovery factor will be smaller than those shown in the table.
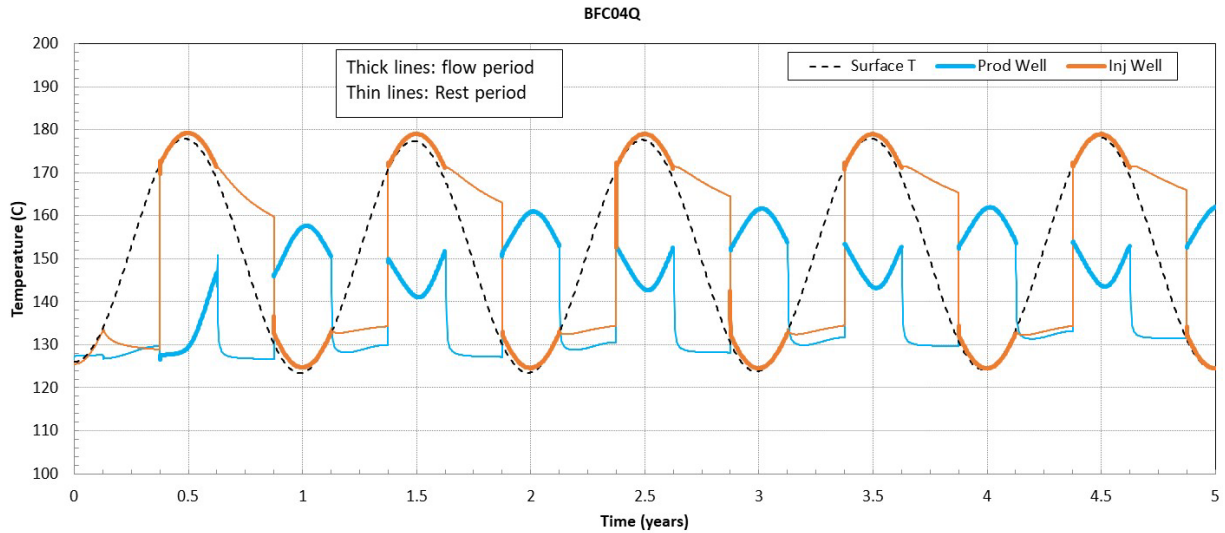
Figure 41. Inlet and outlet temperatures for the larger-scale flow-through model.

Table 8. Energy recovery factor and range of outlet temperatures for the larger-scale flow-through model.

Year	1	2	3	4
Energy Recovery Factor	0.55	0.63	0.64	0.65
Range of T_{out} (°C)	146-158	151-161	152-162	152-162

2.1.7.8   Larger-Scale Flow-through TH Model Sensitivity Studies

To investigate the effect of fluid flow rate on the larger-scale flow-through model, a range of flow rates were considered, as shown in Table 9. Flow rates are shown as a percentage increase and are relative to the 64x increase applied to account for the larger spatial dimensions of the larger-scale model compared to the smaller-scale model. The 20% increase is denoted the base case. Figure 42 shows the production-well pressure and temperature for larger-scale flow-through model sensitivity studies. The pressure response helps identify each period: flat – rest period, increasing pressure – summer injection period, decreasing pressure – winter production period. During each production period (centered on 1, 2, 3, 4, 5 years), increasing flow rate results in an earlier, higher peak in the outlet temperature, and a lower final outlet temperature. The recovery factors (Table 9) reflect both these trends, yielding a theoretical maximum recovery factor between 60% and 80% increase. We interpolate to a 67% increase and denote this as the optimal case. For this case, the fluid flow rate is 160 kg/s ~ 2500 gpm.

Table 9. Energy recovery factor for the larger-scale flow-through sensitivity studies considering different fluid flow rates. The percentage increase is relative to the 64x increase applied to account for the larger spatial dimensions of the larger-scale model compared to the smaller-scale model. The 20% increase is denoted the base case.

Case\Year	1	2	3	4
BFC04Q – 20% increase	0.554	0.627	0.643	0.654
BFC05Q – 40% increase	0.600	0.658	0.671	0.675
BFC06Q – 60% increase	0.620	0.667	0.678	0.682
BFC07Q – 80% increase	0.625	0.664	0.675	0.678
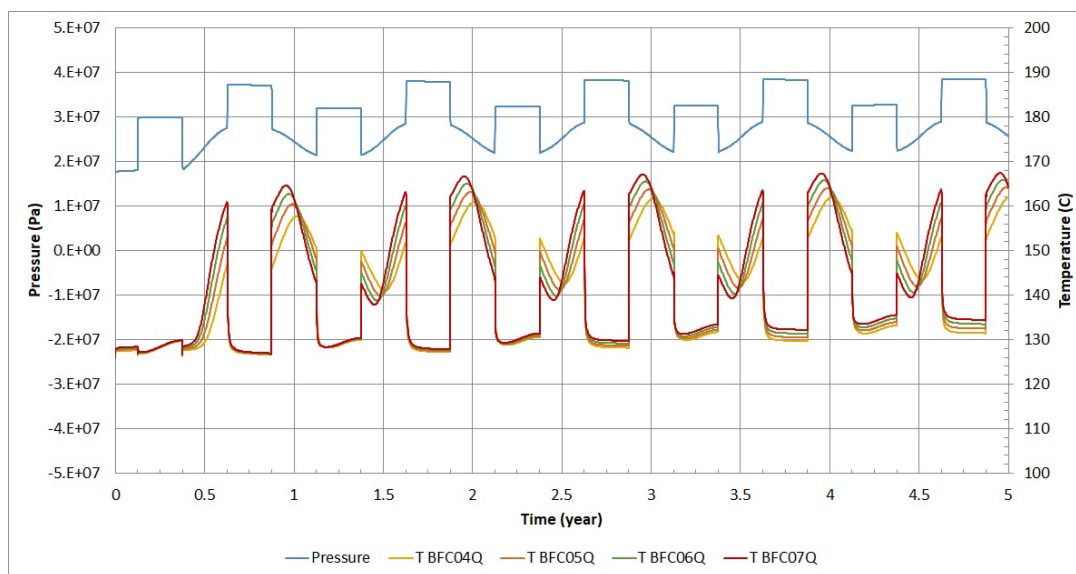
Figure 42. Production-well pressure (blue) and temperature for larger-scale flow-through model sensitivity studies. During each production period (centered on 1, 2, 3, 4, 5 years), increasing flow rate results in an earlier, higher peak in the outlet temperature, and a lower final outlet temperature.

To investigate the effect of heat loss through the cap and bedrock, a case just like the optimal case but with no such heat loss was modeled. This case produced results very similar to the optimal case. Such a result is expected for a thick reservoir, where vertical heat loss is small compared to horizontal heat loss, that is, the widening of the thermal front between the two wells.

To investigate the effect of gravity, a case just like the optimal case but with no gravity was modeled. This case also produced results very similar to the optimal case. Buoyancy forces are strong for the large temperature difference between injection and ambient temperature (180 – 126°C), but buoyancy flow is very small because low-permeability layers hamper vertical flow. The temperature distribution in the formation is controlled by preferential flow through higher-permeability layers, as shown in Figure 43a. To further investigate buoyancy flow, we increase all permeabilities by a factor of 10 and run simulations with and without gravity. The high-permeability model (Figure 43b) shows a very different distribution of temperature than the original permeability model (Figure 43a), but this is but not necessarily all due to buoyancy flow, as gravity (Figure 43b) and no-gravity (Figure 43c) cases are not very different. Rather, the 10 times higher permeabilities create stronger preferential flow, limiting the warmed portion of the formation to a central channel.

61
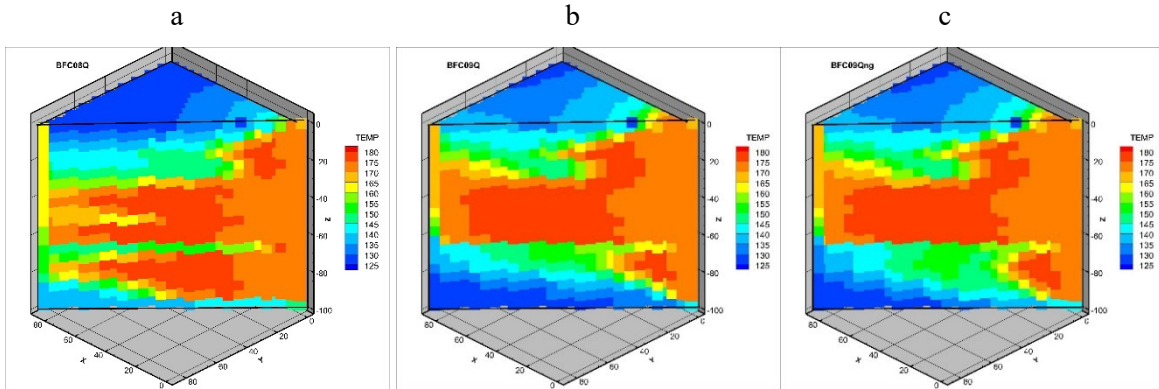
Figure 43. Temperature distributions at the end of the injection period for (a) original permeabilities, (b) 10 times higher permeabilities, and (c) 10 times higher permeabilities with no gravity. Note that in this figure, the injection well is on the right and the production well is on the left.

2.1.7.9   *Larger-Scale Push-pull TH Model Result*

Figure 44 shows the temperatures of the injection/production well for the larger-scale push-pull model for a five-year simulation period for the optimal-case flow rate. Also shown for comparison are the temperatures of the production well for the corresponding flow-through case. Note that the outlet temperature versus time curves have very different shapes: the push-pull curve starts with a plateau then declines, whereas the flow-through curve increases to a maximum then decreases. This difference is strongly reflected in the recovery factor (Table 10), where the push-pull recovery factor is 0.10 higher than the flow-through recovery factor.
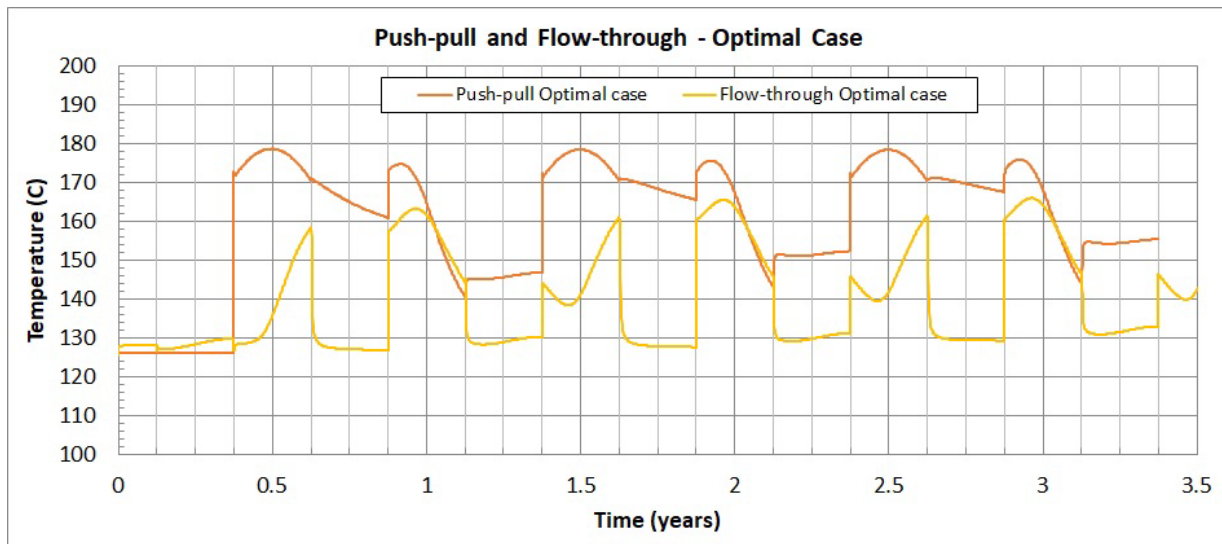
Figure 44. Temperature of the injection/production well for the push-pull case and for the production well for the flow-through case, for the optimal-case flow rate. Note that the push-pull temperatures are consistently higher than the flow-through temperatures during the winter discharge periods (centered on 1,2,3 years).

Table 10. Energy recovery factors comparing the larger-scale flow-through and push-pull models, for the optimal-case flow rate.

Year	1	2	3
Flow-through Recovery Factor	0.62	0.67	0.68
Push-pull Recovery Factor	0.72	0.76	0.78

The difference between push-pull and flow-through operations is even more striking for the lower flow rate of the base case. Figure 45 shows temperature versus time and Table 11 shows energy recovery factor for push-pull and flow-through operations for the base-case flow rate. The push-pull recovery factor is 0.20 higher than the flow-through recovery factor.

Interestingly, the energy recovery factors for the push-pull operation are higher for the base case than for the optimal case, whereas the opposite is true for flow-through operation. Thus, we find that picking the best flow rate to use depends on the operation mode being employed. Nominally, we expect recovery factor to increase with heated volume: a bigger hot plume has a smaller surface-to-volume ratio, so less conductive heat loss. But here, the higher flow rate for "optimal" case is too big for the well spacing: the thermal front reaches the supply well during the push period, we lose heat out the supply well, and we cannot recover it during the pull period.

In summary, the push-pull operation produces consistently higher recovery factors than does the flow-through operation. Additionally, the best flow rate to use must be determined independently for each mode of operation.
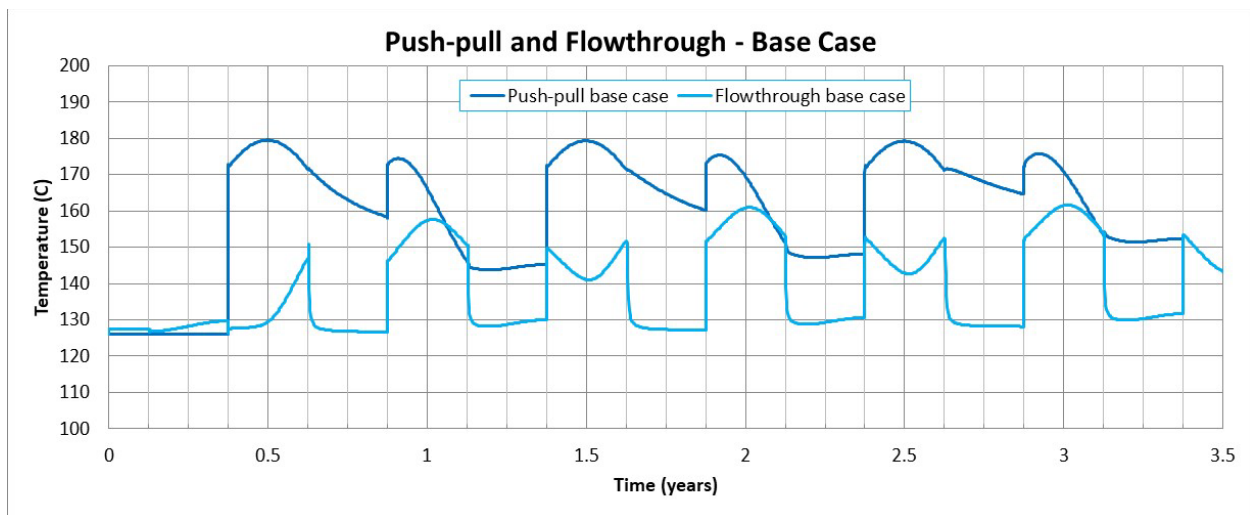
Figure 45. Temperature of the injection/production well for the push-pull case and for the production well for the flow-through case, for the base-case flow rate. Note that the push-pull temperatures are consistently higher than the flow-through temperatures during the winter discharge periods (centered on 1, 2, 3, years).

Table 11. Energy recovery factors comparing the larger-scale flow-through and push-pull models, for the base-case flow rate.

Year	1	2	3
Flow-through Recovery Factor	0.55	0.63	0.64
Push-pull Recovery Factor	0.75	0.81	0.84

2.1.7.10 Physics-Based Geochemical/Thermal-Hydrological-Chemical (THC) Case Studies

Simulation Tools and Thermodynamic Data Sources

TOUGHREACT-EOS7 V4 (Sonnenthal et al., 2021; Xu et al., 2006) with brine option (Spycher et al., 2021b) was used in this study to conduct geochemical and reactive transport simulations. These simulations were performed using a thermodynamic database developed by Jove-Colon et al. (2007) (see also Alai et al., 2005; EQ3/6 data0.ypf.R2 Pitzer database), unless indicated otherwise.

Geochemical Modeling

The potential for mineral scaling to affect the RTES systems described previously was investigated by geochemical and thermal-hydrological-chemical (THC – reactive transport) simulations. Geochemical modeling was performed with brines from the Weber/Tensleep (Green River Basin) and Lower Tuscaloosa (Gulf Coast Basin) sandstones to investigate their scaling potential upon heating to temperatures near 200°C. Similar modeling was also performed with brines for the Mt. Simon and St. Peter sandstones (Illinois Basin) for comparison, with results reported by Spycher et al. (2021a) and summarized in Figure 46. Results show that the precipitation of retrograde solubility minerals, primarily anhydrite and calcite, depends on the brine chemistry, notably its sulfate content, rather than its salinity. Therefore, scaling potential is not necessarily correlated with the total dissolved solids concentration (TDS) of these brines. These simulations show that large amounts of primarily anhydrite are found to precipitate when heating brine from the Weber Sandstone. In contrast, the simulated heating of even higher TDS brine from the Lower Tuscaloosa Formation shows about ten times less precipitation. Accordingly, THC simulations of RTES in these formations show significant plugging around the injection well in the case of the Weber/Tensleep Formation, and much less scaling in the Lower Tuscaloosa Formation, as discussed in the next section.
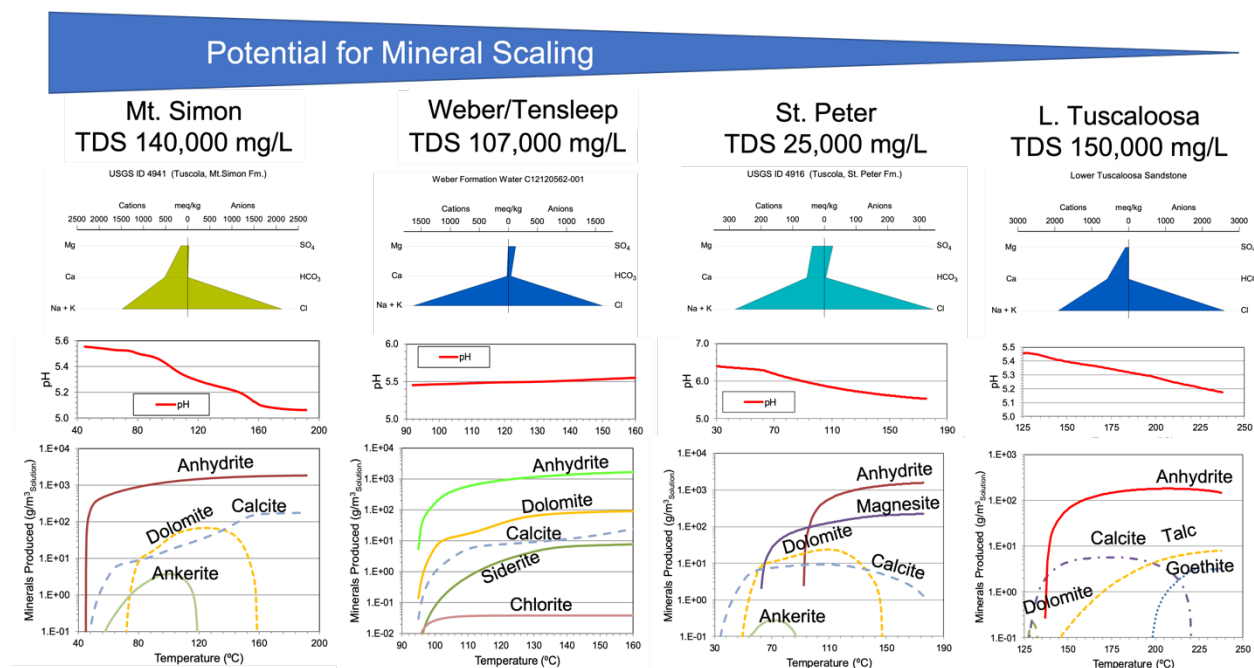
Figure 46. Computed pH evolution and amounts of mineral precipitation (in grams per initial cubic meter of brine; bottom two graphs) upon heating deep brines from their formation temperature. The brine compositions are shown as Stiff diagrams (top graphs). Comparatively, for each case, the total amount of precipitation decreases from left to right. Note that the y-axis scale on the right-most plot of produced minerals (Lower Tuscaloosa brine) is 10x smaller than on the other graphs.

2.1.7.11 Reactive Transport Modeling

Initial reactive transport simulations were conducted using the Weber/Tensleep Formation brine by modeling the deep injection of this brine after heating it to 160°C and removing solid phases precipitated upon heating, as discussed in McLing et al. (2019). Despite the removal of precipitated salts in the heated brine prior to injection (mostly $CaSO_4$, Figure 46), these simulations showed that the rising temperature in the formation, together with brine-rock interactions, were sufficient to reduce injectivity to nearly zero after two months of injection, mostly caused by the precipitation of carbonate minerals and anhydrite (McLing et al., 2019). Therefore, THC modeling efforts were redirected to the Lower Tuscaloosa Formation, as this brine showed significantly less potential for mineral scaling than the other brines studied (Figure 46). The Lower Tuscaloosa Formation has been extensively studied as part of a pilot CO_2 geologic storage project at the Cranfield oil field in Natchez, Mississippi (e.g., Lu et al., 2012; Hovorka et al., 2013), providing a wealth of data for model development, as described below.

2.1.7.12 THC Model Geochemical Development

Reactive transport models were developed making use of the same numerical grids and input parameters as the thermal-hydrological models previously discussed, plus inputs needed to describe the geochemical system (brine and rock compositions) and chemical reactions (kinetic and thermodynamic data). The brine composition was obtained from Soong et al. (2016) for the Lower Tuscaloosa sandstone, and the mineralogy of that formation was taken as the average mineral amounts reported by Lu et al. (2012) (Figure 47). In a first step, to obtain chemically near-steady initial conditions, the composition of the brine was reconstructed for in-situ conditions (e.g., Palandri and Reed, 2001) by computing the aqueous silica and total dissolved carbonate concentration at depth from equilibrium with quartz and calcite, respectively, and pH from charge balance. The brine-mineral system was then numerically reacted for a period of 1000 years at the formation temperature (126°C) and pressure (300 bar). The mineral reactive surface areas were initially estimated from spherical grain sizes of 100 microns then adjusted as necessary to obtain a reasonable agreement between the reported brine chemistry and mineralogical data at the end of the 1000-year simulation (Figure 47). Kinetic rate constants were taken mostly from Palandri and Kharaka (2004).

The brine composition resulting from these initial manipulations was used as the initial formation water composition. The initial composition of the injected water was taken as the composition of the formation brine heated to 180°C after removal of the solids formed at that temperature (mostly anhydrite, see Figure 46). Subsequently, the injected water composition was assigned the composition of the produced water, such as to model recirculation of the fluid. Solids subsequently precipitated in the heat exchanger at the surface were not removed and allowed to re-dissolve upon temperature fluctuations.

Analyte	Brine Composition* (ppm)	1000-year Reacted (ppm)	Reported Range** (mg/L)
pH	~6 @ 25°C	5.46 @ 126°C	5.6 - 6.4 @ 25°C
TDS (calc)	150714	151060	
density (kg/L)	1.115 (calc)		
Cl-	92223	92175	86212-95300
SO4-2	238	238	25-55
HCO3-	NA	103	278-580
HS-	NA	1	NA
Br-	432	432	297-437
SiO2(aq)	NA	59	NA
Al+3	1.06	1.7E-07	0.25-9
Ca+2	11798	12936	7636-11700
Mg+2	1035	468	770-1052
Fe+2	124	31	95-532
K+	412	490	272-604
Na+	43743	43421	39581-49192
Sr++	696	696	512-723
B+3	1.9	2	NA
Ba+2	9.6	9.5	43-99

* Soong et al. (2016)
**Lu et al. (2012)

Minerals	Reacted Sat. Index	Composition (wt.%)
quartz	0.00	79.40
Fe-chlorite	0.00	11.80
kaolinite	-0.04	3.10
illite	0.02	1.30
calcite	0.00	1.10
K-feldspar	-0.41	0.50
albite	0.00	0.50
dolomite	0.00	0.40
ankerite	0.00	0.10
FeS (as pyrrhotite)	0.00	0.10
anhydrite	-0.08	
chalcedony	-0.21	
barite	-0.25	
goethite	-0.53	
strontianite	-0.57	
siderite	-1.15	
talc	-0.05	
magnesite	-0.97	

Figure 47. Brine chemistry, formation mineralogy, and potential secondary minerals selected for the reactive transport simulation (highlighted minerals are close to saturation).

2.1.7.13 THC Simulations

Results of THC simulations of a small-scale (~30-m well spacing), flow-through, system modeled as a five-spot configuration into the Lower Tuscaloosa Sandstone at the Cranfield oil field site were presented by Spycher et al. (2021a) as part of this study. These results showed that at elevated injection temperatures (180°C), the formation permeability around injection wells at this site could increase due primarily to quartz dissolution, but that significant amounts of sulfate and carbonate mineral scale could form in surface heat exchangers. Modeling the co-injection of CO_2 at the heat exchanger inlet was predicted to entirely mitigate carbonate precipitation but not sulfate precipitation. These THC modeling results can be found in Spycher et al. (2021a) and are not repeated here. Instead, in the present report, we discuss similar results from more recent, larger-scale (~120-m well spacing) THC simulations conducted during the later stages of this study. In these larger-scale simulations, the residence time of the brine circulating within the formation was set to be about the same as in the earlier, smaller-scale simulations. As a result, the larger-scale model results are quite similar to the smaller-scale model results presented by Spycher et al. (2021a). For this reason, here, results are presented only for the larger-scale models, focusing on the differences in geochemical behavior between flow-through and push-pull cases, rather than smaller- and larger-scale cases.

THC simulations were set up using the same TH model grids and parameters as previously described together with the brine and mineralogy data shown in Figure 467. The general setup of the flow-through and push-pull model is summarized in Figure 48. The models are run for a period of 3 years, with temperature distributions as shown on Figure 49.
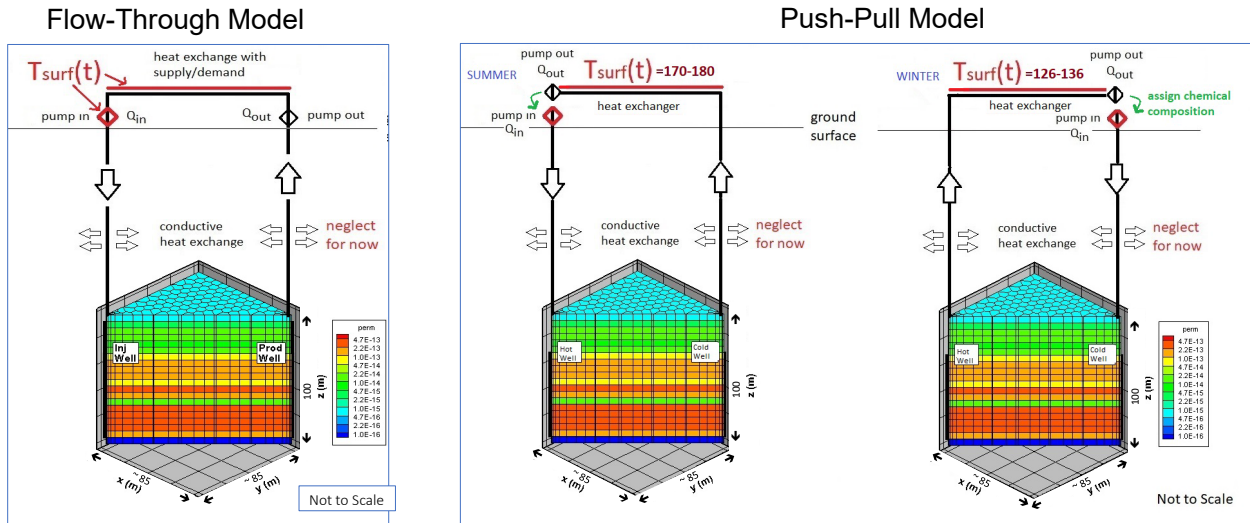
Figure 48. Comparison of the general configuration of the modeled flow-through (left) and push-pull (right) models.
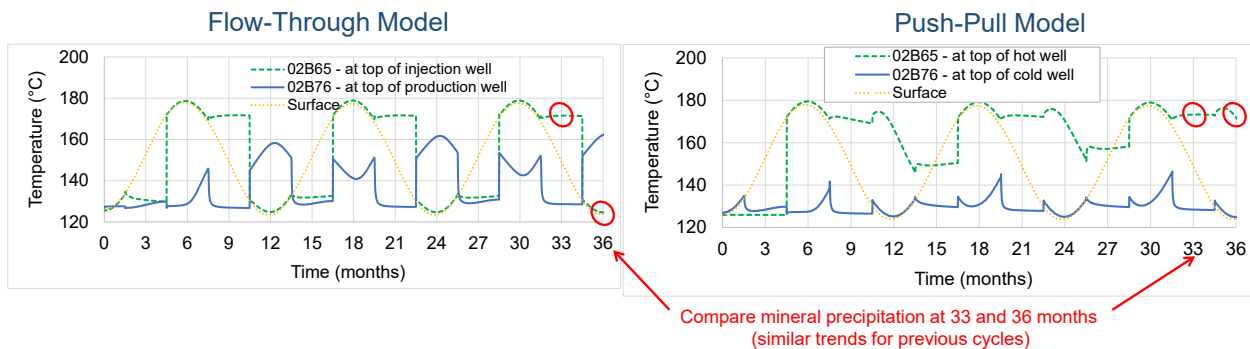
Figure 49. Comparison of the imposed (surface and injection/hot wells) and predicted (production/cold wells) temperature trends in the flow-through (left) and push-pull (right) models.

The results of THC simulations after 3 years of continuous operation are shown in Figure 50 through Figure 53 for both the flow-through and push-pull cases. The most noticeable difference between the two cases is that retrograde solubility minerals (primarily anhydrite and calcite), which tend to precipitate around the injection well as the temperature rises, re-dissolve around the injection well in the flow-through case during cycles when the temperature drops at this well. In the push-pull case, however, the temperature remains elevated at the hot well and these minerals do not re-dissolve. As a result, a significant total porosity decrease is computed at the hot well in the flow-through case, whereas a slight porosity increase occurs around the injection well (Figure 50 and Figure 51).
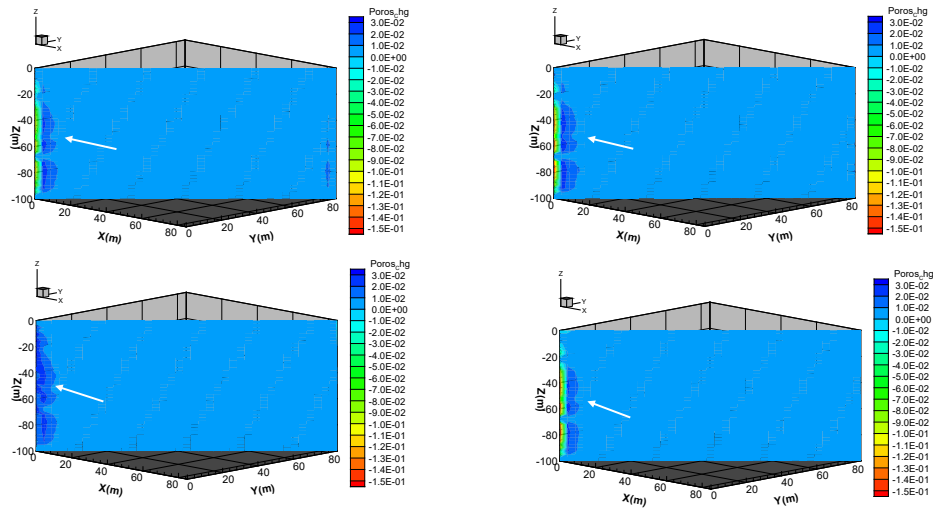
Figure 50. Computed total porosity change (positive for increase) resulting from mineral precipitation and dissolution after 33 and 36 months of operation of the flow-through (left) and push-pull (right) systems.
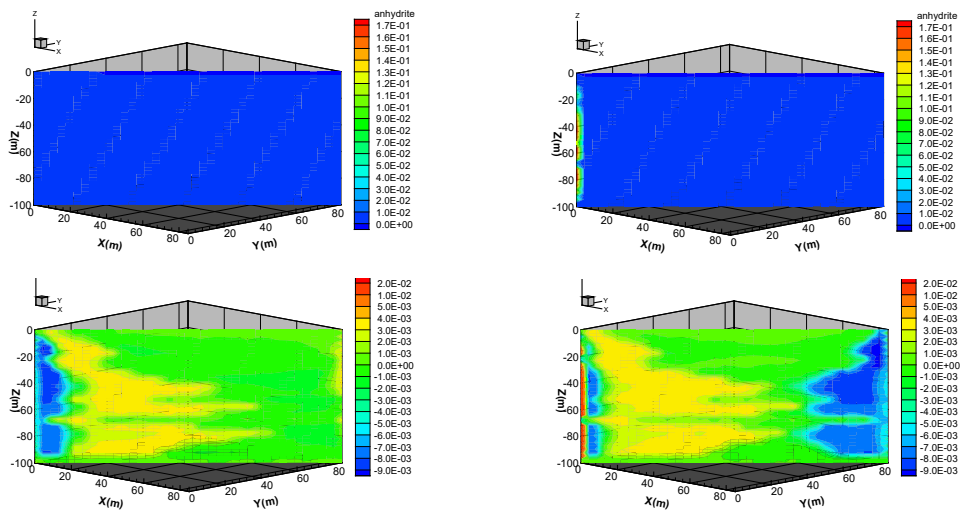
Figure 51. Computed volume fraction change (positive corresponds to a porosity decrease) of anhydrite and calcite after 36 months operation of the flow-through (left) and push-pull (right) systems.

In both cases, regions of porosity increase are caused by the dissolution of quartz around the modeled injection and hot wells (Figure 52, top). However, in the push-pull case, the quartz dissolution at the hot well is not sufficient to offset the porosity decrease from anhydrite and calcite precipitation. Another difference between these two cases is the noticeable dissolution of calcite at the cold well in the push-pull case (Figure 51), where it is partly replaced by dolomite (not shown). Fe-Ca carbonates, modeled as ankerite, are also predicted to cyclically precipitate and re-dissolve near the injection well in the flow-through case, and in contrast build up near the cold well in the push-pull case (not shown). In both cases, talc (a proxy for Mg-clays) is predicted to precipitate at some distance from the modeled injection/hot wells (Figure 52, bottom), driven in part from the dissolution of Mg-bearing chlorite near these wells. At an increasing distance from the injection well, some replacement of dolomite by calcite is predicted to

68

occur in both cases (not shown; see similar trends in Spycher et al., 2021a). It is also noted that no significant porosity change is predicted at the production/cold wells.
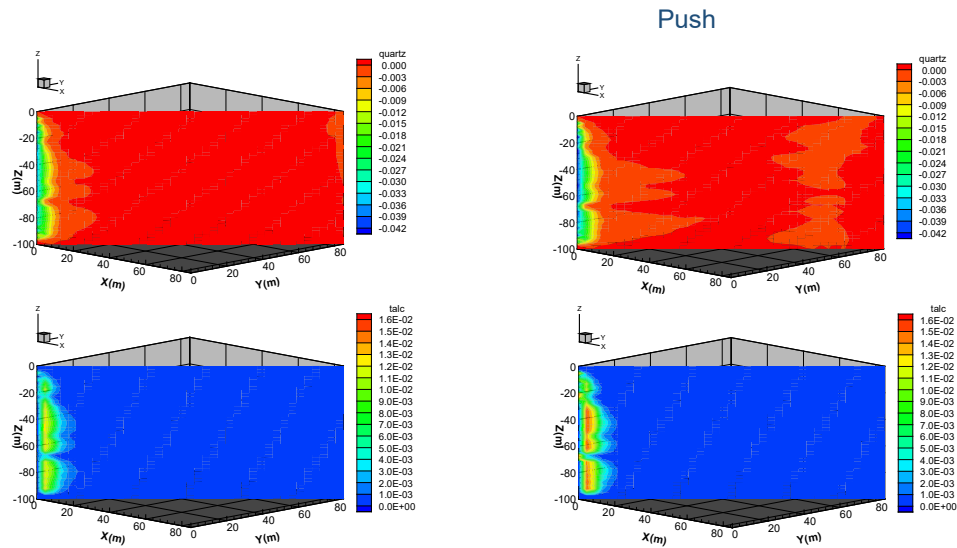
Figure 52. Computed volume fraction change of quartz and talc (positive corresponds to a porosity decrease) after 36 months operation of the flow-through (left) and push-pull (right) systems.

The evolution of mineral precipitation in the simulated heat exchangers follows the complex temperature trend in each exchanger (Figure 53) that results from the combination of the injection/production and rest cycles, and ambient temperature variations imposed above the ground surface (Figure 49). As temperature rises, carbonate and sulfate minerals precipitate but then re-dissolve when the temperature decreases. Ca, Mg, and Fe carbonates compete with one another depending on their relative solubility at any given temperature, resulting in cyclic periods of predominant calcite, ankerite, and to a much lesser extent dolomite deposition. The main differences observed between the modeled cases is the absence of anhydrite precipitation in the push-pull case, but significant cyclic precipitation of anhydrite in the flow-through case (Figure 53). However, it is noted that in the push-pull case, anhydrite precipitates and builds up at the hot end of the heat exchanger and around the hot well (Figure 51-top).

In summary, the flow-through case seems to induce more mineral precipitation in the heat exchanger but less around the injection well than in the push-pull case. However, it should be noted that predicted trends of mineral precipitation are (expectedly) sensitive to the modeled temperature histories and should be viewed as more qualitative than quantitative. This is especially true for the heat exchanger, which is very crudely modeled here as a concept rather than an actual heat exchanger design. Differences in predicted geochemical behavior between push-pull and flow-through systems may vary depending on site-specific conditions. Also, as shown in the next section and Section 2.1.6, the results of geochemical and THC simulations are subject to significant thermodynamic data uncertainty at elevated temperature, pressure, and salinity.
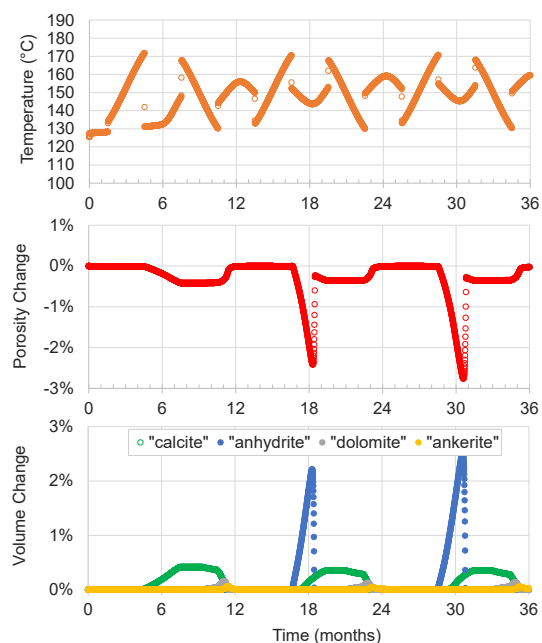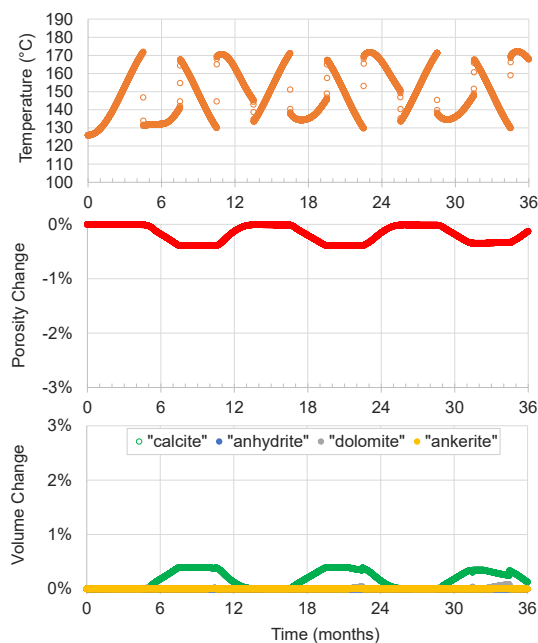
Figure 53. Model results computed at the middle of the modeled heat exchanger (60 m from inlets/outlets). Computed volume fraction change (positive corresponds to a porosity decrease) of quartz and talc (a proxy for Mg-clays) after 36 months of operation of the flow-through (left) and push-pull (right) systems.

2.2   Task 2 Results

2.2.1   Task 2.1 Stochastic Simulation-enabled Machine Learning (ML) Models for Optimization

In order to quickly evaluate the suitability of any given formation for the application of RTES, we proposed a workflow to co-optimize RTES performance metrics by combining physics-based stochastic simulation, data-driven modeling, and multi-objective optimization. For the stochastic hydrothermal simulations, we used the MOOSE framework as it can solve multi-physics coupled problems implicitly using high-performance parallel computing clusters and it includes a stochastic tool module that automatically launches hundreds of simulations with ranges of parameters sampled from any given distribution (Permann et al., 2020). Different from the physics-based site-specific simulations outlined above, the stochastic simulations only considered fluid flow and heat transfer in a homogeneous fully saturated generic reservoir with low-permeability caprock and bedrock as barriers. A doublet well-configuration and two operation scenarios were simulated with stochastic formation parameters (i.e., reservoir depth, permeability, porosity, thermal conductivity, and thickness) and operational conditions (i.e., doublet distance, injection temperature, and rate). For each of the realized simulations, the performance of the RTES was recorded, including charging duration, operation duration, thermal energy recovery rate, and storage capacity. With the stochastic simulations, an immense amount of data connecting stochastic input parameters with output RTES performance metrics were generated and used to train two artificial neural network (ANN) models using the TensorFlow[4] python package, which corresponds to the two operational scenarios (flow-through and push-pull). These ANN models were

---

4   https://www.tensorflow.org/

70

further employed with a genetic optimization algorithm, implemented and open-sourced as Geatpy[5] to obtain the Pareto fronts of the competing RTES performance metrics for four potential formations, including Mt. Simon Sandstone, Weber Sandstone, Saint Peter Sandstone, and the Lower Tuscaloosa Sandstone. The detailed modeling approach is described in our recent American Rock Mechanics Association (ARMA) paper (Jin et al., 2021) and full journal paper under review (Jin et al., 2022a).

To quickly generate stochastic simulation data, we assumed that the RTES operates with a single-phase fluid injection/extraction out of the fully saturated, isotropic homogeneous reservoir. We also assumed the pores were incompressible. Figure 54 shows the geometry and boundary conditions of a generic reservoir used for the stochastic simulation. Only a half of the full 3D domain was simulated due to its symmetrical condition.
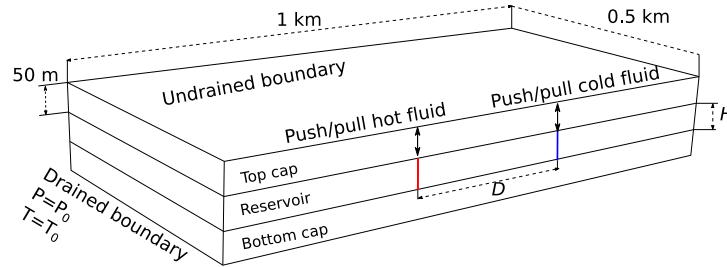
Figure 54. The geometry and boundary conditions used for the stochastic TH simulations.

Two operational scenarios were considered: continuous operation and seasonal cycling. Here, we only briefly introduce the seasonal cycle as shown in Figure 55. For detailed description of the model configuration as well as those for the continuous operation, please refer to our publications (Jin et al., 2021, Jin et al., 2022). The predicted temperature evolution at the middle of the hot well shows that the system has been gradually warmed up because a portion of injected thermal energy is retained in the formation after extraction for each cycle. The vertical temperature distribution demonstrates the effect of buoyancy flow.
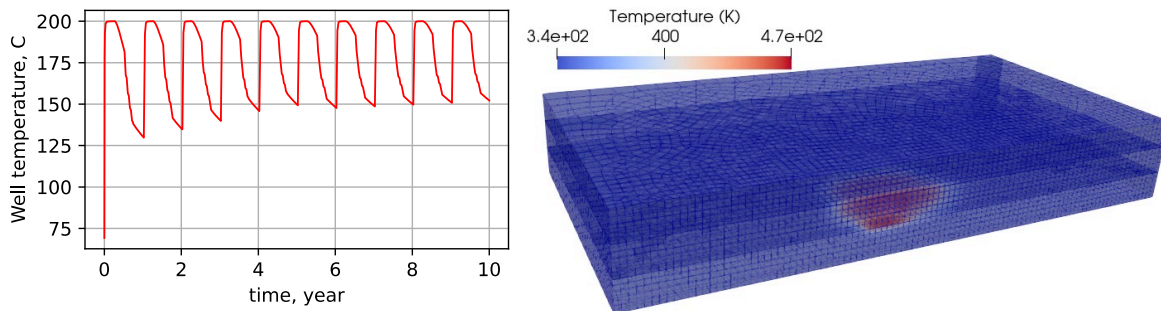
Figure 55. Demonstration of the seasonal injection-storage-extraction-rest cycle operation. Left: the predicted evolution of temperature at the middle of the hot well for 10 years of operation. Right: the simulated temperature distribution (K) at the end of injection in the first year. These results were obtained for the model with a formation thickness of 50m, a depth of 2000m, a permeability of $10^{12}\ m^2$, a porosity of 0.01, a thermal conductivity of $2\ W/m \cdot K$, a well distance of 200 m, an injection rate of 1.5 kg/s, and an injection temperature of 200°C.

Figure 56 shows histograms of successfully simulated cases for the seasonal cycle operation scenario. For all the formation characteristics (green) and operational conditions (magenta), we provided a uniform distribution for all input parameters from which to sample using the Monte Carlo method. The resulting non-uniform distribution in flow rates and permeabilities in Figure 56 shows the simulations with some combination of input parameters are not physically reasonable. For example, a high injection rate with a low permeability formation may result in hydraulically fracturing the formation. Figure 56 also shows the histograms of the simulated performance metrics (blue). The recovery efficiency is defined as the ratio of recovered thermal energy from extraction over total injected thermal energy. The operating time is the average days that the system can function to generate electricity for each yearly cycle. And the annual storage is the amount of thermal energy that the formation can store with the given formation characteristics and operation conditions. The non-uniform distributions of the performance metric indicate the nonlinear relationships between input parameters and the output results.
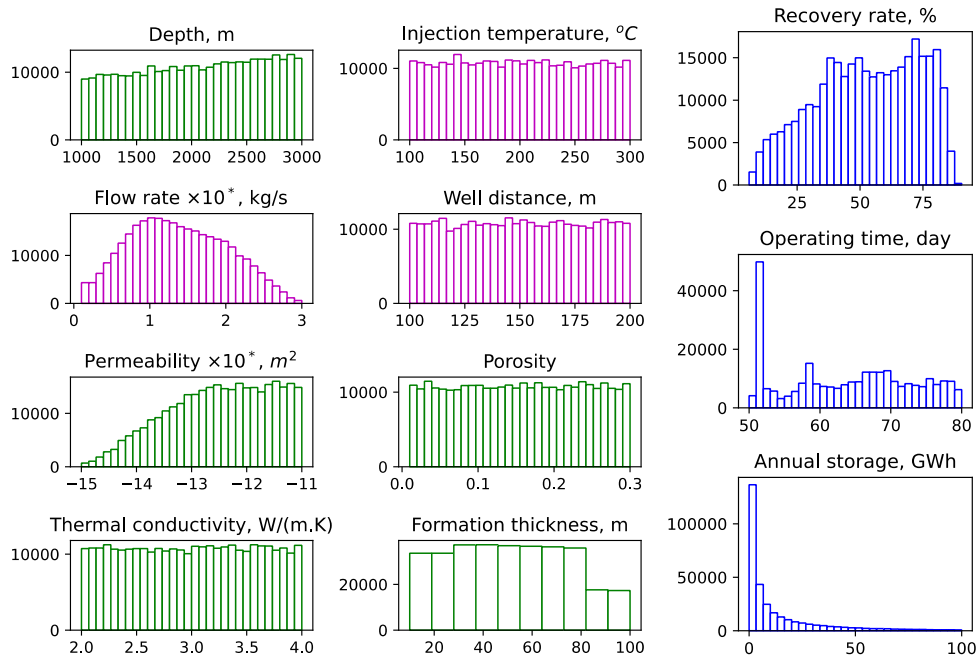
Figure 56. Histograms of the input and output parameters for all the realized simulations of the seasonal cycle operation. The y-axis stands for the realized simulation numbers after screening. Formation characteristics are in green; operation conditions are in magenta; performance metrics are in blue.

Physics-based computational modeling is a great approach to evaluate the suitability of any potential site for the RTES system. However, it requires an experienced modeler with an in-depth understanding of physics and numerical methods. In addition, parameter sweeping requires a large amount of computational resources, which may not be accessible for all stakeholders. With the extremely large data volumes generated in this effort, we established a regression machine learning model to connect the input parameter and the output performance shown in Figure 56. This machine learning model, serving as a surrogate model of the physics model, can enable stakeholders to run artificial simulations in a blink of eye using minimal computational resources. Despite the many advantages of the machine learning model, its accuracy is bounded by the training data. In this project, we employed the artificial neural network (ANN) implemented in TensorFlow to carry out the learning and training processes. With all data shown in Figure 56, 80% and 10% of randomly chosen data were used to train and validate the model during the learning process. The remaining 10% of the data were used to test the robustness of the trained model. The comparison of all RTES performance metrics between the ANN prediction and the physics modeling prediction showed a good match, indicating the ANN model captures all the nonlinear connections.

72
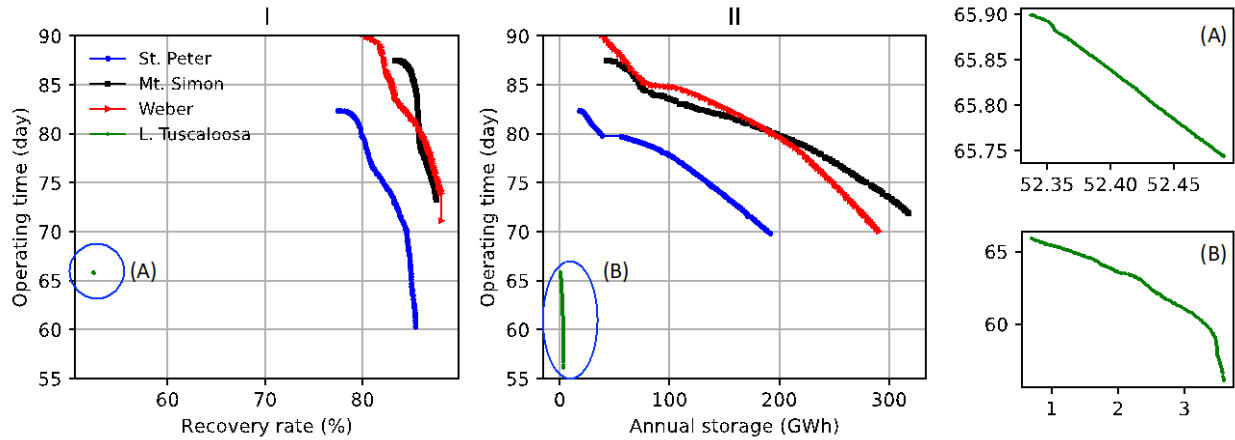
Figure 57. Comparison of the multi-objective Pareto fronts for the identified four sites using the validated neural network model and a genetic optimization algorithm. The genetic algorithm produces points along the Pareto front, and we connect those points to present the Pareto front.

The well-trained ANN model can be used by stakeholders who have basic python program skills to quickly evaluate the suitability of any given formation for the potential implementation of RTES. In this project, we examined four potential sandstone formations, (i.e., Mt. Simon, Weber/Tensleep, St. Peter, and Lower Tuscaloosa) using the ANN model and an optimization python package Geatpy based on the genetic algorithm. Note that this analysis is only based on TH modeling, and thus doesn't account for any impacts associated with water-rock interaction and brine chemistry. Figure 57 shows the obtained Pareto fronts of the performance metrics for the four formations. The Pareto front is defined as the optimal solution boundary for a multi-objective optimization problem when objectives have competing effects. For example, the left subfigure of Figure 57 shows that the maximum operating time decreases with the maximum recovery rate for all formations, all other possible solutions should be located on the lower-left side of the Pareto front lines. The obtained Pareto fronts obtained in Figure 57demonstrate that the RTES developed in the Weber sandstone and the Mt. Simon sandstone have a better performance than systems developed in the other two formations. A detailed explanation of the ANN model application is provided in our paper (Jin et al., 2022a).

2.2.2   Task 2.2 Physics-Based Hydro-Thermo-Mechanical Case Studies

The TH and THC modeling in the two previous sections was performed using the TOUGH3 and TOUGHREACT family of codes, which solve the governing equation using the finite difference method. We solve the hydro-thermo-mechanical (THM) coupled process using the MOOSE framework, which is a multi-physics solver using the finite element method (FEM). Because of the numerical method differences, the FEM model needs a different mesh as shown in Figure 58. We modeled a quarter of the domain as compared to 1/8 of the domain in TOUGH because FEM solves the problem better with a hexahedron-meshed domain. We also explicitly simulated the caprock and the bedrock. Given these differences, we iteratively compared the simulation of the thermal-hydrological problem between the TOUGH3 and MOOSE framework, to make sure we have the same model set-up. Note the THM modeling only focused on the Lower Tuscaloosa Formation.

73
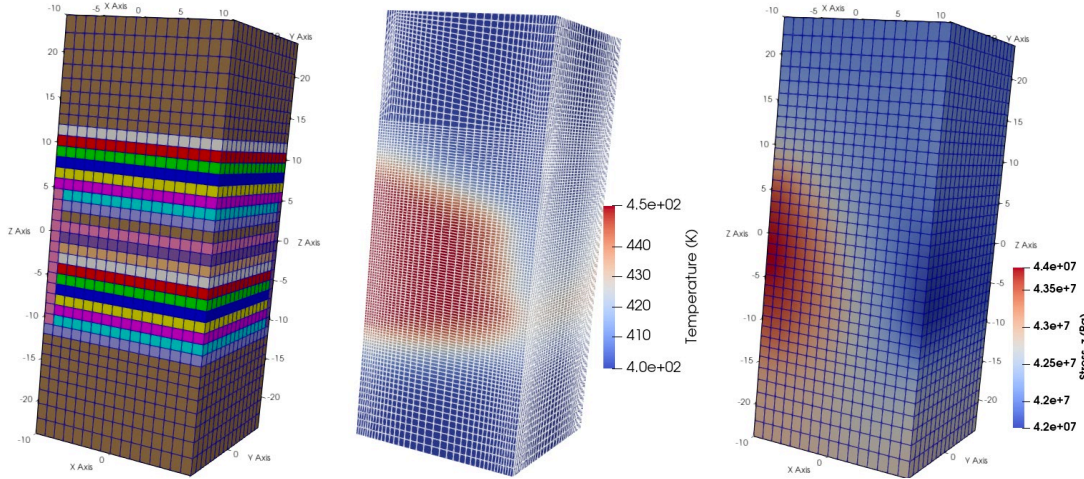
Figure 58. Left: MOOSE FEM mesh for 20 layers of formation, caprock and bedrock. The single element columns at the corner across layers 6-19 have been assigned with high permeability to mimic the injection and extraction wells. Center: Simulated temperature distribution during the injection for a fine-meshed case. Right: Predicted vertical stress distribution during injection.
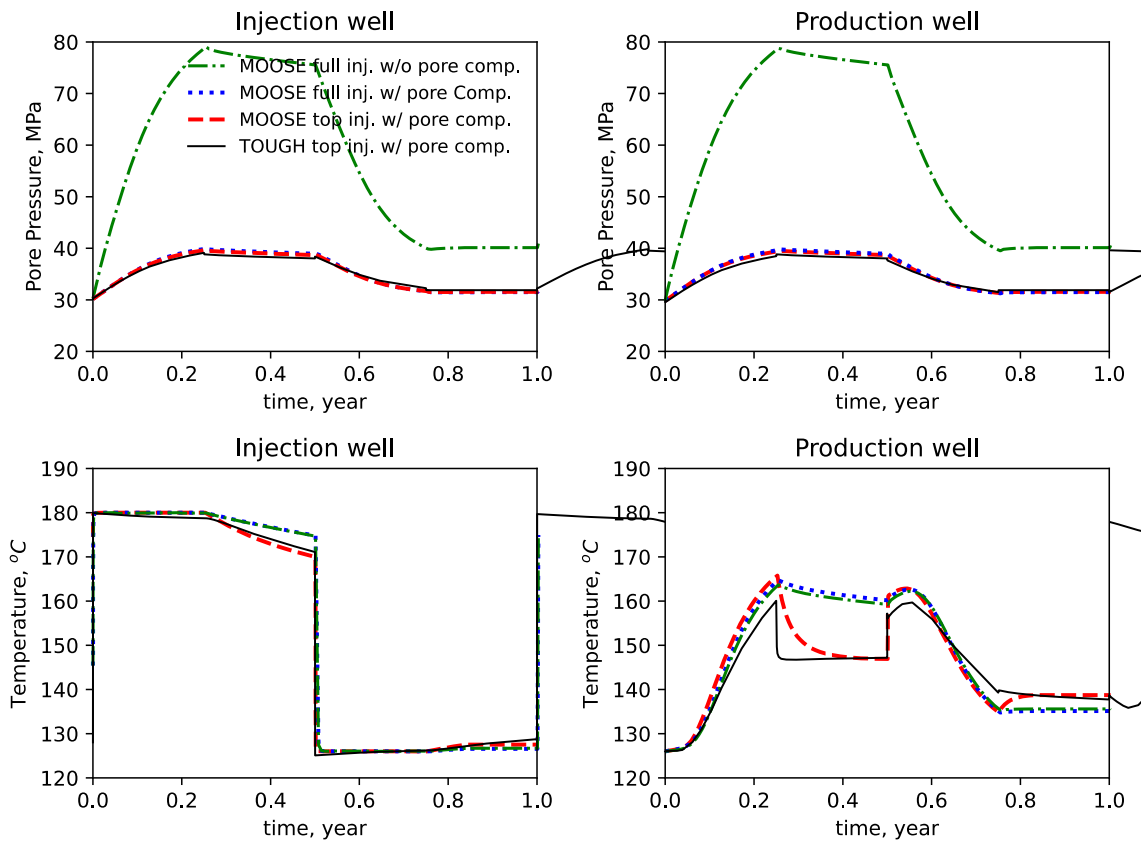
Figure 59. Comparison of pressure and temperature evolutions at the injection and production well with a year of injection-storage-extraction-rest cycle with different boundary conditions and model set-ups. For the benchmark study, we used a constant injection temperature of 180ºC, and the injection starts at the beginning of the simulation.

Here, we use MOOSE to illustrate equivalent capabilities as they compare with the TOUGH modeling work. For this benchmark study, we employed flow-through operation with constant injection/extraction rate at 3 kg/s and injection temperature at 180ºC for the smaller-scale model. Fluid property defined in IAPWS-IF97 for water was used for all the simulations; all the other parameters for heat transfer and fluid flow are kept the same as the TOUGH model introduced previously. For caprock and bedrock, we used an isotropic homogeneous permeability of 1e-18 m^2 to approximate no-flow boundary conditions and used the same thermal conductivity 2.51 $W/m \cdot K$ as the Lower Tuscaloosa Formation to diffuse heat. As shown in Figure 59, the simulation starts with injection, followed by storage, extraction, and rest, with each period having a duration of three months. The MOOSE simulation started with a case where the pore compressibility was not considered and resulted in a high-pressure buildup in both the injection and extraction wells. After the inclusion of pore compressibility, the MOOSE-predicted evolution of well pressure matches well with the TOUGH prediction. MOOSE has the capability to simulate wells using line sinks, in contrast to TOUGH3, which realizes well function using high-permeable elements. The full well injection using line sink in the MOOSE simulation predicted a different temperature evolution at the extraction well shown in the bottom right subfigure of Figure 59. In order to match the TOUGH model set-up, we adopted the same method as the TOUGH model and assigned high permeability to the corner elements that overlay with the well shown in Figure 58. With all these adjustments, we obtained an excellent match of the temperature and pressure evolution results between the MOOSE model (red dashed lines) and the TOUGH3 model (black solid lines) shown in Figure 59.
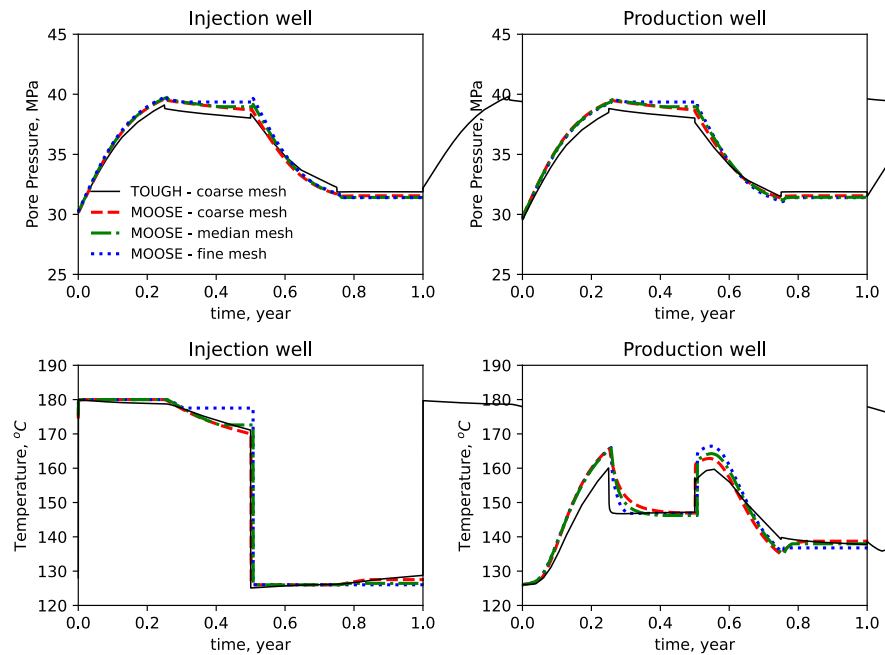
Figure 60. Mesh-density investigation by comparing temperature and pore pressure evolution at the injection and production wells predicted by the MOOSE FEM simulations with the same injection temperature and fluid cycle as in Figure 58.

We further conducted a mesh sensitivity study for the same problem. A demonstration of fine mesh and coarse mesh is presented as the middle and right subfigures of Figure 58. The simulated pressure and temperature evolution at the two wells for three different mesh densities are shown in Figure 60. We observe almost no difference for the pressure evolution at both wells and an insignificant difference of the temperature evolution at the extraction well during the extraction season. We concluded that the results are mesh independent and we performed all following simulations using a coarse mesh.
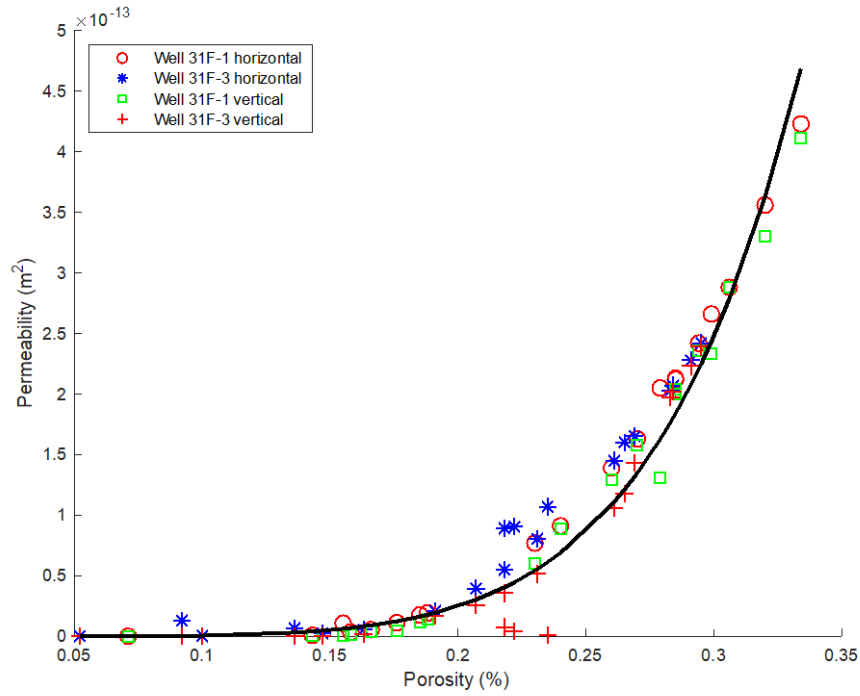
Figure 61. Fitted Kozeny-Carmen relationship between the measured porosity and measured permeability (Doughty and Freifeld, 2013).

Table 12. Geomechanics parameters extracted from the literature (Jung and Espinoza, 2017; Kim and Hosseini, 2013) and used for the THM simulations.

Parameter	Units	Value
In-situ vertical stress	MPa	67.3
In-situ horizontal stress	MPa	42.9
Shear modulus	GPa	8.38
Poisson's ratio	-	0.225
Thermo-expansion coefficient	1/K	0.00001
Biot coefficient	-	0.9
Kozeny-Carmen exponent m	-	2
Kozeny-Carmen exponent n	-	5

Theoretically, the mechanical effect on the RTES performance is such that the effective stress change and thermal expansion induce volumetric strain variation, and the volumetric strain linearly correlates to porosity. The varying porosity can change the formation permeability, enhancing or impeding the flow. We collected the porosity and the permeability measurements from the literature (Doughty and Freifeld, 2013) for the Lower Tuscaloosa Formation. These well log measurements, as shown in Figure 61, fit well to the Kozeny-Carmen relationship expressed as $\kappa = f\phi^n/(1-\phi)^m$, and the fitted exponents n and m are listed in Table 12. Note that f is a fitting coefficient and needs to be adjusted for each layer by substituting the different combination of porosity and permeability. All other geomechanics parameters collected from literature for the Lower Tuscaloosa Formation are also listed in Table 12. The no-flow (undrained) boundary conditions for temperature and pressure were applied to all the surfaces, which are the same as the TH simulations presented above. For mechanical boundary conditions, we constrained the displacement in the direction of z-, x- and y-axis for the bottom, west, and south surfaces, respectively. For the top, east and north surfaces, we applied the in-situ effective stresses listed in Table 12 to ensure force equilibrium in each direction. An example of the simulated stress profile during injection is shown as the right subfigure of Figure 58.
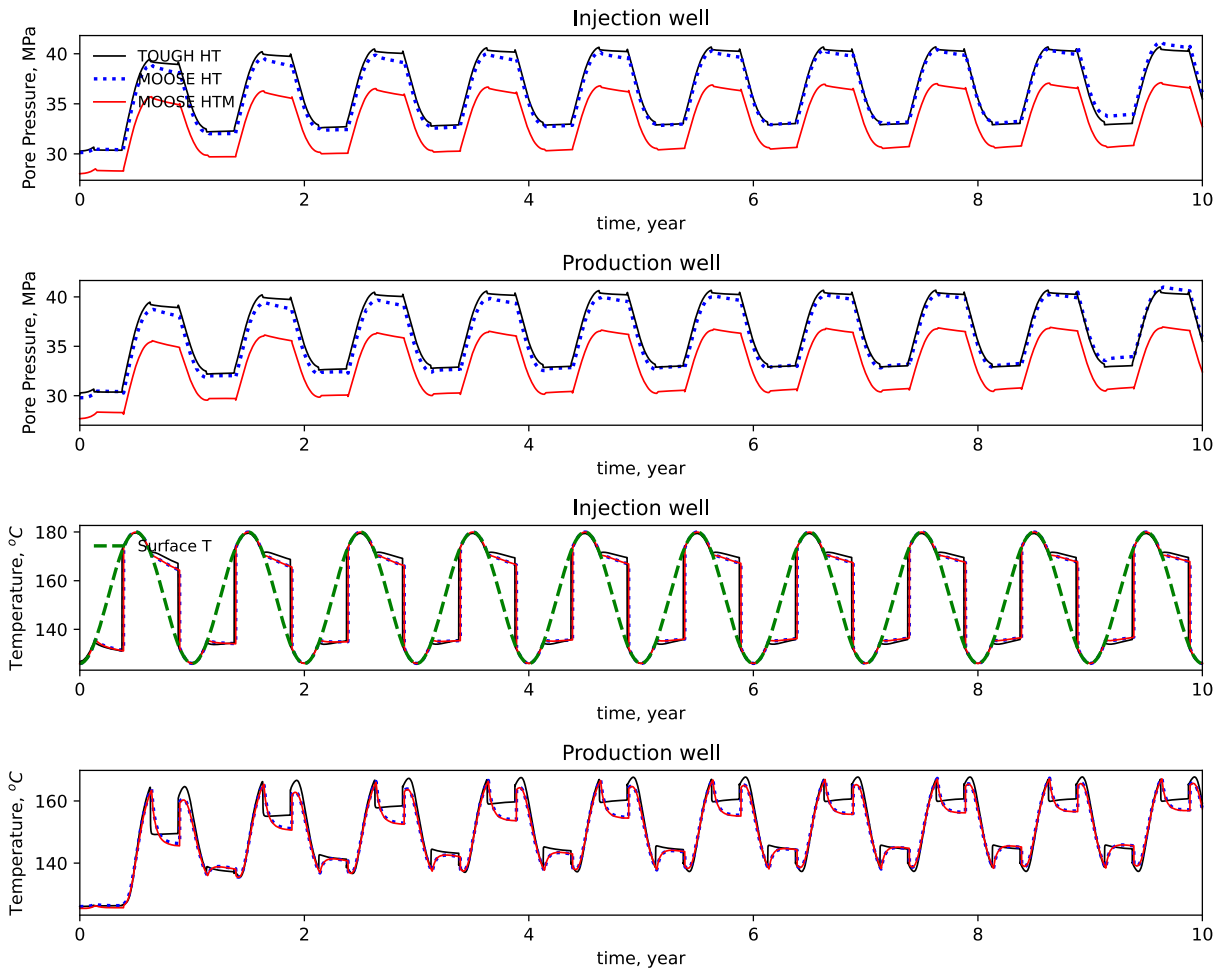
Figure 62. Simulated pressure and temperature evolution at the injection and production wells for the flow-through operation scenario with geomechanical effects considered for the simulation labeled MOOSE HTM. Ten years were simulated with sinusoid injection temperature, the same as the previous TH and THC sections.

77

Following the flow injection cycle described in Section 2.1.7 we used a sinusoid temperature profile (green dashed line in Figure 63) as the injection temperature to represent the seasonal climate variation. The injection season is in the summer of each year $0.375 < t < 0.625$ with surface temperature close to the maximum, while the extraction is in the winter of each year $t < 0.125 \,\&\, t > 0.875$ with temperature close to the minimum. The injection and extraction rates were fixed at 3 kg/s. We initially modeled the flow-through operation scenario with injection at the injection well and extraction at the production well throughout the year. Figure 62 compares the predicted temperature and pressure evolution at the injection and production wells for 10 years for the MOOSE TH model, MOOSE THM model, and TOUGH3 TH model. The good match between the TOUGH3 TH model and the MOOSE TH model further demonstrates the consistent configuration of the two numerical platforms for the same problem. The THM model and the TH models yield different pressure evolutions; however, their predicted temperature evolutions have nearly no difference. By coupling geomechanics, the thermal expansion and the stress-induced volumetric increase both contributed to an increase in porosity, which increased the permeability around the injection well. The increased permeability results in decreased pore pressure as shown in Figure 62.
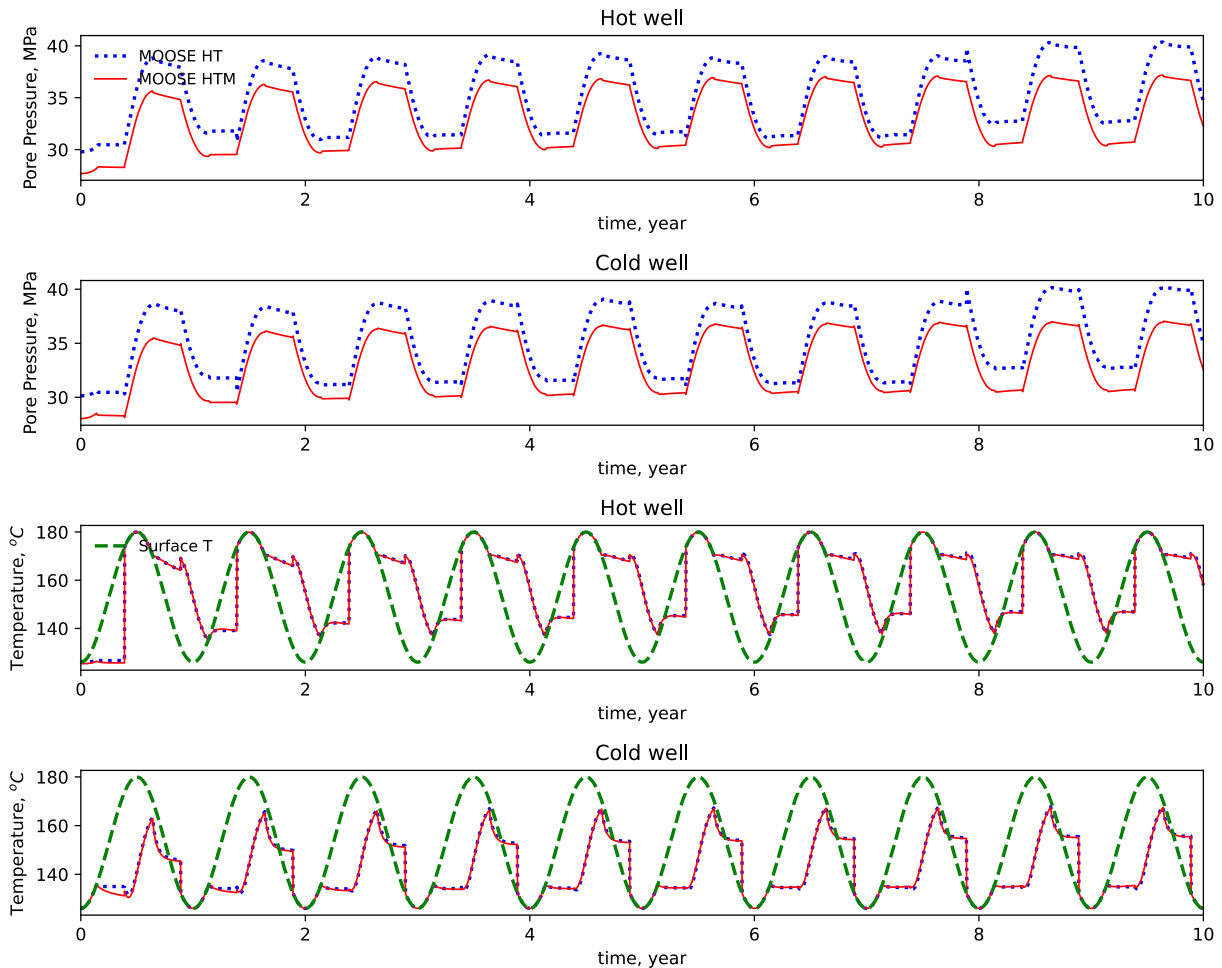
Figure 63. Simulated pressure and temperature evolution at the injection and production wells for the push-pull operation scenario with geomechanics effect considered. Ten years were simulated with sinusoid injection temperature, the same as the previous TH and THC sections.
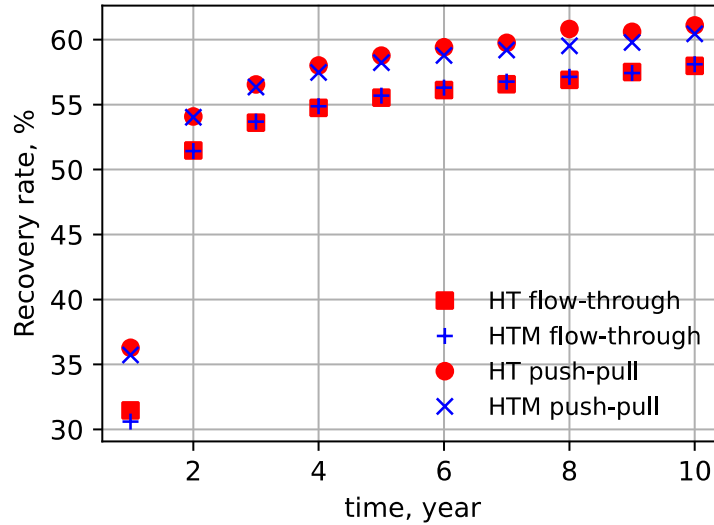
Figure 64. Comparison of annual recovery rate between the TH and THM simulations for the flow-through and the push-pull operation scenarios.

With the same model configuration, we simulated the push-pull operation scenario (i.e., hot fluid injected in the hot well and cold fluid extracted from the cold well during the summer, and the opposite during the winter). The injection rate and the sinusoid injection temperature were kept the same as the flow-through case. Figure 63 shows the predicted pore pressure and temperature evolution at the hot and cold wells for 10 years of operation of the push-pull operation. The pressure evolution pattern is similar to the pattern of the flow-through case in Figure 62, although the temperature variation pattern differs significantly. The THM and TH models predict the same temperature evolution as the flow-through case. In contrast, the THM model results in a smaller pore pressure than the TH model due to the increase in geomechanics-induced permeability.

Figure 64 shows the calculated thermal energy recovery rate for the THM and TH models with flow-through and push-pull operation scenarios. Because the THM and TH models predicted almost the same temperature evolution, the recovery rates are similarly consistent. The push-pull operation scenario has a better recovery rate than the flow-through case, which is the same as reported in Section 2.1.7. Note the low recovery rate in the first year is because the simulations start during first-year winter, at which time no hot fluid had been injected in the system. A detailed report on the effect of mechanical deformation on RTES performance with comparison to the geochemical reaction influence is summarized in the ARMA paper (Jin et al., 2022b).

3.   SUMMARY

The RTES (or ATES) technology involves injection of heated brine into a deep geologic formation to store grid-scale excess energy and utilize that energy when demand is high. This technology has the potential to play a significant role in meeting the energy storage shortfall in the coming decades by assisting with peak demand ramping, easing stress on transmission, providing regional storage to support sustainable direct use geothermal applications, and providing a variety of grid stabilization benefits. Many distributed geologic formations around the globe have the potential to provide the storage capacity required to accommodate periods of excess and insufficient renewable energy production on daily to seasonal time scales. Despite its potential, it has not been adequately tested for its long-term technological performance, economic viability, or environmental integrity. This INL-LBNL project effort has the goal of advancing the science of RTES, particularly in the initial reservoir characterization, suitability testing, thermal storage modeling, and operational scenario testing. The work conducted for this project includes (1) lessons learned from past high-temperature reservoir (geological) thermal energy storage (RTES) projects; (2) experimental investigation and numerical simulations for potential sedimentary reservoirs in the US and (3) development of a numerical simulation tool for optimizing formation properties and design parameters to maximize thermal energy storage performance.

3.1   Lessons Learned from Previous High-temperature Aquifer Thermal Energy Storage Projects

The low-temperature (<25°C) ATES technology has been tested since 1960s at various locations around the world. A handful of these systems in Europe have been designed and operated to store thermal waters at high-temperatures (>50°C). We reviewed several high-temperatures and a few moderate temperature (25-50°C) ATES projects in Germany and the Netherlands. The evaluation of design, deployment, and operational challenges of these systems in Europe provided valuable lessons learned for the future adoption of this technology. Many of the thermal energy storage projects reviewed in this study encountered various operational issues and were terminated because of their poor performance. Most of the adverse operational issues were related to insufficient site characterization such as poor assessment of reservoir heterogeneity that impacted injection and production rates, reservoir rock and water chemistry that resulted in enhanced precipitation (scaling) of carbonate minerals as temperature increases. Poor well-field design that resulted in early thermal breakthrough because of insufficient separation of wells or imbalance in the hot and cold portions of the aquifer also contributed to poor performance. Additionally, degraded quantity and quality of excess heat available in the summer for reservoir recharge due to competing demand of heat for other applications, reduction in production, or poor economics were mentioned as reasons for unsatisfactory performance of some systems. In one case, the installation of a cation exchange water treatment system (Ca replacement with Na in the water) to mitigate carbonate scaling created a new issue, clay swelling in the reservoir, with consequences of decreasing injectivity. Over time, many of these projects had a lack of spare capacity and backup wells that exacerbated their continuous operation and eventually led to closure of some of these systems.

Although most of the high temperature ATES systems in Europe have been suspended or terminated, our review of these systems also identified several practices and factors that improve the overall design and performance. Specifically, site characterizations with drilling of wells and field testing are essential to verify reservoir conditions prior to finalizing system design and initiating construction. Numerical modeling conducted using site-specific parameters obtained from pre-design and pre-construction field testing can predict fluid and heat flow, and identify geochemical reactions that may impact system performance in the future. Evaluation of risk associated with various components of the system can help identify high risk factors and devise appropriate mitigation measures. Additionally, installing and operating an integrated monitoring system to continuously gauge system performance can help identify issues before they can seriously impact operations. It is important to implement good operational practices during the design of the well field, completion of wells, construction, and operation of the

system. The practices range from selecting of the material types for the well casing to avoiding introduction of oxygen into the reducing reservoirs by constantly maintaining nitrogen as a headspace gas. Finally, a system that is flexible with operations can make it suitable and still applicable with the changing thermal energy supply and demand in the future.

3.2 Experimental Assessment of Scaling Potential and Efficacy of Geochemical Models

The transfer and interaction of high enthalpy fluid with surface and subsurface infrastructure is conducive to creating potentially adverse geochemical consequences, such as dissolution and precipitation of minerals as well as corrosion of different components of the system. We conducted three batches of time-series, high-temperature and pressure laboratory experiments using materials from the Weber Sandstone (Green River Basin, Wyoming) and the Lower Tuscaloosa Formation (Gulf Coast Basin, Mississippi) in bench-top reaction cells. Both post-experiment brine and mineralogical characterization data were used to assess the efficacy and limitations of the geochemical activity models used to predict scaling and other brine-rock reactions in RTES systems. The goal of initial geochemical modeling activities during the design phase of a project would be to obtain insight and guidance on site screening, selection, and characterization. Our experimental data show that the geochemical modeling results with parameterized Pitzer formalism could provide adequate guidance to assess a potential reservoir for favorable and unfavorable characteristics (e.g., scaling and corrosion potential). However, with increasing salinity and temperature (>200°C), the modeling results could be less useful because of associated higher uncertainties in the input parameters and restricted applicability of available activity models at those extreme conditions. Nevertheless, uncertainties in the geochemical model are probably less significant than the uncertainties arising from uncharacterized reservoir physical and chemical heterogeneities (e.g., permeability, porosity, mineralogy, etc.). On the other hand, site-specific geochemical modeling is also conducted to support design and operation of the RTES system. In this case, the accuracy of geochemical simulations (supported by experimental studies) is critical because the modeling results can have significant impact on the design, magnitude, and cost and scope of scale mitigation or brine treatment systems requirements for an RTES system. The current level of uncertainties in the modeling results, particularly at higher salinity and higher temperature, needs to be addressed by updating the parametrization of the Pitzer formalism with results from more recent studies focused on high salinity brines at high temperature and as a function of total pressure.

In addition, laboratory experiments were designed to evaluate the use of CO_2 (nominally with P_{CO2} of 5, 16, or 50 bars) as an anti-scaling strategy to prevent the precipitation of carbonate minerals. Experimental as well as modeling results demonstrate that addition of CO_2 can inhibit carbonate scale formation in surface RTES infrastructure during thermal charging. However, geochemical results also indicate that the injected hot CO_2 charged brine will promote dissolution of carbonate minerals in the reservoir, potentially increasing the future scaling potential of the brine if it is recycled. Fortuitously, the laboratory experiments also provided data to assess the corrosion potential of possible RTES infrastructure and well materials (i.e., 316 SS). Experiments with the Lower Tuscaloosa Formation and its representative formation brine (high in chloride content but low in scaling potential) resulted in clear evidence of some corrosion of the stainless steel (316 SS) experimental reaction cells. Therefore, an understanding of brine chemistry beyond predicting the formation of scaling minerals is important as the potential for corrosion (impacting the choice of RTES infrastructure materials) exists even for brines with low scale formation potential.

3.3 Thermal-hydrological Models

TH simulations were conducted for both Weber Sandstone (charge/injection of 160°C brine into 94°C formation) and Lower Tuscaloosa Formation (charge/injection of 180°C brine into 126°C formation). These modeling simulations were conducted using TOUGH with assumption of a pair of wells operating as injection and production wells (flow-through operation) or as an injection/production well and a supply well (push-pull operation) with equal magnitude of injection and production rates. Operationally, the system could go on for multiple years with each annual cycle consisting of three months of charging during periods of energy excess (summer), three months of thermal energy storage, three months of discharge during periods of energy shortage (winter), and three months of rest.

The TH modeling results for the Weber Sandstone with the single-well push-pull and the doublet well pair configurations, production (outlet) temperature drops from 160°C to 120°C during the first-year withdrawal. Although the range of production temperatures improved gradually to 160°C to 140°C over the period of the first 5 years of simulation, the large variation in production temperature range could be an issue for incorporating RTES into a thermal power-plant that would require a nearly constant feed water temperature for the best performance. TH modeling with an alternative five-spot well configuration resulted in a better (more constant) production temperature range of 141°C to 146°C after the first three years of operation. Additional TH modeling indicated that increasing well separation so that it is greater than the extent of the thermal plume can keep the production temperature within the smallest range of variation, making it suitable for power-plant operations.

For the Lower Tuscaloosa Formation, the TH simulations were conducted using the five-spot well configuration with two modes of operations – flow-through operation (dedicated injection and production wells) and push-pull operation (one well can be injection and production well and other wells as supply wells). For both modes of operations, smaller- and larger-scale simulations were conducted. Both smaller-scale flow-through and push-pull modelling results show the overall warming up (increasing storage capacity) of the reservoir over multiple years of operations because of the improved charging and decreasing conductive heat losses to over- and underlying rock formations. Similarly, the energy recovery factor gradually increases over the first three years in both modes of operations and is likely to be stable thereafter. However, the energy recovery factors for flow-through cases are smaller than for the push-pull case. Our TH modeling results show greater energy recovery for the larger-scale flow-through systems than the smaller-scale flow-through systems because of less conductive heat loss occurring in the larger heated reservoir volume due to a smaller surface-to-volume ratio. Sensitivity studies conducted for the larger-scale flow-through system that considered a range of flow rates show that increasing flow rate results in an earlier, higher peak in the outlet temperature, and a lower final outlet temperature. Increasing the flow rate is also found to increase energy recovery factors and decreasing heat loss. Additional modeling activities conducted to investigate the effect of gravity show the presence of strong buoyancy forces for the large temperature difference between injection and ambient temperature (180 – 126°C). However, buoyancy flow is found small because of low-permeability layers, which hamper vertical flow. When the permeability of the reservoir is increased, a different distribution of temperatures in the reservoir occurred because the preferential flow through the higher permeability layers overwhelmed the buoyancy effect. Larger-scale push-pull TH modelling results show a higher energy recovery factor than the flow-through mode of operation by 0.10 to 0.20 at different flow rates, with higher recovery factors observed with the lower flow rates. Also, the energy recovery factors for the push-pull operation are higher for the base case than for the optimal case, whereas the opposite is true for flow-through operation. Therefore, the best flow rate to use depends on the operation mode being employed.

3.3.1 Thermal-hydrological-chemical Models

THC modeling was conducted with TOUGHREACT to examine the potential deleterious effects of geochemical reactions, such as dissolution and scaling, upon heating (to 180°C to 200°C) of the brines and the reservoir. For this study, geochemical modeling was performed with brines from the Weber Sandstone and Lower Tuscaloosa Formation and compared with similar results for Mt. Simon and St. Peter sandstones (Illinois Basin). Results show that the precipitation of minerals with retrograde solubility, primarily anhydrite and calcite, depends on the brine chemistry, notably its sulfate content, rather than its salinity. Therefore, scaling potential is not necessarily correlated with the total dissolved solids concentration (TDS) of these brines. These simulations show that large amounts of primarily anhydrite are found to precipitate when heating brine from the Weber Sandstone. In contrast, the simulated heating of even higher TDS brine from the Lower Tuscaloosa Formation shows about ten times less precipitation. Accordingly, THC simulations of RTES in these formations show significant plugging around the injection well in the case of the Weber Sandstone, and much less scaling in the Lower Tuscaloosa Formation.

3.4 Thermal-hydrological-mechanical and Stochastic Simulation-enabled Machine Learning (ML) Models for Optimization

In addition to the TH and THC modeling, THM modeling for the mechanical-induced changes in heat transfer and stochastic simulations for the optimization of RTES operational parameters were conducted using MOOSE framework. For THM modeling, Tensor Mechanics and Porous Flow modules in MOOSE were used with the Lower Tuscaloosa Formation as the test case considering five-spot well configuration and two modes of operations – flow-through and push-pull with 3 kg/s and 1.5 kg/s injection rates, respectively. Modeling results indicate that the thermal front reaches to the production well in flow-through mode at the end of the first charging cycle because of the higher injection rate. On the other hand, the thermal front does not reach the supply wells by the end of the first charge cycle, largely because of its lower injection rate. After the first withdrawal cycle, the residual thermal energy in the reservoir is located near the production well and the injection/production well in flow-through and push-pull modes of operations, respectively. Although both the thermal expansion and effective stress change contribute to the changes in porosity in the reservoir, the THM modeling results indicate that greater changes in porosity are caused by changes in geomechanical conditions (i.e., changes in effective stress) in the reservoir. During the charging period (summer months), geomechanical effects result in increasing reservoir porosity. Since the impacts from retrograde mineral precipitation in reducing reservoir porosity around the injection well is greater than the increase in porosity from geomechanical effects, the net porosity in the reservoir near the injection well decreases during the charging period. In the flow-through mode of operation, the geochemical processes reverse during the utilization period with the injection of heat-extracted cooler brine that helps dissolve the minerals precipitated during the charging period. However, in the push-pull mode of operation, the temperature in the reservoir near the injection/production well constantly remains higher all the time and facilitates continuous buildup of the scaling minerals. This observation indicates that the push-pull mode may have a sustainability risk as the continuous operation may eventually buildup enough scale to completely fill originally available porosity in the near-well formation.

Stochastic simulation-enabled Machine Learning (ML) modeling was conducted to develop a workflow to determine the suitability of any potential site for the RTES system and optimize RTES performance metrics. For this, a homogeneous and fully saturated generic reservoir with low-permeability under- and overlying units was considered for simulations using a suite of stochastic formation parameters such as reservoir depth, thickness, permeability, porosity, and thermal conductivity, and operational conditions such as well separation, injection temperature, and flow rates. A doublet well-configuration and two operation scenarios – flow-through and push-pull – were simulated stochastically. For each of the realized simulations, the performance of the RTES was recorded, including charging duration, operation duration, thermal energy recovery rate, and storage capacity. With the stochastic simulations, an immense amount of data connecting stochastic input parameters with output RTES performance metrics were generated and used to train two artificial neural network (ANN) models, one for each mode of operation. Consequently, these ANN models were further employed with a genetic optimization algorithm to obtain the Pareto fronts of the competing RTES performance metrics for four potential RTES systems in the Mt. Simon Sandstone, Weber Sandstone, Saint Peter Sandstone, and the Lower Tuscaloosa Sandstone with continuous charge-discharge and seasonal cycles. The modeling results indicate that the RTES performance is dependent on the operational scenarios (i.e., continuous or seasonal cycles). For example, the recovery rate of the Mt. Simon Sandstone is low for a continuous charge-discharge cycle, yet, this site has a high recovery rate for the seasonal cycle. Modeling results show that the RTES performance metrics are site-specific, with each test site has different minimum and maximum ranges for operational parameters. The stochastic simulation-based machine learning models also reveal a competing effect among various RTES performance metrics, such that increasing one performance metric leads to negatively impacting the other. The present modeling approach did not single out the most optimal RTES reservoirs with a single set of optimal solutions for operational parameters. However, inclusion of geochemical consequences in the stochastic modeling would improve its applicability in selection of RTES sites.

3.5 Future Work

A careful evaluation of the RTES work completed to date, including this project and the other Beyond Batteries research plus projects around the world such as DeepStor, reveal a number of technical and economic issues that need to be addressed before large-scale deployment of RTES can be realized. A list of some of important future work that needs to be done is listed below.

- Techno-economic Assessment of RTES

  - Couple topside-reservoir assessment of cost and efficiencies
  - Optimize thermal storage and energy usage options, including multiple thermal energy offtakers to maximize energy usage
  - Evaluate different metrics

- Lowering Technical Risks

  - Potential issues with scaling and corrosion for formation brines at elevated temperatures
    - Upgrading subsurface reactive transport models to high TDS capability
    - Flow-through experiments at reservoir-relevant conditions (brines, rocks, T & P)
  - Address modeling limitations at high TDS
  - Test mitigation measures to support reservoir sustainability
  - Conduct mesoscale experiments to demonstrate viability

- Pilot studies (in conjunction with European partners – VESTA DeepStor, & new Geothermica proposals)

  - Moderate temperature (50-100°C)
  - High temperature (>150°C)

- Other concerns (from European project reviews)

  - Adequate reservoir capacity, permeability, and seal (subsurface characterization)
  - Induced seismicity risk

4.   ACKNOWLEDGMENTS

5. REFERENCES

AgriHolland, 2014, Greenhouse heating from geothermal energy in Agriport A7 put into use (translated from Dutch). ECW Network web article https://www.ecwnetwerk.nl/nieuws/kasverwarming-uit-geothermie-in-agriport-a7-in-gebruik-genomen/ (last downloaded February, 2, 2021).

Agster, G., Bäzner, K, Christensen, S., Gaschnitz, R., Hellmann, M., Kabus, F., Kirsch, R., Liebsch-Dörschner, T., Nommensen, B., Scheer, W., Schenck, P.-F., and Thomsen, C., 2004, Geothermie in Schleswig-Holstein. Landesamt für Natur und Umwelt des Landes Schleswig-Holstein, ISBN: 3-923339-96-8, 110 p.

Alai, M., Sutton, M., and Carroll, S., 2005, Evaporative evolution of a Na–Cl–NO$_3$–K–Ca–SO$_4$–Mg–Si brine at 95°C: Experiments and modeling relevant to Yucca Mountain, Nevada, *Geochemical Transactions*, 6 (2), pp. 31-45. https://doi.org/10.1186/1467-4866-6-31

Bakema, G., Pittens, B., Buik, N., and Drijver, B., 2019, HEATSTORE Design considerations for high temperature storage in Dutch aquifers. In: Kallesøe, A.J. & Vangkilde-Pedersen, T. (eds): Underground Thermal Energy Storage (UTES) – state-of-the-art, example cases and lessons learned. HEATSTORE project report, GEOTHERMICA – ERA NET Cofund Geothermal. Appendix 2.

Bakema, G., and Drijver, B., 2019, HEATSTORE State of the art HT-ATES in the Netherlands. In: Kallesøe, A.J. & Vangkilde-Pedersen, T. (eds): Underground Thermal Energy Storage (UTES) – state-of-the-art, example cases and lessons learned. HEATSTORE project report, GEOTHERMICA – ERA NET Cofund Geothermal. Appendix 1.

Bartels, J., Kabus, F., and Schmidt, T., 2003, Seasonal aquifer solar heat storage at Rostock-Brinckmanshöhe – First operational experience and aquifer simulation. Futurestock 2003, 9th International Conference on Thermal Energy Storage, Warsaw, Poland, 59-64.

Bauer, D., Marx, R., Nußbicker-Lux, J., Ochs, F., Heidemann, W., and Müller-Steinhagen, H., 2010, German central solar heating plants with seasonal storage. Solar Energy, 84, 612-623.

Bethke, C. M., 2007, Geochemical and biogeochemical reaction modeling: Second edition. Cambridge University Press, 543 p., https://doi.org/10.1017/CBO9780511619670

Bloemendal, M., Beernink, S., Hartog, N., and van Meurs, B., 2019, Transforming ATES to HT-ATES, Insights from Dutch Pilot Project. European Geothermal Congress 2019, Den Haag, 5 p.

Bloemendal, J. M., Beernink, S., van Bel, N., Hockin, A., and Schout, G., 2020, Open bodemenergiesysteem Koppert-Cress met verhoogde opslagtemperatuur – Evaluatie van energiebesparingen en grondwatereffecten. KWR 2020.156

Bloemendal, M., Vardon, P. J., Pijnenborg, M., Sudintas, G., Medema, A., Marif, K., Beernink, S., van Veldhuizen, F., Snelleman, S., and van Oort, T., 2021, A techno-economic evaluation of high temperature thermal aquifer storage (HT-ATES) for use with the geothermal well on the TU Delft campus, in *Proceedings World Geothermal Congress 2020+1*, 9 p.

Blounot, C. W., and Dickson, F. W., 1969, The solubility of anhydrite (CaSO$_4$) in NaCl-H$_2$O from 100 to 450°C and 1 to 1000 bars, *Geochimica et Cosmochimica Acta,* 33(2), pp. 227-245, https://doi.org/10.1016/0016-7037(69)90140-9.

Blanc, P., Lassin, A., Piantone, P., Azaroual, M., Jacquemet, N., Fabbri, A., and Gaucher, E. C., 2012, Thermoddem: A geochemical database focused on low temperature water/rock interactions and waste materials, *Applied Geochemistry*, 27, 2107-2116, https://doi.org/10.1016/j.apgeochem.2012.06.002

Böttcher, O., 2012, Energy efficient and sustainable—federal buildings in Germany. REHVA Journal, 49(3), 41-45.

Dai, Z., Kan, A. T., Zhang, F., Yan, F., Ruan, G., Bhandari, N., Zhang, Z., Liu, Y., Al-Saiari, H. A., and Tomson, M. B., 2016, A Thermodynamic Model for the Solution Density and Mineral Solubility Predictions up to 250°C, 1,500 bars for Na-K-Mg-Ca-Ba-Sr-Cl-CO_3-HCO_3-SO_4-CO_2 aq Systems, SPE-179892-MS SPE International Oilfield Scale Conference and Exhibition, Aberdeen, Scotland, UK, 11–12 May 2016, https://doi.org/10.2118/179892-MS

Dijkstra, H., de Boer, C., Griffioen, J., and Koenen, M., 2020, Workflow to evaluate the risk of mineral scaling in a HT-ATES system and application to a potential site in Middenmeer, The Netherlands, TNO report, R10437, 56 p.

Dinkelman D., 2019, Optimization of technical and economic efficiency of HT-ATES combined with geothermal energy – Case study modelling of Agriport A7, Middenmeer. Msc thesis, Utrecht University.

Doughty, C., and Freifeld, B. M., 2013, Modeling CO_2 injection at Cranfield, Mississippi: Investigation of methane and temperature effects, *Greenhouse Gas Science and Technology*, 3, pp. 475-490, https://doi.org/10.1002/ghg.1363

Drijver, B., 2011, High temperature aquifer thermal energy storage (HT-ATES): Water treatment in practice, 2011, 1st National Congres Bodemenergie, Utrecht, the Netherlands, 5 p.

Drijver, B., 2012, Meer met Bodemenergie Hogetemperatuuropslag Kennisoverzicht en praktijkmetingen rondom hogetemperatuur-warmteopslagsystemen. Report nr. 6. Bioclear, Deltares, IF Technology, and Wageningen University.

Drijver, B., Bakema, G., and Oerlemans, P., 2019, State of the art of HT-ATES in the Netherlands, *European Geothermal Congress,* 5 p.

Ellis, A. J., 1963, The solubility of calcite in sodium chloride solutions at high temperatures. *American Journal of Science,* 261(3), pp. 259-267, https://doi.org/10.2475/ajs.261.3.259

Fleuchaus, P., Godschalk, B., Stober, I., and Blum, P., 2018, Worldwide application of aquifer thermal energy storage – A review. *Renewable and Sustainable Energy Reviews*, 94, pp. 861-876, https://doi.org/10.1016/j.rser.2018.06.057

Fleuchaus, P., Schüppler, S., Bloemendal, M., Guglielmetti, L., Opel, O., and Blum, P., 2020, Risk analysis of High-Temperature Aquifer Thermal Energy Storage (HT-ATES). Renewable and Sustainable Energy Reviews, 133, 110153.

Godschalk, B., 2020, HTO a key role in the energy transition? (Translated from Dutch). IF Technology, Netherlands, web article https://iftechnology.nl/kennisbank/hto-een-sleutelrol-in-de-energietransitie/ (last downloaded February, 2, 2021).

Ginosar, D. M., and Wendt, D. S., 2021, Metrics for the evaluation of reservoir thermal energy storage, Idaho National Laboratory Report INL/EXT-20-60839.

GWB, 2021, Geochemist's Workbench release 15.0.0, Aqueous Solutions. LLC, Champaign, IL USA.

Harvie, C. E., Møller, N., and Weare, J. H., 1984, The prediction of mineral solubilities in natural waters: The Na-K-Mg-Ca-H-Cl-SO$_4$-OH-HCO$_3$-CO$_3$-CO$_2$-H$_2$O system to high ionic strengths at 25°C, *Geochimica et Cosmochimica Acta,* 48:723-751, https://doi.org/10.1016/0016-7037(84)90098-X

Helgeson, H. C., 1969, Thermodynamics of hydrothermal systems at elevated temperatures and pressures. American Journal of Science, 267 (7), pp. 729-804, https://doi.org/10.2475/ajs.267.7.729

Hopman, L., 2015, Beschikking wijziging vergunning Waterwat Kopper Cress B.V. Monster, in Zuid-Holland, P. (Ed.), Den Haag.

Hovorka, S. D., Meckel, T. A., and Treviño, R. H., 2013, Monitoring a large-volume injection at Cranfield, Mississippi—Project design and recommendations. *International Journal of Greenhouse Gas Control*, 18, pp. 345-360, https://doi.org/10.1016/j.ijggc.2013.03.021

Jin, W., Podgorney, R., and McLing, T., 2020, THM Coupled Numerical Analysis on the Geothermal Energy Storage & Extraction in Porous Fractured Reservoir, in *Proceedings, 54th US Rock Mechanics/Geomechanics Symposium*, ARMA 20-1338

Jin, W., Podgorney, R., McLing, T., and Carlsen, R. W., 2021, Geothermal battery optimization using stochastic hydro-thermal simulations and machine learning algorithms, in *Proceedings, 55th US Rock Mechanics/Geomechanics Symposium*, ARMA 21-1243

Jin, W., Atkinson, T., Doughty, C., Neupane, G., Spycher, N., McLing, T., Dobson, P., Smith, R., and Podgorney, R., 2022a, Machine learning assisted high-temperature geological thermal storage optimization, *Renewable Energy*, under review.

Jin, W., Dobson, P., Doughty, C., Spycher, N., McLing, T., Neupane, G., Smith, R., and Atkinson, T., 2022b, Influence of mechanical deformation and mineral dissolution/precipitation on reservoir thermal energy storage. 56th US Rock Mechanics/Geomechanics Symposium, Santa Fe, NM, ARMA 22-2068.

Jove-Colon, C., Wolery, T., Rard, J., Wijesinghe, A., Jareck, R., and Helan, K., 2007, Pitzer database development: Description of the Pitzer geochemical thermodynamic database data0.ypf.R2. Appendix I. In In-Drift Precipitates/Salts Model, Report ANL-EBS-MD-000045 REV 03.

Jung, H., and Espinoza, D. N., 2017, Chemo-Poromechanical Properties of Tuscaloosa Sandstone: Implications on CO$_2$ Geological Storage, 51st U.S. Rock Mechanics/Geomechanics Symposium, 25-28 June. ARMA, San Francisco, California, USA, 2017-0303

Jung, Y., Pau, G. S. H., Finsterle, S., and Doughty, C., 2018, TOUGH3 User's Guide, V1.0. LBNL-2001093, Lawrence Berkeley National Laboratory, Berkeley, California.

Kabus, F., 2003, Aquifer storge of waste heat arising from a gas and steam cogeneration plant. Futurestock 2003, 9th International Conference on Thermal Energy Storage, Warsaw, Poland, 543-548.

Kabus, F., Hoffmann, F., and Möllmann, G., 2005, Storage of waste heat arising from a gas and steam cogeneration plant – concept and first operating experience. Proceedings World Geothermal Congress 2005, Antalya, Turkey, 5 p.

Kabus, F. and Seibt, P., 2000, Aquifer thermal energy storage for the Berlin Reichstag building-new seat of the German parliament. In Proceedings, World Geothermal Congress 2000, Kyushu-Tohoku, Japan, 3611-3615.

Kabus, F., Seibt, P., and Poppei, J., 2000, Aquifer thermal energy stores in Germany. In Proceedings, Symposium on Heating and co-generative systems in urban settlements and industry, 4 & 5 October 2000, Macedonia, Book 1, 58-66.

Kabus, F., Wolfgramm, M., Seibt, A., Richlak, U., and Beuster, H., 2009, Aquifer thermal energy storage in Neubrandenburg – Monitoring throughout three years of regular operation. Proc. 11th Int. Conf. Energy Storage (Effstock), Stockholm, Sweden.

Kallesøe, A.J., and Vangkilde-Pedersen, T. (eds)., 2019, Underground Thermal Energy Storage (UTES) – state-of-the-art, example cases and lessons learned. HEATSTORE project report, GEOTHERMICA – ERA NET Cofund Geothermal. 130 pp + appendices. https://www.heatstore.eu/documents/HEATSTORE_UTES%20State%20of%20the%20Art_WP1_D1.1_Final_2019.04.26.pdf

Kim, S. H., and Hosseini, S.A., 2013, Above-zone pressure monitoring and geomechanical analyses for a field-scale CO_2 injection project in Cranfield, MS, Society of Chemical Industry, Greenhouse Gas Science and Technology, Volume 4, Issue 1, pp. 81-98. https://doi.org/10.1002/ghg.1388

Labus, M. and Labus, K., 2018 Thermal conductivity and diffusivity of fine-grained sedimentary rocks, Journal of Thermal Analysis and Calorimetry, 132, 1669-1676, https://doi.org/10.1007/s10973-018-7090-5.

Lerm, S., Westphal, A., Miethling-Graff, R., Alawi, M., Seibt, A., Wolfgramm, M., and Würdemann, H., 2013, Thermal effects on microbial composition and microbially induced corrosion and mineral precipitation affecting operation of a geothermal plant in a deep saline aquifer, *Extremophiles*, 17, pp. 311-327, https://doi.org/10.1007/s00792-013-0518-8

Lu, J., Kharaka, Y., Thordsen, J., Horita, J., Karamalidis, A., Griffith, C., Hakala, J. A., Ambats, G., Cole, D. R., Phelps, T. J., Manning, M. A., Cook, P. J., and Hovorka, S. D., 2012, CO_2–rock–brine interactions in Lower Tuscaloosa Formation at Cranfield CO_2 sequestration site, Mississippi, U.S.A. *Chemical Geology*, 291, pp. 269–277, https://doi.org/10.1016/j.chemgeo.2011.10.020

Lu, J., Kordi, M., Hovorka, S. D., Meckel, T. A., and Christopher, C. A., 2013, Reservoir characterization and complications for trapping mechanisms at Cranfield CO_2 injection site, International Journal of Greenhouse Gas Control, 18, 361–374, http://dx.doi.org/10.1016/j.ijggc.2012.10.007

Maqsood, A. and K. Kamran, 2005, Thermophysical properties of porous sandstones: Measurements and comparative study of some representative thermal conductivity models, International Journal of Thermophysics, 26, 5, 1617-1632, 2005, https://doi.org/10.1007/s10765-005-8108-3.

McLaughlin, J. F., and Garcia-Gonzalez, M., 2013, Detailed geologic characterization of core and well data from the Weber and Madison Formations and associated seals at a potential CO_2 sequestration site in southwest Wyoming: defining the lithologic, geochemical, diagenetic, and burial histories relative to successful CO_2 storage, In Geological CO_2 storage characterization (R.C. Surdam, ed.) Springer, New York, pp. 55-96, http://dx.doi.org/10.1007/978-1-4614-5788-6_6.

McLaughlin, J. F., Bentley, R. D., and Quillinan, S. A., 2013, Regional geologic history, CO_2 source inventory, and groundwater risk assessment of a potential CO_2 sequestration site on the Rock Springs Uplift in southwest Wyoming, In Geological CO_2 storage characterization (R.C. Surdam, ed.), Springer, New York, pp. 33-54, http://dx.doi.org/10.1007/978-1-4614-5788-6_5

McLing, T. L., Wendt, D., Dobson, P., Doughty, C., Spycher, N., Roberson, D., and McLaughlin, J. F., 2019, Dynamic Earth Energy Storage: Terawatt-Year, Grid-Scale Energy Storage using Planet Earth as a Thermal Battery (GeoTES): Seedling Project Final Report. Idaho National Laboratory, INL/EXT-19-53932, https://dx.doi.org/10.15121/1638710

Mississippi Oil and Gas Board, 1966, Mississippi Oil and Gas Board (MOGB), Cranfield Field, Cranfield unit, basal Tuscaloosa reservoir, Adams and Franklin Counties. pp. 42–58.

Neupane, G., Smith, R. W., McLing, T. L., McLaughlin, J. F., Spycher, N., and Dobson, P. F., 2020, Geochemistry of Geologic Thermal Energy Storage (GeoTES) systems: assessment of the Weber Sandstone, western Wyoming, USA, *Geothermal Resources Council Transactions*, **44**:1110-1122.

Neupane, G., Smith, R. W., McLing, T. L., Atkinson, T. A., McLaughlin, J. F., Spycher, N., and Dobson, P. F., 2021, Experimental Assessment of Geochemistry of Geologic Thermal Energy Storage (GeoTES) Systems. *GRC Transactions* **45**:1149-1166.

Nußbicker-Lux, J., Bauer, D., Marx, R., Heidemann, W., and Müller-Steinhagen, H., 2009, Monitoring results from German central solar heating plants with seasonal thermal energy storage. EFFSTOCK 2009, Stockholm, Sweden.

Oerlemans, P., 2018, Modelling Heat Transport in a High Temperature ATES System, Master's Thesis, Utrecht University.

Palandri, J., and Kharaka, Y. K., 2004, A compilation of rate parameters of water–mineral interaction kinetics for application to geochemical modeling, U.S. Geological Survey, Open File Report 2004-1068, 64 pp, https://doi.org/10.3133/ofr20041068

Palandri, J., and Reed, M. H., 2001, Reconstruction of in situ composition of sedimentary formation waters, *Geochimica et Cosmochimica Acta,* 65, 1741–1767, https://doi.org/10.1016/S0016-7037%2801%2900555-5

Pavlov, G. K., and Oleson, B. W., 2012, Thermal energy storage – A review of concepts and system for heating and cooling applications in buildings: Part 1 – Seasonal storage in the ground. HVAC&R Research, 18 (3), 515-538.

Permann, C. J., Gaston, D. R., Andrš, D., Carlsen, R. W., Kong, F., Lindsay, A. D., ... & Martineau, R. C., 2020, MOOSE: Enabling massively parallel multiphysics simulation. *SoftwareX*, *11*, 100430.

Pruess, K., 2004, The TOUGH codes - a family of simulation tools for multiphase flow and transport processes in permeable media, *Vadose Zone Journal*, 3(3), pp. 738–746, https://doi.org/10.2113/3.3.738

Quillinan, S. A., and McLaughlin, J. F., 2013, Reservoir fluid characterization of the Weber Sandstone and Madison Limestone on the Rock Springs Uplift in southwest Wyoming, In: Geological CO_2 Storage Characterization (R.C. Surdam, ed.), Springer, New York, 151-167.

Reed M. H., and Palandri, J., 2006, SOLTHERM.H06, a database of equilibrium constants for minerals and aqueous species. Available from the authors, University of Oregon, Eugene, Oregon, https://dx.doi.org/10.15121/1805737

Rinehart, A. J., Dewers, T. A., Broome, S. T., and Eichhubl, P., 2016, Effects of CO_2 on mechanical variability and constitutive behavior of the Lower Tuscaloosa Formation, Cranfield Injection Site, USA, International Journal of Greenhouse Gas Control. 53, pp. 305–318, https://doi.org/10.1016/j.ijggc.2016.08.013

Robertson, E.C., Thermal properties of rocks, U.S. Geological Survey Open File Report 88-441, 1988.

Sanner, B., Kabus, F., Seibt, P., and Bartels, J., 2005, Underground thermal energy storage for the German Parliament in Berlin, system concept and operational experience. Proceedings World Geothermal Congress 2005, Antalya, Turkey, 8 p.

Schmidt, T., Kabus, F., and Müller-Steinhagen, H., 2000, The Central Solar Heating Plant with Aquifer Thermal Energy Store in Rostock, Germany. Terrastock 2000, Stuttgart, Germany, 473-478.

Schmidt, T., and Muller-Steinhagen, H., 2004, The Central Solar Heating Plant with Aquifer Thermal Energy Store in Rostock – Results after four years of operation, EuroSun 2004, 5th ISES Europe Solar Conference, Freiburg, Germany.

Schmidt, T., and Müller-Steinhagen, H., 2005, Erdsonden- und Aquifer-Wärmespeicher in Deutschland. OTTI Profiforum Oberflachennahe Geothermie, Regenstauf, 12 p.

Seibt, P., and Kabus, F., 2006, Aquifer thermal energy storage – Projects implemented in Germany. Proceedings ECOSTOCK 2006. 10th International Conference on Thermal Energy Storage, May 31-June 2, 2006, The Richard Stockton College of New Jersey, Pomona, New Jersey, USA. 8 pp.

Seibt, P., Kabus, F., Wolfgramm, M., Bartels, J., and Seibt, A., 2010, Monitoring of hydrogeothermal plants in Germany – an overview. Proceedings World Geothermal Congress 2010, Bali, Indonesia, 7 p.

Seibt, P., and Kellner, T., 2003, Practical experience in the reinjection of cooled thermal waters back into sandstone reservoirs. Geothermics, 32, 733-741.

Seibt, P., and Wolfgramm, M., 2008, Practical experience in the reinjection of thermal waters into sandstone. United Nations University Geothermal Training Programme, Workshop for Decision Makers on Direct Heating Use of Geothermal Resources in Asia, organized by UNU-GTP, TBLRREM and TBGMED, Tianjin, China, 11-18 May, 2008.

Shafer, L. R., 2013, Assessing injection zone fracture permeability through identification of critically stressed fracture orientations at the Rock Springs Uplift CO_2 sequestration site, SW Wyoming. MS Thesis, University of Wyoming

Shi, W., Kan, A.T, Zhang, N., and Tomson, M., 2013, Dissolution of calcite at up to 250° C and 1450 bar and the presence of mixed salts. *Industrial and Engineering Chemistry Research*, 52(6), pp. 2439−2448 http://dx.doi.org/10.1021/ie302190e

Sonnenthal, E. L., Spycher, N., Xu, T., and Zheng, L., 2021, TOUGHREACT V4.12-OMP and TReactMech V1.0 Geochemical and Reactive-Transport User Guide. Lawrence Berkeley National Laboratory Report LBNL-2001410, Berkeley, California

Soong, Y., Howard, B. H., Dilmore, R. M., Haljasmaa, I., Crandall, D. M., Zhang, L., Zhang, W., Lin, R., Irdi, G. A., Romanov, V. N., and McLendon, T. R., 2016, CO_2/brine/rock interactions in Lower Tuscaloosa Formation. *Greenhouse Gas Sci Technol*. **6**, 824–837 https://doi.org/10.1002/ghg.1611

Spycher, N., Doughty, C., Dobson, P. F., Neupane, G., Smith, R. W., Jin, W., Atkinson, T. A., and McLing, T. L., 2021a, Evaluation of Mineral Scaling during High-Temperature Thermal Energy Storage in Deep Saline Aquifers. *GRC Transactions* **45**:1201-1215

Spycher, N., Zhang, G., Sonnenthal, E. L., and Molins, S., 2021b, TOUGHREACT-Brine: Supplement to TOUGHREACT-V4.0-OMP User's Guide for modeling concentrated solutions and osmosis using the Pitzer ion-interaction model. Lawrence Berkeley National Laboratory Report LBNL-2001387, Berkeley, CA

Surdam, R. C., Jiao, Z., Stauffer, P. H., and Miller, T., 2009, An integrated strategy for carbon management combing geologic CO_2 sequestration, displaced fluid production, and water treatment, Wyoming State Geologic Survey Challenges in Geologic Resource Development No. 8

Surdam, R. C., 2013, Geological CO_2 storage characterization: The key to deploying clean fossil energy technology, Springer Science & Business Media

Ueckert, M., and Baumann, T., 2019, Hydrochemical aspects of high-temperature aquifer storage in carbonaceous aquifers: evaluation of a field study. *Geothermal Energy*, 7:4, 22 p. http://dx.doi.org/10.1186/s40517-019-0120-0

Ueckert, M., Niessner, R., and Baumann, T., 2016, High temperature aquifer storage. Proceedings, 41st Workshop on Geothermal Reservoir Engineering, Stanford University, 12 p.

Ueckert, M., Wismeth, C., and Baumann, T., 2020, Crystallization of calcium carbonate in a large-scale push-pull heat storage test in the Upper Jurassic carbonate reservoir. Geothermal Energy, 8:7, 23 p.

van Loon, L. M. J., and van der Heide, K., 1992, High temperature ATES at the University of Utrecht, the Netherlands. In: Aquifer Thermal Energy (Heat and Chill) Storage, Papers presented at the 1992 Intersociety Energy Conversion Engineering Conference, San Diego, California, E. A. Jenne (ed.), PNL-8381, 47-49.

van Unen, M., van der Valk, K., Koomneef, J., Brunner, L., and Koenen, M., 2020, HEATSTORE risk assessment for HT-ATES applied to demonstration case Middenmeer, The Netherlands. TNO report 2020 R10192, 34 p.

van Velden P., 2019, Underground hot water storage of 85°C improves efficiency of doublets (translated from Dutch). Vakblad Onder Glas web article, 28 march, 2019 https://www.onderglas.nl/ondergrondse-warmwateropslag/ (last downloaded February 2, 2021)

Vardon, P. J., Bruhn, D. F., Steiginga, A., Cox, B., Abels, H., Barnhoorn, A., Drijkoningen, G., Slob, E., and Wapenaar, K., 2021, A geothermal well doublet for research and heat supply of the TU Delft Campus. Proceedings World Geothermal Congress 2020+1, Reykjavik, Iceland, 6 p.

Vetter, A., Mangelsdorf, K., Schettler, G., Seibt, A., Woldframm, M., Rauppach, K., and Vieth-Hillebrand, A., 2012, Fluid chemistry and impact of different operating modes on microbial community at Neubrandenburg heat storage (Northeast German Basin). Organic Geochemistry, 53, 8-15.

Vinsome, P. K. W., and Westerveld, J., 1980, A simple method for predicting cap and base rock heat losses in thermal reservoir simulators. *Journal of Canadian Petroleum Technology*, 19(3), pp. 87–90. https://doi.org/10.2118/80-03-04

Wendt, D. S., Huang, H., Zhu, G., Sharan, P., McTigue, J., Kitz, K., Green, S., McLennan, J., and Neupane, G., 2019, Flexible geothermal power generation utilizing geologic thermal energy storage: Final Seedling Project Report. Idaho National Laboratory, INL/EXT-19-53931, 85 p. https://doi.org/10.2172/1524048

Westphal, A., Lerm, S., Meithling-Graff, R., Seibt, A., Wolfgramm, M., and Würdemann, H., 2016, Effects of plant downtime on the microbial community composition in the highly saline brine of a geothermal plan in the North German Basin. Applied Microbiology and Biotechnology, 100, 3277-3290.

Willemsen, A., 1992, PHREEQM-2D: A computer model to calculate geochemical reactions during transport of groundwater: Model description and application to the Utrecht University ATES. In: Aquifer Thermal Energy (Heat and Chill) Storage, Papers presented at the 1992 Intersociety Energy Conversion Engineering Conference, San Diego, California, E.A. Jenne (ed.), PNL-8381, 89-98.

Wolery, T. J., and Jarek, R. L., 2003, EQ3/6, Version 8.0, Software User's Manual. Software Document Number 10813-UM-8.0-00, U.S. Department of Energy, Office of Civilian Radioactive Waste Management, Office of Repository Development, 1261 Town Center Drive, Las Vegas, Nevada 89144.

Wolfgramm, M., Rauppach, K., and Puronpää-Schäfer, P., 2011, Geothermal energy storage system at the parliament buildings in Berlin: Operation, monitoring and rehabilitation of N_2-charged groundwater wells. Arab Water World, XXXV(4), 33-35.

Wolfgramm, M., and Seibt, A., 2006, Geochemisches Monitoring des geothermalen Tiefenspeichers in Neubrandenburg, GtV-Tagung: 15.-17.11.2006 in Karlsruhe: 388-397.

Xu, T., Sonnenthal, E. L., Spycher, N., and Pruess, K., 2006, TOUGHREACT - A simulation program for non-isothermal multiphase reactive geochemical transport in variably saturated geologic media: Applications to geothermal injectivity and CO2 geological sequestration. *Computers & Geoscience*, 32(2), 145–165. https://doi.org/10.1016/j.cageo.2005.06.014

Yang, T., Liu, W., Kramer, G. J., and Sun, Q., 2021, Seasonal thermal energy storage: A techno-economic literature review. Renewable and Sustainable Energy Reviews, 139, 110732.

Zenke, J., Seibt, P., and Kabus, F., 2000, Increase of the efficiency of the Neubrandenburg geothermal heating plant through surplus heat storage in summer. Proceedings World Geothermal Congress 2000, Kyushu-Tohuku, Japan, 5 p.

6. APPENDICES

Appendix A, Brine Chemistry

Appendix B, Experimental Characterization

Appendix C, TOUGHREACT Comparison

Appendix D, Published Papers Resulting from Phase I of this Project

Appendix A

Brine Chemistry

Appendix A5: Measured experimental brine compositions from high temperature and pressure experiments. Test I, II, and III designate the experimental series, Cells 1-8 designate the pressure vessel, and Out 1-7 identify the sampling event. A total of 21 experiments were conducted including three replicates and two brine-only blanks (Test II Cell 4 and Test III Cell 1). Test I-II and Test III used Weber and Tuscaloosa brines and rock (excepting blanks), respectively. SIB Test I, II, and III are the unreacted synthetic brines used in the respective Test series. pH and DIC were calculated using GWB as described in the text.

Sample ID	Time day	P bar	T C	pH	DIC mmolal	Cl- mmolal	F- mmolal	SO4-- mmolal	Al+++ mmolal	Ca++ mmolal	Fe++ mmolal	Mg++ mmolal	K+ mmolal	SiO2(aq) mmolal	Na+ mmolal	Sr++ mmolal
SIB Test I			22	5.50	4.74E+01	1.39E+03		1.10E+02	3.81E-02	1.92E+00	1.38E-02	2.99E-01	4.53E+01		1.39E+03	
Test I Cell 1 Out 1	1	26.46	200	5.71	1.02E+02	1.41E+03		1.11E+02		9.59E-01	1.01E-01	1.71E-01	4.62E+01	2.85E+00	1.41E+03	2.25E-03
Test I Cell 1 Out 2	2	25.93	200	5.71	9.71E+01	1.43E+03	2.73E-01	1.12E+02		6.74E-01	8.35E-02	1.28E-01	4.63E+01	2.70E+00	1.41E+03	6.28E-03
Test I Cell 1 Out 3	4	25.84	200	5.64	9.33E+01	1.44E+03	2.74E-01	1.13E+02		1.27E+00	8.06E-02	4.28E-02	5.03E+01	3.07E+00	1.55E+03	8.07E-03
Test I Cell 1 Out 4	8	25.66	200	5.79	1.01E+02	1.51E+03	6.03E-01	1.17E+02		1.48E+00	6.98E-02		5.14E+01	3.14E+00	1.59E+03	8.68E-03
Test I Cell 1 Out 5	16	25.21	200	5.84	9.87E+01	1.54E+03	2.74E-01	1.21E+02	1.50E-02	1.51E+00	4.34E-02		5.17E+01	3.06E+00	1.42E+03	8.08E-03
Test I Cell 1 Out 6	32	23.09	200	5.80	8.08E+01	1.59E+03		1.25E+02		1.30E+00	3.95E-02		5.85E+01	2.94E+00	1.90E+03	8.94E-03
Test I Cell 1 Out 7	64	23.02	200	5.73	7.48E+01	1.57E+03	4.94E-01	1.26E+02		1.20E+00	3.68E-02		5.84E+01	2.98E+00	1.78E+03	7.02E-03
Test I Cell 2 Out 1	1	15.75	200	6.25	1.13E+01	1.39E+03		1.11E+02			6.13E-02	1.28E-01	3.65E+01	2.42E+00	1.29E+03	6.49E-03
Test I Cell 2 Out 2	2	15.86	200	6.30	1.24E+01	1.40E+03		1.17E+02	1.65E-02	1.29E+00	4.67E-02	8.51E-02	4.19E+01	2.69E+00	1.19E+03	5.90E-03
Test I Cell 2 Out 3	4	16.02	200	6.18	1.29E+01	1.50E+03		1.25E+02		8.53E-01	3.06E-02	8.52E-02	4.35E+01	2.89E+00	1.19E+03	4.85E-03
Test I Cell 2 Out 4	8	16.45	200	6.05	1.60E+01	1.56E+03		1.27E+02		6.98E-01	7.01E-02	8.53E-02	4.30E+01	3.04E+00	1.14E+03	4.26E-03
Test I Cell 2 Out 5	16	16.76	200	5.91	1.96E+01	1.57E+03	4.92E-01	1.26E+02		1.01E+00	3.28E-02	8.55E-02	4.73E+01	3.92E+00	1.47E+03	3.08E-03
Test I Cell 2 Out 6	32	17.04	200	5.89	2.29E+01	1.54E+03	3.28E-01	1.26E+02	7.63E-02	8.82E-01	1.56E-01	4.28E-02	5.06E+01	4.29E+00	1.59E+03	4.04E-03
Test I Cell 2 Out 7	64	17.34	200	5.85	2.50E+01	1.52E+03	6.02E-01	1.24E+02		5.97E-01	2.74E-02	8.56E-02	5.20E+01	4.03E+00	1.60E+03	4.63E-03
Test I Cell 3 Out 1	1	7.53	160	5.67	1.48E+01	1.35E+03		1.09E+02		1.96E+00	8.44E-02	8.51E-02	4.27E+01	7.85E-01	1.26E+03	
Test I Cell 3 Out 2	2	7.39	160	5.80	1.47E+01	1.41E+03	7.08E-01	1.10E+02		2.94E+00	8.24E-02	1.28E-01	4.36E+01	1.21E+00	1.21E+03	1.06E-03
Test I Cell 3 Out 3	4	7.31	160	5.87	1.49E+01	1.40E+03	2.83E-01	1.14E+02		1.88E+00	1.08E-01	1.28E-01	4.63E+01	1.66E+00	1.28E+03	3.44E-03
Test I Cell 3 Out 4	8	7.2	160	5.81	1.31E+01	1.48E+03	4.36E-01	1.19E+02	2.30E-02	1.76E+00	5.84E-02		4.54E+01	1.76E+00	1.32E+03	6.03E-03
Test I Cell 3 Out 5	16	7.11	160	5.72	1.16E+01	1.44E+03	2.73E-01	1.18E+02		2.15E+00	7.20E-02		4.48E+01	1.89E+00	1.41E+03	8.16E-03
Test I Cell 3 Out 6	32	7.11	160	5.76	1.22E+01	1.51E+03	5.47E-01	1.25E+02		1.79E+00	3.63E-02		5.02E+01	1.94E+00	1.56E+03	8.77E-03
Test I Cell 3 Out 7	64	7.14	160	5.99	1.58E+01	1.54E+03	3.29E-01	1.26E+02	4.51E-02	1.79E+00	9.20E-02		5.45E+01	1.91E+00	1.70E+03	8.19E-03
Test I Cell 4 Out 1	1	10.37	160	5.68	4.10E+01	1.39E+03		1.11E+02		3.34E+00	1.79E-01	1.71E-01	4.66E+01	7.76E-01	1.38E+03	
Test I Cell 4 Out 2	2	10.14	160	5.65	3.80E+01	1.45E+03		1.20E+02	2.34E-01	7.19E+01	3.55E-01	3.35E+00	5.76E+01	1.65E+00	2.03E+03	1.02E-02
Test I Cell 4 Out 3	4	9.92	160	5.81	4.09E+01	1.50E+03	5.46E-01	1.24E+02		2.51E+00	1.45E-01	8.54E-02	4.85E+01	1.71E+00	1.35E+03	1.78E-03
Test I Cell 4 Out 4	8	9.76	160	5.77	3.79E+01	1.49E+03	5.46E-01	1.19E+02	1.12E-02	2.54E+00	8.73E-02	8.54E-02	4.65E+01	1.89E+00	1.36E+03	2.37E-03
Test I Cell 4 Out 5	16	9.61	160	5.82	3.82E+01	1.50E+03	4.38E-01	1.21E+02		2.44E+00	1.53E-01	4.28E-02	4.75E+01	2.10E+00	1.54E+03	4.74E-03

Test I Cell 4 Out 6	32	9.5	160	5.84	3.78E+01	1.52E+03		1.22E+02	1.27E-02	2.23E+00	6.78E-02	4.28E-02	5.23E+01	2.17E+00	1.67E+03	7.12E-03
Test I Cell 4 Out 7	64	9.44	160	5.83	3.70E+01	1.53E+03	2.19E-01	1.23E+02		1.95E+00	6.46E-02		5.18E+01	1.91E+00	1.66E+03	5.34E-03
Test I Cell 5 Out 1	1	10.4	160	5.56	3.87E+01	1.39E+03	2.18E-01	1.16E+02		2.87E+00	1.52E-01	1.71E-01	4.45E+01	8.00E-01	1.35E+03	
Test I Cell 5 Out 2	2	10.14	160	5.47	3.54E+01	1.41E+03		1.15E+02		2.53E+00	1.40E-01	1.28E-01	4.32E+01	1.00E+00	1.24E+03	9.45E-04
Test I Cell 5 Out 3	4	9.89	160	5.72	3.77E+01	1.45E+03	4.91E-01	1.17E+02		2.41E+00	1.05E-01	1.28E-01	4.85E+01	1.63E+00	1.42E+03	1.07E-03
Test I Cell 5 Out 4	8	9.67	160	5.76	3.69E+01	1.46E+03		1.22E+02	8.45E-03	2.28E+00	8.85E-02	8.53E-02	4.44E+01	1.81E+00	1.25E+03	2.60E-03
Test I Cell 5 Out 5	16	9.47	160	5.70	3.35E+01	1.48E+03		1.19E+02		2.07E+00	1.26E-01	8.53E-02	4.45E+01	1.86E+00	1.27E+03	4.73E-03
Test I Cell 5 Out 6	32	9.3	160	5.65	3.09E+01	1.48E+03	6.01E-01	1.19E+02		1.94E+00	6.45E-02	4.27E-02	4.96E+01	2.06E+00	1.54E+03	6.40E-03
Test I Cell 5 Out 7	64	9.11	160	5.67	2.96E+01	1.51E+03		1.24E+02		1.97E+00	1.08E-01	4.28E-02	5.09E+01	1.99E+00	1.60E+03	4.51E-03
Test I Cell 6 Out 1	1	17.95	200	6.05	3.30E+01	1.47E+03		1.13E+02		1.03E+00	2.62E-02		4.16E+01	3.29E+00	1.23E+03	7.09E-03
Test I Cell 6 Out 2	2	17.87	200	5.99	3.17E+01	1.43E+03		1.18E+02		1.42E+00	2.47E-02	1.28E-01	4.71E+01	3.07E+00	1.35E+03	9.23E-03
Test I Cell 6 Out 3	4	17.99	200	5.85	2.99E+01	1.42E+03		1.16E+02		1.45E+00	3.12E-02	8.53E-02	4.82E+01	3.29E+00	1.40E+03	9.11E-03
Test I Cell 6 Out 4	8	18.18	200	5.86	3.14E+01	1.54E+03	8.19E-01	1.20E+02	1.54E-02	1.55E+00	5.74E-02	4.70E-01	4.70E+01	2.88E+00	1.27E+03	9.59E-03
Test I Cell 6 Out 5	16	18.18	200	5.87	3.20E+01	1.53E+03	9.29E-01	1.24E+02	1.62E-02	1.30E+00	1.86E-02	8.54E-02	4.85E+01	2.94E+00	1.34E+03	7.82E-03
Test I Cell 6 Out 6	32	18.32	200	5.83	3.51E+01	1.58E+03	8.78E-01	1.29E+02		1.33E+00	3.51E-02	8.57E-02	5.63E+01	3.35E+00	1.74E+03	5.11E-03
Test I Cell 6 Out 7	64	18.26	200	5.85	3.52E+01	1.66E+03	2.20E-01	1.35E+02		1.17E+00	1.68E-02	8.58E-02	5.85E+01	3.00E+00	1.75E+03	2.62E-03
Test I Cell 7 Out 1	1	28.01	200	5.66	1.12E+02	1.39E+03	3.83E-01	1.08E+02		1.35E+00	9.33E-02	1.28E-01	4.32E+01	2.60E+00	1.29E+03	
Test I Cell 7 Out 2	2	27.47	200	5.67	1.08E+02	1.40E+03		1.09E+02	1.31E-02	8.80E-01	6.78E-02	1.28E-01	4.12E+01	2.62E+00	1.17E+03	4.03E-03
Test I Cell 7 Out 3	4	27.25	200	5.67	1.06E+02	1.42E+03	2.73E-01	1.11E+02		1.17E+00	6.21E-02	8.55E-02	4.55E+01	2.93E+00	1.31E+03	6.40E-03
Test I Cell 7 Out 4	8	26.73	200	5.61	9.94E+01	1.43E+03	3.66E+00	9.82E+01		1.48E+00	8.13E-02	8.53E-02	4.27E+01	2.73E+00	1.22E+03	6.75E-03
Test I Cell 7 Out 5	16	26.23	200	5.63	9.61E+01	1.50E+03	6.03E-01	1.17E+02	5.13E-02	1.22E+00	4.38E-02		4.87E+01	3.01E+00	1.53E+03	7.48E-03
Test I Cell 7 Out 6	32	25.7	200	5.67	9.40E+01	1.48E+03		1.16E+02		1.19E+00	4.98E-02		4.99E+01	3.14E+00	1.56E+03	7.25E-03
Test I Cell 7 Out 7	64	25.11	200	5.77	9.40E+01	1.50E+03	5.48E-01	1.17E+02		1.17E+00	3.43E-02		4.99E+01	3.17E+00	1.57E+03	7.96E-03
Test I Cell 8 Out 1	1	19.56	160	5.18	1.04E+02	1.42E+03		1.12E+02		2.46E+00	1.86E-01	3.42E-01	4.36E+01	6.58E-01	1.22E+03	
Test I Cell 8 Out 2	2	18.96	160	5.26	9.97E+01	1.43E+03		1.08E+02		2.36E+00	2.07E-01	4.27E-01	4.73E+01	9.09E-01	1.34E+03	1.19E-03
Test I Cell 8 Out 3	4	18.41	160	5.38	9.80E+01	1.44E+03		1.13E+02		2.33E+00	2.13E-01	3.42E-01	4.96E+01	1.20E+00	1.44E+03	9.49E-04
Test I Cell 8 Out 4	8	17.86	160	5.38	9.58E+01	1.51E+03	1.20E+00	1.14E+02		2.54E+00	1.62E-01	4.27E-01	4.85E+01	1.32E+00	1.29E+03	2.37E-03
Test I Cell 8 Out 5	16	17.44	160	5.51	9.66E+01	1.47E+03	4.92E-01	1.15E+02	1.39E-02	2.05E+00	1.10E-01	2.56E-01	4.67E+01	1.68E+00	1.37E+03	1.66E-03
Test I Cell 8 Out 6	32	17.03	160	5.47	8.99E+01	1.53E+03	2.74E-01	1.21E+02	4.01E-02	2.26E+00	8.73E-02	2.14E-01	5.06E+01	1.95E+00	1.61E+03	2.02E-03
Test I Cell 8 Out 7	64	16.58	160	5.16	7.62E+01	1.60E+03		1.27E+02		2.03E+00	8.13E-02	1.72E-01	5.61E+01	1.95E+00	1.71E+03	1.91E-03
SIB Test II			22	7.00	1.10E+01	1.49E+03		1.24E+02		2.80E+00			5.08E+01		1.62E+03	8.30E-04
Test II Cell 2 Out 1	1	55.09	250	6.02	1.90E+02	1.45E+03		1.12E+02		7.04E-01	4.88E-02		4.65E+01	5.06E+00	1.42E+03	2.15E-03
Test II Cell 2 Out 2	2	55.22	250	6.05	1.96E+02	1.48E+03		1.13E+02		8.61E-01	3.67E-02		4.40E+01	5.55E+00	1.43E+03	1.91E-03
Test II Cell 2 Out 3	4	54.97	250	6.03	1.95E+02	1.48E+03		1.14E+02		7.31E-01	5.06E-02		4.88E+01	6.30E+00	1.52E+03	2.51E-03
Test II Cell 2 Out 4	8	54.6	250	6.02	1.88E+02	1.49E+03		1.15E+02	2.40E-02	7.31E-01	3.30E-02		4.94E+01	5.86E+00	1.50E+03	2.03E-03
Test II Cell 2 Out 5	16	54.62	250	6.05	1.89E+02	1.49E+03		1.18E+02	8.53E-03	7.04E-01	4.85E-02		4.92E+01	5.95E+00	1.43E+03	2.63E-03
Test II Cell 2 Out 6	32	54.65	250	6.03	1.91E+02	1.49E+03		1.17E+02		7.31E-01	4.14E-02		5.42E+01	6.50E+00	1.52E+03	2.75E-03
Test II Cell 2 Out 7	73	53.76	250	6.01	1.83E+02	1.50E+03	6.06E-01	1.21E+02		9.93E-01	6.83E-02		7.45E+01	7.11E+00	1.60E+03	4.06E-03

Test II Cell 4 Out 1	1	55.05	250	6.00	1.95E+02	1.45E+03	4.41E-01	1.19E+02		7.58E-01	7.89E-02		5.06E+01	2.74E-01	1.58E+03	
Test II Cell 4 Out 2	2	54.57	250	6.02	1.90E+02	1.46E+03		1.19E+02		8.36E-01	7.21E-02		4.95E+01	3.14E-01	1.56E+03	
Test II Cell 4 Out 3	4	54.44	250	6.01	1.89E+02	1.46E+03		1.19E+02		8.10E-01	7.12E-02		4.90E+01	2.72E-01	1.58E+03	
Test II Cell 4 Out 4	8	54.82	250	6.01	1.94E+02	1.48E+03		1.22E+02		7.32E-01	7.03E-02		5.07E+01	2.30E-01	1.58E+03	
Test II Cell 4 Out 5	16	54.3	250	6.01	1.89E+02	1.52E+03		1.22E+02	1.90E-02	7.06E-01	7.56E-02		5.04E+01	2.02E-01	1.60E+03	
Test II Cell 4 Out 6	32	54	250	6.04	1.85E+02	1.53E+03		1.25E+02		8.88E-01	6.47E-02		4.95E+01	2.07E-01	1.51E+03	
Test II Cell 4 Out 7	73	53.26	250	6.04	1.79E+02	1.53E+03	3.31E-01	1.26E+02		7.05E-01	6.95E-02		4.86E+01	2.11E-01	1.55E+03	
Test II Cell 6 Out 1	1	41.69	250	6.30	5.54E+01	1.44E+03		1.19E+02		8.76E-01	2.79E-02		4.59E+01	7.03E+00	1.44E+03	4.60E-03
Test II Cell 6 Out 2	2	42	250	6.22	5.84E+01	1.50E+03		1.27E+02		1.04E+00	4.16E-02		4.77E+01	7.99E+00	1.53E+03	3.80E-03
Test II Cell 6 Out 3	4	42.35	250	6.18	6.25E+01	1.50E+03		1.22E+02		8.32E-01	3.10E-02		5.14E+01	7.92E+00	1.57E+03	5.11E-03
Test II Cell 6 Out 4	8	42.64	250	6.06	5.95E+01	1.49E+03		1.20E+02	2.71E-02	7.56E-01	6.57E-02		4.97E+01	7.17E+00	1.57E+03	9.78E-03
Test II Cell 6 Out 5	16	42.75	250	6.17	6.59E+01	1.54E+03		1.31E+02	9.66E-03	6.51E-01	8.20E-02		5.16E+01	6.72E+00	1.55E+03	1.25E-02
Test II Cell 6 Out 6	32	43.02	250	6.16	6.79E+01	1.56E+03		1.27E+02		7.02E-01	9.71E-02		5.14E+01	7.14E+00	1.52E+03	7.73E-03
Test II Cell 6 Out 7	73	43.11	250	6.15	6.84E+01	1.62E+03		1.19E+02	8.50E-03	4.16E-01	1.11E-01		5.34E+01	6.82E+00	1.52E+03	5.12E-03
Test II Cell 7 Out 1	1	44.12	250	6.21	7.76E+01	1.41E+03	5.11E-01	1.10E+02	1.64E-02	8.88E-01	4.31E-02		4.17E+01	5.40E+00	1.33E+03	3.08E-03
Test II Cell 7 Out 2	2	44.56	250	6.17	8.36E+01	1.45E+03		1.11E+02	1.35E-02	1.14E+00	2.61E-02		4.46E+01	6.01E+00	1.41E+03	3.09E-03
Test II Cell 7 Out 3	4	44.52	250	6.15	8.47E+01	1.44E+03		1.16E+02		8.83E-01	3.17E-02		4.89E+01	6.48E+00	1.52E+03	3.45E-03
Test II Cell 7 Out 4	8	44.52	250	5.95	7.25E+01	1.49E+03		1.20E+02	2.51E-02	8.31E-01	3.75E-02		4.80E+01	6.37E+00	1.50E+03	3.09E-03
Test II Cell 7 Out 5	16	44.62	250	6.16	8.60E+01	1.49E+03		1.18E+02		8.31E-01	4.10E-02		4.77E+01	6.58E+00	1.48E+03	2.50E-03
Test II Cell 7 Out 6	32	45.07	250	6.16	9.09E+01	1.50E+03		1.24E+02		9.10E-01	3.68E-02		4.84E+01	6.68E+00	1.46E+03	2.74E-03
Test II Cell 7 Out 7	73	45.25	250	6.15	9.30E+01	1.55E+03	1.65E-01	1.26E+02		1.09E+00	3.27E-02		4.87E+01	6.83E+00	1.47E+03	2.50E-03
Test II Cell 8 Out 1	1	53.83	250	6.06	1.83E+02	1.49E+03		1.11E+02	6.20E-03	8.61E-01	5.24E-02		4.64E+01	6.05E+00	1.47E+03	2.62E-03
Test II Cell 8 Out 2	2	53.38	250	6.08	1.77E+02	1.48E+03	2.75E-01	1.13E+02		8.08E-01	4.15E-02		4.45E+01	5.88E+00	1.40E+03	1.79E-03
Test II Cell 8 Out 3	4	53.69	250	6.05	1.83E+02	1.49E+03		1.15E+02		9.13E-01	7.55E-02		4.72E+01	6.09E+00	1.51E+03	2.75E-03
Test II Cell 8 Out 4	8	53.33	250	6.03	1.77E+02	1.50E+03		1.16E+02		7.31E-01	6.98E-02		4.81E+01	6.16E+00	1.53E+03	2.75E-03
Test II Cell 8 Out 5	16	53.18	250	6.07	1.77E+02	1.50E+03		1.16E+02		8.08E-01	4.17E-02		5.02E+01	6.19E+00	1.47E+03	2.27E-03
Test II Cell 8 Out 6	32	53.31	250	6.06	1.80E+02	1.52E+03		1.18E+02		8.35E-01	5.36E-02		5.24E+01	6.59E+00	1.49E+03	2.51E-03
Test II Cell 8 Out 7	73	52.71	250	6.05	1.71E+02	1.51E+03	2.20E-01	1.17E+02		9.13E-01	5.71E-02		5.30E+01	6.68E+00	1.48E+03	2.74E-03
SIB Test III			22	7.00	2.62E+00	2.91E+03		6.55E-01		3.34E+02		4.94E+01	8.97E+00		2.03E+03	3.99E-02
Test III Cell 1 Out 1	1	65.3	200	3.19	2.77E+02	3.16E+03				3.49E+02	7.05E-01	5.14E+01	9.62E+00		2.13E+03	4.09E-02
Test III Cell 1 Out 2	2	64	200	3.67	3.06E+02	3.15E+03				2.69E+02	7.40E-01	3.96E+01	7.31E+00	9.82E-02	1.66E+03	2.70E-02
Test III Cell 1 Out 3	4	62.6	200	3.50	2.72E+02	3.10E+03				3.21E+02	1.34E+00	4.77E+01	8.83E+00		1.97E+03	4.06E-02
Test III Cell 1 Out 4	8	61.6	200	3.63	2.58E+02	3.09E+03				3.42E+02	2.26E+00	5.08E+01	9.37E+00		2.11E+03	4.07E-02
Test III Cell 1 Out 5	16	60.4	200	3.62	2.53E+02	3.21E+03	1.57E+00			3.41E+02	3.93E+00	5.13E+01	9.15E+00		2.10E+03	4.08E-02

Test III Cell 1 Out 6	32	58.7	200	3.58	2.38E+02	3.25E+03	2.33E+00				3.53E+02	8.12E+00	5.69E+01	9.73E+00	1.59E-01	2.18E+03	4.10E-02
Test III Cell 1 Out 7	80	56.9	200	3.91	2.34E+02	3.27E+03					3.44E+02	1.55E+01	5.38E+01	9.66E+00	2.79E-01	2.13E+03	4.09E-02
Test III Cell 2 Out 1	1	20.4	140	4.14	9.21E+01	3.12E+03					3.48E+02	9.51E-01	5.18E+01	9.63E+00	6.88E-01	2.11E+03	5.39E-02
Test III Cell 2 Out 2	2	19.8	140	4.28	9.00E+01	3.10E+03					3.44E+02	9.08E-01	5.07E+01	9.44E+00	8.44E-01	2.09E+03	5.38E-02
Test III Cell 2 Out 3	4	19.3	140	4.34	8.83E+01	3.06E+03					3.40E+02	1.05E+00	5.06E+01	8.94E+00	1.10E+00	2.07E+03	5.37E-02
Test III Cell 2 Out 4	8	18.8	140	4.38	8.51E+01	3.08E+03					3.47E+02	1.18E+00	5.15E+01	9.40E+00	1.41E+00	2.10E+03	5.38E-02
Test III Cell 2 Out 5	16	18.4	140	4.14	8.41E+01	2.83E+03					3.26E+02	1.31E+00	4.79E+01	8.34E+00	1.43E+00	1.92E+03	5.32E-02
Test III Cell 2 Out 6	32	18	140	4.05	8.00E+01	2.98E+03					3.31E+02	1.87E+00	5.46E+01	9.36E+00	1.68E+00	2.04E+03	5.35E-02
Test III Cell 2 Out 7	80	17.6	140	3.97	7.62E+01	3.60E+03					3.80E+02	3.14E+00	5.26E+01	9.48E+00	2.06E+00	2.19E+03	5.48E-02
Test III Cell 3 Out 1	1	18	200	4.44	2.24E+01	3.01E+03					3.25E+02	3.35E-01	4.74E+01	9.02E+00	3.40E+00	1.98E+03	5.33E-02
Test III Cell 3 Out 2	2	18	200	4.20	2.20E+01	2.68E+03					3.07E+02	2.68E-01	4.35E+01	8.55E+00	3.61E+00	1.87E+03	5.26E-02
Test III Cell 3 Out 3	4	18	200	4.44	2.23E+01	2.95E+03					3.41E+02	5.03E-01	4.88E+01	9.24E+00	4.28E+00	2.09E+03	5.34E-02
Test III Cell 3 Out 4	8	17.9	200	4.17	2.12E+01	2.75E+03					3.36E+02	6.86E-01	4.74E+01	9.29E+00	4.25E+00	2.05E+03	5.30E-02
Test III Cell 3 Out 5	16	17.9	200	4.44	2.16E+01	2.71E+03					3.28E+02	1.10E+00	4.68E+01	8.88E+00	4.10E+00	1.98E+03	5.29E-02
Test III Cell 3 Out 6	32	17.7	200	4.05	2.01E+01	2.89E+03					3.37E+02	2.24E+00	5.13E+01	9.10E+00	4.21E+00	2.07E+03	5.33E-02
Test III Cell 3 Out 7	80	17.4	200	4.56	1.92E+01	3.11E+03					3.92E+02	4.66E+00	4.89E+01	9.83E+00	4.53E+00	2.14E+03	6.73E-02
Test III Cell 4 Out 1	1	88.5	250	3.81	3.40E+02	3.43E+03					3.39E+02	2.48E+00	4.81E+01	9.25E+00	8.13E+00	2.06E+03	5.50E-02
Test III Cell 4 Out 2	2	87.9	250	3.53	3.26E+02	3.33E+03					3.56E+02	3.43E+00	4.91E+01	9.58E+00	8.58E+00	2.16E+03	6.87E-02
Test III Cell 4 Out 3	4	85.7	250	3.68	3.08E+02	3.21E+03					3.62E+02	4.97E+00	4.86E+01	9.89E+00	8.91E+00	2.21E+03	6.85E-02
Test III Cell 4 Out 4	8	84.9	250	3.61	3.03E+02	2.99E+03					3.54E+02	7.31E+00	4.59E+01	9.93E+00	8.74E+00	2.16E+03	6.79E-02
Test III Cell 4 Out 5	16	83.5	250	3.57	3.05E+02	2.95E+03					3.25E+02	1.08E+01	3.86E+01	8.91E+00	7.98E+00	1.99E+03	6.76E-02

Test III Cell 4 Out 6	32	84.6	250	3.64	3.04E+02	2.44E+03				3.30E+02	1.97E+01	3.66E+01	9.31E+00	8.20E+00	2.00E+03	7.99E-02
Test III Cell 4 Out 7	80	84.2	250	3.79	3.05E+02	3.35E+03				3.57E+02	3.56E+01	2.64E+01	1.22E+01	9.63E+00	2.16E+03	9.63E-02
Test III Cell 5 Out 1	1	39.2	250	4.33	1.77E+01	3.08E+03				3.35E+02	2.23E+00	4.56E+01	9.24E+00	6.73E+00	2.04E+03	5.35E-02
Test III Cell 5 Out 2	2	39.2	250	4.51	1.54E+01	2.65E+03				2.84E+02	2.92E+00	3.87E+01	7.63E+00	5.88E+00	1.73E+03	5.24E-02
Test III Cell 5 Out 3	4	39.6	250	4.39	2.02E+01	3.36E+03				3.38E+02	5.46E+00	4.36E+01	8.92E+00	6.69E+00	2.02E+03	6.75E-02
Test III Cell 5 Out 4	8	39.7	250	4.19	1.96E+01	2.45E+03				3.10E+02	8.15E+00	3.68E+01	8.47E+00	6.22E+00	1.89E+03	6.54E-02
Test III Cell 5 Out 5	16	39.9	250	4.37	2.02E+01	2.58E+03	1.45E+00			2.92E+02	1.23E+01	2.97E+01	7.86E+00	5.67E+00	1.76E+03	6.54E-02
Test III Cell 5 Out 6	32	40.2	250	4.49	2.26E+01	2.64E+03				3.06E+02	2.12E+01	2.72E+01	8.44E+00	5.99E+00	1.77E+03	7.88E-02
Test III Cell 5 Out 7	80	40.8	250	4.20	2.79E+01	3.06E+03				3.33E+02	3.65E+01	1.76E+01	1.10E+01	7.19E+00	2.01E+03	9.37E-02
Test III Cell 6 Out 1	1	52.6	250	3.92	1.03E+02	2.84E+03				3.28E+02	2.26E+00	4.58E+01	9.59E+00	7.45E+00	1.99E+03	5.33E-02
Test III Cell 6 Out 2	2	51.6	250	3.94	9.75E+01	3.20E+03				3.38E+02	3.19E+00	4.59E+01	8.82E+00	7.71E+00	2.02E+03	5.39E-02
Test III Cell 6 Out 3	4	51.3	250	3.90	9.43E+01	2.91E+03				3.38E+02	5.06E+00	4.42E+01	9.17E+00	7.62E+00	2.03E+03	6.69E-02
Test III Cell 6 Out 4	8	51.5	250	3.91	9.59E+01	3.32E+03				3.45E+02	8.43E+00	4.25E+01	9.40E+00	7.88E+00	2.15E+03	6.79E-02
Test III Cell 6 Out 5	16	51.2	250	3.77	9.37E+01	3.07E+03				3.37E+02	1.33E+01	3.74E+01	9.32E+00	7.59E+00	2.09E+03	6.73E-02
Test III Cell 6 Out 6	32	51	250	3.94	9.19E+01	3.10E+03				3.85E+02	2.19E+01	3.60E+01	1.03E+01	8.74E+00	2.09E+03	9.44E-02
Test III Cell 6 Out 7	80	50.9	250	3.97	9.36E+01	3.34E+03				3.62E+02	3.41E+01	2.26E+01	1.10E+01	8.15E+00	2.03E+03	9.50E-02
Test III Cell 7 Out 1	1	70.8	200	3.68	3.23E+02	2.77E+03				3.45E+02	1.68E+00	4.52E+01	8.53E+00	3.24E+00	1.78E+03	5.36E-02
Test III Cell 7 Out 2	2	70.6	200	3.65	3.08E+02	3.10E+03				3.41E+02	1.56E+00	4.94E+01	9.54E+00	3.93E+00	2.07E+03	5.44E-02
Test III Cell 7 Out 3	4	67.6	200	3.52	2.90E+02	2.99E+03				3.37E+02	1.85E+00	5.01E+01	9.29E+00	4.27E+00	2.08E+03	5.42E-02
Test III Cell 7 Out 4	8	68	200	3.43	2.94E+02	3.05E+03				3.34E+02	2.26E+00	4.93E+01	9.31E+00	4.47E+00	2.06E+03	5.43E-02
Test III Cell 7 Out 5	16	66.1	200	3.51	2.87E+02	3.02E+03				3.25E+02	2.99E+00	4.81E+01	9.07E+00	4.40E+00	2.02E+03	5.41E-02

Test III Cell 7 Out 6	32	64.3	200	3.61	2.75E+02	2.98E+03				3.33E+02	4.50E+00	4.87E+01	9.12E+00	4.48E+00	2.05E+03	5.41E-02
Test III Cell 7 Out 7	80	62.4	200	3.53	2.50E+02	3.08E+03				3.61E+02	9.60E+00	5.38E+01	1.00E+01	4.95E+00	2.29E+03	6.81E-02
Test III Cell 8 Out 1	1	29.6	200	4.15	8.67E+01	2.91E+03				3.28E+02	9.43E-01	4.88E+01	9.16E+00	3.27E+00	2.04E+03	5.34E-02
Test III Cell 8 Out 2	2	29.3	200	3.99	8.40E+01	3.04E+03				3.46E+02	8.43E-01	5.00E+01	9.27E+00	3.90E+00	2.07E+03	5.37E-02
Test III Cell 8 Out 3	4	28.9	200	4.28	8.21E+01	3.08E+03				3.51E+02	9.71E-01	5.06E+01	9.29E+00	4.22E+00	2.14E+03	5.38E-02
Test III Cell 8 Out 4	8	28.3	200	3.73	7.71E+01	3.13E+03				3.53E+02	1.35E+00	5.13E+01	9.46E+00	4.47E+00	2.17E+03	5.40E-02
Test III Cell 8 Out 5	16	27.7	200	3.98	7.32E+01	3.32E+03				3.71E+02	2.30E+00	5.87E+01	1.02E+01	4.76E+00	2.27E+03	5.44E-02
Test III Cell 8 Out 6	32	26.9	200	4.03	6.96E+01	3.29E+03				3.92E+02	4.13E+00	5.42E+01	9.85E+00	4.93E+00	2.17E+03	6.78E-02
Test III Cell 8 Out 7	80	26.3	200	4.29	6.77E+01	3.41E+03				4.13E+02	8.18E+00	5.42E+01	1.03E+01	5.32E+00	2.12E+03	6.81E-02

Appendix B

Experimental Characterization

Experimental equipment and characterization of experimental materials.
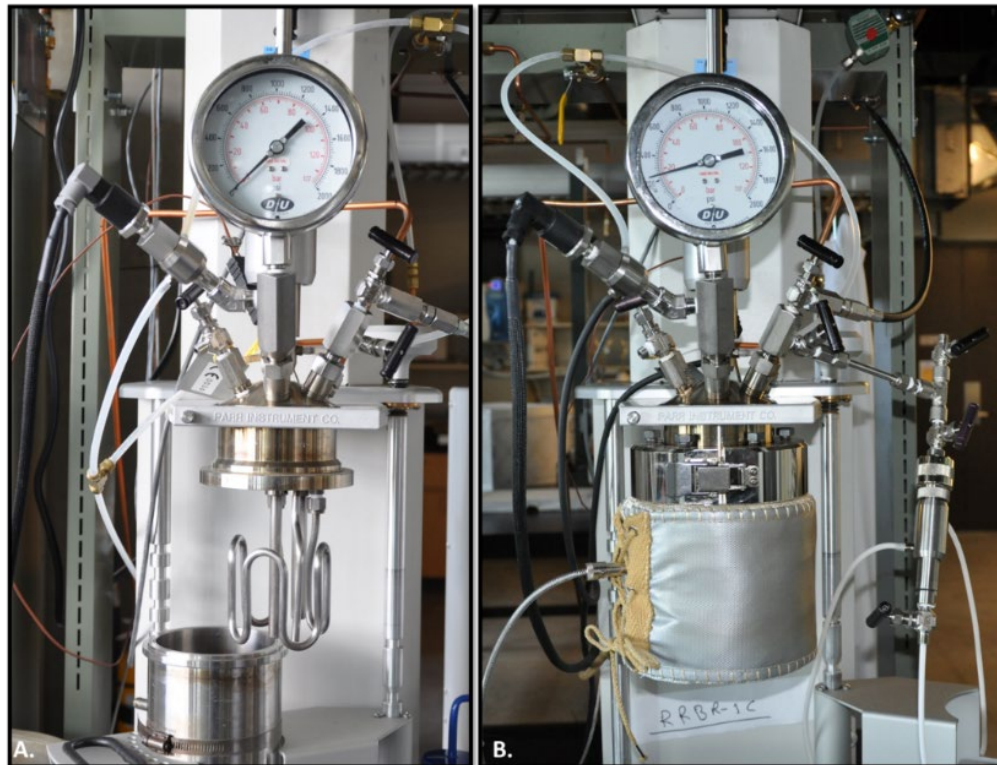
Figure B-1. (A.) Parr® reactor system ((Model 4523 Parr® Instrument) showing reaction vessel, cooling coil, pressure gauge, and thermistor, and (B.) Parr® system with attached sampling vessel (Model 4351-I-D-V-C Parr® Instrument) during actual testing condition.
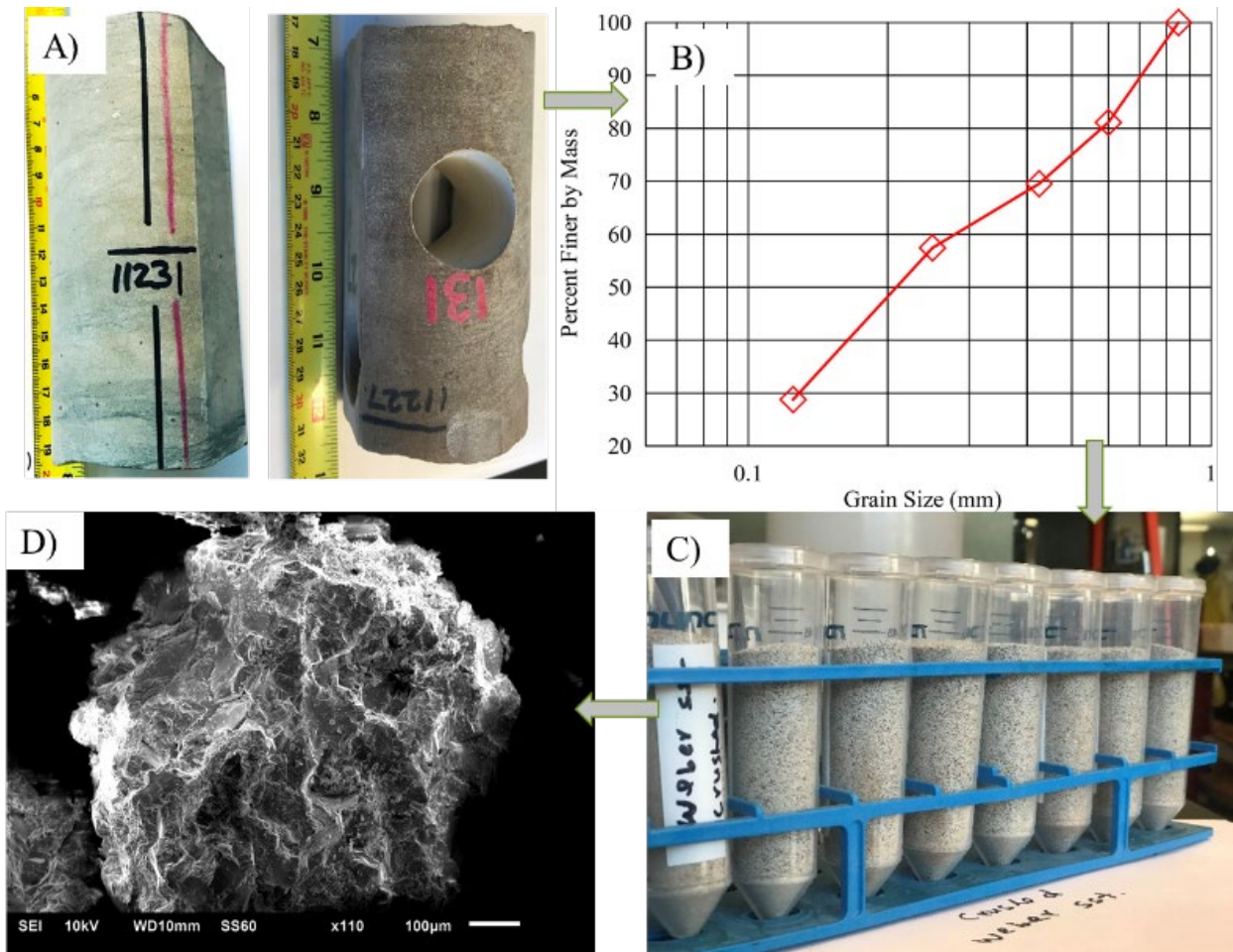
Figure B-2. A) Photograph of core-segments of the upper Weber Sandstone retrieved from RSU#1. B) Grain-size distribution plot for crushed and sieved Weber Sandstone core. C) Crushed, sieved, and washed sandstone with grain-size from 0.15 mm to 0.85 mm. D) Scanning electron microscope (SEM) image of a typical quartz grain in the crushed rock.
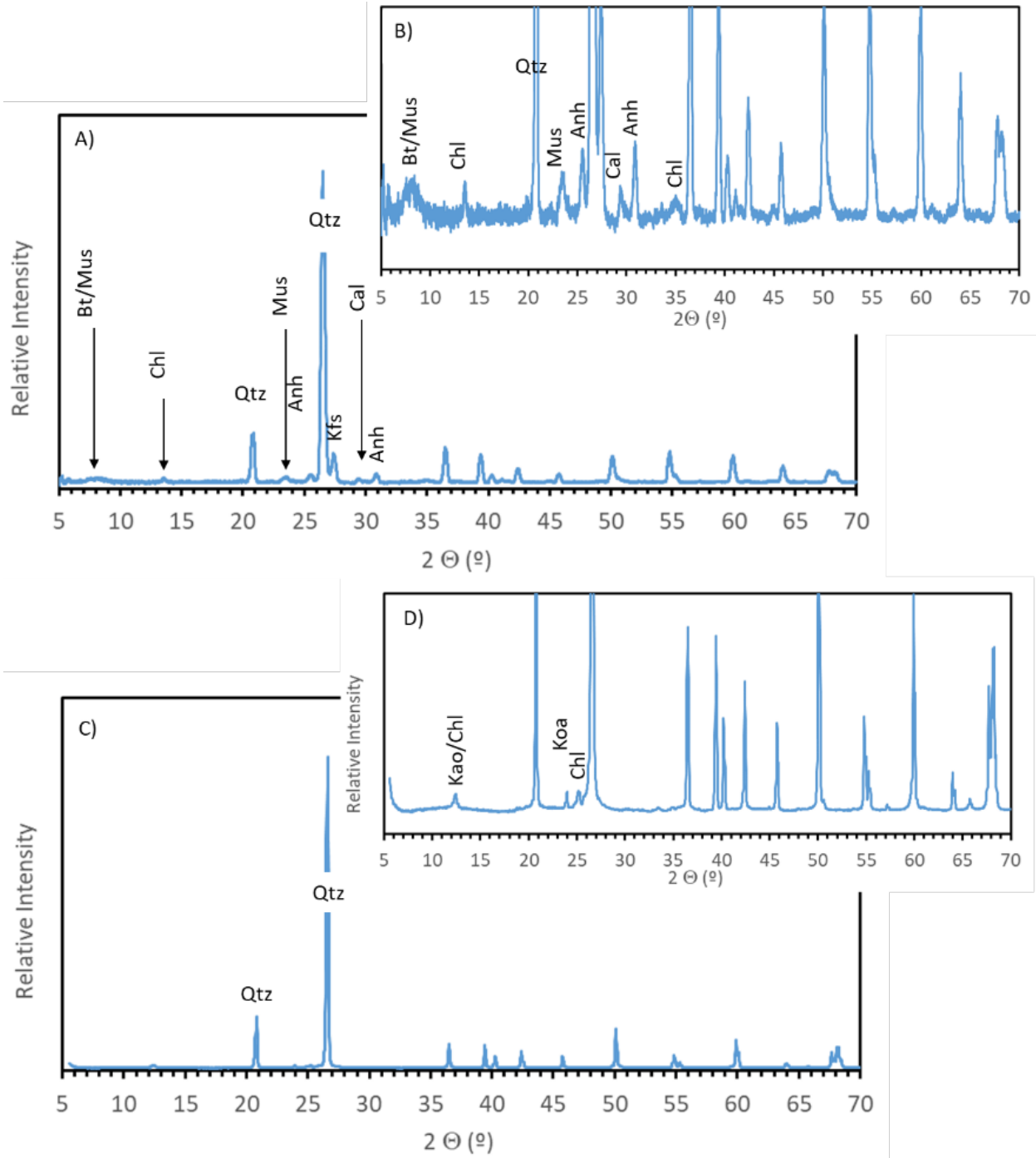
Figure B-3. X-ray diffraction patterns for the pre-experimental Weber Sandstone (A) and Lower Tuscaloosa Formation (C) rocks. The XRD spectra in B and D are enlarged portions of A and B, respectively, that reveal the diffraction peaks of small amounts of non-quartz minerals. Minerals are: Qtz = quartz, Kao = kaolinite, Chl = chlorite, Anh = anhydrite, Bt = biotite, Mus = muscovite, Kfs = K-feldspar, and Cal = calcite.
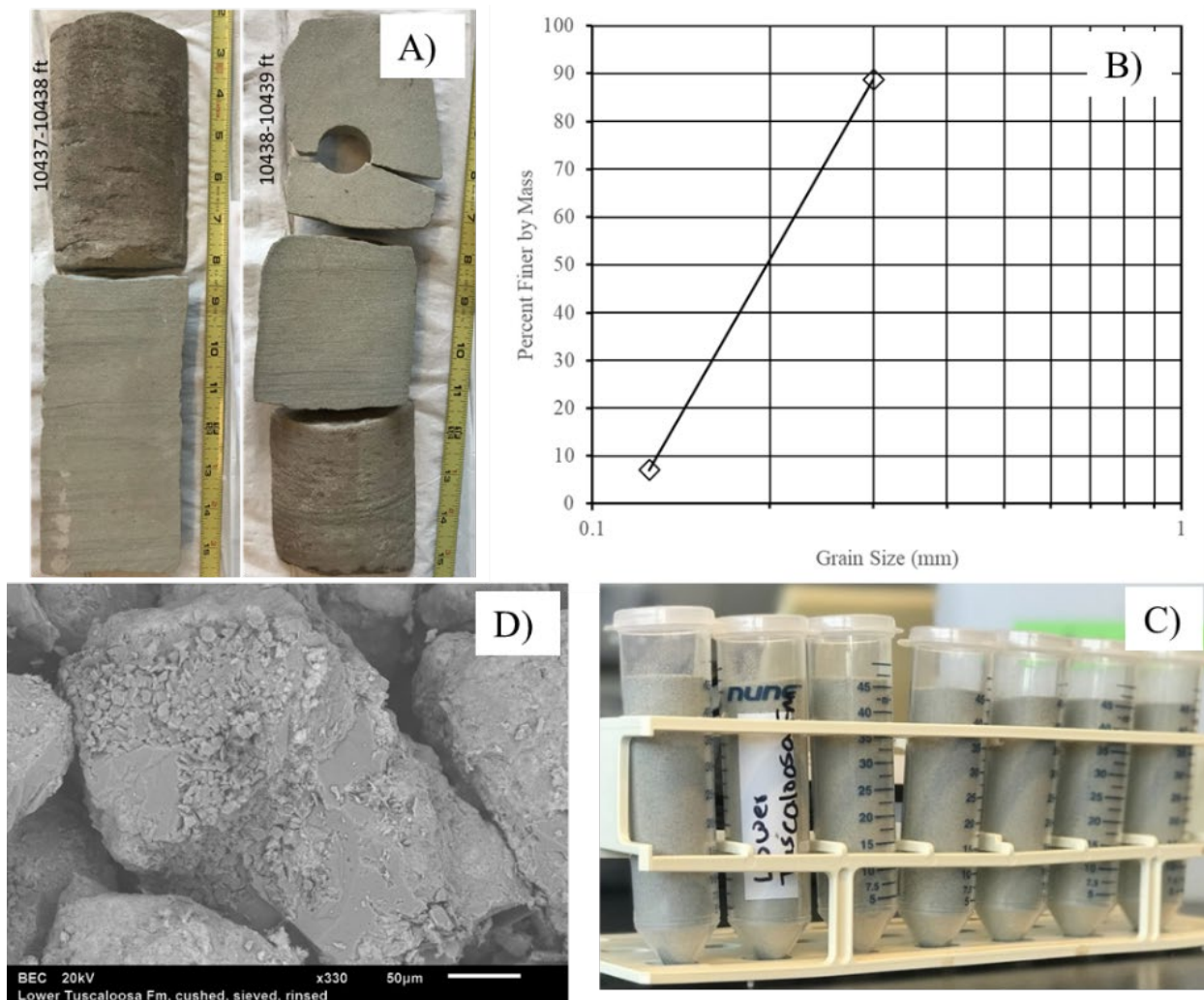
Figure B-4. A) Photograph of core-segments of the Lower Tuscaloosa Formation retrieved from Well CFU-31-F2. B) Grain-size distribution plot for crushed and sieved Lower Tuscaloosa Formation sandstone core. C) Crushed, sieved, and washed sandstone with grain-size from 0.125 mm to 0.300 mm. D) Scanning electron microscope (SEM) image of a typical clay-coated quartz grain in the crushed rock.
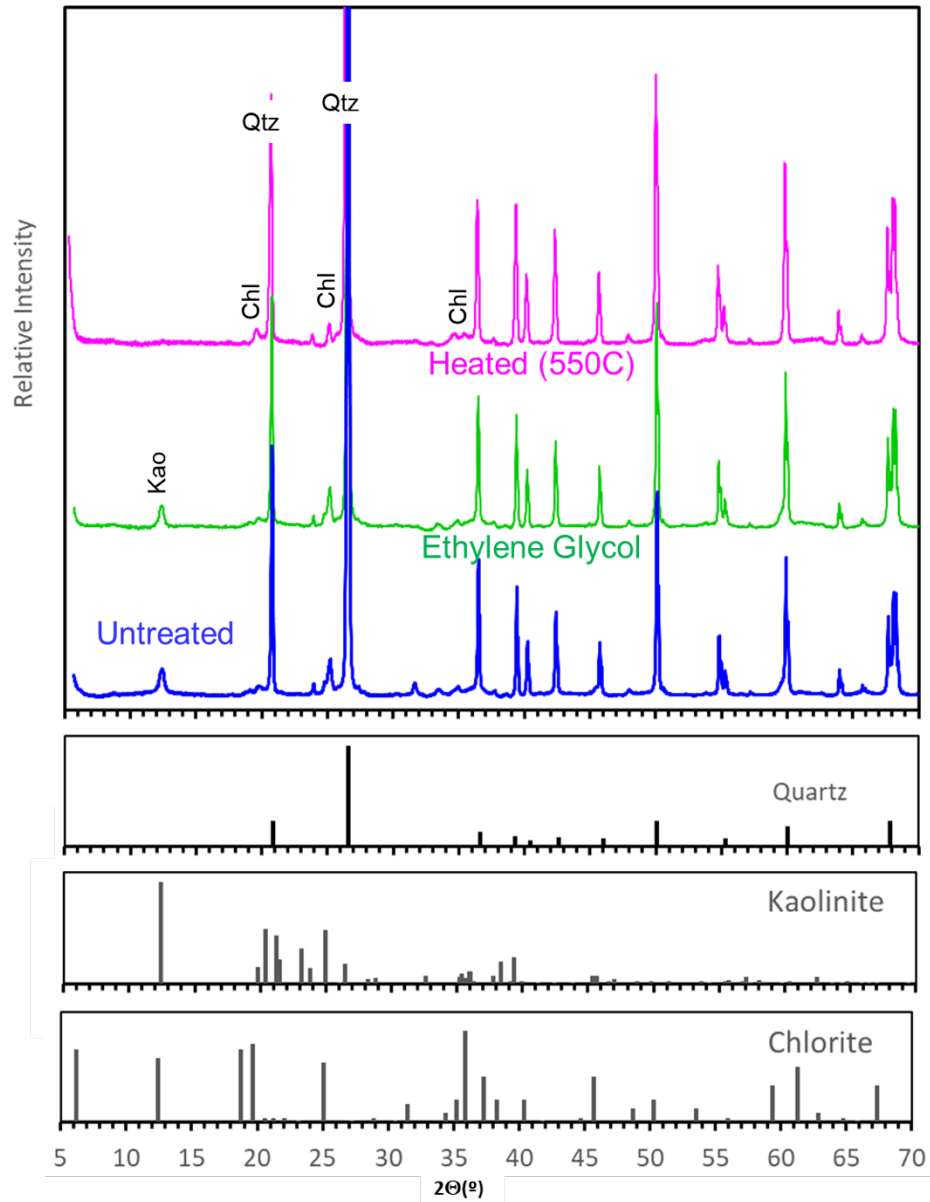
Figure B-5. XRD spectra of the pre-experimental Lower Tuscaloosa Formation rock. The spectra were collected using fine-fraction collected in pan after crushing and sieving. The fine in the pan was not used for brine-rock interaction experiment. However, these XRD spectra are used to identify the clay minerals that coat the quartz grains.
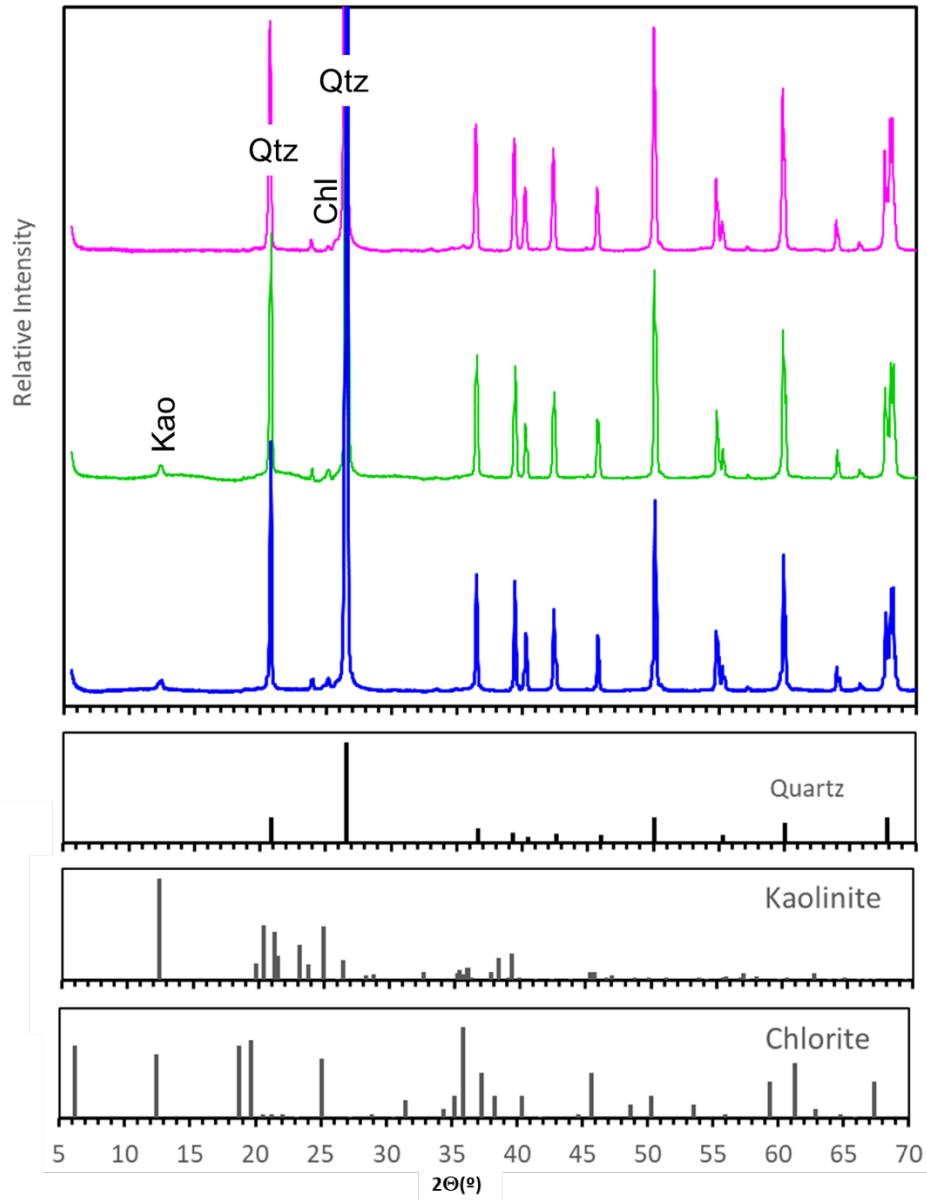
Figure B-6. XRD spectra of the pre-experimental Lower Tuscaloosa Formation rock.
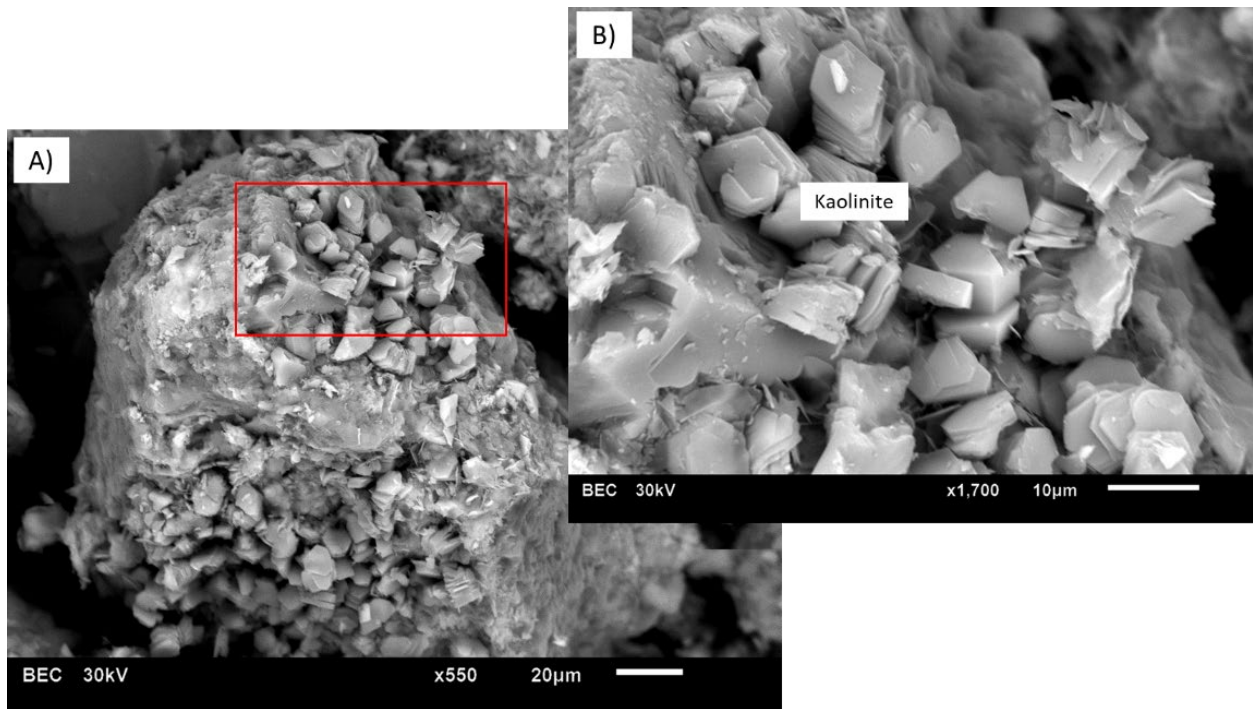
Figure B-7. Scanning electron microscopy images of the pre-experimental Lower Tuscaloosa Formation (crushed) rock. A) A rock grain (quartz) coated with clays. B) An enlarged part of a grain (red box in A) showing platy kaolinite.
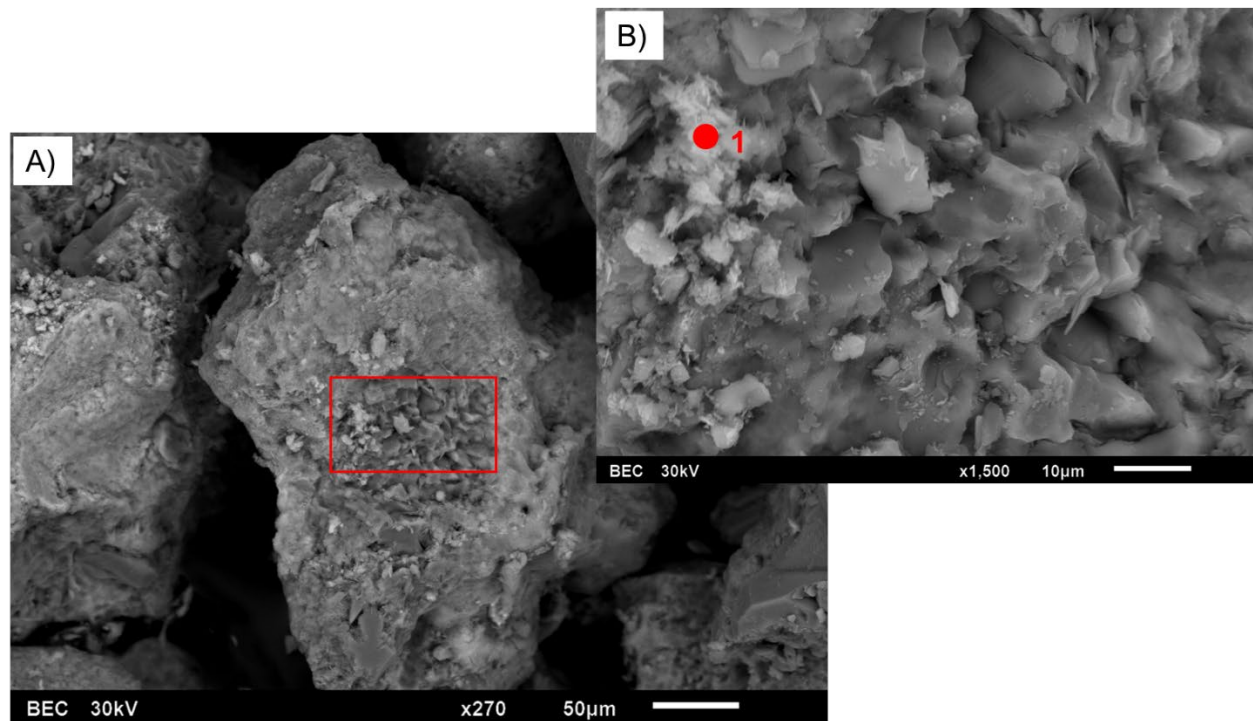
Figure B-8. Scanning electron microscopy images of the pre-experimental Lower Tuscaloosa Formation (crushed) rock. A) A rock grain (quartz) coated with clays. B) An enlarged part of a grain (red box in A) showing chlorite.
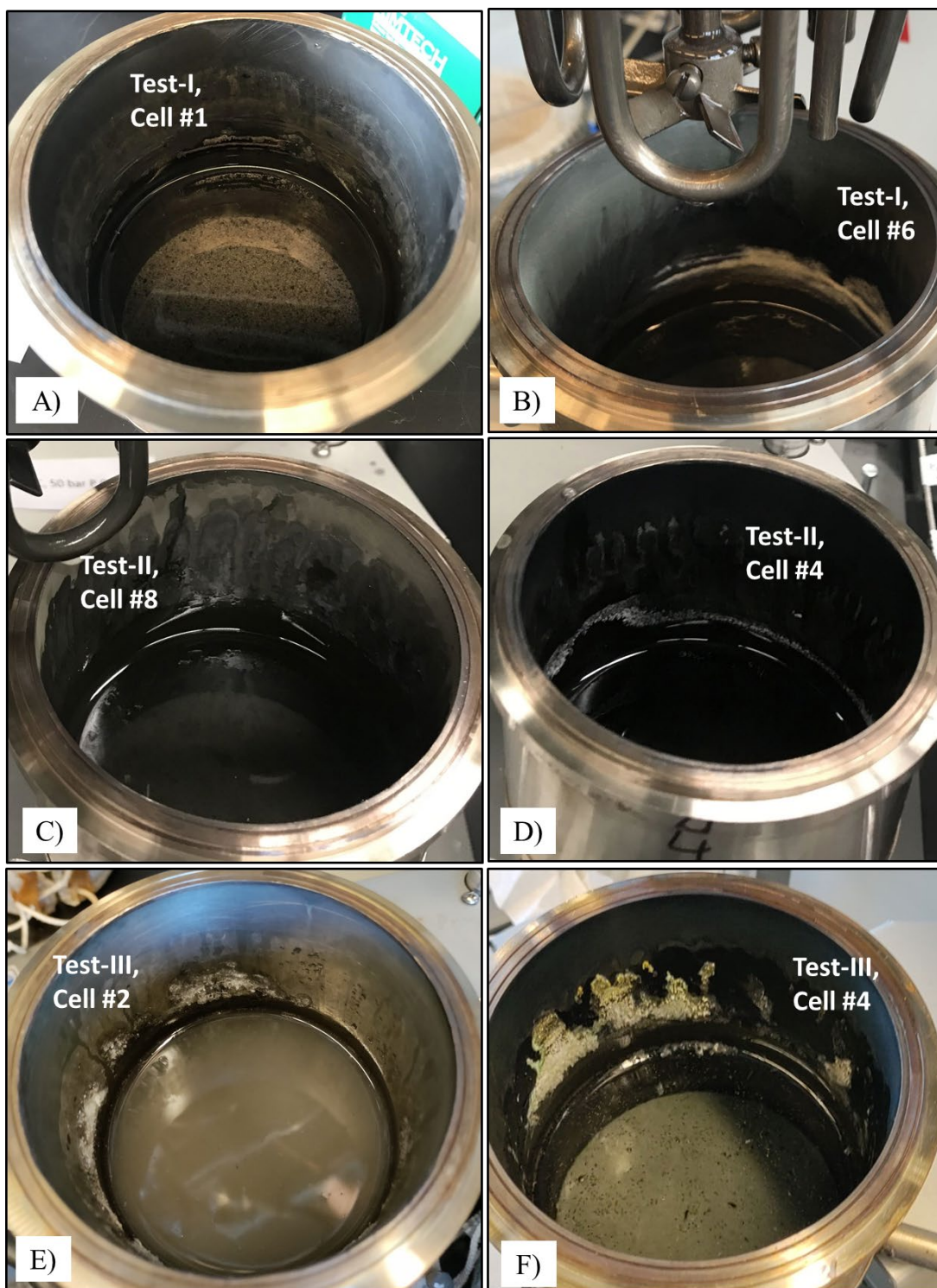
Figure B-9. Photographs of post-experimental reaction cells. The inside diameter of the reaction cell is 10 cm. (A) T = 160ºC, P_{CO2} = 1.7 bars, (B) T = 200ºC, P_{CO2} = 3.4 bars, (C) T = 250ºC, P_{CO2} = 15.9 bars, (D) T = 250ºC, P_{CO2} = 17.4 bars, no rock, (E) T = 140ºC, P_{CO2} = 15.3 bars, and (F) T = 250ºC, P_{CO2} = 42.6 bars. Test-I and Test-II were conducted with Weber Sandstone and Test-III were conducted with Lower Tuscaloosa Formation.
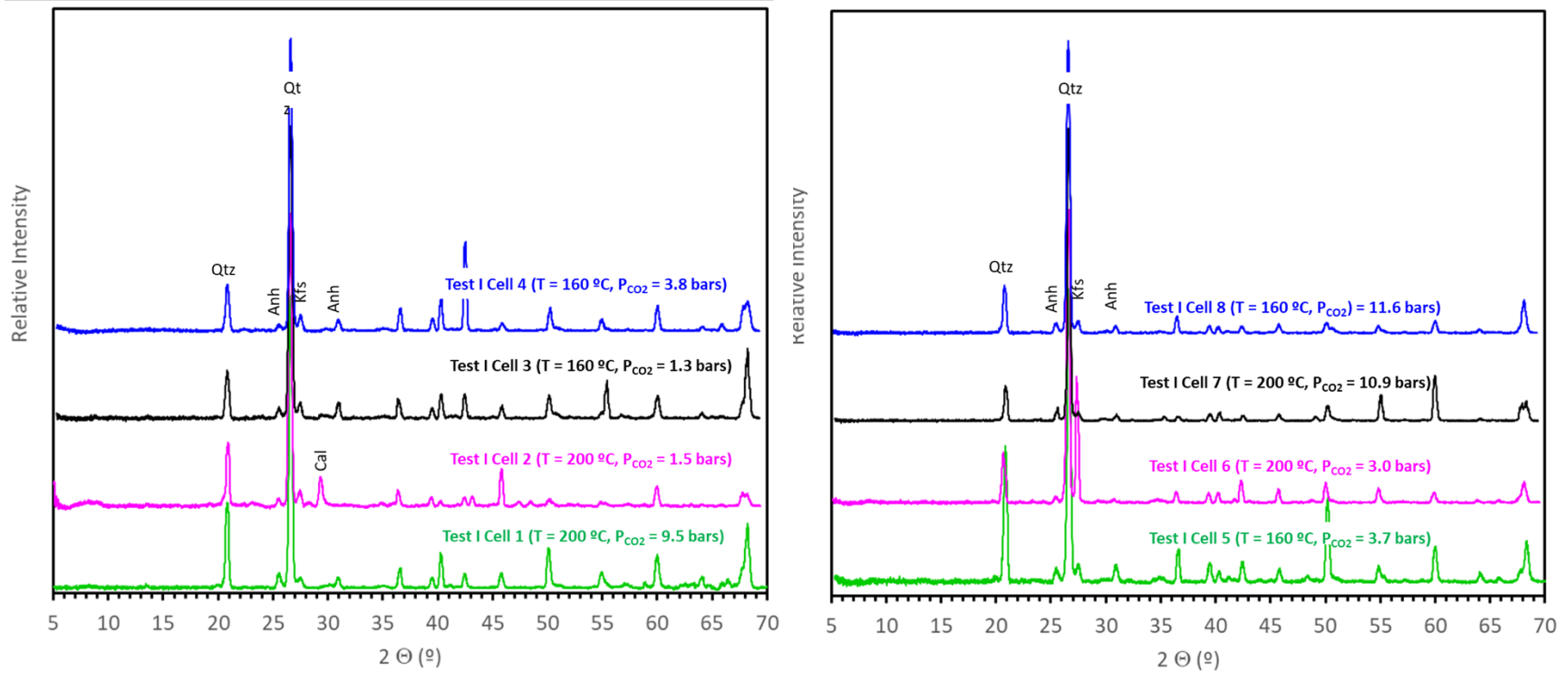
Figure B-10. XRD spectra of post-experimental (Test-I) bulk samples (Weber Sandstone).
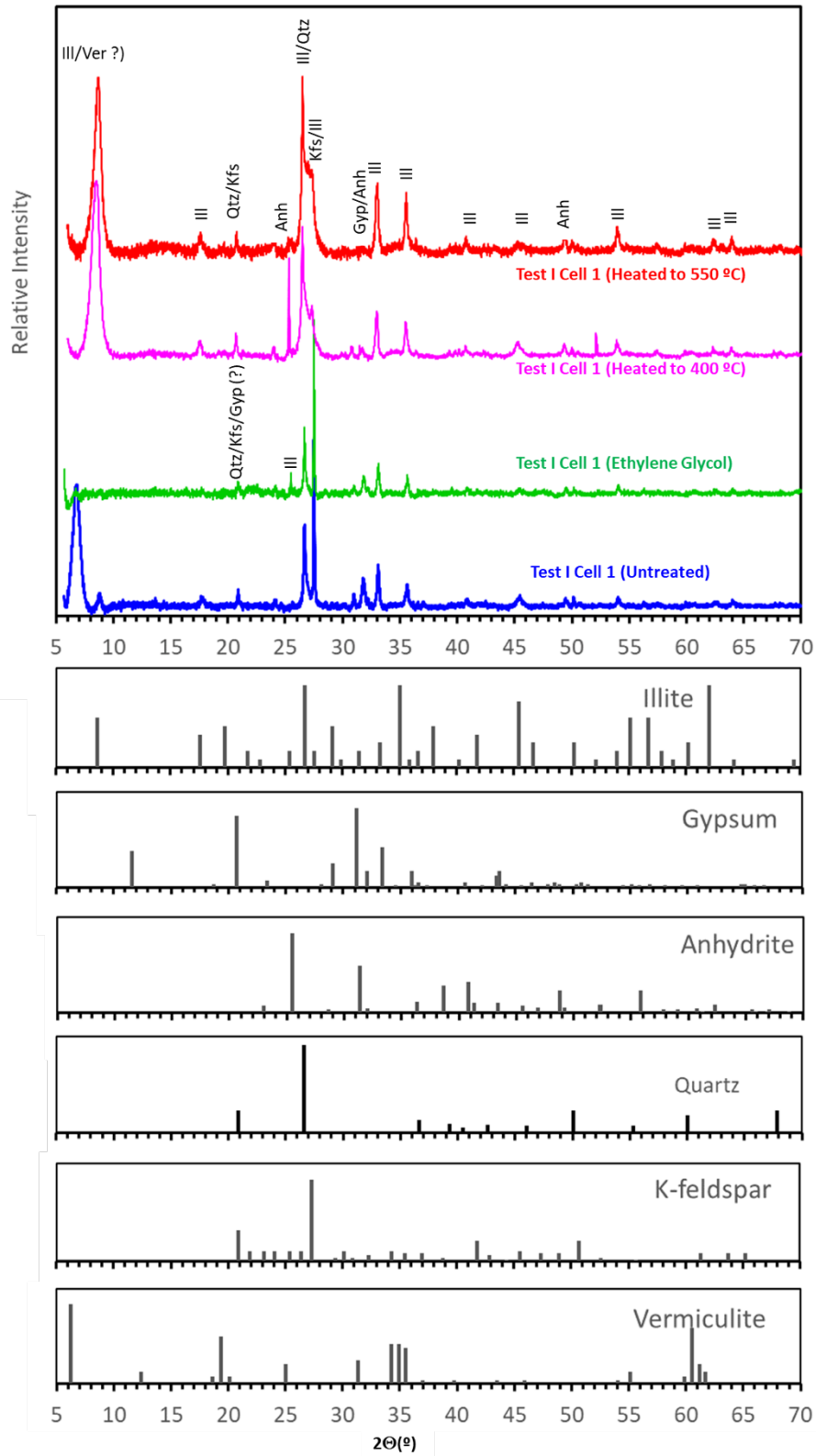
Figure B-11. XRD spectra of post-experimental Test-I Cell 1 (T = 200 °C, P_{CO2} = 9.5 bars) clay sample.
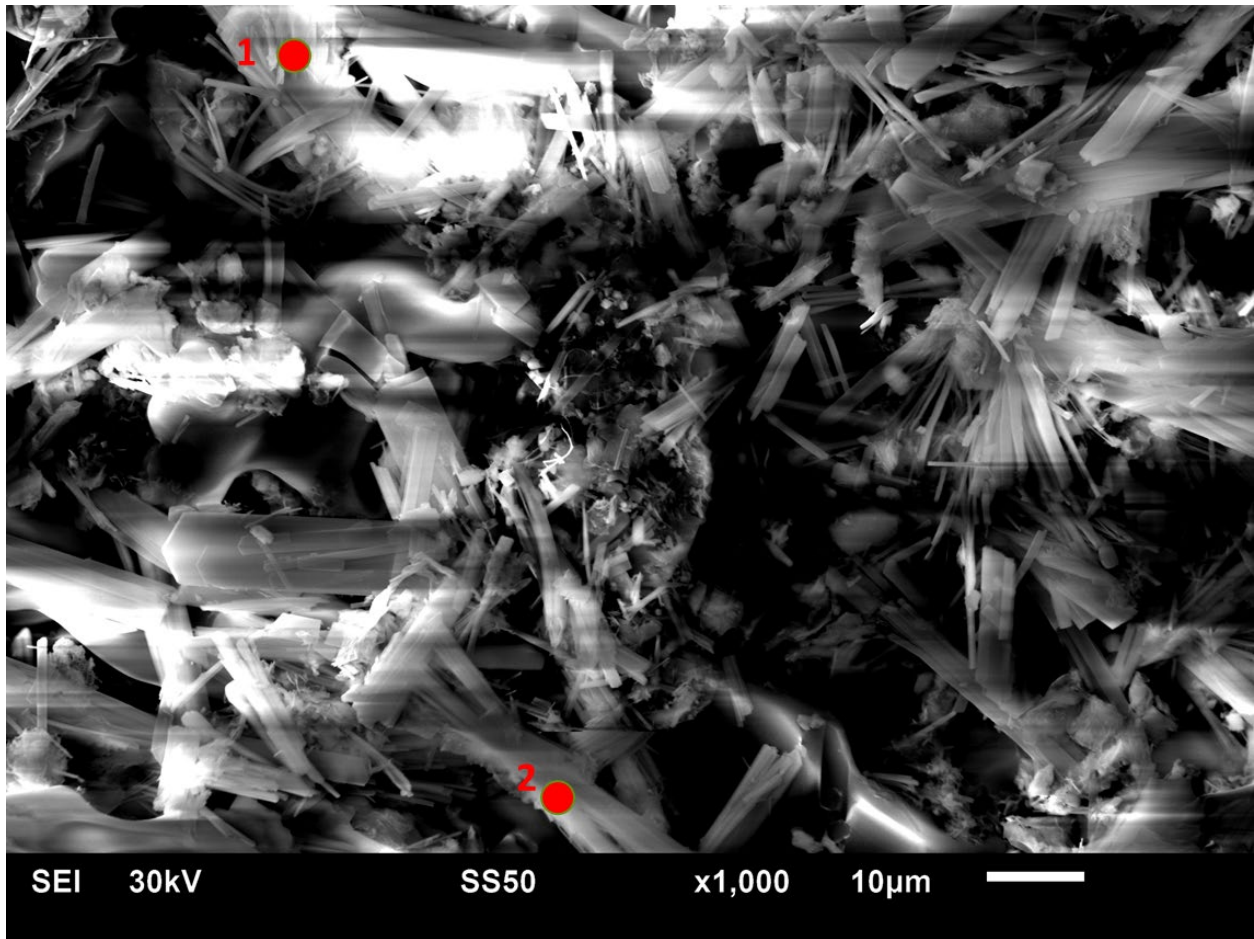
Figure B-12. SEM image of post-experimental Test-I Cell 1 (T = 200 ºC, P_{CO2} =9.5 bars) reacted rock sample. Points 1 and 2 shows anhydrite and Mg-Fe-clays (illite/vermiculite), respectively.
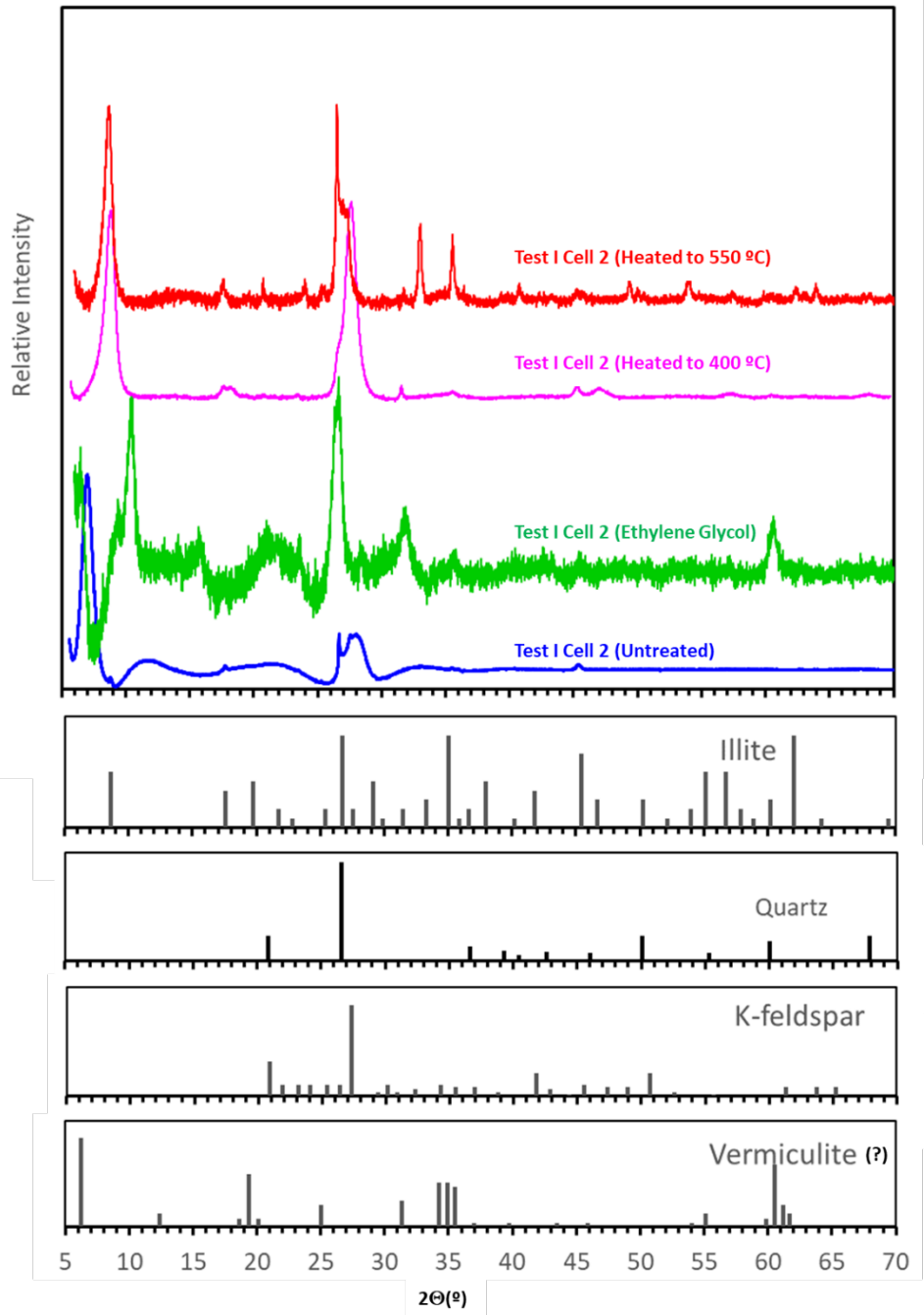
Figure B-13. XRD spectra of post-experimental Test-I Cell 2 (T = 200 ºC, P_{CO2} = 1.5 bars) clay sample.
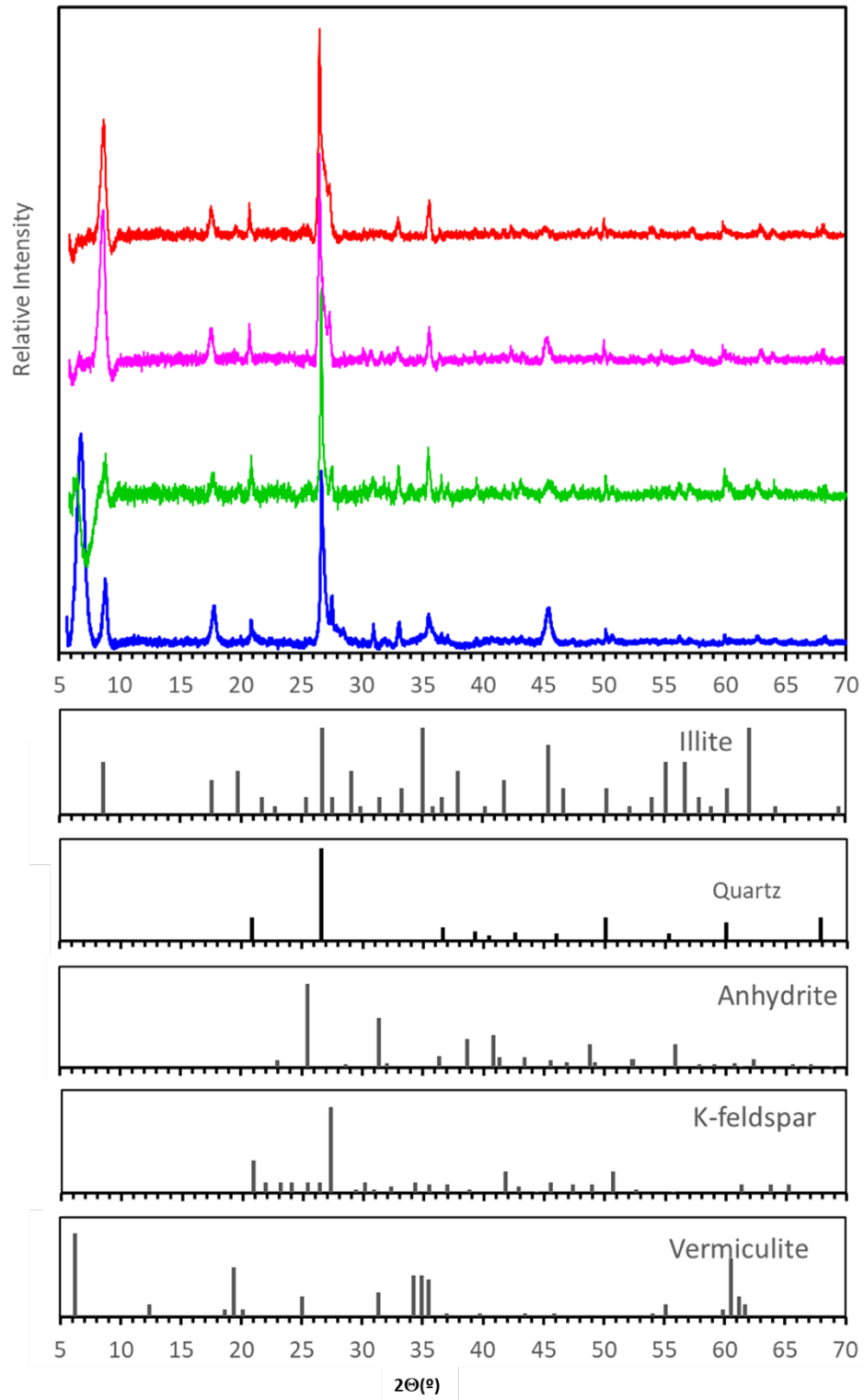
Figure B-14. XRD spectra of post-experimental Test-I Cell 3 (T = 160 ºC, P_{CO2} = 1.3 bars) clay sample.
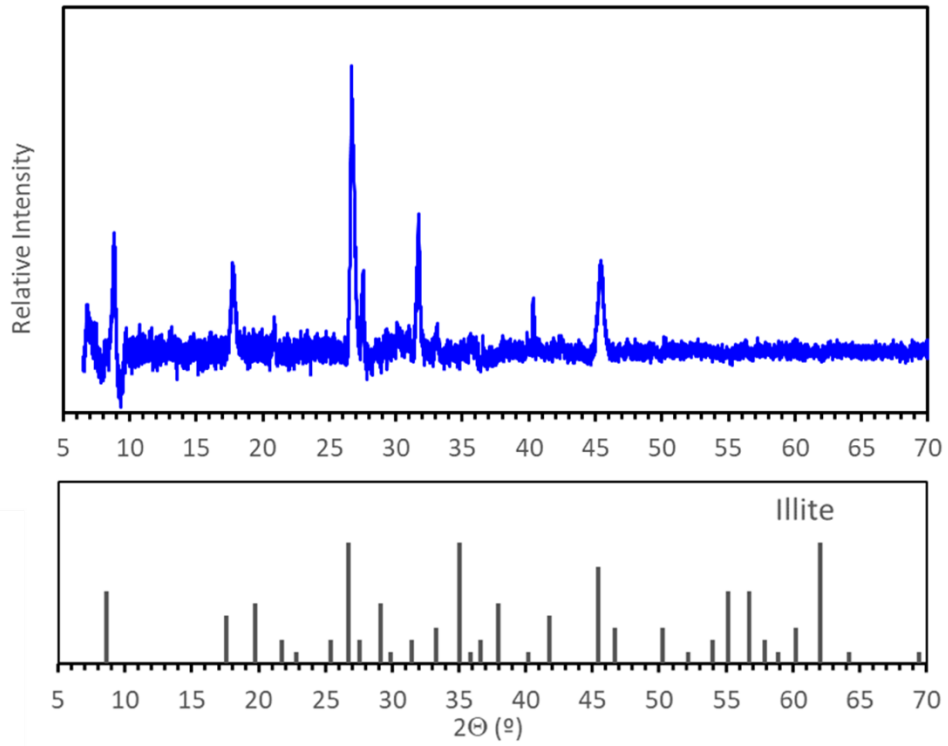
Figure B-15. XRD spectrum of post-experimental Test-I Cell 4 (T = 160 ºC, P_{CO2} = 3.8 bars) clay sample.
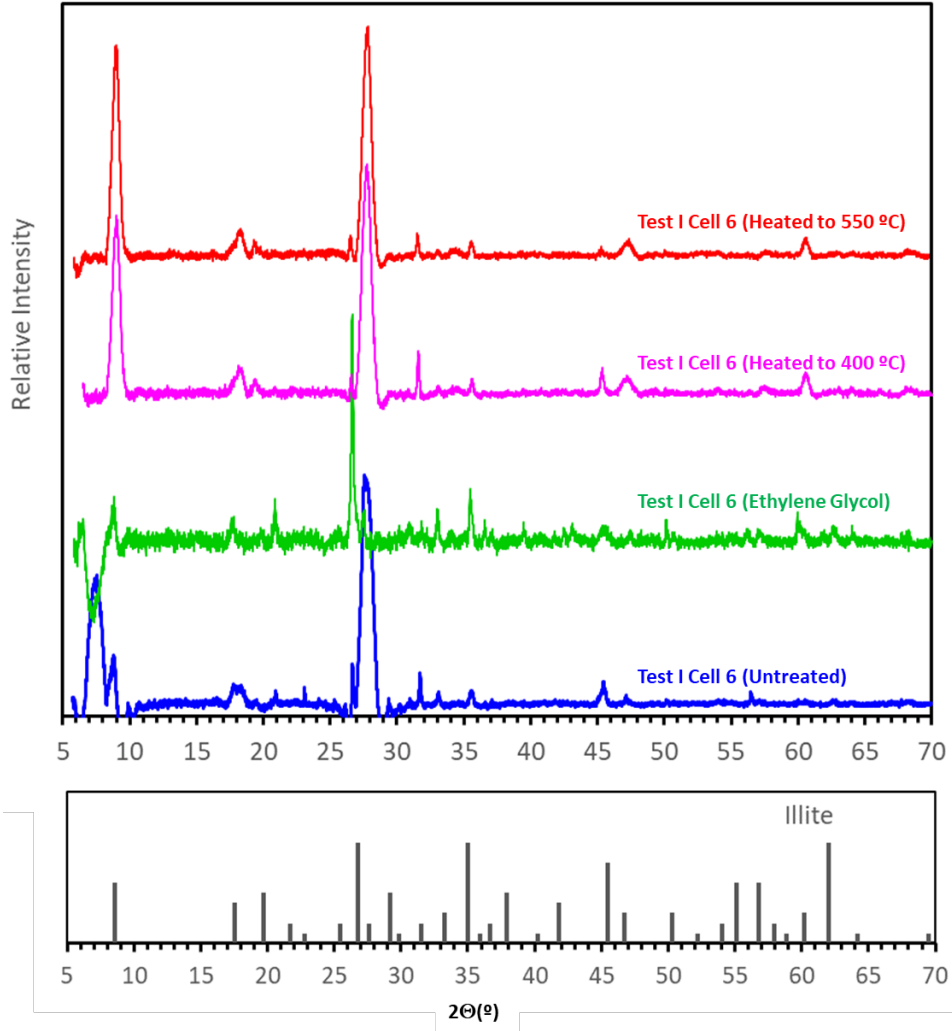
Figure B-16. XRD spectra of post-experimental Test-I Cell 6 (T = 200 ºC, P_{CO2} = 3.0 bars) clay sample.
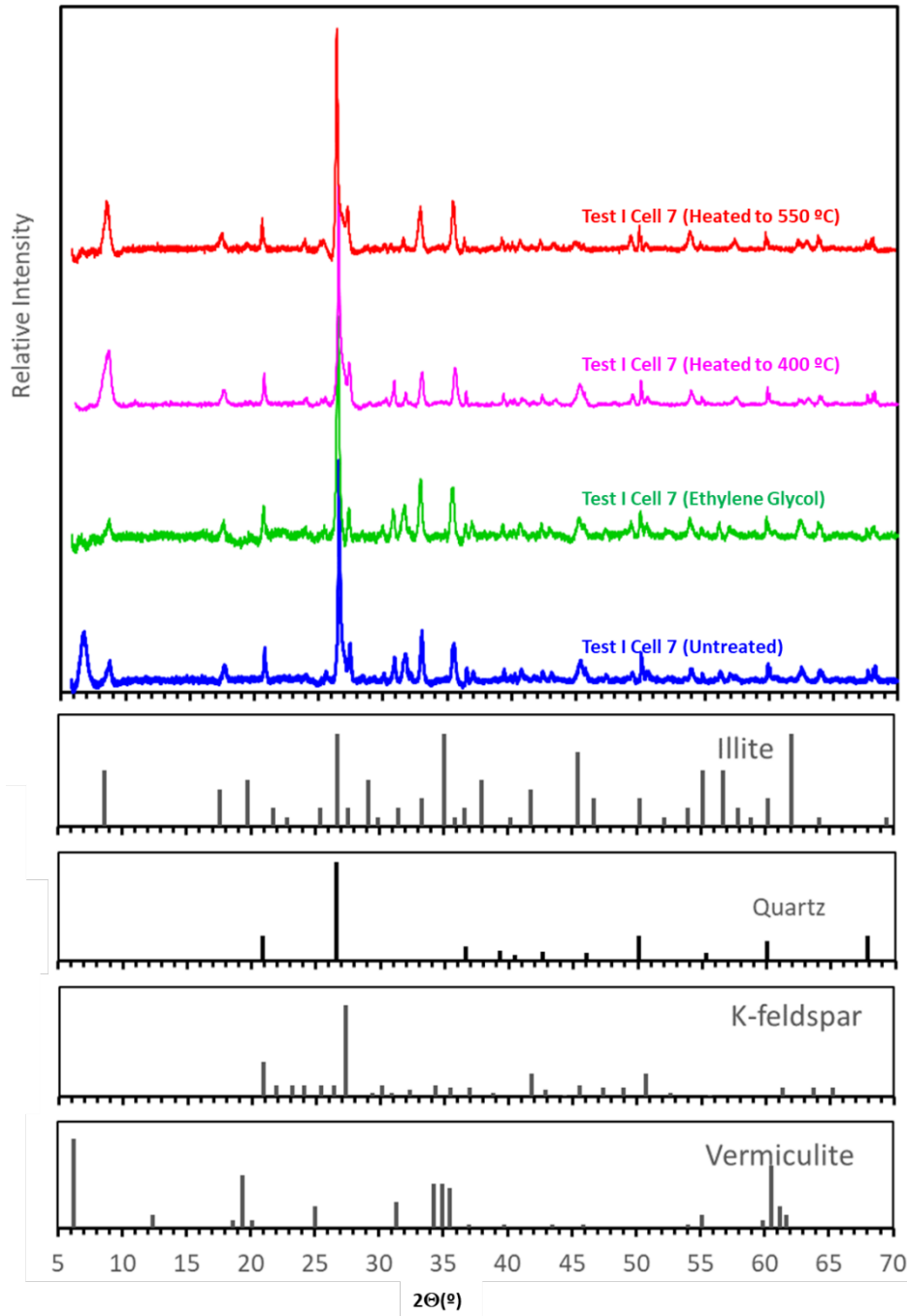
Figure B-17. XRD spectra of post-experimental Test-I Cell 7 (T = 200 ºC, P_{CO2} = 10.9 bars) clay sample.
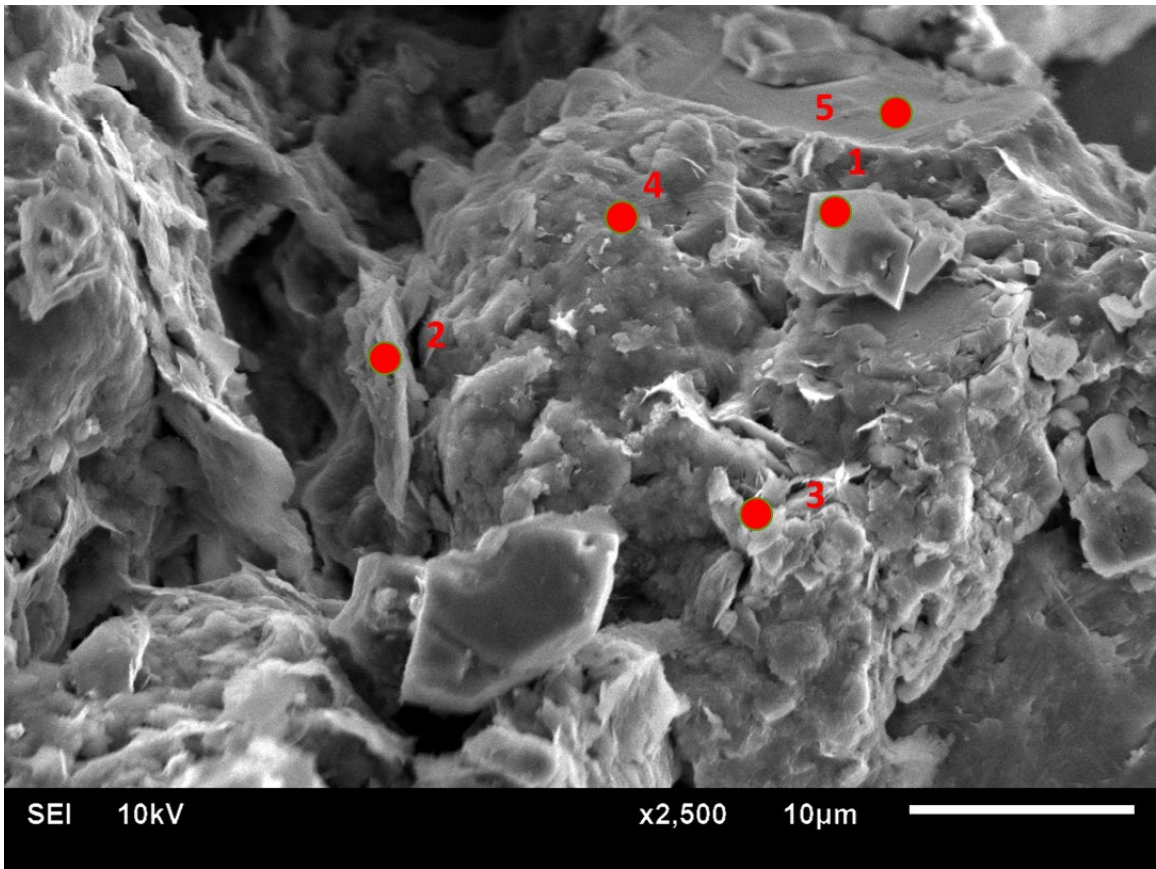
Figure B-18. SEM image of post-experimental Test-I Cell 7 (T = 200 ºC, P$_{CO2}$ =10.9 bars) reacted rock sample. Points are: 1. Fe-Ca carbonate (ankerite), 2 & 3. Fe-Mg clay (illite [glauconite?]), and 4 & 5. Quartz.
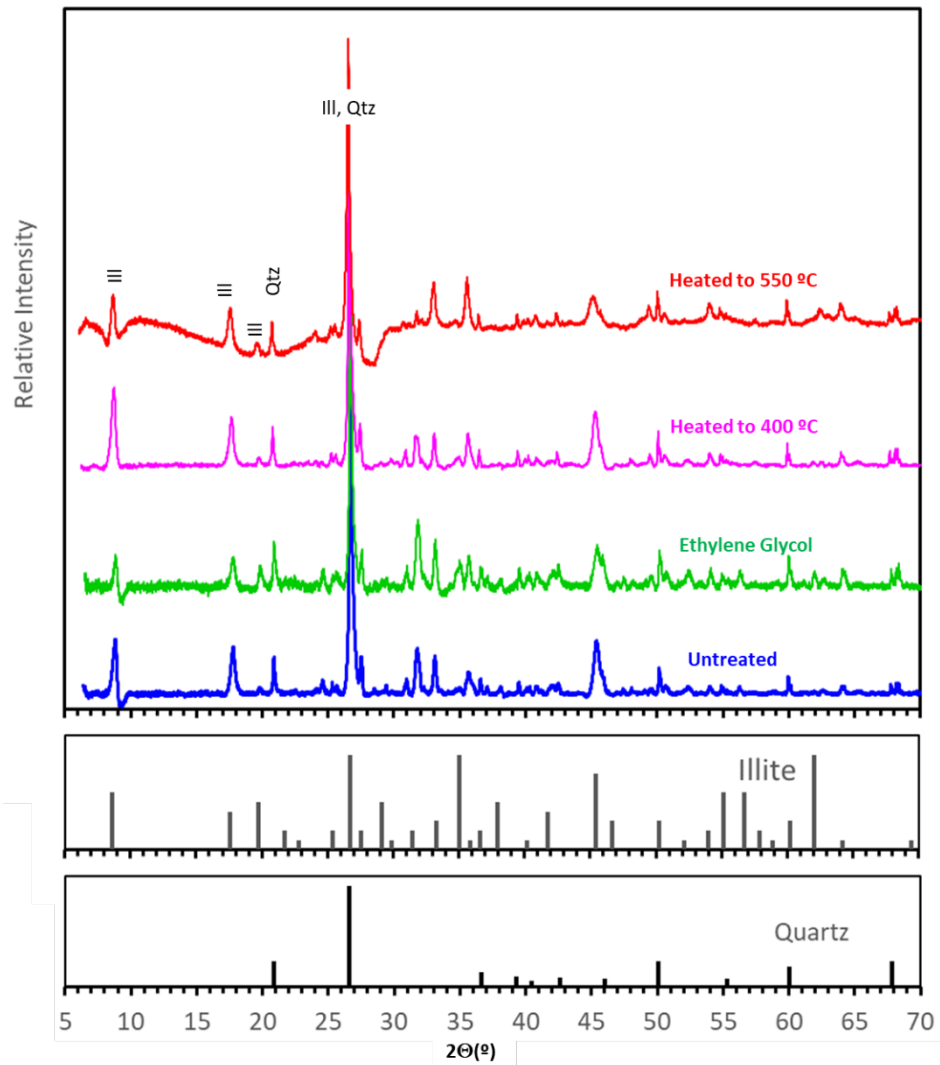
Figure B-19. XRD spectra of post-experimental Test-I Cell 8 (T = 160 ºC, P_{CO2} = 11.6 bars) clay sample.
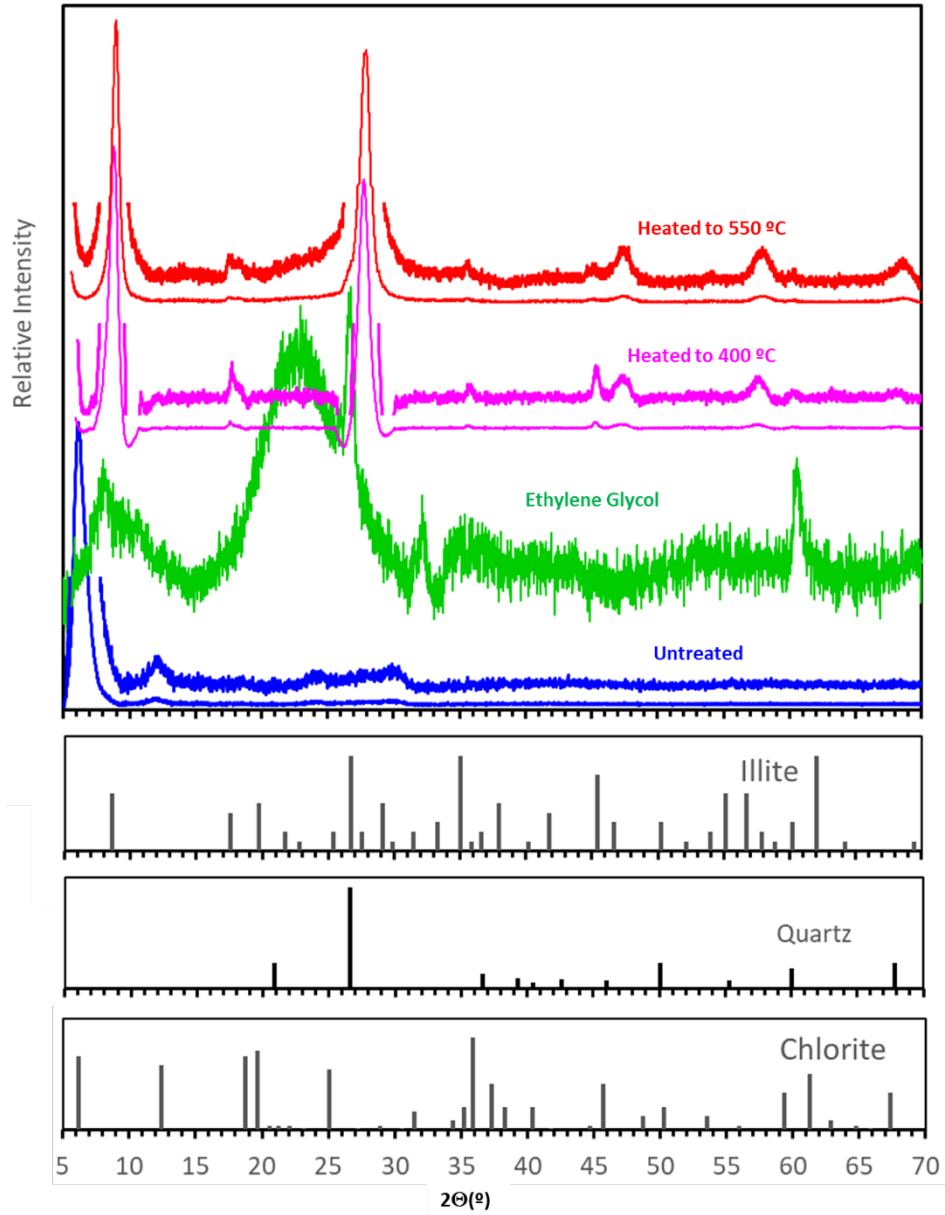
Figure B-20. XRD spectra of post-experimental Test-II Cell 2 (T = 250 ºC, P$_{CO2}$ = 14.7 bars) clay sample.
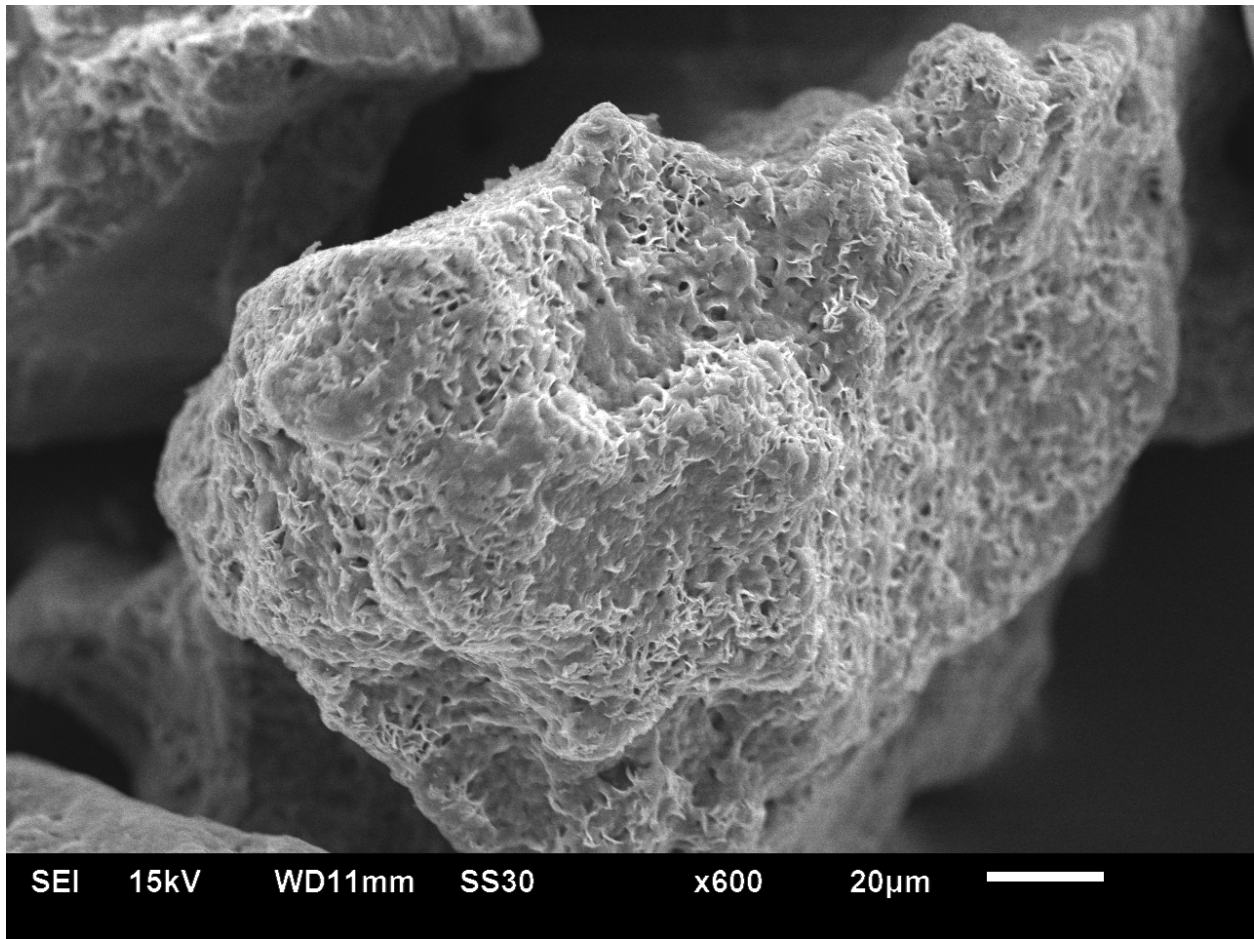
Figure B-21. SEM image of post-experimental Test-II Cell 2 (T = 250 ºC, P_{CO2} =14.7 bars) reacted rock sample. The quartz grain is coated with secondary Fe-Mg-Ca clays (illite (glauconite) and chlorite).
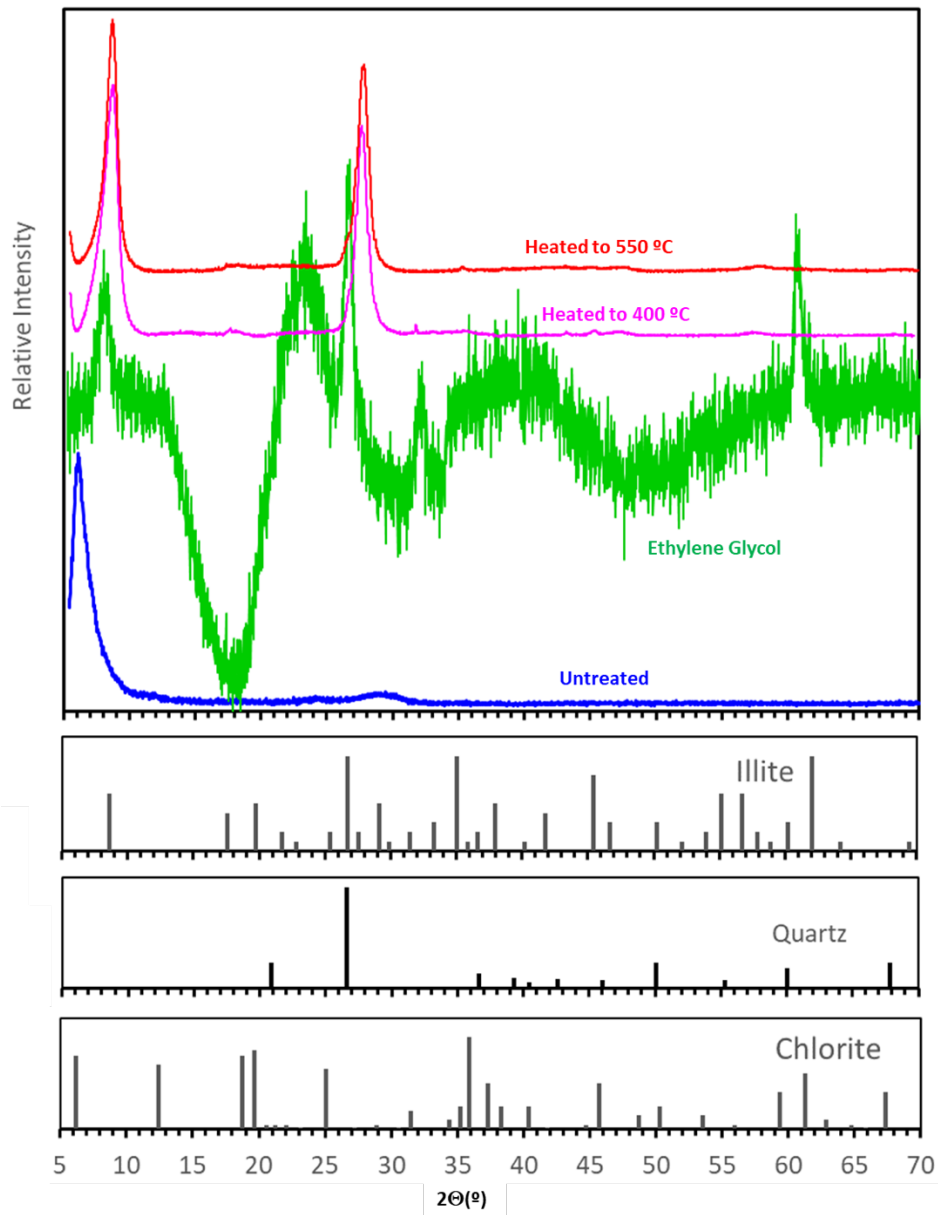
Figure B-22. XRD spectra of post-experimental Test-II Cell 8 (T = 250 ºC, P_{CO2} = 11.6 bars) clay sample.
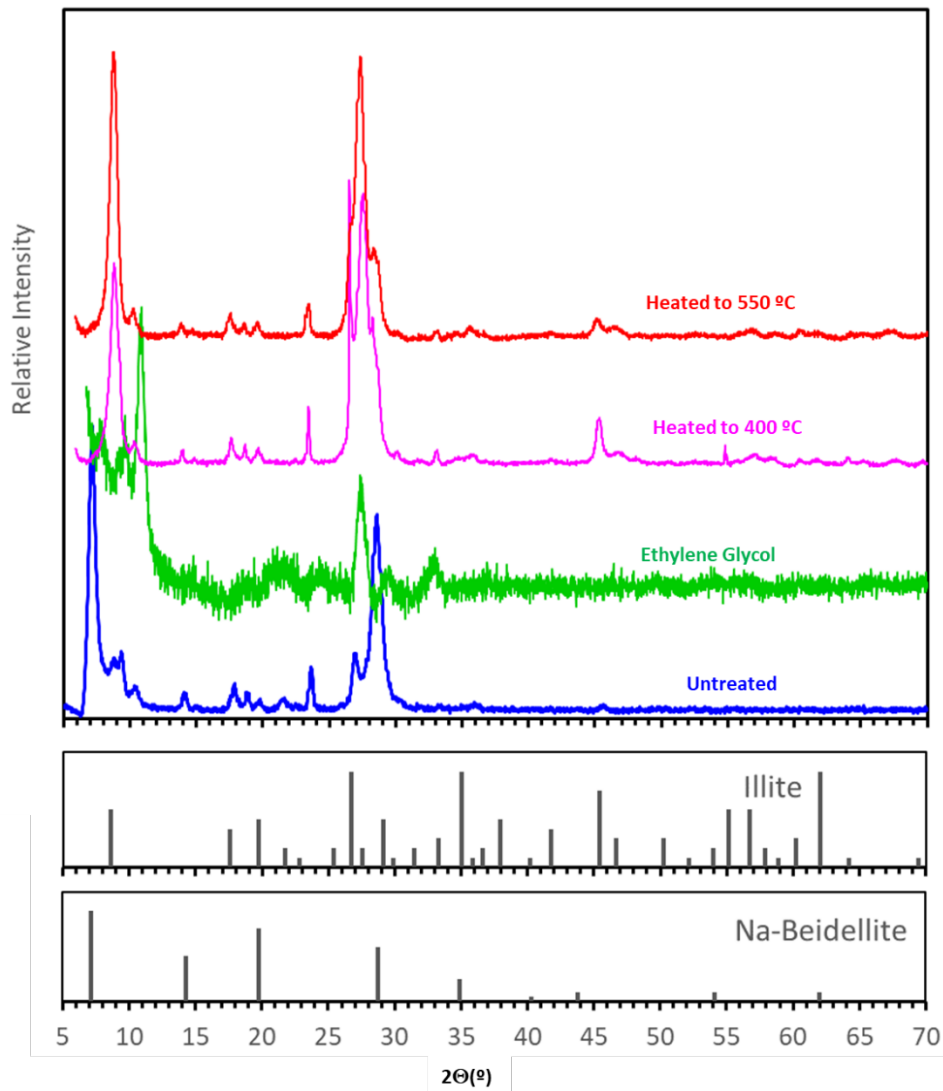
Figure B-23. XRD spectra of post-experimental Test-II Cell 6 (T = 250 ºC, P_{CO2} = 4.2 bars) clay sample.
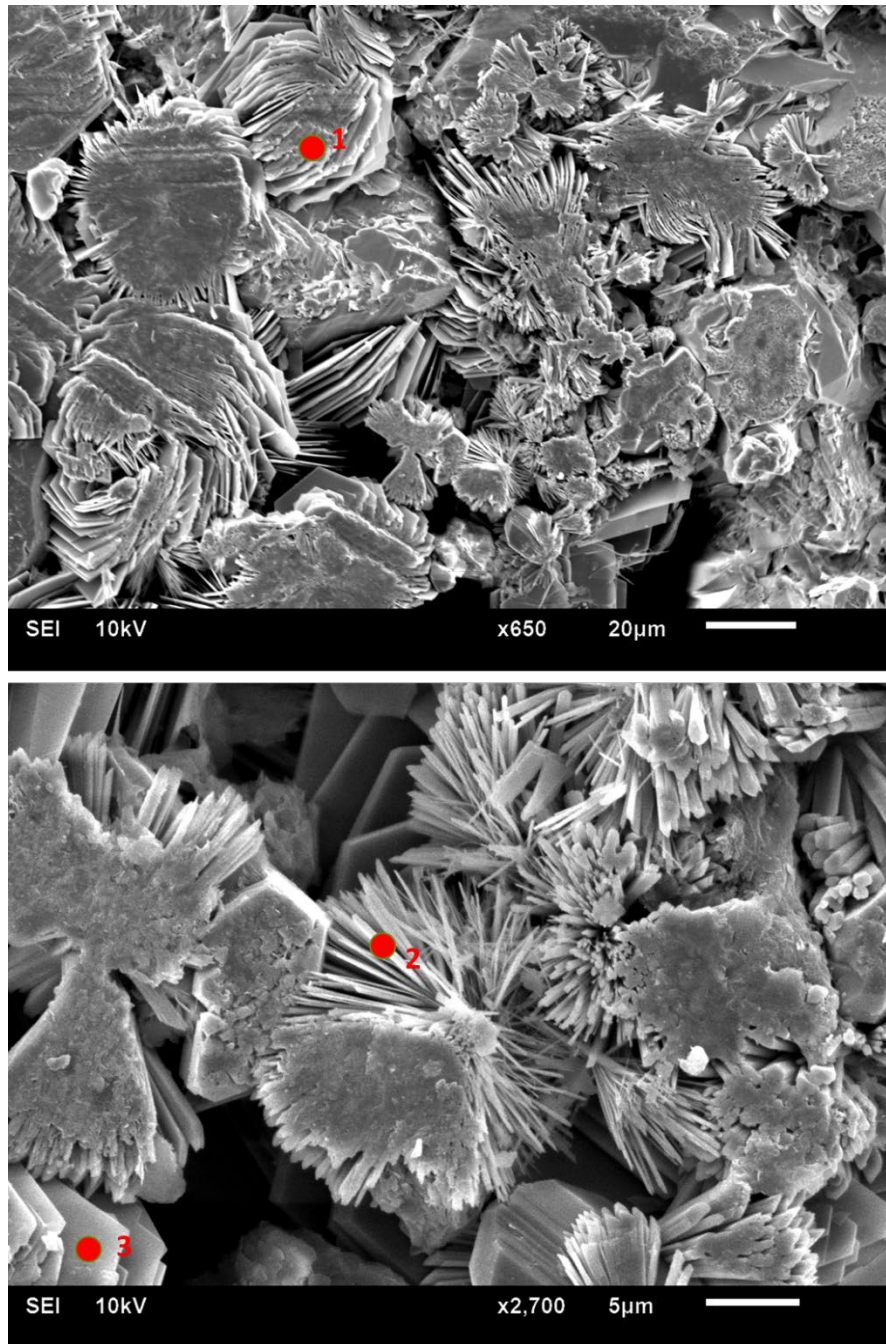
Figure B-24. SEM images of post-experimental Test-II Cell 6 (T = 250 ºC, P_{CO2} =4.2 bars) reacted rock sample. Points 1 and 2: Na-Ca clays (Beidellite), ad 3: Fe-Mg-Ca clays (illite).
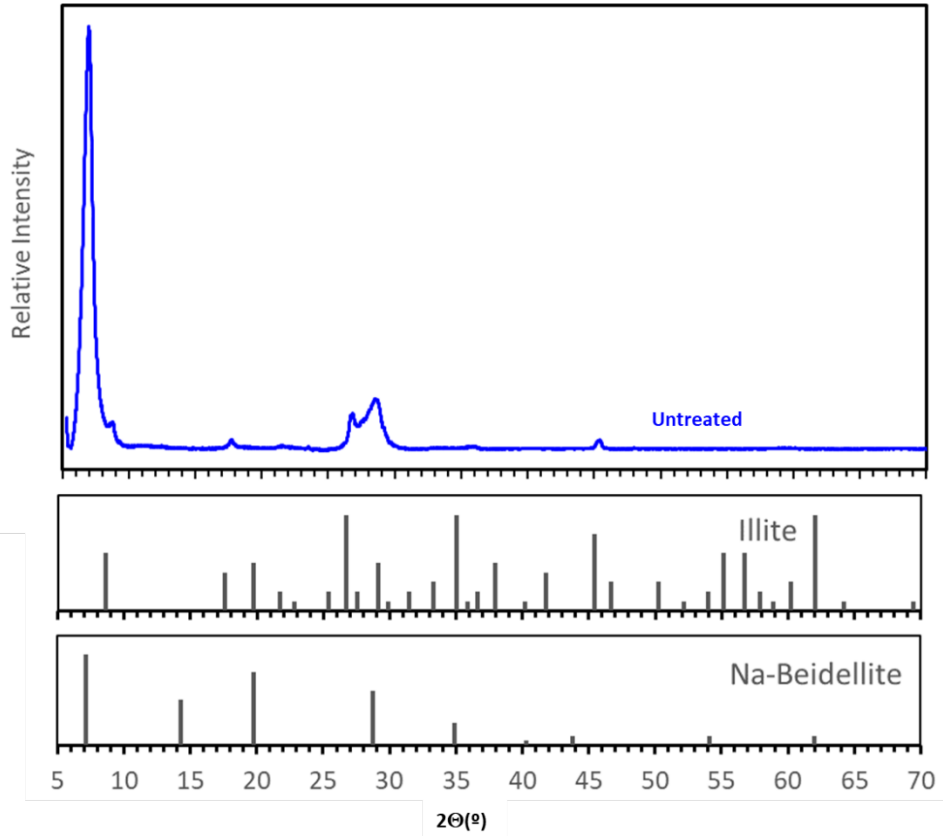
Figure B-25. XRD spectrum of post-experimental Test-II Cell 7 (T = 250 ºC, P$_{CO2}$ = 6.0 bars) clay sample.
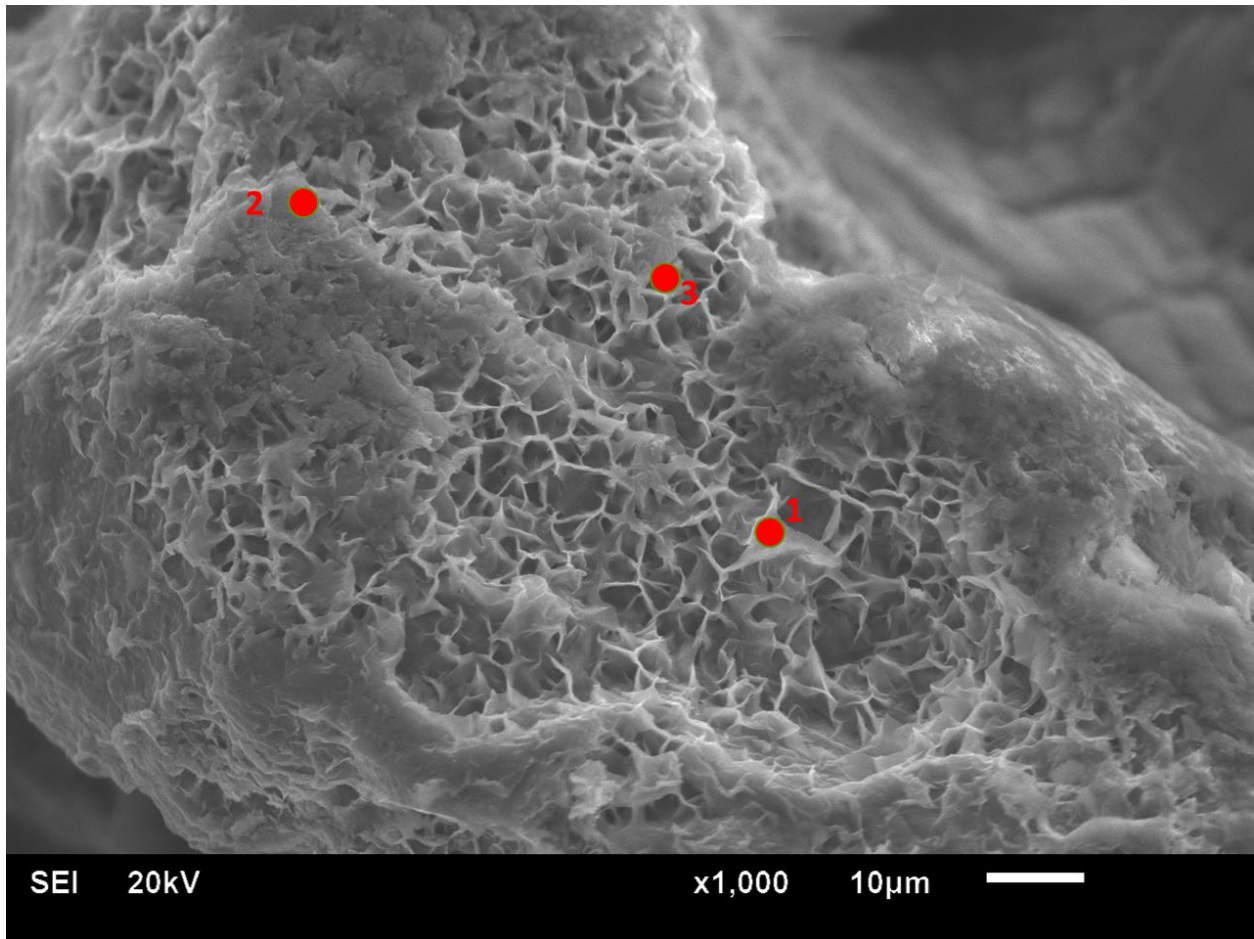
Figure B-26. SEM image of post-experimental Test-II Cell 7 (T = 250 ºC, P_{CO2} = 6.0 bars) reacted rock sample. Points 1 - 3: Fe-Mg-Ca clays (illite).
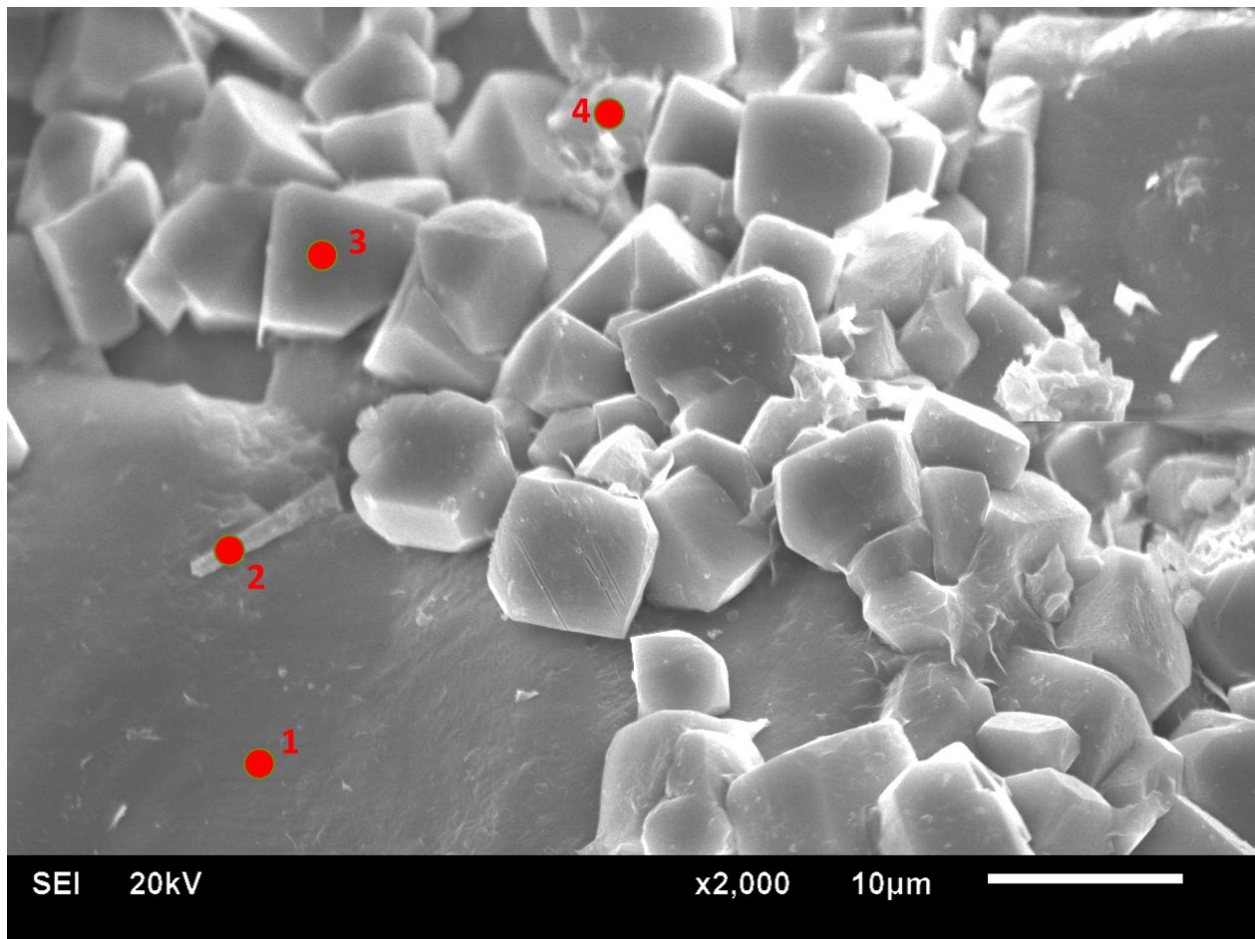
Figure B-27. SEM image of post-experimental Test-II Cell 7 (T = 250 ºC, P_{CO2} = 6.0 bars) reacted rock sample. Points are: 1. Quartz, 2. K-Na-Ca clays (beidellite?), 3. Calcite, 4. Fe-Mg-Ca clays (illite).
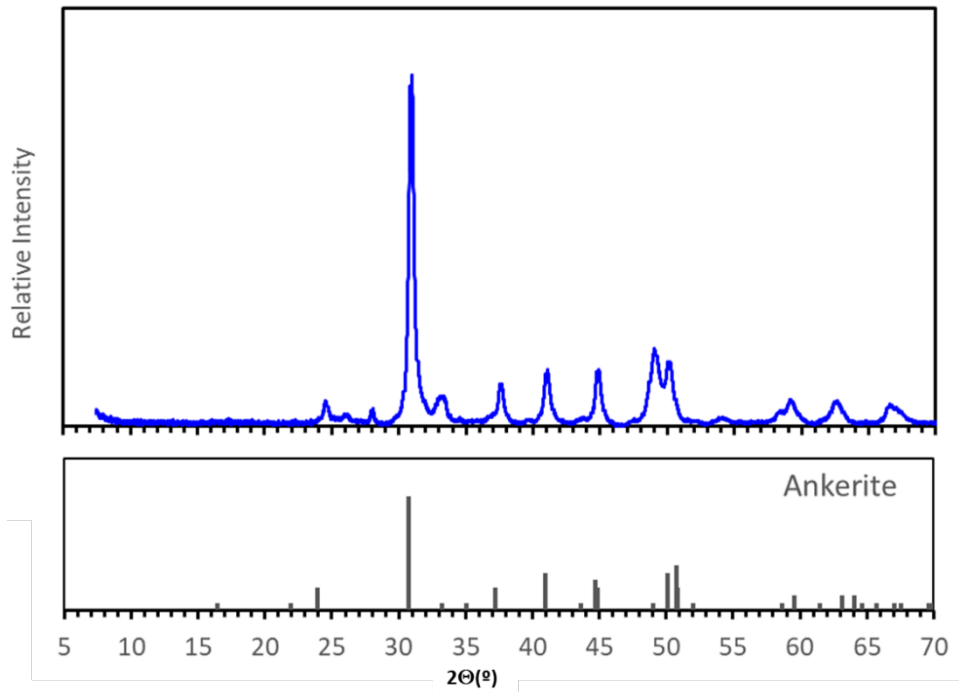
Figure B-28. XRD spectrum of post-experimental Test-III Cell 1 (T = 250 ºC, P_{CO2} = 44.6 bars) scale deposits retrieved from the reaction cell wall. Test-III Cell 1 was brine only reaction cell without Lower Tuscaloosa Formation rock.
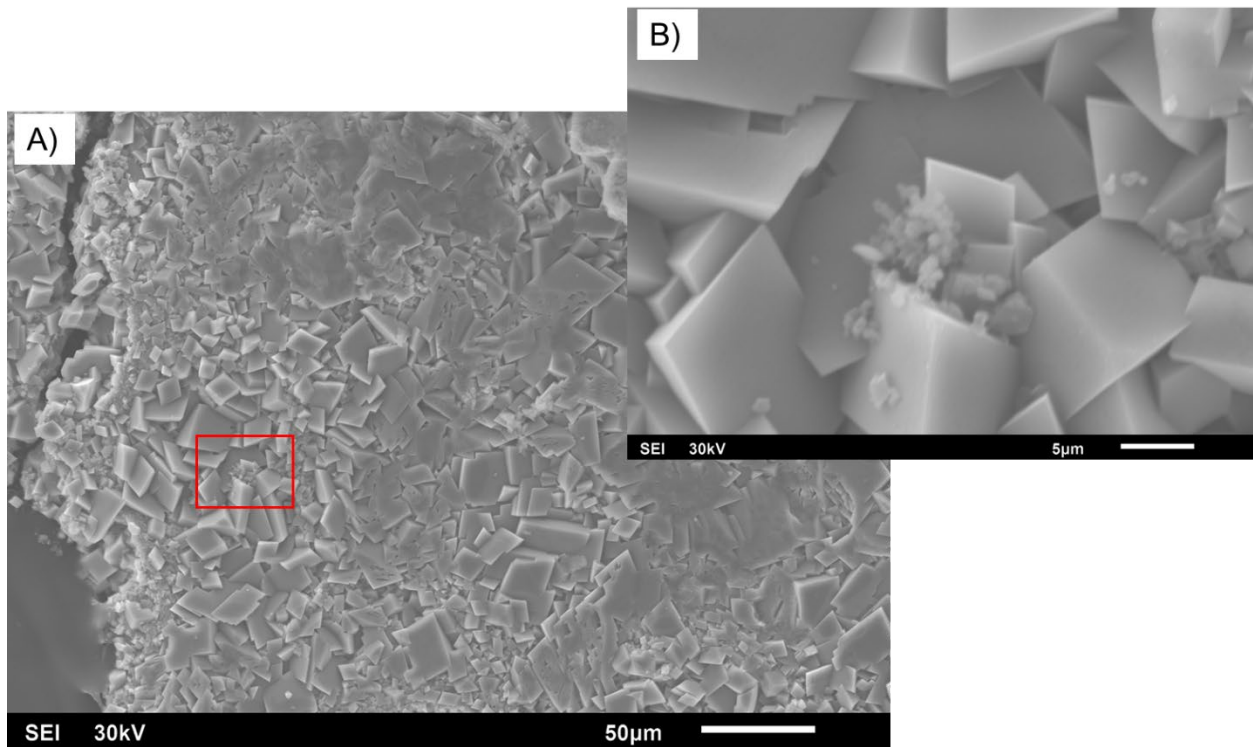
Figure B-29. SEM images (A and B) of post-experimental Test-III Cell 1 (T = 250 ºC, P_{CO2} = 44.6 bars) scale deposits retrieved from the reaction cell wall. Image B is an enlarged part of a scale (red box in A) showing Ni-containing euhedral ankerite crystals.
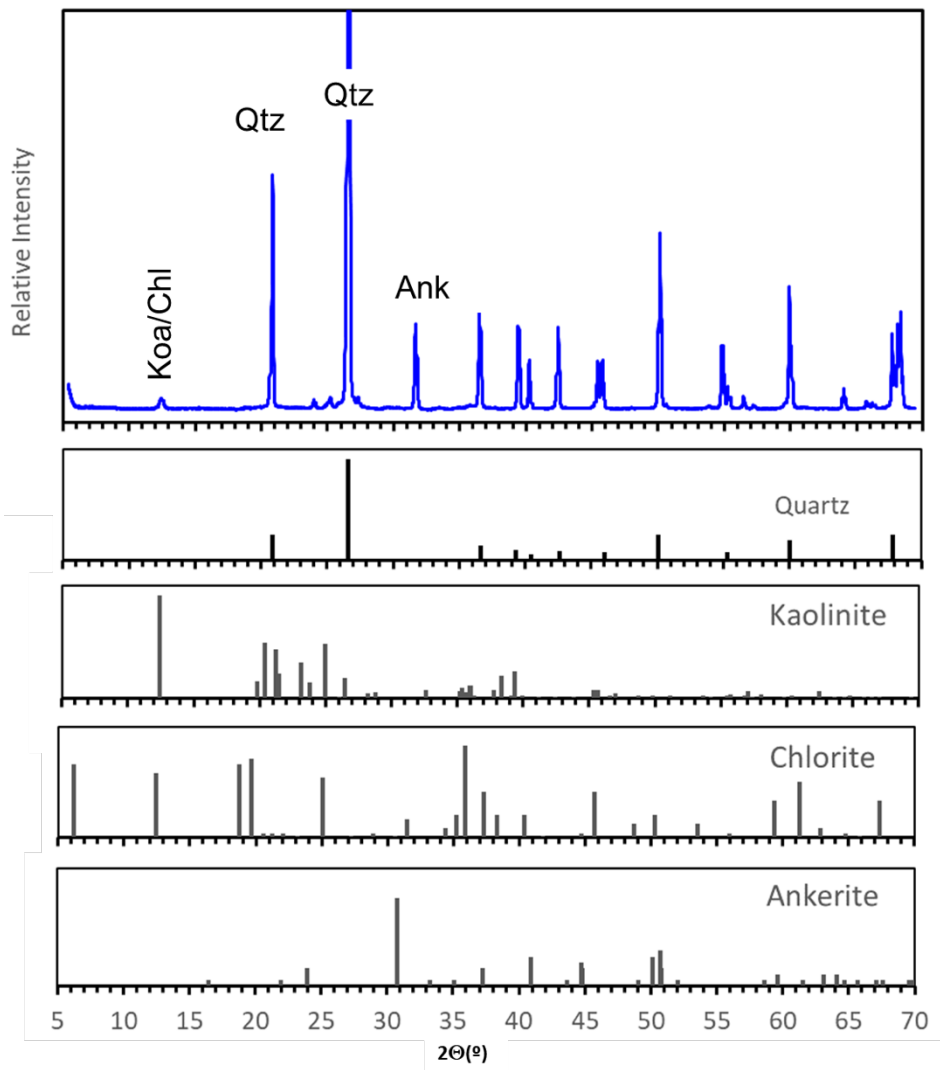
Figure B-30. XRD spectrum of whole-rock of post-experimental Test-III Cell 2 (T = 140 ºC, P_{CO2} = 15.3 bars).
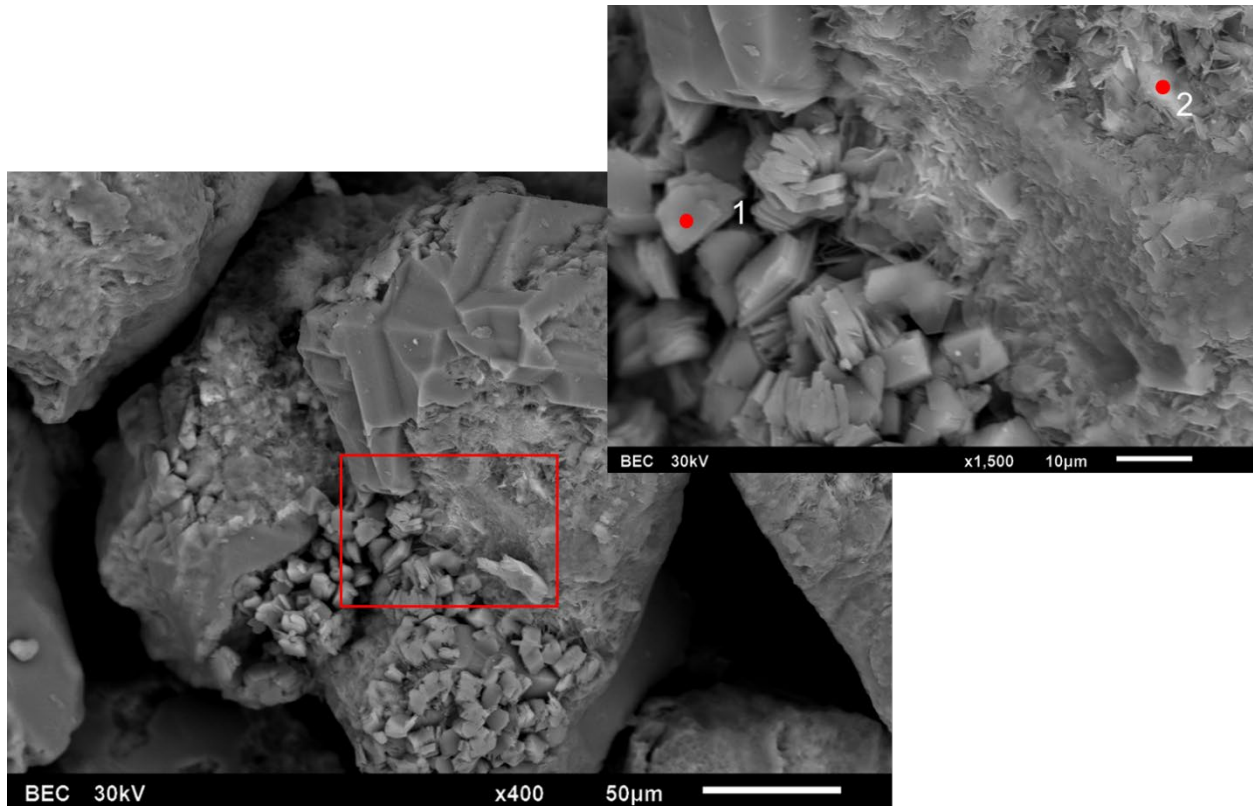
Figure B-31. Scanning electron microscopy images of the post-experimental Lower Tuscaloosa Formation from Test-III Cell 2 (T = 140 ºC, P_{CO2} = 15.3 bars). A) A rock grain (quartz) coated with clays. B) An enlarged part of a grain (red box in A) showing kaolinite (point 1) and chlorite (point 2).
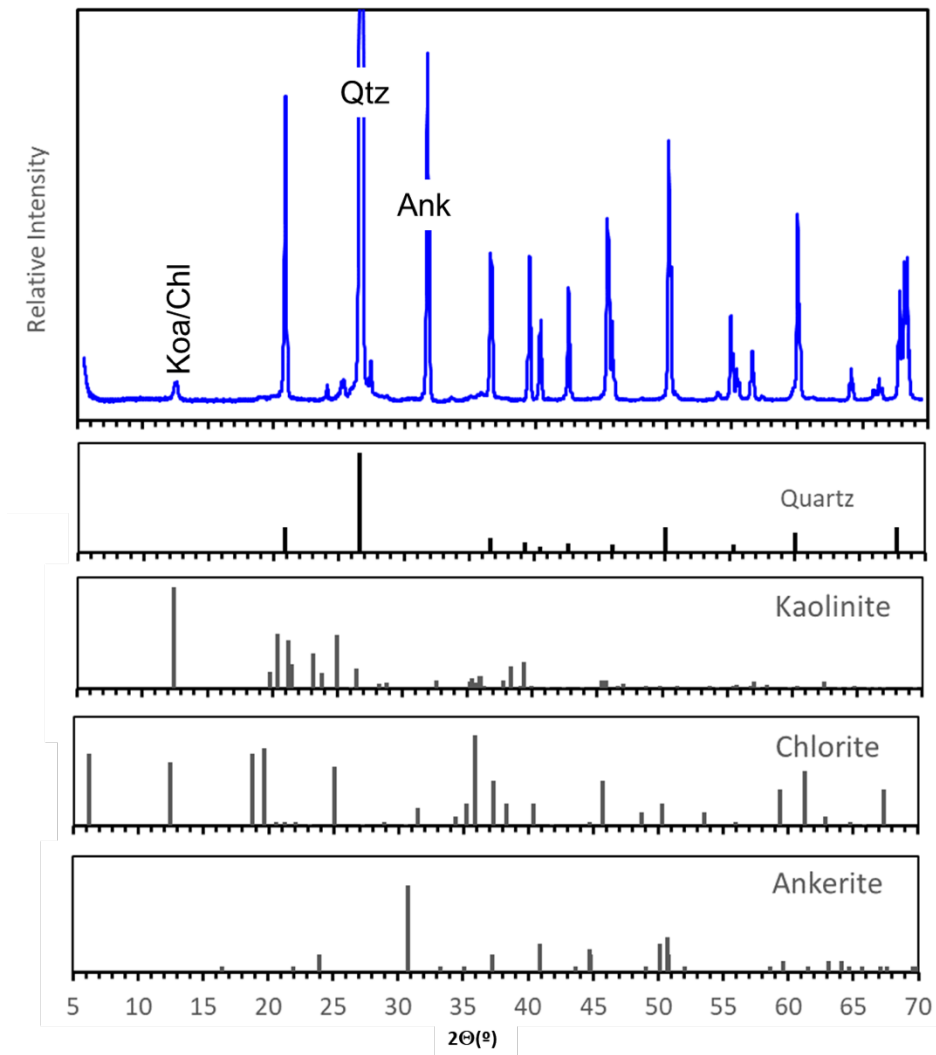
Figure B-32. XRD spectrum of whole-rock of post-experimental Test-III Cell 3 (T = 250 ºC, P_{CO2} = 3.5 bars).
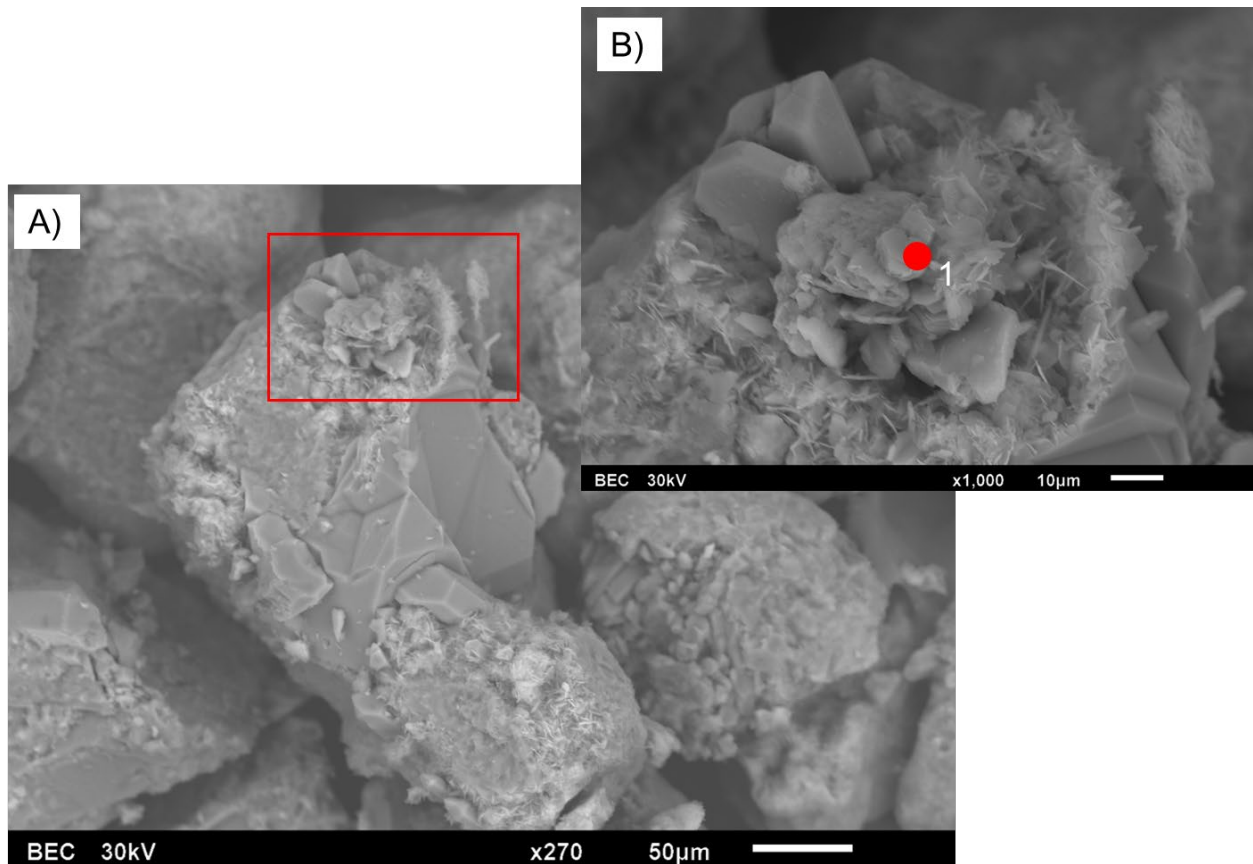
Figure B-33. Scanning electron microscopy images of the post-experimental Lower Tuscaloosa Formation from Test-III Cell 3 (T = 250 ºC, P_{CO2} = 3.5 bars). A) A rock grains (quartz) coated with clays. B) An enlarged part of a grain (red box in A) showing kaolinite (point 1).
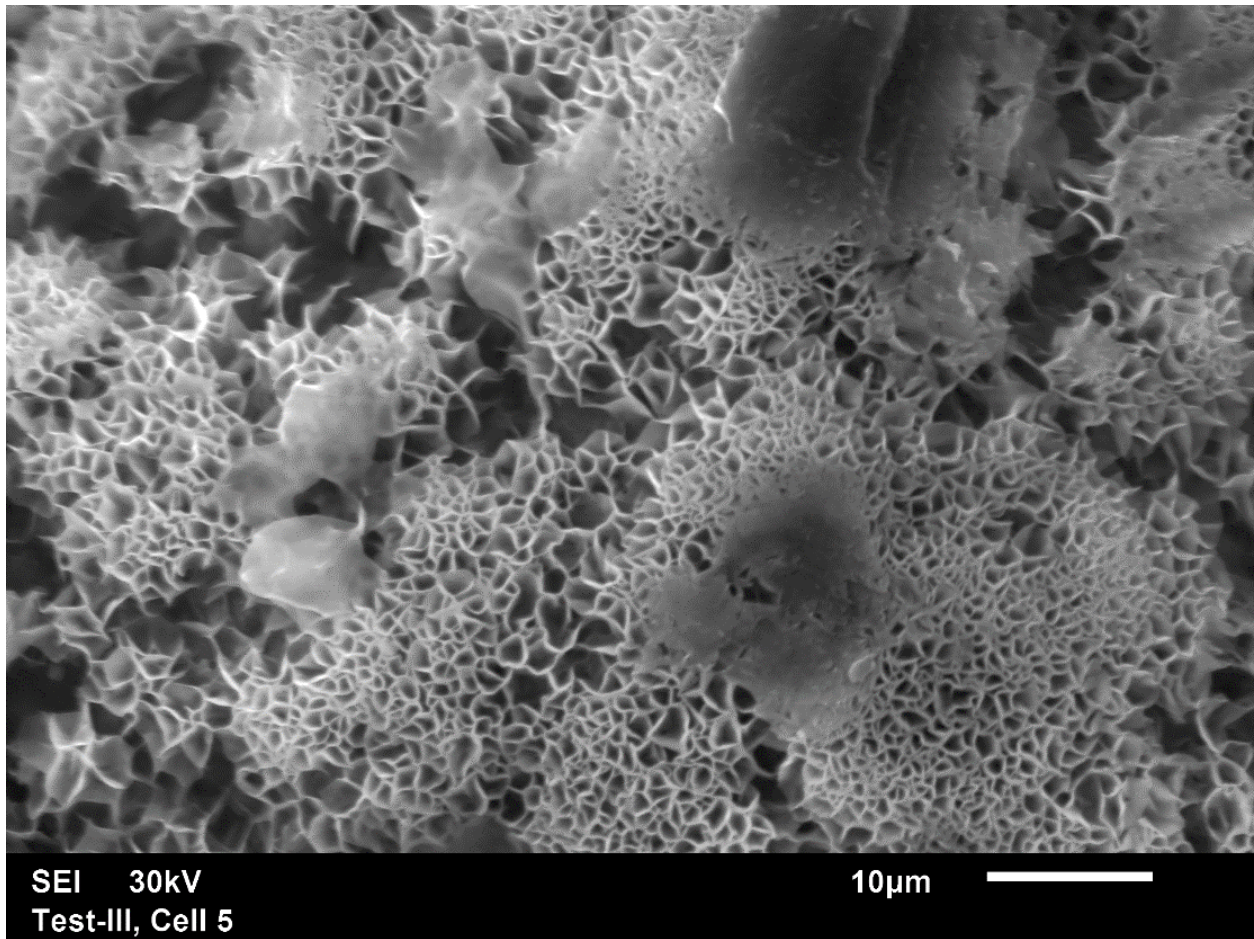
Figure B-34. Scanning electron microscopy image of the post-experimental Lower Tuscaloosa Formation from Test-III Cell 5 (T = 250 ºC, P_{CO2} = 2.7 bars). The grain coating material is Na-Fe-Ca-Mg-Ni clay minerals.
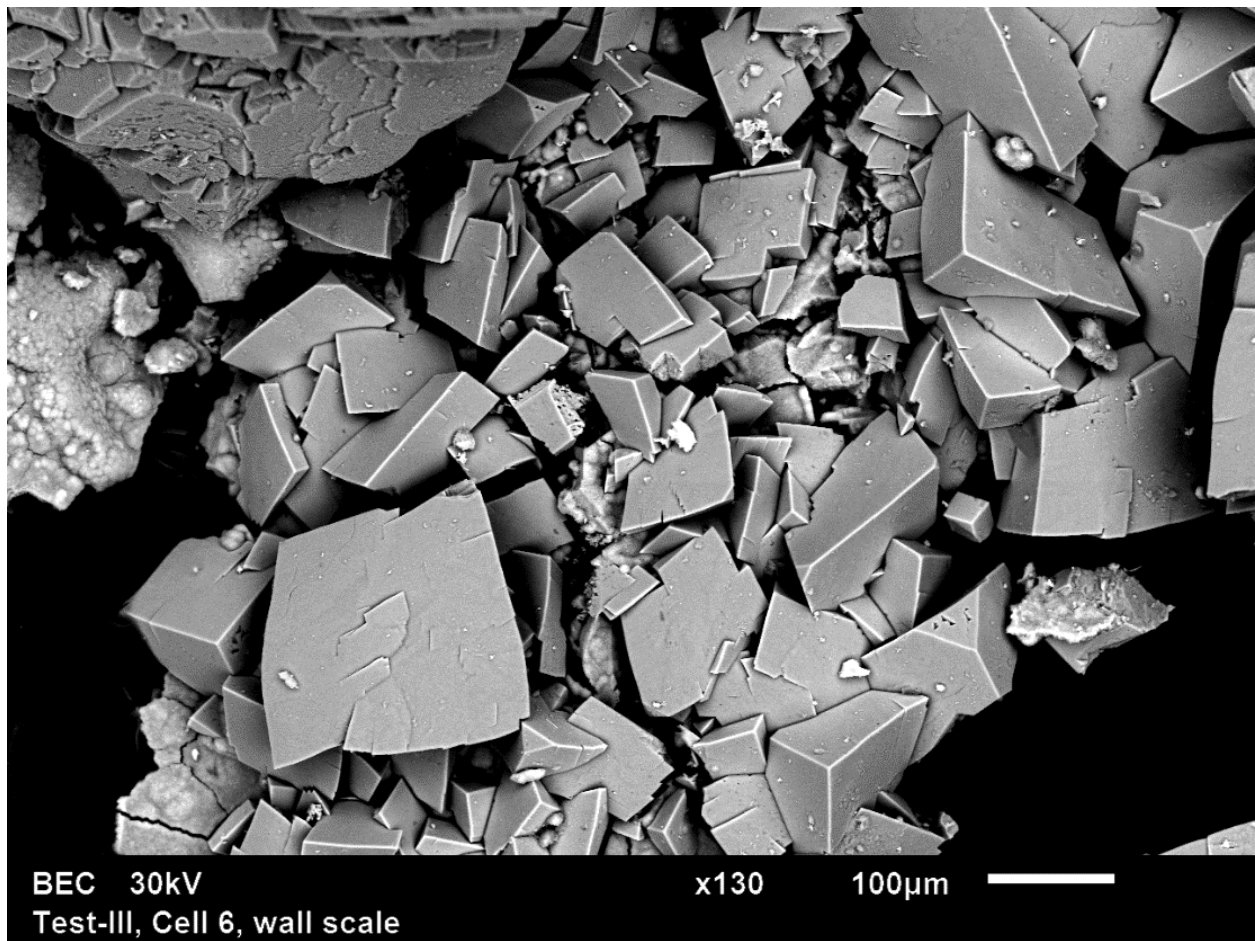
Figure B-35. Scanning electron microscopy image of the reaction cell wall-scale from Test-III Cell 6 (T = 250 ºC, P_{CO2} = 13.1 bars). The grains are ankerite crystals.
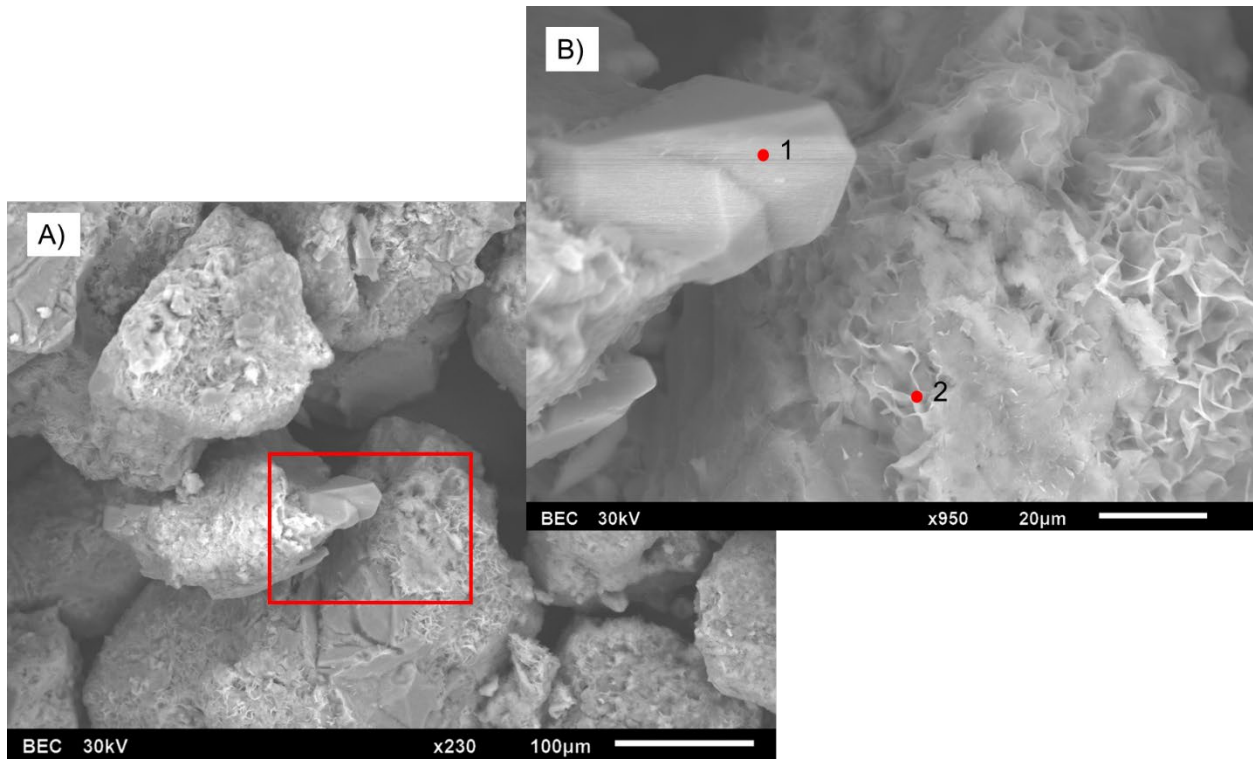
Figure B-36. Scanning electron microscopy images of the post-experimental Lower Tuscaloosa Formation from Test-III Cell 6 (T = 250 ºC, P_{CO2} = 13.1 bars). A) Several rock grains (quartz) coated with secondary minerals. B) An enlarged part of a grain (red box in A) showing secondary quartz (point 1) and Mg-Fe clay (chlorite) (point 2).
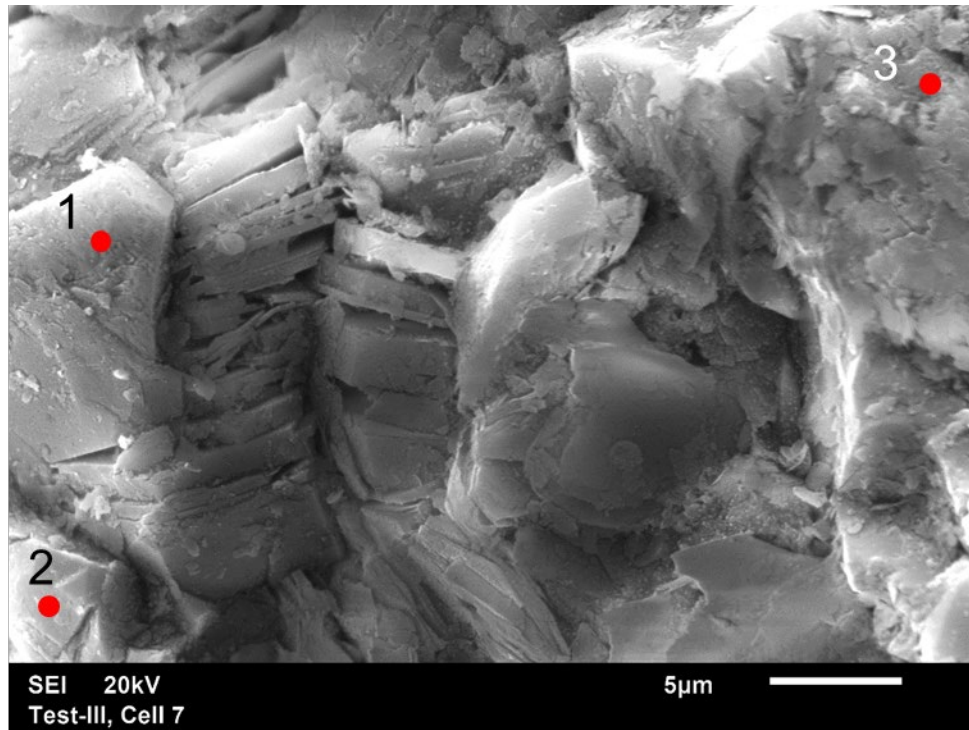
Figure B-37. Scanning electron microscopy images of the post-experimental Lower Tuscaloosa Formation from Test-III Cell 7 (T = 250 ºC, P_{CO2} = 49.8 bars). Points 1 & 2 are kaolinite, point 3 is Fe-Mg clays.
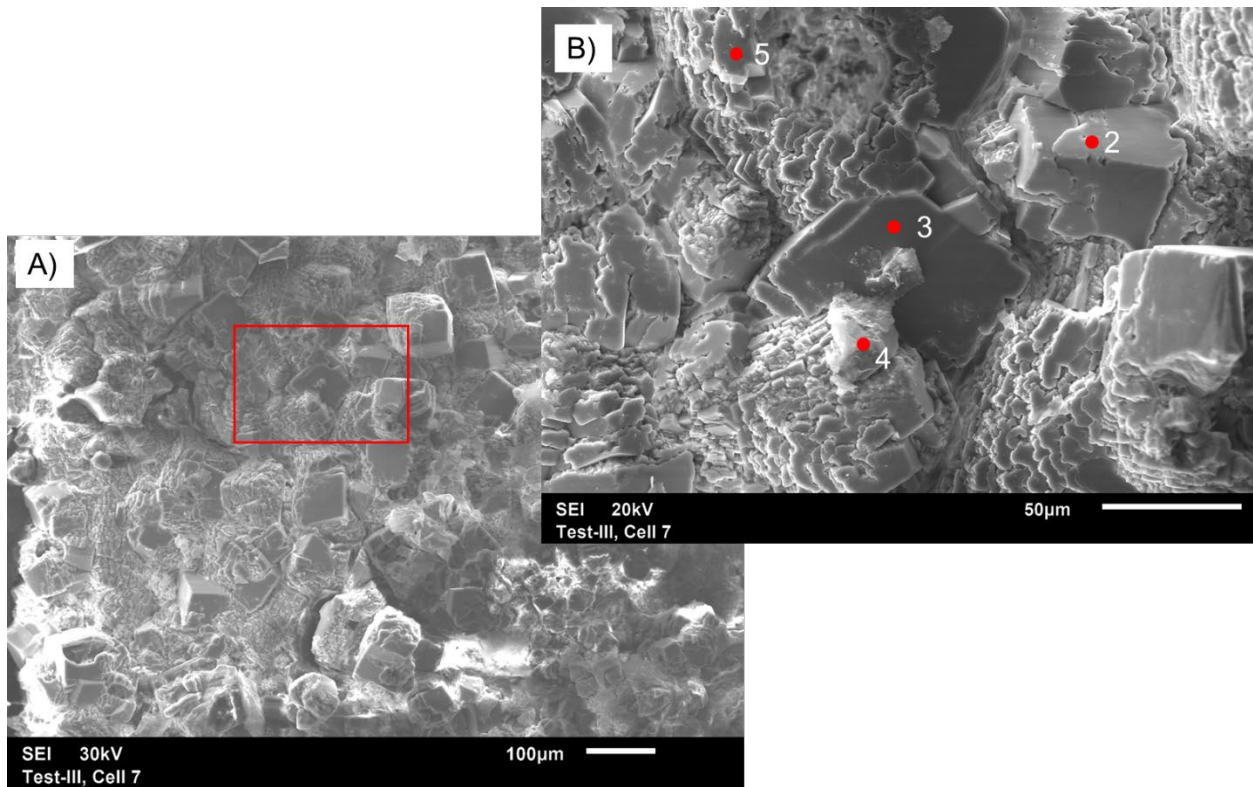
Figure B-38. Scanning electron microscopy images of the post-experimental Lower Tuscaloosa Formation from Test-III Cell 7 (T = 250 ºC, P_{CO2} = 49.8 bars). A) Rock grains are coated with secondary minerals. B) An enlarged part of a grain (red box in A) showing secondary calcite (points 2, 3, & 5) and Mg-Fe clay (point 4).

Appendix C

TOUGHREACT Comparison
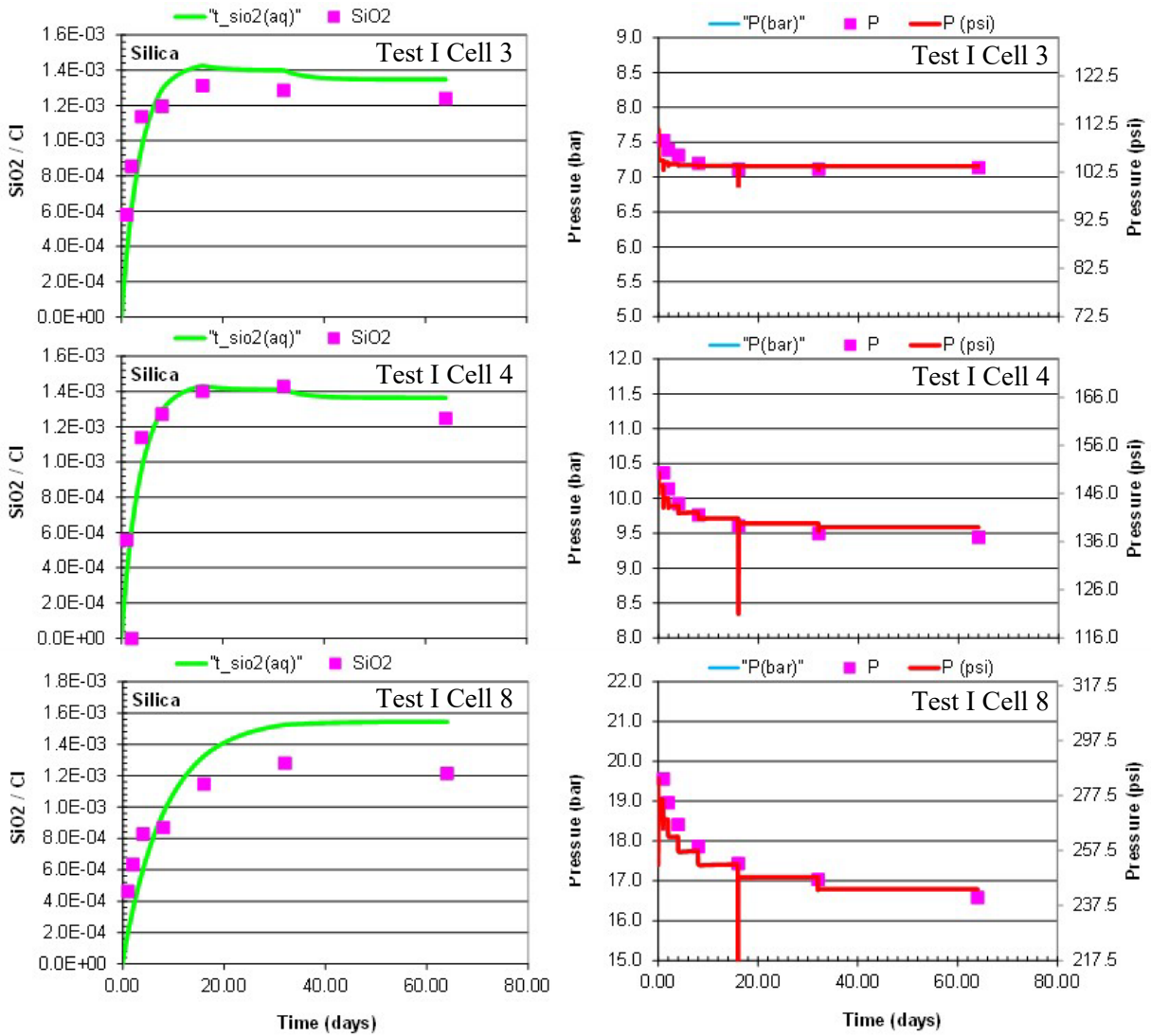
Figure C-1. Comparison of measured and model calibrated normalized $SiO_{2,aq}$ concentration and total pressure for 160°C Weber brine-rock experiments 160°C using TOUGHREACT ECO2N together with the Pitzer data0.ypf.R2 thermodynamic database.
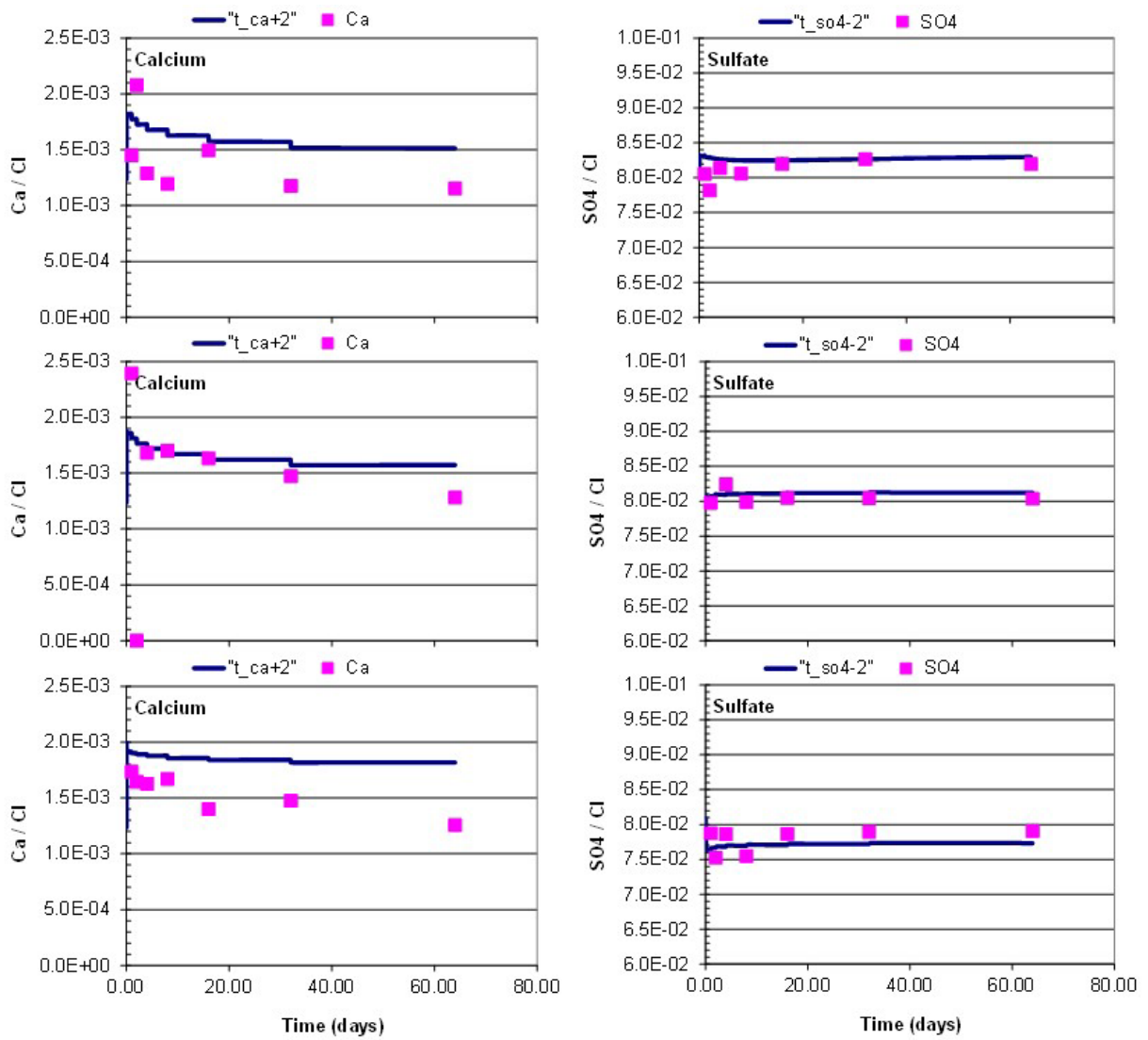
Figure C-2. Comparison of measured and simulated normalized Ca and SO_4 concentrations for 160°C Weber brine-rock experiments using TOUGHREACT ECO2N together with the Pitzer data0.ypf.R2 thermodynamic database.
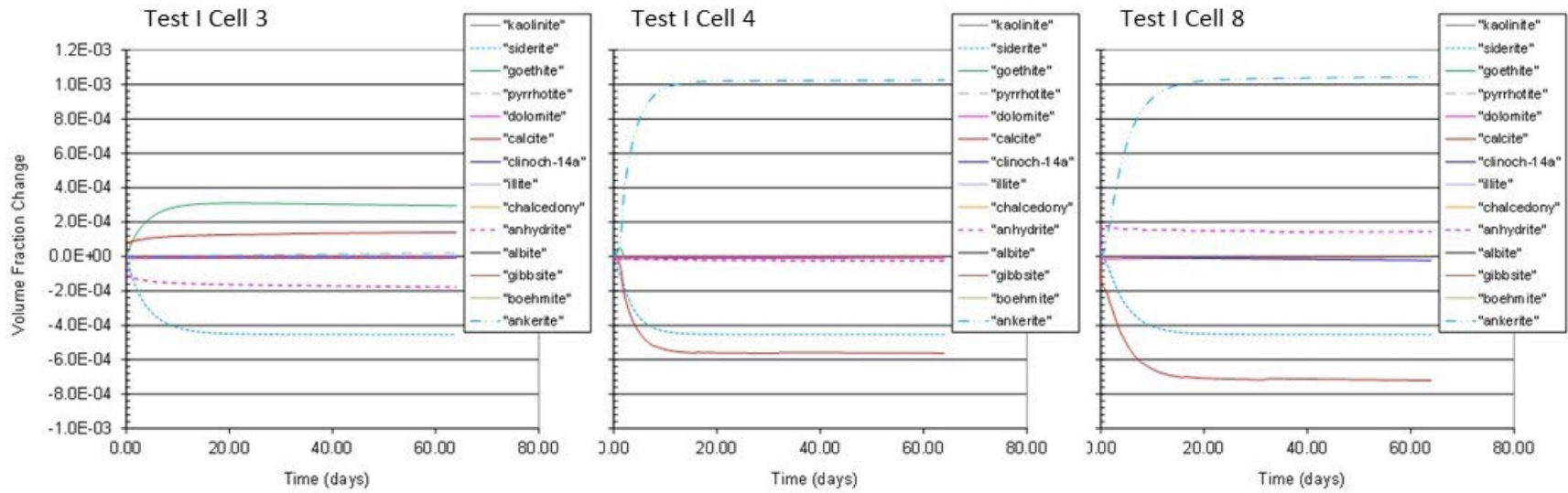
Figure C-3. Simulated mineral dissolution and precipitation for 160°C Weber brine-rock experiments using TOUGHREACT ECO2N together with the Pitzer data0.ypf.R2 thermodynamic database.
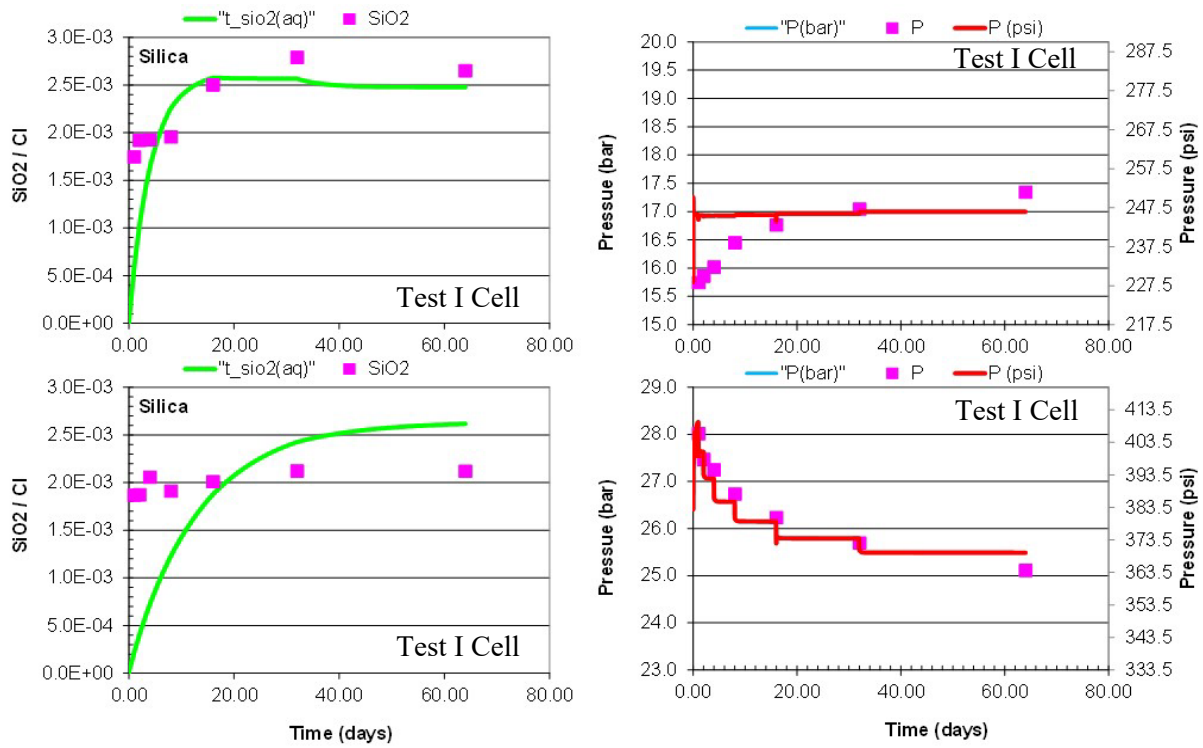
Figure C-4. Comparison of measured and model calibrated normalized $SiO_{2,aq}$ concentration and total pressure for 200°C Weber brine-rock experiments using TOUGHREACT ECO2N together with the Pitzer data0.ypf.R2 thermodynamic database.
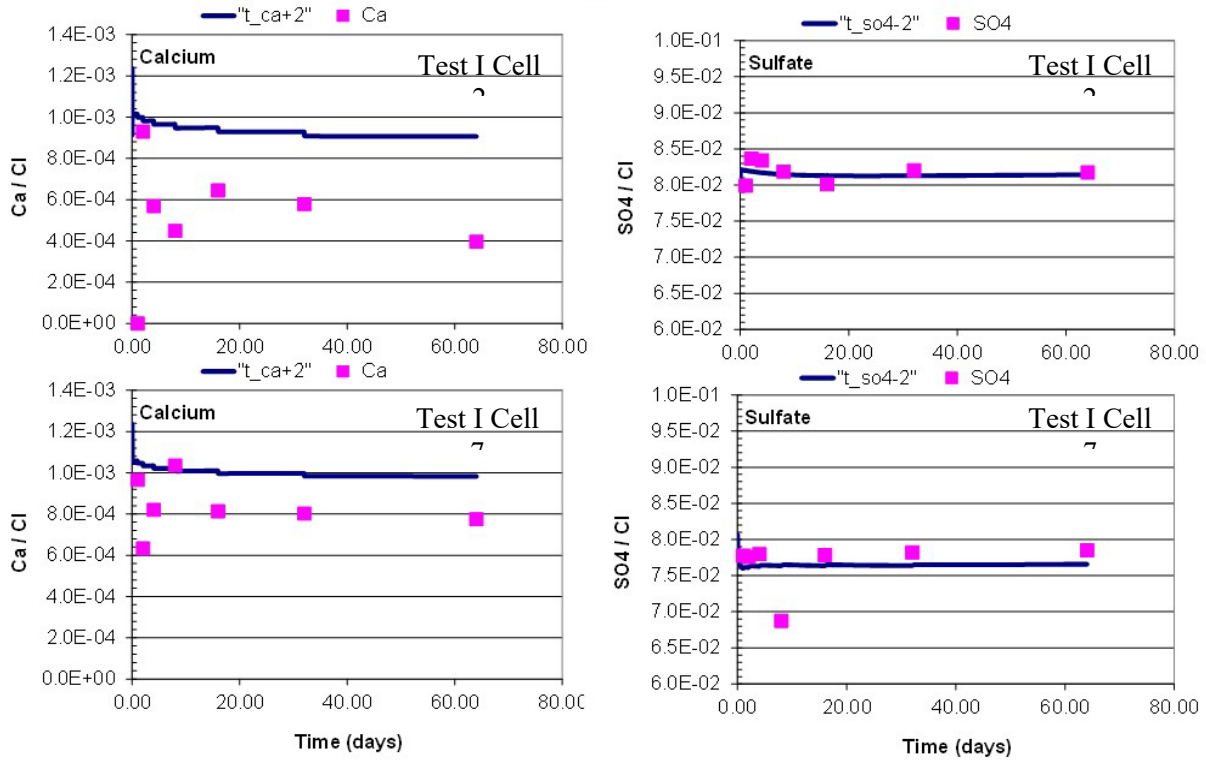
Figure C-5. Comparison of measured and simulated normalized Ca and SO₄ concentrations for 200°C Weber brine-rock experiments using TOUGHREACT ECO2N together with the Pitzer data0.ypf.R2 thermodynamic database.
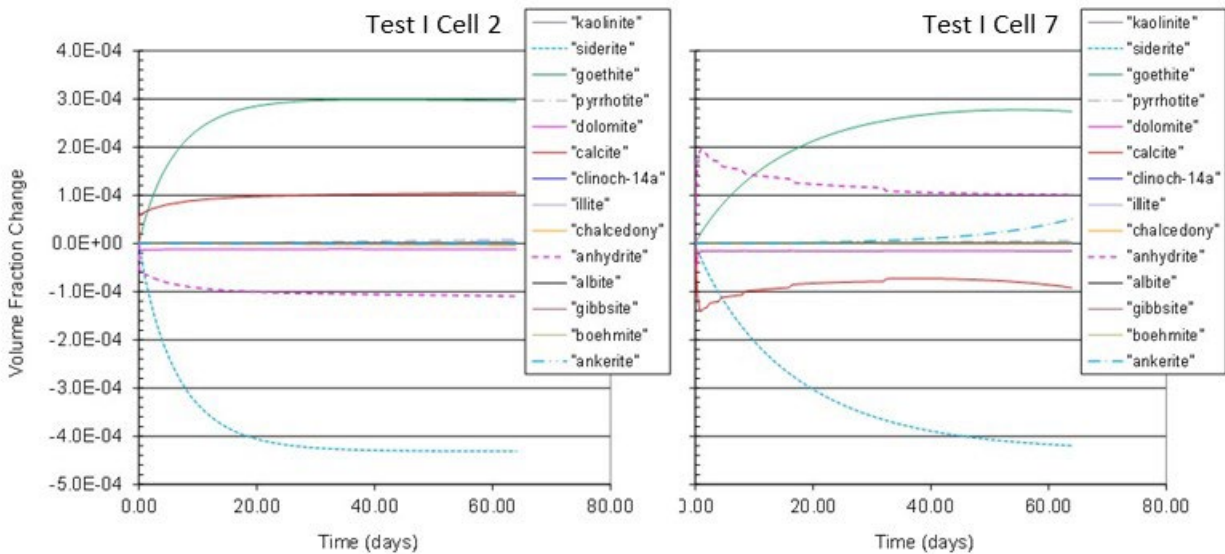

Figure C-6. Simulated mineral dissolution and precipitation for 200°C Weber brine-rock experiments using TOUGHREACT ECO2N together with the Pitzer data0.ypf.R2 thermodynamic database.
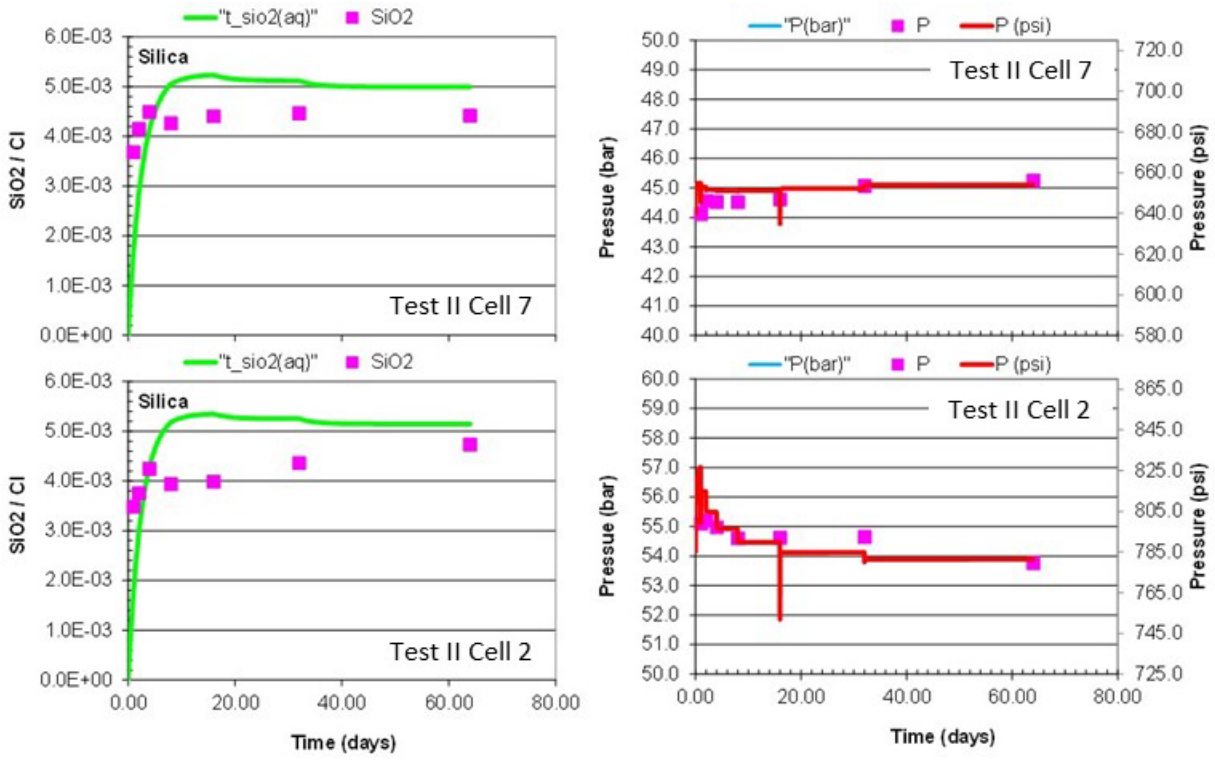
Figure C-7. Comparison of measured and model calibrated normalized $SiO_{2,aq}$ concentration and total pressure for 250°C Weber brine-rock experiments using TOUGHREACT ECO2N together with the Pitzer data0.ypf.R2 thermodynamic database.
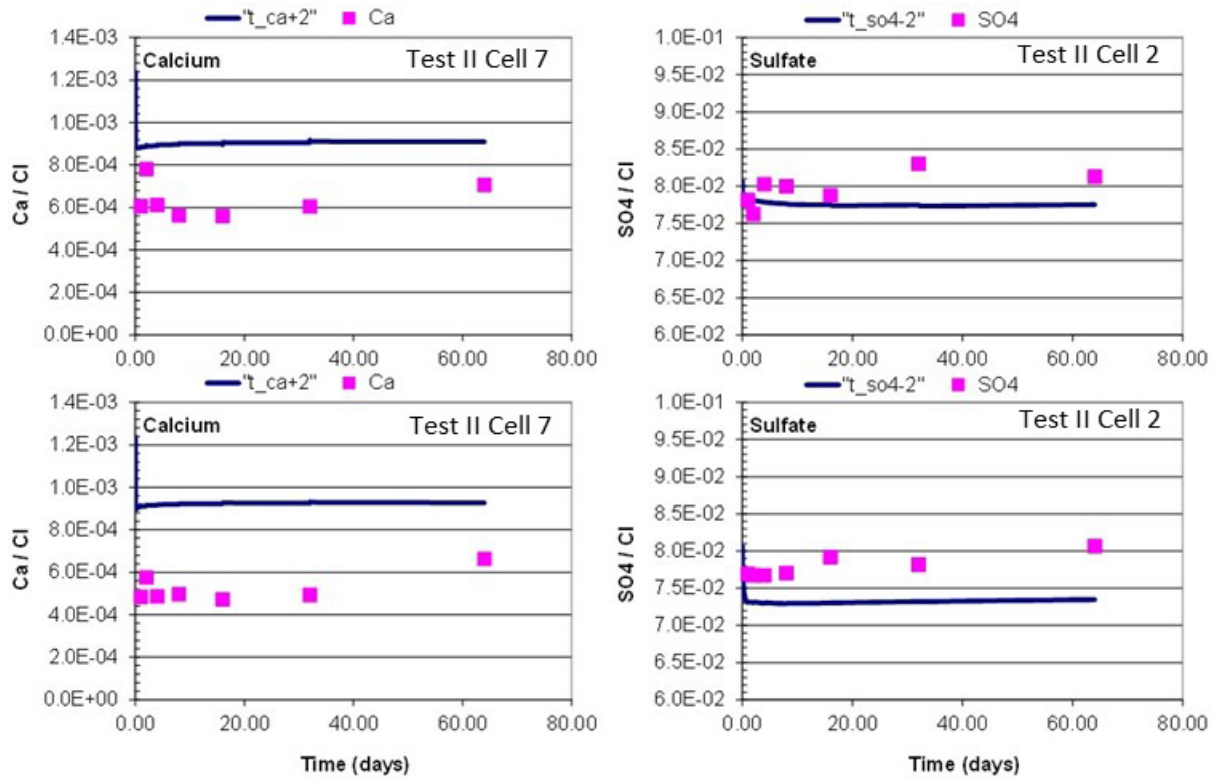
Figure C-8. Comparison of measured and simulated normalized Ca and SO₄ concentrations for 250°C Weber brine-rock experiments using TOUGHREACT ECO2N together with the Pitzer data0.ypf.R2 thermodynamic database.
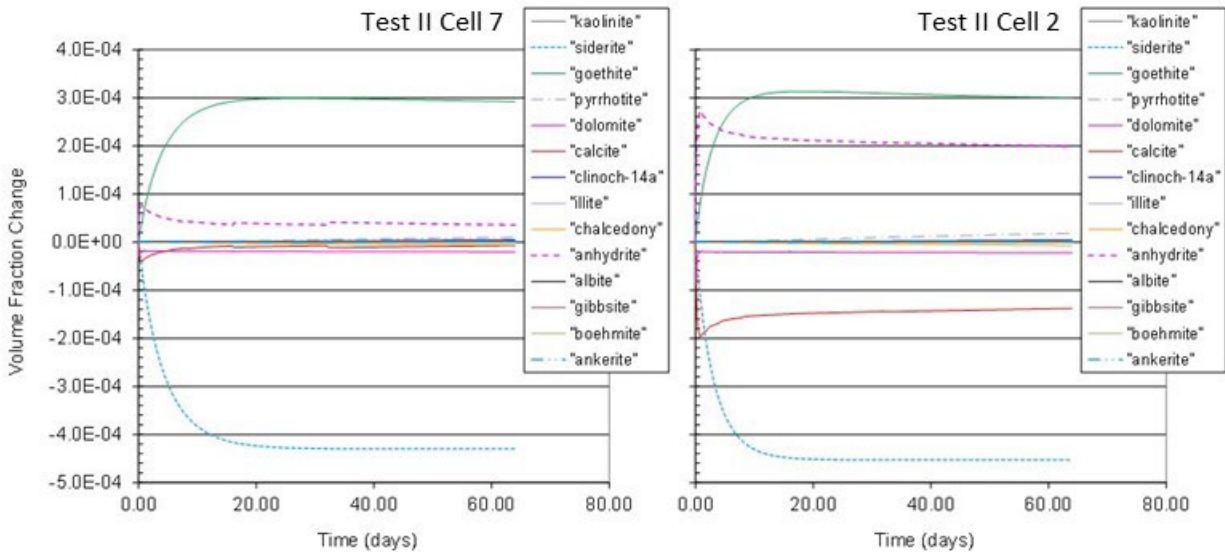

Figure C-9. Simulated mineral dissolution and precipitation for 250°C Weber brine-rock experiments using TOUGHREACT ECO2N together with the Pitzer data0.ypf.R2 thermodynamic database.

144
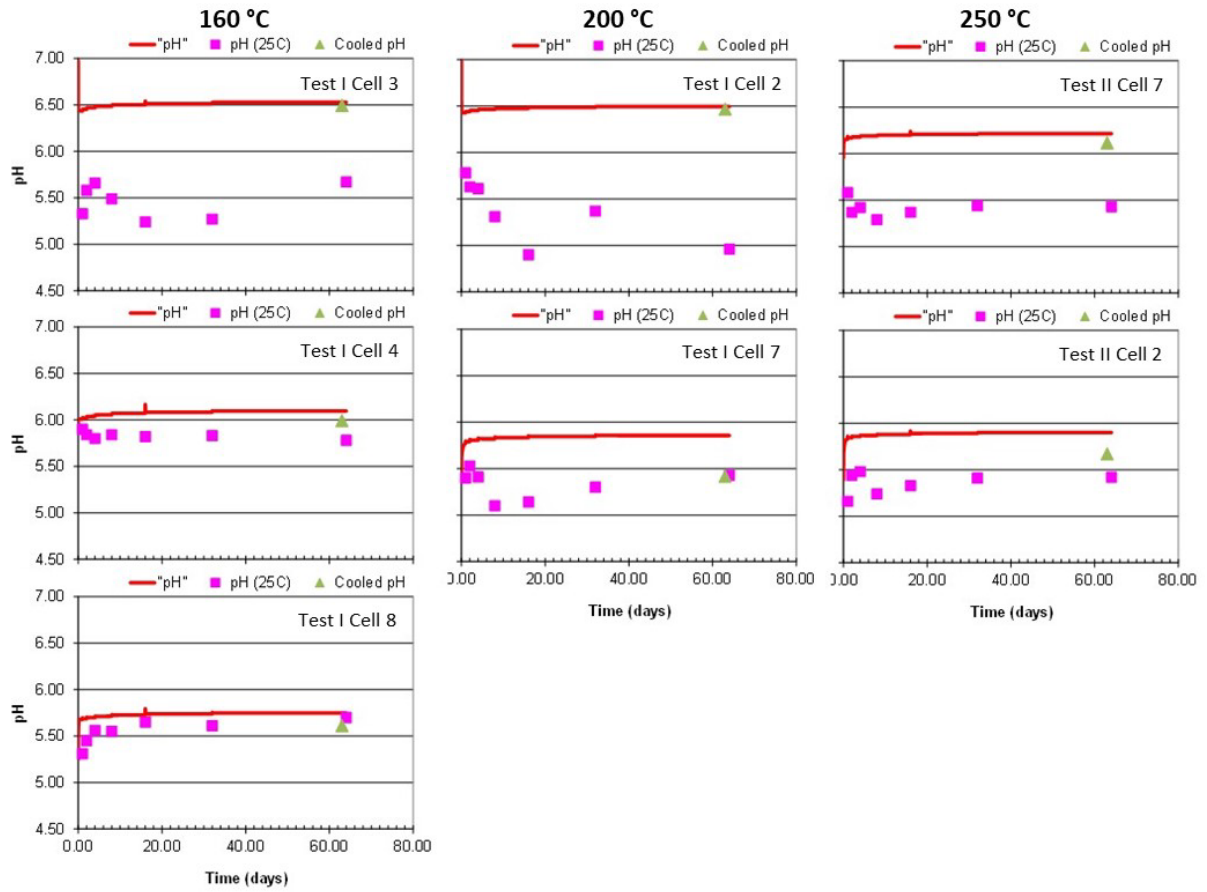
Figure C-10. Comparison of observed and simulated pH values Weber brine-rock experiments using TOUGHREACT ECO2N together with the Pitzer data0.ypf.R2 thermodynamic database.

Appendix D

Published Papers Resulting from Phase I of this Project

Jin, W., Atkinson, T., Doughty, C., Neupane, G., Spycher, N., McLing, T., Dobson, P., Smith, R., and Podgorney, R. 2022. "Machine learning assisted high-temperature geological thermal storage optimization," *Renewable Energy*, under review.

Jin, W., Atkinson, T. Neupane, G., McLing, T., Doughty, C., Spycher, N., Dobson, P., and Smith, R. 2022. "Influence of mechanical deformation and mineral dissolution/precipitation on reservoir thermal energy storage," *56th US Rock Mechanics/Geomechanics Symposium,* Santa Fe, NM, ARMA 22-2068.

Jin, W., Podgorney, R., McLing, T., and Carlsen, R.W. 2021. "Geothermal battery optimization using stochastic hydro-thermal simulations and machine learning algorithms," *55th US Rock Mechanics/Geomechanics Symposium*, Houston, TX, ARMA 21-1243.

Neupane, G., Smith, R.W., McLing, T.L., Atkinson, T.A., McLaughlin, J.F., Spycher, N., and Dobson, P.F. 2021. "Experimental assessment of geochemistry of geologic thermal energy storage (GeoTES) systems," *GRC Transactions* **45**, 1149-1167.

Neupane, G., Smith, R.W., McLing, T.L., McLaughlin, J.F., Spycher, N., and Dobson, P.F. 2020. "Geochemistry of Geologic Thermal Energy Storage (GeoTES) systems: assessment of the Weber Sandstone, western Wyoming, USA," *Geothermal Resources Council Transactions* **44**, 1110–1122.

Spycher, N., Doughty, C., Dobson, P., Neupane, G., Smith, R., Jin, W., Atkinson, T., and McLing, T. 2021. "Evaluation of mineral scaling during high-temperature thermal energy storage in deep saline aquifers," *GRC Transactions* **45**, 1201-1215.